VOLCANOLOGY AND GEOCHEMISTRY OF THE CRETACEOUS VOLCANICLASTIC DEPOSITS AND BASALTS FROM ORI MASSIF, SHATSKY RISE OCEANIC PLATEAU

Irina Romanova

BSc (2007), MSc (2009)

Submitted in fulfilment of the requirements for the degree of

Doctor of Philosophy

School of Earth, Environmental and Biological Sciences

Science and Engineering Faculty

Queensland University of Technology

2017

Keywords

Shatsky Rise
IODP Expedition 324
Large Igneous Province
Oceanic plateau
Cretaceous magmatism
Basalt
Volcaniclastic deposits
Phreatomagmatic volcanism
Surtseyan-style shallow-marine volcanism
Paleoelevation
Nd-Hf isotope geochemistry
Magmatic sources
Seawater alteration
Magnesium
Element mobility
Mantle plume and spreading ridge interaction
North-western Pacific

Abstract

Oceanic plateaus are an important class of Large Igneous Provinces (LIPs) and represent the most voluminous examples of oceanic intraplate magmatism, with crustal thicknesses reaching 10-40 km and areal extents exceeding 0.1 Mkm^2. Formation of oceanic plateaus remains highly debated, with arguments that they form during impact of a mantle plume head with oceanic lithosphere or that they represent anomalously high degrees of melting associated with shallow plate tectonic processes. Shatsky Rise in the North-Western Pacific is one of the largest (~500,000 km^2) and oldest (145-135 Ma) non-accreted oceanic plateaus and provides evidence that is consistent with both models for oceanic plateau formation. Studies of magnetic lineations and bathymetry showed that Shatsky Rise was formed at a triple junction of oceanic spreading ridges and has three edifices (Tamu, Ori and Shirshov Massifs) progressively decreasing in age and in volume.

Research from this thesis has been focused on Ori Massif, the second largest and oldest edifice from the central part of the Shatsky Rise, to provide constraints on its formation and evolution. The Ori Massif has been investigated in terms of paleoelevations that this edifice reached upon formation, source contributions to this edifice, and seawater alteration effect on the primary magmatic signatures of basalts from this edifice. This was achieved with the petrographic, lithostratigraphic, major and trace element and Hf-Nd isotope geochemical, mineralogical and multivariate analyses of samples retrieved from Ori Massif during the Integrated Ocean Drilling Program Expedition 324.

Volcaniclastic deposits from the summit of Ori Massif, are ~30 m thick and predominantly composed of juvenile fragments (from 70 to 100 modal % on a cement-free basis) with minor amounts of accidental lithics and singular shallow-marine fossils. The abundance of poorly to moderately vesicular quenched glass fragments, mainly angular lithics along with cored juvenile clasts within the volcaniclastic succession suggests explosive fragmentation of basaltic magma and pre-existing rocks during phreatomagmatic eruptions. The volcaniclastic succession from Ori Massif is characterised by poor sorting, thick-bedded to massive structure and contains no sharp erosional boundaries or sedimentary interbeds, and therefore is interpreted to represent

one eruptive unit. Preservation of gentle textures and forms of the glass fragments within the deposits imply relatively limited reworking processes during transportation from the vent. The volcaniclastic material was produced during shallow-marine to near sea-level Surtseyan style phreatomagmatic eruptions at the summit of Ori Massif, transported by mass flow processes and deposited below wave base. This indicates that Ori Massif reached very shallow water depths during its formation, but that there is no direct evidence for plateau emergence.

Basaltic fragments from the volcaniclastic deposits, Ori Massif, demonstrate N-MORB-like and transitional to depleted MORB trace element and Hf-Nd isotope compositions, that are different to the underlying picrite-like lavas. This indicates change in chemical composition of magma during final stages of Ori Massif formation. The Hf-Nd isotope data (εHf_t = 13.3-18; εNd_t = 8.9-10.8) suggest presence of a relatively more depleted Pacific MORB component in the source of Shatsky Rise. The Hf-Nd isotope compositions from Shatsky Rise, Hess Rise, Ojin Rise and Cooperation seamount follow a common compositional trend, suggesting mixing of a common most depleted Pacific MORB source mantle with an enriched component, such as PREMA or HIMU. Overall, basalts from Shatsky Rise demonstrate more depleted Hf-Nd isotope compositions and more variety within the MORB field, compared to those of Ontong Java, Manihiki and Hikurangi oceanic plateaus. Such compositional differences are interpreted as a result of Shatsky Rise magma interaction with an active MOR-system upon emplacement.

Whole-rock samples from the flanks of Ori and Tamu Massifs show similar, predominantly smectitic and minor calcite alteration. The onset of seawater alteration of oceanic basalts is largely dependent on the initial crystallinity and presence and abundance of olivine. Two compositionally-contrasting alteration processes are defined: 1) olivine-normative Higher-Mg tholeiitic basalts undergo olivine decomposition to saponite clays and calcite, resulting in Mg-loss by 2-3 wt.%, which releases significant amounts of Mg^{2+} into seawater providing a source of Mg^{2+} for redistribution throughout the oceanic crust and to the ocean; and 2) Higher-Fe tholeiitic basalts contain traces of olivine phenocrysts and act as sinks for Mg^{2+} during low temperature alteration. High crystallinity rocks from both groups are associated with Ca-gain, whereas increasing contents of altered glass lead to Mg-uptake and Ca-loss.

The HFSE and REE predominantly behave conservatively and correlate with MgO enrichment or depletion.

Ori Massif is associated with the greatest range in vertical dynamics, compositional variability and alteration styles across the Shatsky Rise. Formation of Ori Massif can be explained by less intense interaction with an active spreading ridge system, relative to Tamu and Shirshov Massifs, and a more pronounced involvement of a mantle plume during construction of this Shatsky Rise edifice.

Table of Contents

List of Figures

List of Tables

List of Abbreviations

ALS	Australian Laboratory Services
BSE	Bulk Silicate Earth
CCD	Calcite Compensation Depth
CAMP	Central Atlantic Magmatic Province
CARF	Central Analytical Research Facility
CFB	Continental Flood Basalt
CMB	Core–mantle boundary
Cpx	Clinopyroxene
DSDP	Deep Sea Drilling Project
DMM	Depleted MORB Mantle
EM1	Enriched Mantle 1
EM2	Enriched Mantle 2
E-MORB	Enriched-MORB
EPMA	Electron Probe Micro-Analyser
EPR	East Pacific Rise
Exp.	Expedition
FG	Fresh Glass
FOZO	Focus Zone
G	Glauconite
GEOMAR	Research Centre for Marine Geosciences
HALIP	High Arctic Large Igneous Province
HCA	Hierarchical Cluster Analysis
HFSE	High Field Strength Elements
HIMU	High-μ, where μ is $^{238}U/^{204}Pb$
HREE	Heavy Rare Earth Elements
ICP-MS	Inductively Coupled Plasma Mass Spectrometer
ICP-OES	Inductively Coupled Plasma Optical Emission Spectroscopy
IODP	Integrated Ocean Drilling Program
LA-ICP-MS	Laser Ablation-Inductively Coupled Plasma Mass Spectrometer
LIP	Large Igneous Province
LLVP	Large Low-Velocity Province
LOI	Loss on Ignition
LREE	Light Rare Earth Elements
mbsf	meters below sea floor
mbsl	meters below sea level
MC-ICP-MS	Multicollector-Inductively Coupled Plasma Mass Spectrometer
MOR	Mid Ocean Ridge
MORB	Mid-Ocean Ridge Basalt
NAIP	North Atlantic Igneous Province
NGR	Natural Gamma Radiation

N-MORB	Normal-MORB
NW	North-Western
ODP	Ocean Drilling Program
OJP	Ontong Java Plateau
OIB	Oceanic Island Basalt
Ol	Olivine
PC	Principal Component
PCA	Principal Component Analysis
PGE	Platinum Group Elements
Plag	Plagioclase
PREMA	PREvalent MAntle
QUT	Queensland University of Technology
RA	Relative Alteration (parameter)
REE	Rare Earth Elements
RIF	Radiogenic Isotope Facility
SOPITA	South Pacific Isotopic and Thermal Anomaly
Strat.	Stratigraphic
TAS	Total Alkali versus Silica
TB	Tholeiitic Basalt
T-MORB	Transitional-MORB
UQ	University of Queensland
WR	Whole-rock
XRD	X-Ray Diffraction

Statement of Original Authorship

The work contained in this thesis has not been previously submitted to meet requirements for an award at this or any other higher education institution. To the best of my knowledge and belief, the thesis contains no material previously published or written by another person except where due reference is made.

Signature: QUT Verified Signature

Date: June 2017

Acknowledgements

I would like to sincerely thank my principal supervisor, Dr David Murphy, for introducing me to this interesting project, the Integrated Ocean Drilling Program (IODP) research and overseas collaborations that have significantly broadened my level of expertise. I thank David for his support over the years, multiple discussions of aspects of my research, introducing me to various analytical laboratory methods and reviews of drafts. I sincerely appreciate the opportunities and funding he has provided me to collaborate with other researchers and present my work at international conferences. I am grateful to David for giving me an opportunity to visit the IODP core repository in Texas A&M University (USA) to personally observe the cores from the IODP Expedition 324 and collect samples for this thesis.

My associate supervisor, Associate Professor Scott Bryan, is greatly acknowledged for his support and assistance during my studies. I would like to thank Scott for insightful and invaluable feedback on volcanology, geochemistry and scientific writing. I thank Scott for sharing his views on research problems, particularly for placing my research into a wider context of Large Igneous Province (LIP) formation and global significance. I am grateful to Scott for inviting me to the International Union of Geodesy and Geophysics (IUGG) Scientific Field Trip, where I learned about the beauty and geology of the Whitsunday Silicic LIP.

Queensland University of Technology (QUT) is acknowledged for providing the International Tuition Fee Waiver Scholarship and Postgraduate Research Award for living allowance. Additionally, QUT partially covered the analytical costs and partially funded travel to an international conference (Goldschmidt, 2013).

I would like to thank Professor David Gust for reviewing my dissertation and for the insightful comments during my candidature, which helped me to improve the research design, methodology and thesis structure. I appreciate the guidance from David I received during teaching at QUT.

Professor Godwin Ayoko is thanked for internal review of the thesis. I appretiate two external examiners for the insightful comments, which helped me to improve my document. I am very thankful to Dr Patrick Hayman, Dr Jessica Trofimovs, Dr Charlotte Allen, Dr Luke Nothdurft, Dr Craig Sloss and Dr Christoph Schrank from

QUT and to Associate Professor Gideon Rosenbaum (University of Queensland, UQ) for providing invaluable suggestions at different stages of this research.

This PhD research would not have been possible without the IODP Expedition 324 to Shatsky Rise oceanic plateau, where my principal supervisor Dr David Murphy was involved as an igneous petrologist focusing on alteration. I am grateful for this opportunity to collaborate with the IODP Expedition 324 Scientists. I would like to especially thank Dr Ken Heydolph and Dr Jörg Geldmacher from GEOMAR, Germany, for collaboration during preparation of Heydolph et al. (2014) manuscript. Dr Jörg Geldmacher and Dr Folkmar Hauff are acknowledged for providing the Hf-Nd isotope geochemistry data and contributions towards the future manuscripts. I greatly appreciate Co-Chief Expedition 324 Scientist Dr Takashi Sano (National Museum of Nature and Science, Japan) and Dr Akira Ishikawa (University of Tokyo, Japan) for samples and advices that significantly improved the "alteration manuscript". Professor William W. Sager (University of Houston, USA) is acknowledged as the Co-Chief Expedition 324 Scientist, working for over 30 years on Shatsky Rise, his interest and encouragement towards my studies and also for help during my visit to Texas A&M University (USA). I appreciate Dr Adélie Delacour (Université Jean Monnet, France), Dr Renat Almeev (University of Hannover, Germany), Professor Anthony A.P. Koppers (Oregon State University, USA) and Associate Professor Andrew R. Greene (Hawai'i Pacific University, USA) for discussions related to Shatsky Rise. I greatly acknowledge the remaining IODP Expedition 324 Scientists and post-cruise researchers for their input in knowledge on Shatsky Rise.

Queensland University of Technology Central Analytical Research Facility (CARF), QUT X-ray and particles laboratory and University of Queensland Radiogenic Isotope Facility (RIF) are acknowledged for providing facilities, training and technical support for the necessary analyses. I would like to sincerely thank Ms Irina Kinaev and Dr Sunny Hu for the unwavering support and guidance during my work at QUT and UQ clean laboratories and enthusiasm regarding method development. My thanks are extended to Ms Aarshi Bhargav and Dr Ai Nguyen for an exceptional technical support during laboratory analyses. Dr Yue-xing Feng is greatly acknowledged for assistance with Pb-Sr-Nd isotope analyses. Dr Daniel D. R. Owen is thanked for assistance with multivariate analyses and teaching me the key concepts for statistical data analysis. I am thankful to Dr Henry Spratt, Ms Karine Moromizato,

Mr Tony Raftery and Mr Tri Nguyen for assistance with XRD analyses and teaching me methods of data interpretation. Dr Kathryn Stewart is thanked for technical support during microscope investigations. Mr Duncan Burke-Shyne, Mr Gus Luthje, Mr Donald McAuley, Mr Peter Colles, Ms Anna-Marie Venn are thanked for help with sample and thin section preparation. Dr Linda Nothdurdft, Mr Will Stearmen, Mr Shane Russell and Ms Alice Strazzabosco are appreciated for technical support.

I am thankful to the Head(s) of School at QUT EEBS Adjunct Professor Peter Mather and Professors David Gust, Martin Sillence and Stuart Parsons for support during my studies. Support from administration officers Susan Teare, Sarie Gould, Courtney Innes, Noelene Davies and Samantha Talbot and research higher degree officers, especially Tiziana La Mendola, Andrea Russo and Rachael Krinks, has been invaluable throughout my candidature. QUT Academic Language and Learning Service, especially Ms Karyn Gonano, is thanked for provinding training sessions.

I would like to extend my sincerest gratitude to my teachers, colleagues and co-authors from different parts of the World, who inspired and encouraged me during my undergraduate and postgraduate studies. I wish to acknowledge Professor Vladislav S. Shatsky (Institute of Geochemistry SB RAS), Professor Mikhail I. Kuzmin (Institute of Geochemistry SB RAS) and Professor Gennady N. Anoshin (Novosibirsk State University). I am grateful to many postgraduate colleagues and friends from QUT, UQ and beyond, whose support and encouragement helped me at different points of my candidature. Special thanks to Alexandra, Coralie, Stefan, Clément, Des, Alaa, Jorge, Adam, Martin, Zhenjiao, Alex, George, Gemma, Gabriela, Sergii, Anastasia, Dmitry, Maxim, Padma, Daniel, Pavel, Claudio, Charmaine, Sharon, Melina, Dareeju and Genevieve. My PhD adventure would not be as great without you.

I sincerely appreciate my family for constant support, care and encouragement during preparation of this dissertation. I am entirely indebted for inheriting geological genes and adventurous spirit for over three generations.

I dedicate this thesis to my parents, Dr Antonina Vernikovskaya and Professor Valery Vernikovsky, and my husband, Mikhail Romanov, for unwavering support over the years, your help to get me through all the troubles and for sharing times of little success. I described myriad of details about my research to you and you have always believed in me.

Chapter 1: Introduction

1.1 RESEARCH BACKGROUND AND PROBLEM

Oceanic Plateaus are the largest examples of Large Igneous Provinces (LIPs), each representing extensive areas (>0.1 Mkm^2) of over-thickened oceanic crust, and believed to have formed in relatively short periods of time (~3 Myr) from abnormally high degree of melting of mantle material (Larson, 1991; Kerr, 2005, 2014). Large Igneous Provinces are considered amongst the most voluminous magmatic events in Earth's history (Bryan & Ernst, 2008; Bryan & Ferrari, 2013) and are often correlated with global environmental changes such as mass extinctions (Courtillot, 2002; White & Saunders, 2005; Wignall, 2005; Sobolev et al., 2011), and tectonic events such as supercontinent break-up (Hill, 1991; Condie, 2004; Santosh et al., 2009). Moreover, they are broadly associated with the formation of large-scale world-class Cu-Ni & Platinum Group Elements (PGE) and rare-metal ore deposits (Naldrett, 1999; Pirajno, 2007; Zhang et al., 2008) as well as with the emplacement of diamondiferous kimberlites and carbonatites (Dobretsov & Vernikovsky, 2001; Schissel & Smail, 2001; Ernst & Bell, 2010; Torsvik et al., 2010a).

Large Igneous Provinces occur both on continental and oceanic crust, mainly in intraplate tectonic settings (Condie, 2001; Bryan & Ernst, 2008). On continents, LIPs are recorded from the Archean to Cenozoic (Tomlinson & Condie, 2001), while their presence on oceanic crust is limited to Mesozoic due to ocean crust consumption at subduction zones (Ernst & Buchan, 2001). Oceanic LIPs are subdivided into oceanic plateaus (e.g., Cretaceous-Tertiary Ontong Java, West-Pacific) and oceanic basin flood basalts (e.g., Cretaceous Nauru Basin, West-Pacific). The continental LIPs are classified into: a) continental flood basalt (CFB) provinces (e.g., the Permian-Triassic Siberian Traps, Russia), b) giant continental dyke swarms, sills and mafic ultramafic intrusive provinces (e.g., the Palaeoproterozoic Bushveld complex, South Africa), c) Archean greenstone belts (e.g., Superior, Canada), d) volcanic rifted margins (e.g., Paleogene North Atlantic), and e) silicic LIPs (e.g., Cretaceous Whitsunday, Australia), according to Bryan and Ernst (2008). The global LIP record since Pangea assembly ca. 320 Ma is shown in Figure 1.1.

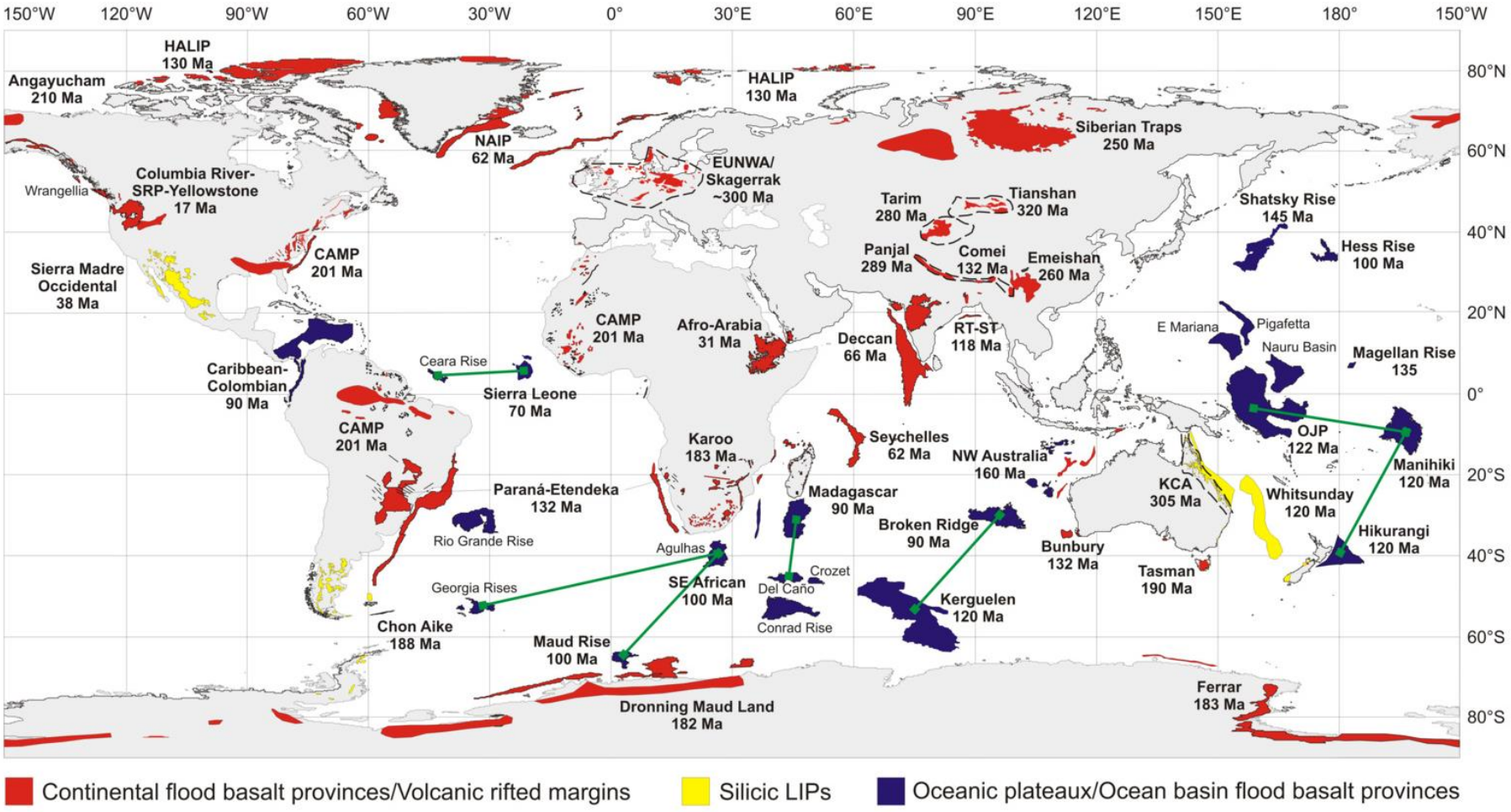

Figure 1.1. Worldwide distribution of LIPs since Pangea assembly ca. 320 Ma. Shatsky Rise is located in the north-western Pacific. The ages correspond to the onset of the main or first phase of magmatism. Green lines connect oceanic LIPs subsequently rifted apart by mid-ocean ridge spreading. Abbreviations: CAMP, Central Atlantic Magmatic Province; NAIP, North Atlantic Igneous Province; OJP, Ontong Java Plateau. Source: (Bryan & Ferrari, 2013).

Mafic igneous rocks, which are mostly represented by tholeiitic basalt lavas with a minor portion of alkaline basalts, dominate LIP magmatism. Variations in SiO_2 and volatile content reflect the presence of rare ultramafic (e.g., carbonatites, kimberlites) and in some cases, substantial volumes of silicic igneous rocks (Bryan et al., 2002; Bryan & Ferrari, 2013). High-Mg rocks (e.g., picrites) may also be present and they are interpreted to play an important role as indicators of mantle composition and temperatures (Campbell, 2005; Kerr & Mahoney, 2007).

The plume-head hypothesis has been widely used to explain such episodic, large-volume and rapidly emplaced igneous events (Richards et al., 1989; Campbell, 2005). However, a plume head origin is still not demonstrated for any particular oceanic plateau, as well as for many other LIPs (Tejada et al., 2002; Ingle & Coffin, 2004; Foulger & Anderson, 2005; Ukstins Peate & Bryan, 2008; Sager et al., 2011). From a variety of alternative mechanisms for LIP formation (Ernst et al., 2005; Saunders, 2005) the most popular is the model that LIPs are formed by shallow lithospheric processes (e.g., King & Anderson, 1998; Foulger et al., 2005; Anderson & Natland, 2007; Foulger, 2010). Deciphering the role of deep-seated mantle plumes versus shallower, plate tectonic/boundary controls in the origin of oceanic plateaus and other LIPs is a fundamental problem in the Earth Sciences.

Although accessibility to continental LIPs is better than to oceanic examples, oceanic plateaus are preferred to flood basalts in testing the plume-head hypothesis (Campbell, 2007; Kerr, 2014). This is because continental crust comprises rocks of various compositions and ages ranging from Archean to present, and it is much thicker than the oceanic crust. The huge structural, chemical and age contrasts of continental crust and sub-continental lithospheric mantle result in massive variation in melting dynamics and the potential for a large amount of crustal contamination of mantle-derived magmas (Arndt et al., 1993). Oceanic plateaus do not have these complexities, because they form on oceanic crust, which is generally ~7 km thick and has a much simpler structure and composition (White et al., 1992; Cloos, 1993; Jenner & O'Neill, 2012; Gale et al., 2013).

Many oceanic plateaus, including the two largest (Ontong Java and Kerguelen), were emplaced during the mid-Cretaceous Supercron, which was also a time of no geomagnetic polarity reversals that produce the ridge-parallel anomalies (Norton, 2007). Consequently, the setting of these plateaus in relation to spreading centres is

poorly recorded, whereas their temporal progression of magmatism cannot be revealed from studies of magnetic lineations in the surrounding oceanic crust. The Kerguelen plateau also contains evidence for the presence of continental crustal basement significantly complicating its formation and interpretation of basalt geochemistry (Frey et al., 2003). In addition, geochemical, geophysical and geodynamic observations from Ontong Java are contradictory and do not fit either the deep origin or a shallow origin for oceanic plateaus (Tejada et al., 2004; Korenaga, 2005).

Unlike the mid-Cretaceous plateaus, the Shatsky Rise plateau in the North-western Pacific was formed at the Jurassic-Cretaceous boundary, when magnetic reversals were occurring (Figure 1.2). Consequently, the original tectonic setting as well as progression of major magmatic events became available from the magnetic record. It was inferred that the Shatsky Rise consists of three large edifices that were emplaced at a migrating triple junction of oceanic spreading ridges (Sager et al., 1988; Nakanishi et al., 1999; 2015a). The oldest and largest Tamu Massif is followed by younger and smaller Ori and Shirshov Massifs (Figure 1.2). Previous studies revealed that Ori Massif is the most heterogeneous in composition across Shatsky Rise, showing variations from Mid-Ocean Ridge Basalt (MORB)-like to slightly more enriched Oceanic Island Basalt (OIB)-like (Mahoney et al., 2005; Sano et al., 2012; Husen et al., 2013; Heydolph et al., 2014). In terms of mantle plume hypothesis, Ori Massif magmatism represents temporal and compositional transition from the oldest MORB-dominated Tamu Massif (plume head) to the younger Shirshov Massif and trachytes from nearby seamounts (plume tail) (Tejada et al., 2016). While knowledge on compositional variety of the youngest Shirshov Massif remains limited to one eruptive unit (Sager et al., 2010), the volcanism of Ori Massif plays a crucial role for plateau-building. The purpose of this study is to determine the nature of Ori Massif volcanism and to provide constraints on the formation and evolution of the Shatsky Rise.

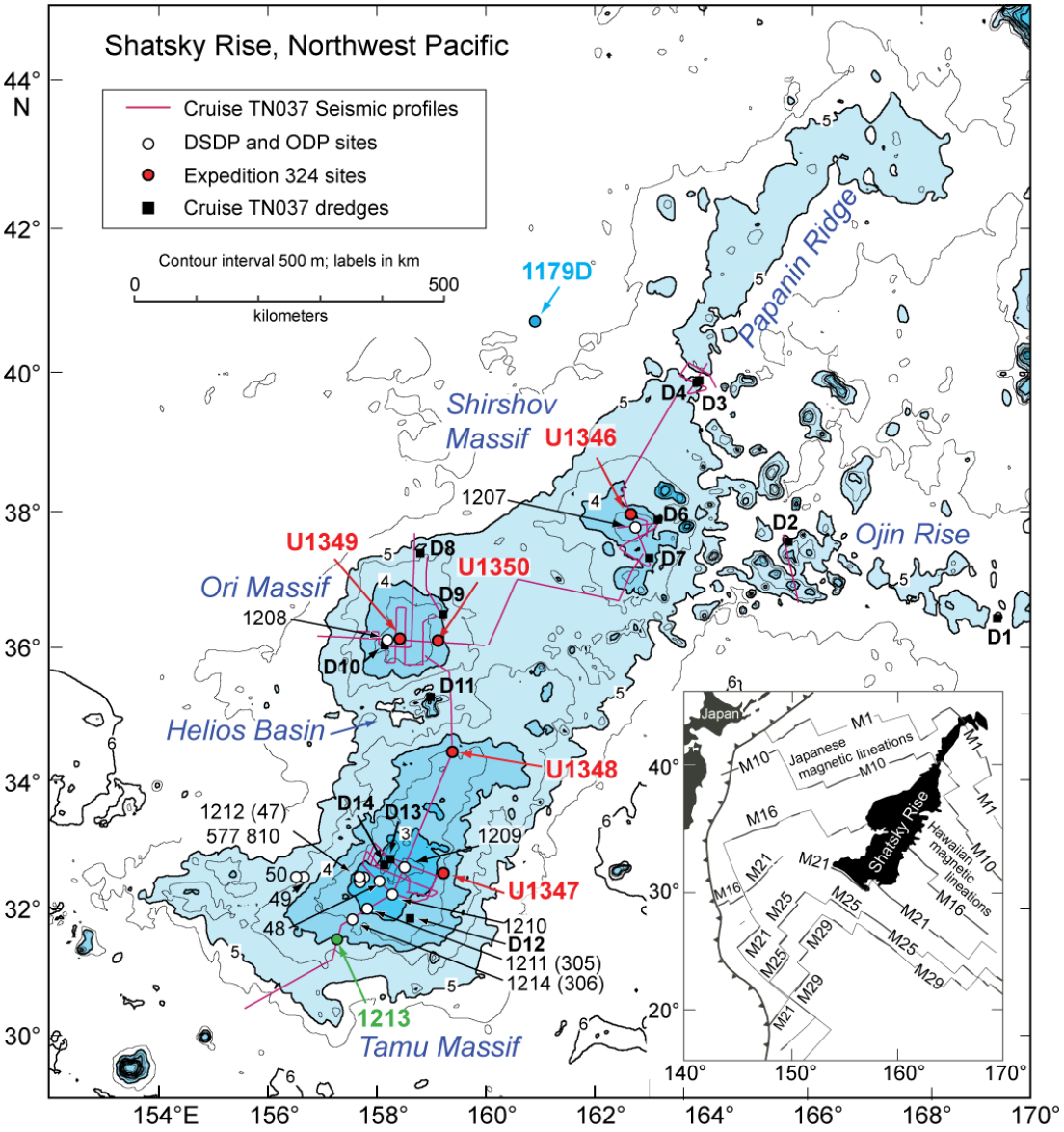

Figure 1.2. Schematic map of the Shatsky Rise with locations of Cruise TN037 seismic tracks and dredges (D1-D14), as well as DSDP, ODP and IODP Expedition 324 drill sites, adopted from Sager et al. (2010). The IODP Expedition 324 drill sites are shown in red. Site 1213 marks the location where igneous rocks were drilled during ODP Leg 198 (Bralower et al., 2002). Hole 1179D drilled during ODP Leg 191 represents contemporary MORB crust nearby Shatsky Rise (Chron M8, ~132Ma; Kanazawa et al., 2001). The locations of Cruise TN037 seismic dredges are after Sager et al. (1995). Elevations are shown in blue. Inset shows Shatsky Rise location in relation to western Pacific lineations (thin lines), trenches (toothed line), and Japan.

1.2 RESEARCH FOCUS AND QUESTIONS

Geological information on pre-, syn- and post-formation bathymetry is necessary during numerical modelling of the lithospheric thermal structure associated with LIP emplacement, which can help in understanding physical mechanisms of LIP formation (Korenaga, 2005). Preliminary paleontological and sedimentological observations from the Shatsky Rise suggested substantial shoaling and emergence for the Shatsky Rise edifices (Sager et al., 1999; 2010). Importantly, lithologies from the summit of Ori Massif are proposed to form in a near shore to subaerial environment (Sager et al., 2010). However, the estimations of volatile saturation depths for basalts by Shimizu et al. (2013) and seismic investigations of Zhang et al. (2015) implied that the Shatsky Rise was largely submarine and might have never been emergent. The first research project aimed to re-examine the conflicting evidence for near sea level to subaerial emergence of Ori Massif. The project focused on **physical volcanology of volcaniclastic deposits from the summit of Ori Massif edifice, with implications for eruption styles and vertical dynamics during Shatsky Rise formation.**

A major consideration in the plume versus plate debate for the formation of oceanic plateau is the origin of the components that melt to generate their large volumes of magmas (Ernst et al., 2005; Bryan & Ferrari, 2013; Kerr, 2014). In the plume model for oceanic plateaus, the earliest stage of volcanism corresponds to impact of the plume head with the lithosphere leading to high degrees of partial melting of a mixture of lower mantle derived material and upper mantle material that has been incorporated into the plume head (Campbell & Griffiths, 1990; Campbell, 2007). The high degrees of melting associated with the plume head ascent and impact is expected to lead to homogenous compositions. As the plume transitions from plume head to plume tail it is expected that the contribution from lower mantle derived material will increase and the degree and extent of melting decrease leading to more geochemical heterogeneity in the resultant lavas. For the Shatsky Rise, which formed in a time period of frequent magnetic reversals, correlation with magnetic lineations indicate a temporal progression of magmatism (Sager et al., 1988; Nakanishi et al., 1999) from the geochemically homogenous Tamu Massif, to the geochemically heterogeneous Ori Massif and the subsequent Shirshov Massif (Mahoney et al., 2005; Sano et al., 2012; Husen et al., 2013; Heydolph et al., 2014), for which only one volcanic eruptive event has been sampled (Sager et al., 2010), and the local seamount magmatism, which is

dominated by trachytes (Tejada et al., 2016). Therefore, Ori Massif is selected for this study to enlarge our understanding into compositional heterogeneities at Shatsky Rise and differentiate source signatures of mantle material that melted to form this oceanic plateau. The second research project investigated **the geochemistry of individual clasts from the late stage volcaniclastic deposits from the Ori Massif edifice, with implications to heterogeneity in the source region of the Shatsky Rise magmas.**

Element mobility associated with low-temperature alteration of submarine basaltic rocks is significant for both the bulk composition of the oceanic crust and ocean chemistry (Alt, 1995; Alt & Mata, 2000; Clayton & Pearce, 2000; Wheat et al., 2002; Staudigel, 2003; Banerjee et al., 2004; Schramm et al., 2005; Bach & Früh-Green, 2010; Von Damm, 2013). Oceanic plateaus are often associated with higher emplacement rates and temperatures upon formation and they may contain lavas of more distinct chemical composition (e.g., Mg-rich rocks), in comparison to the thin oceanic crust (Campbell, 2005; Kerr & Mahoney, 2007; Bryan & Ernst, 2008). Previous studies demonstrated a significant variation in alteration style and intensity in basalts from the three elevated Massifs within the Shatsky Rise (Mahoney et al., 2005; Sager et al., 2010; Sano et al., 2012; Delacour & Guillaume, 2013; Heydolph et al., 2014; Miyoshi et al., 2015). The third research project investigated **the nature and degree of alteration and element mobility in basalts from the flanks of Tamu and Ori Massifs, with implications for seawater alteration effect during oceanic plateau ageing.**

In the context of the proposed projects, the following research questions were addressed:

1. What paleoelevations did Ori Massif reach during formation and did this edifice shoal to emergence?
2. What is the extent of compositional heterogeneity of basalts at the summit of Ori Massif and what does it tell us about mantle sources that melted to form this edifice?
3. How did seawater alteration change the initial chemical composition of igneous rocks from the flanks of Ori and Tamu Massifs?

1.3 SIGNIFICANCE OF THIS PHD PROJECT

This research forms part of the Integrated Ocean Drilling Program (IODP) Expedition 324 International Scientific Group Project. Intraplate volcanism, forming both LIPs and seamounts, is known to coexist with the plate tectonic processes of lithospheric plate formation and consumption, but is relatively poorly understood in terms of the mantle dynamic processes. The main goal for the IODP Expedition 324 Scientific Party was to investigate the age, **physical volcanology**, **petrology**, **geochemistry**, **magmatic sources**, tectonic evolution, geophysics, and sedimentary geology of the Shatsky Rise in order to solve the problem of Shatsky Rise formation and provide a concept for the other Oceanic Plateaus and LIPs in general (Sager et al., 2010; 2011; 2016).

Ori Massif from Shatsky Rise oceanic plateau was selected for this PhD study to 1) assess paleoelevations at the time of construction with implications for eruption styles and geological dimensions of LIPs; 2) assess spatial, temporal and compositional trends that can inform us on mantle source regions contributing to LIP magmatism; and 3) examine element mobility during seawater alteration of basalts from oceanic plateaus. This PhD research project represents an *integrated petrological and geochemical characterisation of the Ori Massif igneous and volcaniclastic rocks. This study provides information on eruption styles, mantle sources and alteration that took place at Ori Massif, Shatsky Rise.*

1.4 RESEARCH PLAN

Three research projects are presented in separate Chapters (3 to 5), written as self-contained manuscripts for future publication. Additionally, I contributed to the IODP collaborative study to investigate the isotope geochemistry of the basement lavas sampled in IODP Expedition 324, Heydolph et al. (2014). Altogether the research projects form a linked study to answer the research questions and achieve the aims outlined in the previous section. Outcomes from these studies provide a contribution towards understanding of formation and seawater alteration of Shatsky Rise with implications for oceanic plateaus and LIPs in general and are addressed in the subsequent synthesis Chapter 6. Details for each of the research projects are given below.

1.4.1 Research project 1 (Chapter 3)

This study targeted volcaniclastic deposits, cored near the summit of Ori Massif, representing the second largest and oldest edifice at Shatsky Rise (Figure 1.2). These deposits were preliminary interpreted as subaerially oxidised conglomerates, potential paleosol and shallow-marine turbidites, and remained the critical evidence for Ori Massif emergence (Sager et al., 2010; 2016). Specifically, the research was addressed towards an understanding of the origin (pyroclastic versus epiclastic) and paleoelevations upon formation and deposition (subaerial, shallow-marine or deep-marine) for these volcaniclastic deposits. This was achieved by petrographic and lithostratigraphic analyses of the core in combination with geophysical downhole log data assessment.

1.4.2 Contribution to collaborative research and research project 2

1.4.2.1 Participation in IODP Expedition 324 collaborative research

During PhD studies, I participated in post-cruise IODP Expedition (Exp.) 324 collaborative research, aiming to contribute to the debates on plume versus plate origin of the Shatsky Rise. This research provided the first comprehensive Nd-Hf-Pb isotope dataset for samples cored from the three elevated Massifs (Sites U1346, U1347, U1349, U1350, 1213, see Figure 1.2) and complemented the major and trace element data obtained for these samples (Sano et al., 2012) and previously obtained Nd-Pb-Sr isotope data on limited samples from Tamu Massif (Site 1213, Mahoney et al., 2005). Outcomes of this collaborative research were published in Heydolph et al. (2014).

The PhD candidate contributed to the research team by participating in discussions, data interpretation and conducting geochemical analyses for samples from Ori and Shirshov Massifs, Sites U1349 and U1346, respectively. The author petrographically assessed cored basaltic material from the two drill holes, analysed the selected samples for trace element and Nd-Pb-Sr radiogenic isotope compositions at QUT and UQ and wrote the resulting analytical methods section for the publication.

1.4.2.2 Research project 2 (Chapter 4)

This study investigated basaltic fragments from the volcaniclastic deposits that were formed during phreatomagmatic activity at late building stage of Ori Massif (as it will be demonstrated in Chapter 3). The deposits contain fragments of juvenile magma and wall-rock lithic clasts, derived by fragmentation of the pre-existing

comagmatic rocks, and therefore, the fragments may represent geochemically distinct magmatic sources. Here, new major element, trace element and Nd-Hf isotope data for basaltic fragments are presented. Isotope data are limited to Nd and Hf systematics, because most of the Pb and all Sr isotope signatures for basalts from Shatsky Rise were proven as highly modified by extensive seawater alteration processes (Heydolph et al., 2014).

1.4.3 Research project 3 (Chapter 5)

The research project investigated the nature and degree of alteration and element mobility in basalts from the flanks of Tamu and Ori Massifs. Importantly, multiple intervals with fresh glass fragments were found in the cores drilled from the flanks of Tamu and Ori Massifs (Sager et al., 2010; Sano et al., 2012). This allowed for a quantitative and qualitative comparison between the fresh glass fragments from the margins of pillow lavas and sheet flows and the altered interiors from the same lithological units. Using a whole-rock – fresh-glass pair analysis I was able to: 1) assess seawater alteration-related element mobility, and 2) evaluate how this mobility relates to location (site), depth, and other rock characteristics, including primary chemical and mineral compositions.

1.5 SAMPLE DATABASE AND MATERIALS

This research used samples and data collected through the IODP Exp. 324 to Shatsky Rise. Volcanic successions from the IODP Exp. 324 were personally examined at the IODP core repository (Texas A&M University, College Station, Texas, USA). Samples used in Chapters 3-5 were collected during this visit and subsequently ordered via post from the IODP core repository. Additional samples, necessary for the Chapter 5, were kindly provided by the IODP Exp. 324 Scientists Dr. Takashi Sano (National Museum of Nature and Science, Japan) and Dr. Akira Ishikawa (University of Tokyo, Japan). As part of the collaborative research project (Heydolph et al., 2014), I worked on samples from Ori and Shirshov Massifs, Sites U1349 and U1346, collected by Dr. David Murphy for this post-cruise research.

The candidate has petrographically examined rock samples from 122 different intervals from all five IODP Exp. 324 drill cores. This analysis allowed a more comprehensive understanding of rock material present at Shatsky Rise and provided background for reasonable characterisation of samples that were eventually selected

for the research projects. The candidate extensively used proceedings from the IODP Exp. 324 (Sager et al., 2010) and the range of publicly available resources generated during the IODP Exp. 324, including digital photographs of the cores and thin sections and downhole log data, including gamma ray, density and resistivity (http://iodp.tamu.edu/database/).

1.6 THESIS STRUCTURE

The thesis comprises six chapters, including an introductory Chapter 1, literature review Chapter 2, three research Chapters 3-5 and a synthesis Chapter 6. The Introduction Chapter 1 establishes the research problem of the LIP formation and Shatsky Rise oceanic plateau, states the research foci and questions, overviews significance of the project, and gives an overview of the research plan, used in this study. Chapter 2 gives an overview on LIPs formation hypotheses and provides necessary geological background on Shatsky Rise from previous investigations. Each of the three research projects is presented in a separate Chapter (3-5) and provides introduction to the research problem, background, methodology and analytical procedures, presents new data and interpretation of the results in view of the current scientific knowledge, provides insights into the formation and evolution of Ori Massif and synthesises the key findings from the research undertaken. The last Chapter 6 provides implications from the research projects for the formation and evolution of the Shatsky Rise in general and discusses possible physical mechanisms for the magmatic origin of the Shatsky Rise and LIPs in general. Chapter 6 also provides suggestions for future studies at Shatsky Rise and beyond.

1.7 LIST OF PUBLICATIONS

Outcomes from research during candidature were published in journal article and presented at several international conferences. Results from the post-cruise IODP Exp. 324 collaborative research were published in:

Heydolph, K., Murphy, D.T., Geldmacher, J., **Romanova, I.V.**, Greene, A., Hoernle, K., Weis, D., & Mahoney, J. (2014). Plume versus plate origin for the Shatsky Rise oceanic plateau (NW Pacific): Insights from Nd, Pb and Hf isotopes. *Lithos*, 200-201: 49-63.

Presentations at international conferences:

Romanova, I.V. & Murphy, D.T. (2013). Differentiating magma sources from conglomerate and breccia clasts, IODP Site U1349, Ori Massif, Shatsky Rise Oceanic Plateau. *Mineralogical Magazine*, 77 (5): 2080. Presented at 23th Annual V.M. Goldschmidt Conference, Florence, Italy.

Geldmacher J., Heydolph K., Murphy D.T., **Romanova I.**, Mahoney J. & Hoernle K. (2012). Combined Sr, Nd, Pb and Hf isotopic constraints on the origin of Shatsky Rise (NW Pacific). AGU Fall Meeting, Abstracts: San Francisco, California, USA.

Romanova I.V. & Murphy D.T. (2012). Dating seawater alteration in the Shatsky Rise basalts from IODP Expedition 324, using U-Pb isotope geochemistry. 34rd International Geological Congress (34IGC), Brisbane, Australia.

Romanova I., Murphy D.T., Geldmacher J. & Heydolph K. (2011). Sr, Nd, Hf and Pb isotope systematics of basaltic samples from IODP Site U1349A, Ori Massif of the Shatsky Rise Oceanic Plateau, Northwest Pacific. AGU Fall Meeting, Abstracts: San Francisco, California, USA. (poster presentation)

Murphy D., Geldmacher J. & **Romanova I.** (2011). Sr, Nd, Hf and Pb isotope characterisation of basalts from IODP Site U1346, Shirshov Massif the youngest edifice of the Shatsky Rise, northwest Pacific. 21st Annual V.M. Goldschmidt Conference, Abstracts: Prague, Czech Republic.

Since presentation at international conferences, substantial modifications and improvements to the research projects were applied and new results were obtained and implemented to the thesis.

Chapter 2: Previous investigations on LIPs and Shatsky Rise

2.1 LARGE IGNEOUS PROVINCE FORMATION HYPOTHESES

The term "large igneous province" was introduced by Coffin and Eldholm (1991) to group transient, large voluminous and high-rate emplacement magmatic events found throughout the Earth's history on both oceanic and continental crust, which "cannot be directly related to "normal mid-oceanic sea-floor spreading" (Coffin & Eldholm, 1993). Key features of LIPs are: 1) they are temporally and spatially related to whole mantle scale thermal upwellings, 2) they are dominated by mantle derived mafic magmas, and thus have contributed to the transport of large amounts of thermal energy from the mantle, and 3) they are common in intraplate tectonic settings, well away from active plate boundaries, and often precede continental breakup or extension (Coffin & Eldholm, 1994b; Romanowicz & Gung, 2002; Burke & Torsvik, 2004; Saunders, 2005; Bryan & Ernst, 2008; Burke et al., 2008; Li & Zhong, 2009).

The mantle plume head hypothesis was proposed to explain such "abnormal" events (Richards et al., 1989; Coffin & Eldholm, 1994b; Farnetani & Richards, 1994). This model implies mantle circulation that coexists with that of plate tectonics (i.e. plate boundary-related magmatism), but differs greatly from it. Plumes are thought to initiate at the base of the lower mantle close to the core-mantle boundary (CMB) from material that is thermally and gravitationally unstable (Richards et al., 1989; Campbell & Griffiths, 1990). Numerical and tank modeling suggests that when hot low-density material gains enough buoyancy it begins to ascend with a large mushroom shaped head, followed by a long plume tail (Figure 2.1). Within this model, the plume head melts by decompression when it ascends and impacts the lithosphere producing huge amounts of magma at the Earth's surface and noticeable elevation (LIPs), whereas the plume tail often drives continued magmatism as a "hot spot" to produce oceanic island chains (OIBs) (Duncan & Richards, 1991; Şengör, 2001; Campbell, 2005). A perfect example of OIB magmatism is the Hawaii-Emperor seamount trail, which shows age progression from present-day till ~70 Ma (Wilson, 1963; Garcia et al., 1987). According to the plume model, the seamounts demonstrate a track of Pacific plate movement above the Hawaiian hotspot.

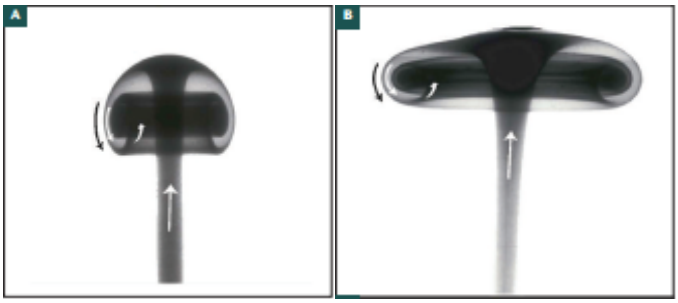

Figure 2.1. Photographs of a laboratory model of a starting thermal plume (a) after the head flattens at the top of its ascent and (b) mid-way through its ascent. Mantle plume has a large mushroom shaped head and a long narrow plume tail. The mantle plume model implies mixing of a hot plume material with cooler ambient mantle. Source: (Griffiths & Campbell, 1990; Campbell, 2007).

The development of seismic tomography allowed determination of high- and low-velocity regions within the Earth's mantle, discernible from the base of the lithosphere downward to the CMB (Zhao, 2001; Burke & Torsvik, 2004; Montelli et al., 2004; 2006; Boschi et al., 2007; Zhao, 2007; Burke et al., 2008; Wolfe et al., 2009). The high-velocity regions were interpreted to contain ancient subducted material, whereas the low-shear wave velocity provinces ($\delta V_s<0$) correlate with the reconstructed locations for LIPs and hotspots at the moment of their formation (Figure 2.2). Presently, two Large Low-Velocity Provinces (LLVPs) are identified below the African continent and the Pacific plate and interpreted as regions of hotter and compositionally denser mantle material, or the long-lived superplumes responsible for intraplate volcanism (Romanowicz & Gung, 2002; Burke & Torsvik, 2004; Burke et al., 2008; Li & Zhong, 2009).

Although many identification criteria for distinguishing mantle plume-derived products seem to be theoretically well-established and acknowledged (e.g., geological setting irrespective to plate tectonics' boundaries, linkage of a hotspot (plume-tail) to a LIP (plume-head), age-progressive volcanism of hotspots, previous uplift for LIPs, isotope (especially high $^{3}He/^{4}He$ ratios) and trace element geochemical observations), no single LIP exhibits all these features (e.g., Courtillot et al., 2003; Foulger, 2005). For example, neither of the largest oceanic plateaus Ontong Java and Kerguelen are consistent with the classical plume model (Frey et al., 2000; Tejada et al., 2004). Furthermore, the chemistry and isotopic composition of OIBs, which are the present-day expression of long lived hotspots, require the existence of different long-term

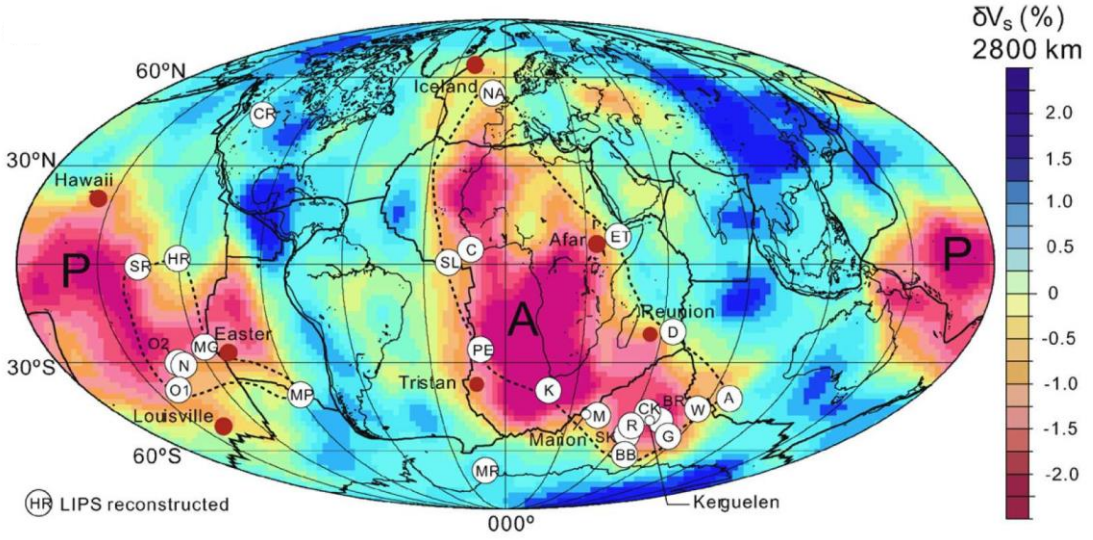

Figure 2.2. Plate tectonic reconstruction over the last 200 Ma, showing locations of LIPs at the time of their formation (Burke & Torsvik, 2004). Background map illustrates the present-day shear wave velocity anomalies near the core–mantle boundary (Becker & Boschi, 2002), interpreted as African (A) and Pacific (P) superplumes (Li & Zhong, 2009). The δV_s colour contours change from red (slower speed regions) to blue (higher speed regions). Red dots indicate locations of hotspots regarded as having a deep origin (Courtillot et al., 2003). Abbreviations for LIPs: SR, Shatsky Rise; HR, Hess Rise; MG, Magellan Rise; MP, Manihiki Plateau; O1, Ontong Java 1; O2, Ontong Java 2; N, Nauru; CR, Columbia River; NA, North Atlantic; C, CAMP; SL, S. Leone Rise; ET, Ethiopia; PE, Parana–Etendeka; K, Karroo; D, Deccan Traps; R, Rajmahal Traps; SK, Southern Kerguelen; CK, Central Kerguelen; BR, Broken Ridge; M, Madagascar; W, Wallaby Plateau; BB, Banbury; A, Argo margin; G, Gascoyne; MR, Maud Rise. Source: (Li & Zhong, 2009).

isolated reservoirs in the lower mantle (see next section for details), but it is still poorly understood where exactly they are located, in what proportions and whether they move through time. Moreover, recently enhanced seismic tomography provides images, tracing plume tails into the lower mantle beneath hotspots, but this imagery cannot identify larger plume-head structures even for the apparently newly developing mantle plumes (e.g., Montelli et al., 2004; 2006). Not all hotspots i.e. plume-tails (e.g. Hawaii, Juan de Fuca, Caroline) can be backtracked to LIPs (plume-heads), while some LIPs have no apparent volcanic track (e.g., Hess Rise, Ontong Java) (Farnetani & Hofmann, 2011). Another subject for debate is the presence of domal uplift, which is supposed to be a key response to plume-head interaction with the lithosphere (Czamanske et al., 1998; Campbell, 2001; Şengör, 2001; Saunders et al., 2007; Sheth, 2007; Ukstins Peate & Bryan, 2008; Dannberg & Sobolev, 2015). For this reason, researchers are

increasingly questioning mantle plume hypothesis, as this model is currently unable to fully explain the formation of all known LIPs and hotspots. One suggestion has been that plumes may be sourced in both the upper mantle and lower mantle (Courtillot et al., 2003).

Table 2.1. Predictions from the popular models of LIP formation (Saunders, 2005)

Prediction / Model	Excess mantle-derived magmatism	Regional uplift / doming	High-T magmas (e.g. picrites and komatiites)	Extraterrestrial material and impact breccias	Hotspot trail leading from LIP	Currently active hotspot
Mantle plume	Yes (unless the plume impinges on the base of thick lithosphere)	Likely (before and / or during magmatism)	Likely (but dense melts may not reach the surface)	No	Likely	Possible
Meteorite impact	Likely	Likely (during magmatism)	Yes (probably abundant)	Yes	Possible	Possible
Edge model, with enhanced mantle convection	Possible (if mantle can ascend sufficiently to decompress and melt)	Likely (during magmatism)	Unlikely	No	Unlikely	Unlikely
Delamination	Possible (if mantle can ascend sufficiently to decompress and melt)	Likely (could be substantial during or after magmatism)	Unlikely	No	Unlikely	Unlikely
Melting of fertile mantle without excess heat	Possible	Unlikely	Unlikely	No	Unlikely	Unlikely

A substantial body of research has been conducted on how LIPs form, which has lead to multiple origins, summarised by Saunders (2005). Because oceanic plateaus show compositional affinities distinct from the OIB (Geldmacher et al., 2003; Thompson et al., 2003; Tejada et al., 2004; White et al., 2004; Hastie & Kerr, 2010; Hoernle et al., 2010; Timm et al., 2011; Tejada et al., 2013; Ussami et al., 2013), the most probable alternatives to the plume model are those of shallow processes: (1) meteorite impact, (2) edge model (with enhaced mantle convection), (3) delamination, and (4) melting of fertile mantle without excess heat (Table 2.1).

While the meteorite impact origin appears attractive (Ingle & Coffin, 2004; Jones, 2005) it has been shown not to be plausible (e.g., Tejada et al., 2004; Korenaga, 2005) for all but a few rare exceptions (e.g., Sudbury; Stoffler et al., 1994). Other alternative models are based on suggestion that there is no need for plumes to exist in order to explain geochemical variations in mantle material (e.g., Anderson, 2005a; Foulger et al., 2005; Foulger, 2010). The edge-driven convection model involves a small-scale convective flow arising from thermal contrasts and differences in lithospheric thickness, for example at the continental-oceanic crust boundary (King & Anderson, 1995, 1998). In contrast, the delamination model invokes detachment of the dense eclogitic bottom from the thick continental crust, causing uplift and subsequent asthenospheric upwelling and decompression melting (Anderson, 2005a, 2007). These two models are proposed for a number of volcanic chains and LIPs from the Atlantic and Indian Oceans (Anderson, 2005a; King, 2007; Regelous et al., 2009; Bardintzeff et al., 2010; Hoernle et al., 2011; Knesel et al., 2011; Perlingeiro et al., 2013; Ussami et al., 2013), formed during and after the supercontitent Pangea break-up, but are hardly recognisable for intraplate structures from the Pacific, emplaced on relatively thin (~6 km) and young (usually < 20 Ma) oceanic crust well away from the continental margins. Lastly, the fertile shallow mantle hypothesis postulates that all irregularities and melting anomalies come from different components (or heterogeneities) hidden in the upper mantle, like “plums in pudding” as opposed to being located and isolated in the lower mantle (Morris & Hart, 1983; Phipps Morgan & Morgan, 1999; Ito & Mahoney, 2005; Machida et al., 2009). Figure 2.3 illustrates the Earth’s cross-section in respect to the mantle plume and shallow mantle melting theories.

Recent global plate tectonic reconstructions have shown a close connection between the intraplate magmatism and plate tectonic boundaries (Sager, 2005; Li & Zhong, 2009; Farnetani & Hofmann, 2011; O'Connor et al., 2012; Seton et al., 2012; Gibbons et al., 2013; Whittaker et al., 2015). For this reason, some authors believe that the plate-tectonic processes, such as plate reorganisations, slab roll-back and back-arc extension, control the “intraplate” magmatism, and there is no need for either fluid dynamic processes or heating from the deep mantle (Norton, 2007; Smith, 2007; James, 2009; James et al., 2011; Long et al., 2012).

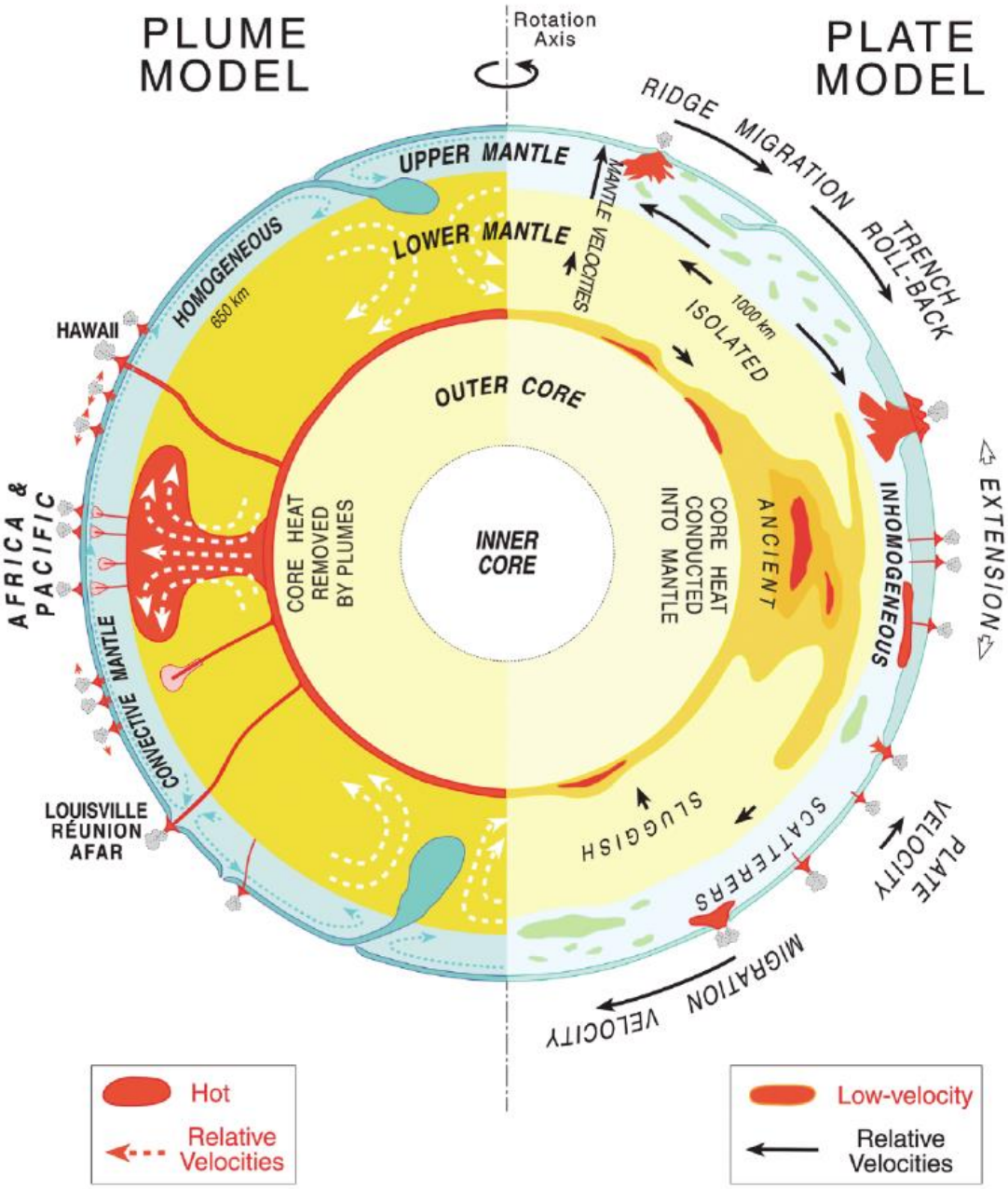

Figure 2.3. Key differences of the plume model (to the left) and plate model (to the right) in Earth's cross-section by Anderson (2005b), modified from Courtillot et al. (2003). In the plume hypothesis heat is derived from the core and is an important factor to produce mantle convection, the lower mantle is heterogeneous, whereas the upper mantle is homogeneous, plumes often initiate the continental break-up and further rifting. The plate model also suggests the two-layered division of mantle, but on the 1000 km depth. The lower mantle is isolated and inaccessible, the upper mantle is characterised by inhomogeneity, mostly represented by recycled crust. According to the "shallow" model, cooling of the plates drives the plates and mantle convection.

Despite the strong scepticism against the plume head hypothesis, mantle plumes remain widely accepted by a majority of scientists. Compared to the mantle plume model, the "plate" models also cannot clearly account for a number of observations related to LIP and hotspot magmatism (Farnetani & Hofmann, 2011): preservation of chemically different long-term isolated reservoirs in the mantle (Hofmann, 2003; Stracke, 2012), numerical simulations favoring existence of thermal boundary layers in the mantle that become repeatedly unstable (Loper & Stacey, 1983; Farnetani & Richards, 1994), presence of seismic anomalies beneath hotspots extending into the lower mantle and partial penetration of the subducted oceanic lithospheric slabs down to the CMB (layer D") (Creager & Jordan, 1984, 1986; Forte & Peltier, 1991; Morgan & Shearer, 1993; Van der Hilst et al., 1997; Boschi et al., 2007; Zhao, 2007; Wolfe et al., 2009) and origin of LIPs and hotspots from the long-lived source provinces, LLVPs (Romanowicz & Gung, 2002; Burke & Torsvik, 2004; Li & Zhong, 2009).

Presently, there is little consensus on how LIPs form. Both theories can be adapted to fit the available data. As mentioned above, mantle plumes may be an important part of mantle convection. While plate tectonic processes (continental drift and oceanic spreading) are widely recognised and well-described, mantle convection dynamics remain yet unsolved (van Keken et al., 2002; 2003). Studies on LIPs, representing large-scale mantle melting events, are particularly important for reconciliation of the geological, geophysical and geochemical observations regarding mantle dynamics (Bryan & Ferrari, 2013).

2.2 PREVIOUS STUDIES ON SHATSKY RISE

2.2.1 Geological location and structure

Shatsky Rise oceanic plateau is located in the Northwestern Pacific, 1600 km east of Japan (Figure 1.2). It is up to 500 km wide with large uplift regions rising to depths of 3.5-2.5 km relative to the surrounding abyssal plain 5000 to 6000 meters below sea level (mbsl) (Sager et al., 1999; Kang et al., 2010). The Shatsky Rise elongated structure trends northeast, with the largest and oldest Tamu Massif followed by the smaller Massifs of Ori and Shirshov, and the waning magmatic activity continued further to the North along the Papanin Ridge and to the East along the Ojin Rise (Sager & Han, 1993; Nakanishi et al., 1999; Sager et al., 2016). The two seamount trails of the Papanin Ridge and Ojin Rise bend eastward, towards the Hess Rise, representing a younger oceanic plateau potentially formed from a common source to Shatsky Rise (Figure 2.4) (Pringle & Dalrymple, 1993; Bercovici & Mahoney, 1994; Nakanishi et al., 1999; Sager et al., 1999; Tejada et al., 2016). The Shatsky Rise structure is further complicated by numerous seamounts, located close to and on top of the three Massifs (Sager et al., 1999; Zhang et al., 2015; 2016a). Among these seamounts are the Toronto Ridge, located at the summit of Tamu Massif; Cooperation Seamount, situated in the Helios Basin between Tamu and Ori Massifs; Earthwatch Seamount, found at the North flank of Shatsky Rise between Shirshov Massif and Papanin Ridge; Victoria Seamount and Seamount 6 from Ojin Rise, located close to the Shatsky Rise and Emperor Seamount Chain, respectively (Figure 2.5) (Sager et al., 1999; Tejada et al., 2016).

Shatsky Rise covers an area of ~5.33 x 10^5 km^2 with a total volume of 6.9 x 10^6 km^3 (Zhang et al., 2016b). The maximum crustal thickness beneath the Shatsky Rise reaches 30 km that is 2-4 times thicker than that of the World Ocean abyssal basins (~ 7 km) (Gettrust et al., 1980; White et al., 1992; Zhang et al., 2016b). Volumes of Tamu (2.5×10^6 km^3), Ori (0.7×10^6 km^3) and Shirshov (0.6×10^6 km^3) Massifs as well as Papanin Ridge (volume 0.4×10^6 km^3) were estimated using the sediment-sill relations together with the crust thickness (Sager et al., 1999). Tamu's average growth rate is between 4.6 and 0.97 km^3/yr, most likely to be ~ 1.8 km^3/yr (Sager, 2005; Sager et al., 2010), compared with 0.1-0.2 km^3/yr for Hawaii (Lipman & Calvert, 2013), the present day most active intraplate volcanism. These high rates for Tamu Massif correspond to those of some other flood basalt provinces (Coffin & Eldholm, 1994b;

Jerram & Widdowson, 2005). Seismic studies on Tamu Massif suggest that it may have grown as a single shield-type volcano, the largest known on Earth (Sager et al., 2013), but further geological evidence is required.

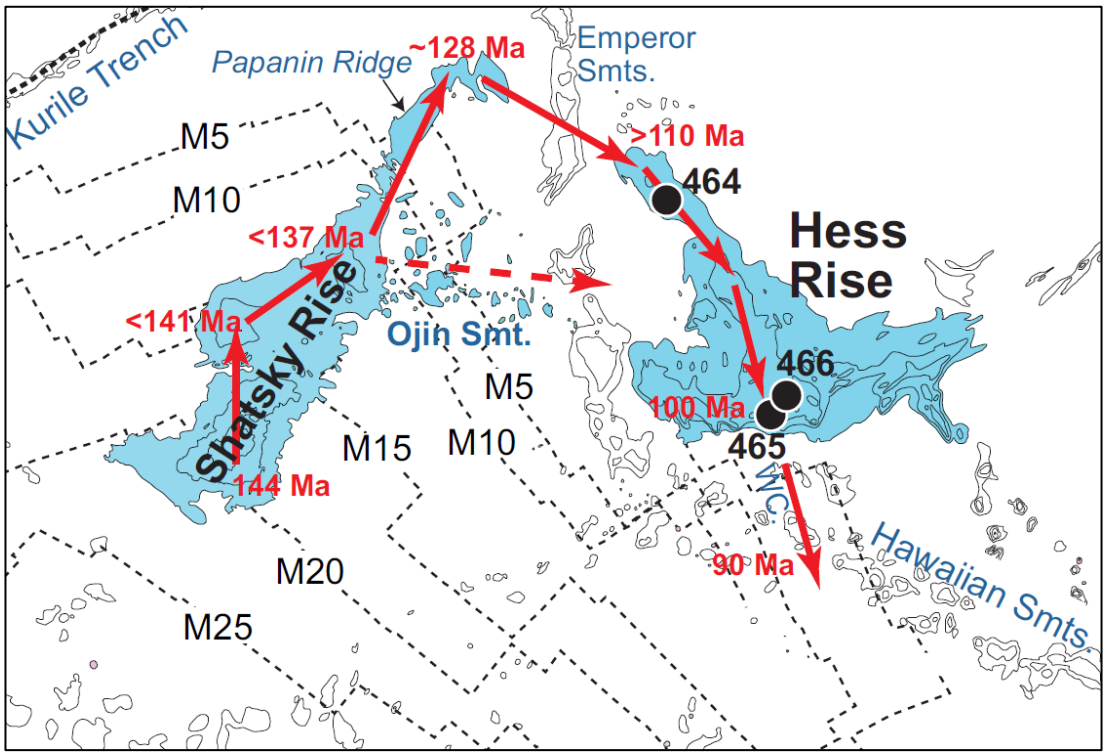

Figure 2.4. Regional map showing locations for Shatsky Rise, Papanin Ridge, Ojin Rise and Hess Rise, relative to the Hawaiian-Emperor seamount trail, after Tejada et al. (2016). Red arrows indicate reconstructed path of intraplate volcanism for 145-90 Myr timeframe, based on assumed ages from magnetic data (Sager, 2005) and ^{40}Ar-^{39}Ar dating (Pringle & Dalrymple, 1993; Mahoney et al., 2005; Geldmacher et al., 2014; Heaton & Koppers, 2014; Tejada et al., 2016). Dashed red arrow demonstrates a possible second hotspot track between Shatsky and Hess Rises, following the Ojin Rise seamount trail, after Sager et al. (1999). Black circles show locations of DSDP drill sites on Hess Rise (Thiede et al., 1981). Dashed black lines indicate seafloor magnetic lineations after Nakanishi et al. (1999). WC = Wentworth Seamount Chain.

2.2.2 Tectonic setting

Since the 1960-s a number of geological expeditions to Shatsky Rise have been organised, including Deep Sea Drilling Project (DSDP) Legs 6 (Fischer et al., 1971), 32 (Larson et al., 1975) and 86 (Wright et al., 1985), Ocean Drilling Program (ODP) Legs 132 (Storms et al., 1971) and 198 (Bralower et al., 2002), IODP Exp. 324 (Sager et al., 2010) and geophysical cruises (Korenaga & Sager, 2012; Sager et al., 2016), including Cruise TN037 (Sager et al., 1995) (Figure 1.2), resulting in a number of

publications, mainly on geophysics (seismology, topography, paleomagnetism) and sedimentology. During these studies it was inferred that the plateau was formed within a period of geomagnetic reversals, unlike many mid-Cretaceous plateaus (Figure 2.6) (Sager et al., 1988; Nakanishi et al., 1999; 2015a).

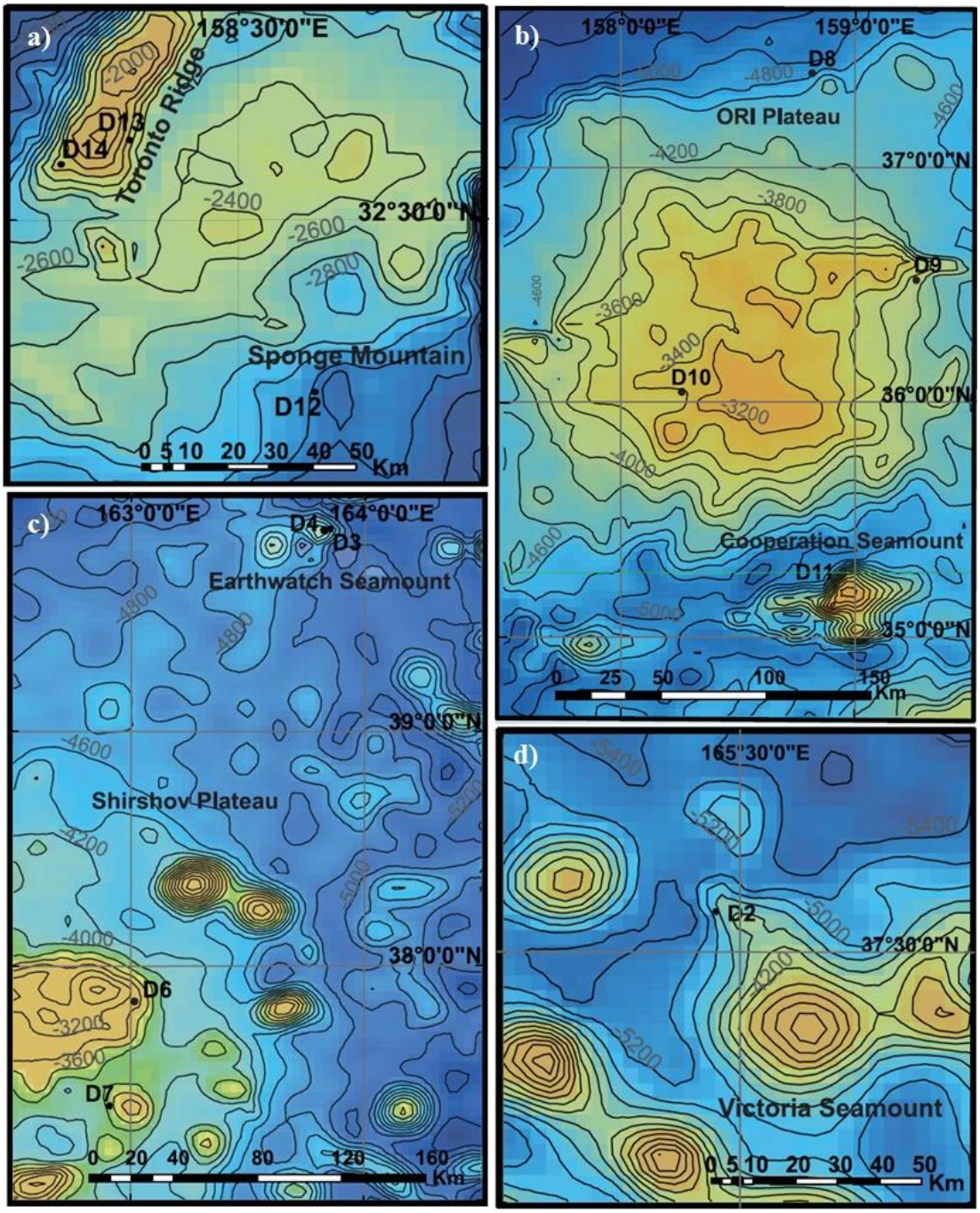

Figure 2.5. Bathymetric maps for Tamu (a), Ori (b) and Shirshov (c) Massifs and Western part of Ojin Rise (d), showing locations of Toronto Ridge, Cooperation, Earthwatch and Victoria Seamounts. Black circles indicate positions of the Cruise TN037 dredges (Sager et al., 1995). Source: (Hein et al., 2012).

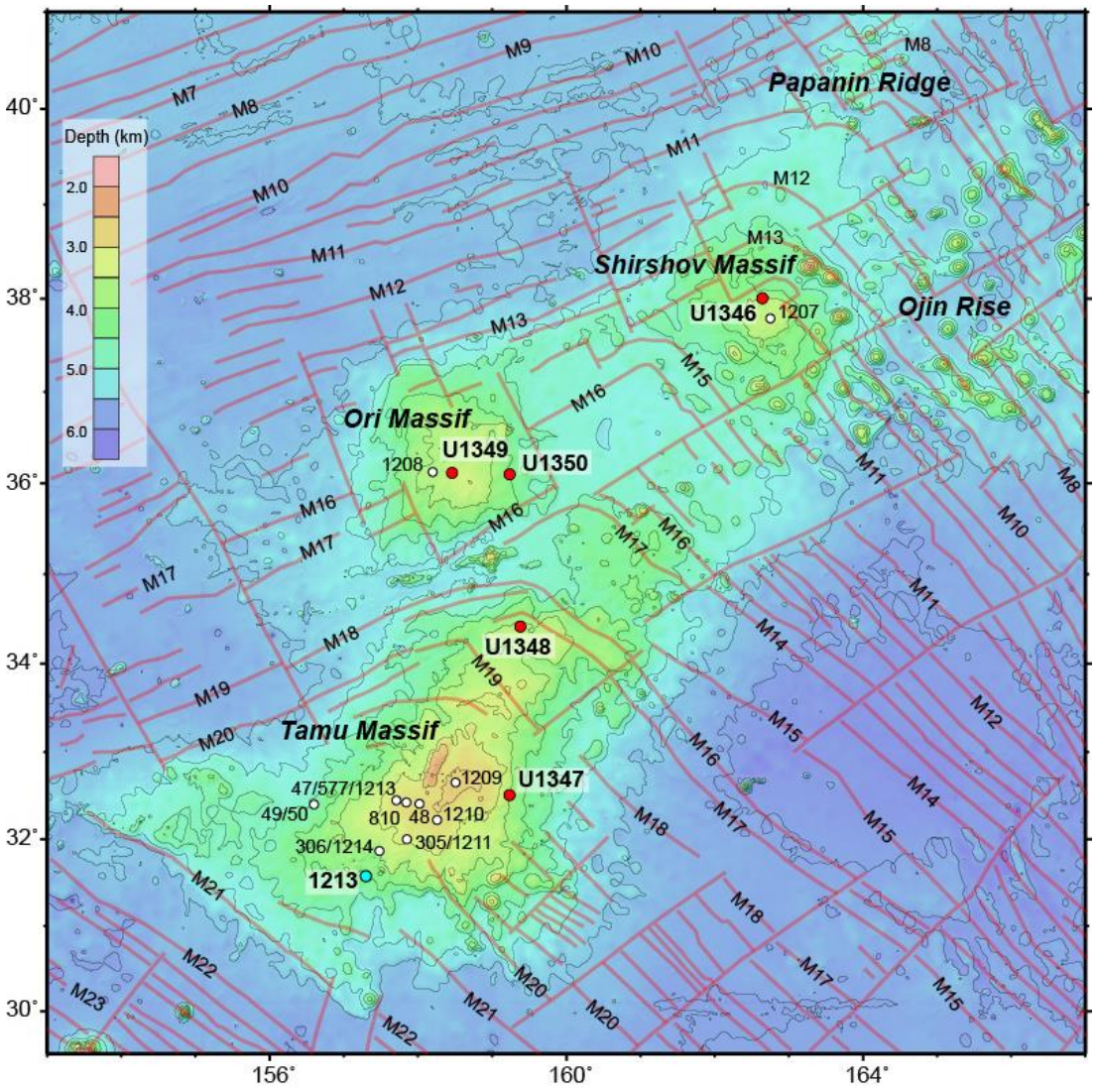

Figure 2.6. The map of Shatsky Rise showing bathymetry, magnetic lineations (red lines) and the locations of Expedition 324 Sites (red circles), Site 1213 (blue circle) and prior drill sites (open circles). Satellite-predicted bathymetry contours are shown at 500 m intervals after Smith and Sandwell (1997). Source: (Sager et al., 2010), modified from Nakanishi et al. (1999).

As inferred from the paleomagnetic data, Shatsky Rise was formed near the paleoequator, within 5º of paleolatitude, and migrated to its present location since Cretaceous (Tominaga et al., 2012; Sager et al., 2015). Studies of magnetic lineations in the surrounding oceanic crust revealed that the Shatsky Rise was formed at an existing triple junction of the Pacific, Farallon, and Izanagi plates during the Late Jurassic to Early Cretaceous time (Figure 2.7), and the entire oceanic plateau magmatism is closely associated with its development (Sager et al., 1988; Nakanishi et al., 1999; Sager, 2005; Nakanishi et al., 2015a; Sager et al., 2015). Recent studies on orientation of joints and veins in the drill cores by Li et al. (2016) confirm that the

formation of Tamu Massif was influenced by seafloor spreading. However, Ori Massif shows no preferred stress field and was likely emplaced off MOR (Li et al., 2016).

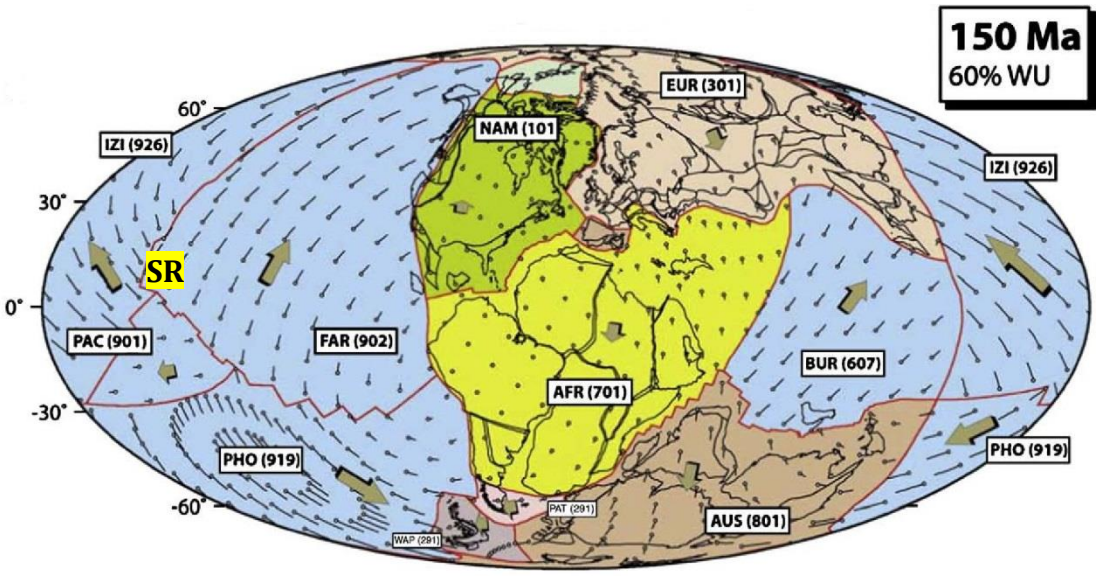

Figure 2.7. Global plate reconstruction for 150 Ma timeframe. Brown arrows show the generalised velocity pattern. WU = world uncertainty. Abbreviations for plates: PAC = Pacific, FAR = Farallon, IZI = Izanagi, PHO = Phoenix, BUR = Burma, NAM = North America, EUR = Europe (Eurasia), AFR = South Africa, PAT = Patagonia, AUS = Australia. SR = Shatsky Rise. Mollweide projection. Source: (Torsvik et al., 2010b).

Although Shatsky Rise was emplaced at an active MOR spreading system, seismic studies do not provide evidence of rifting for the Shatsky Rise edifices (Zhang et al., 2015). This is in contrast to some other LIPs that were separated by rifting during or after formation (e.g., Rio Grande Rise – Walvis Ridge (O'Connor & Duncan, 1990; Ussami et al., 2013); Agulhas plateau – Maud Rise – Georgia Rise (Parsiegla et al., 2008); Madagascar Ridge – Conrad Rise (Gibbons et al., 2013); Kerguelen plateau – Broken Ridge (Frey et al., 2000; Duncan, 2002); Ontong Java Nui (Chandler et al., 2012; 2015); Figure 1.1).

2.2.3 Age of magmatism

Two techniques were applied to determine age of magmatism across Shatsky Rise. Paleomagnetic constraints from the magnetic lineations on oceanic crust revealed that the first portions of Shatsky magma arrived probably as early as M21-M20 (148±1 Ma) and the formation of Tamu Massif continued until M18 (~144 Ma) (Sager et al., 1988; Nakanishi et al., 1999; Sager, 2005; Sager et al., 2015). Later, Ori Massif (M16–M14; ~142–138 Ma) and Shirshov Massif (M15–M13; ~139–137 Ma) were formed

(M-anomaly geomagnetic polarity ages are from the revised timescale after Tominaga and Sager (2010)). These paleomagnetic results are largely consistent with recent ^{40}Ar-^{39}Ar dating of basaltic whole-rock samples and plagioclase separates from Tamu Massif, which yielded 144.6 ± 0.8 Ma (Mahoney et al., 2005) and 131.6-146.4 Ma (Geldmacher et al., 2014). Minimum ^{40}Ar-^{39}Ar age for the eastern part of Ori Massif is ≥117 Ma (Tejada et al., 2016). Further ^{40}Ar-^{39}Ar dating on Shatsky Rise basalts is complicated due to low abundances of plagioclase phenocrysts and alteration.

2.2.4 Basement stratigraphy

Shatsky Rise igneous and volcaniclastic basement is covered with a thick (up to 1.2 km) layer of Early Cretaceous to Quaternary pelagic sediments (radiolarian- and nannofossil-bearing chalks, cherts and calcareous oozes), which gets thinner to absent at the flanks (Sliter & Brown, 1993; Sager et al., 1999; Bralower et al., 2002; Sager et al., 2010). First investigations on the Shatsky Rise igneous basement rocks were based on a single recovered succession of basalts from the southwestern flank of the largest Tamu edifice (ODP, Leg 198, Site 1213, Figure 2.6) (Bralower et al., 2002). During the IODP Exp. 324 five sites were cored, intersecting the uppermost portions of the three elevated Massifs (< 240 meters below seafloor, mbsf, excluding pelagic sediments) (Sager et al., 2010).

Previous investigators have subdivided the volcanic complex of the Shatsky Rise into lava flows, pillow lavas, hyaloclastite and sedimentary deposits, varying in the amount of volcanic and fossiliferous material (Bralower et al., 2002; Koppers et al., 2010; Sager et al., 2010; Tominaga et al., 2015; Sager et al., 2016). I have re-examined the IODP Exp. 324 drill cores, thin sections and the expedition reports and subdivided the cored material into the effusive rocks, primary volcaniclastic and sedimentary deposits, following terminology from White and Houghton (2006) (Figure 2.8). Some of the primary deposits may have been reworked. Revision of the volcaniclastic deposits from Site U1349 is based on results, presented in Chapter 3.

The lithological summary below is based on the drilling results and post-expedition investigations (Bralower et al., 2002; Koppers et al., 2010; Sager et al., 2010; Tominaga et al., 2015; Sager et al., 2016) and was verified during these studies.

Three drill holes penetrated flanks of the largest Tamu Massif: Site 1213 is located on its southern flank, Site U1347 is located on its eastern flank (~200 km

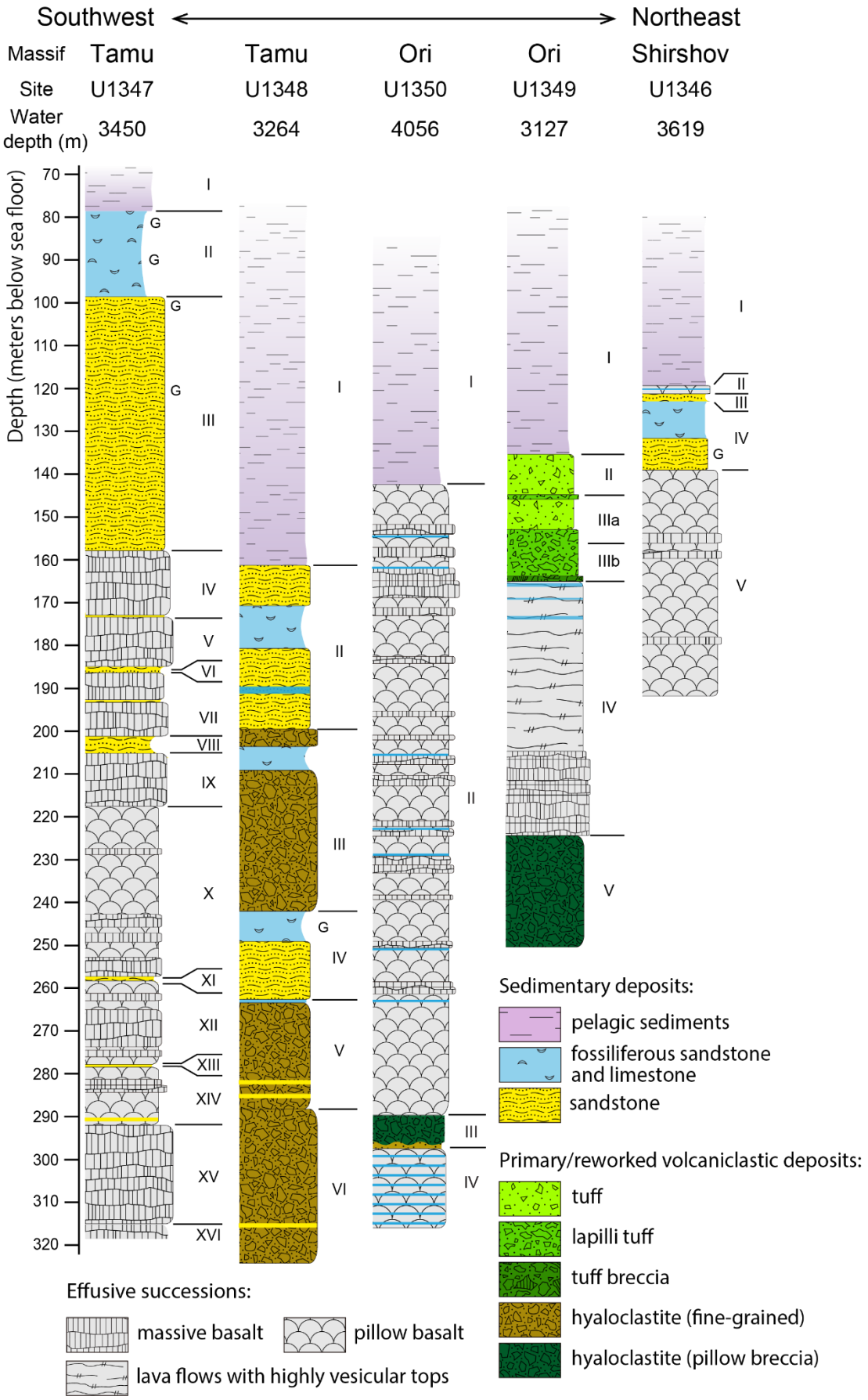
Southwest
Northeast
Massif
Tamu
Tamu
Ori
Ori
Shirshov
Site
U1347
U1348
U1350
U1349
U1346
Water depth (m)
3450
3264
4056
3127
3619
Depth (meters below sea floor)
70
80
90
100
110
120
130
140
150
160
170
180
190
200
210
220
230
240
250
260
270
280
290
300
310
320
I
II
III
IV
V
VI
VII
VIII
IX
X
XI
XII
XIII
XIV
XV
XVI
G
IIIa
IIIb
Sedimentary deposits:
pelagic sediments
fossiliferous sandstone and limestone
sandstone
Primary/reworked volcaniclastic deposits:
tuff
lapilli tuff
tuff breccia
hyaloclastite (fine-grained)
hyaloclastite (pillow breccia)
Effusive successions:
massive basalt
pillow basalt
lava flows with highly vesicular tops

northeast of Site 1213) and Site U1348 is located on its northern flank (~200 km to the North of Site U1347). Thick massive flows (from 1 to 22 m) and thinner pillow lavas (0.2-1 m) are present in the U1347 and 1213 cores. These basalts are non- to moderately vesicular (up to 30% at flow tops) and typically show well-preserved dark-green to black chilled glassy margins. Sheet flow and pillow lava units often display top, core and basal sections with characteristic vesicularity downgrading towards the cores. Sedimentary deposits of volcanic heritage are found in both U1347 and 1213 cores, where they form layers up to 5 m thick in between the massive flows and pillow lava packages and also cover the lava-dominated successions (up to ~80 m in U1347). The sedimentary deposits at U1347 are grey-brown shale-like and fine-grained sandstone, showing abundant bioturbation (e.g., burrows), fine lamination, flame structures and bedding. In contrast, volcanic succession from Site U1348 is entirely composed of structureless and layered dark- to light-grey generally fine-grained hyaloclastite, interlayered with light-green to yellow-grey sedimentary deposits with variable proportions of fossils and fragmented basaltic, typically glassy, material.

Ori Massif was drilled at two locations: Site U1349 is located on the summit of Ori and Site U1350 on its eastern flank (65 km to the East from U1349). Pillow basalts and occasional thin sheet lava flows, similar to those from Tamu, compose most of the volcanic succession at Site U1350. The lowermost portion of core at Site U1350 is composed of pillow lavas with intercalated carbonate sediment. In contrast to U1350, Stratigraphy of Site U1349 is made of relatively thicker lava flows, covered with volcaniclastic deposits. Lava flows from Site U1349 are characterised by grey to grey-brown cores and highly vesicular (~75%) sponge-like reddish-brown tops, where chilled glassy margins are not readily identified. Hyaloclastite deposits from both Sites U1350 and U1349 represent greenish-grey and dark-grey pillow basalt breccia, calcite cemented, where the larger fragments show jigsaw-fit textures, indicating *in situ* deposition.

Figure 2.8 (previous page). Lithologic summary of cores drilled on Shatsky Rise during IODP Exp. 324, compiled and modified after Sager et al. (2010). All Exp. 324 cores were reexamined and subdivided into effusive rocks, primary/reworked volcaniclastic and sedimentary deposits. Roman numbers indicate stratigraphic units, each representing a sequence of similar volcanic facies, such as pillow-lava stacks, packages of sheet flows or sedimentary series as from Sager et al. (2010). Also shown glauconitic (G) occurrences as from the Exp. 324 report.

Shirshov Massif was drilled near the summit at Site U1346. The cored rock material is predominantly composed of pillow basalts potentially from the same eruptive unit, covered with sedimentary deposits, mainly limestone. Pillow basalts and thin flows are well-distinguished by morphologies, pillow contact zones and chilled glassy margins. Inner parts of basaltic units are non-vesicular, getting highly vesicular (up to 50%) towards their outer rims.

Paleomagnetic measurements do not reveal significant variations in paleoinclination at most sites, implying that the volcanic material was emplaced within periods of 100-200 yr (Sites 1213, U1346, U1349, U1347) to 1000 yr (Site U1350) (Carvallo et al., 2013; Sager et al., 2015; 2016). Nevertheless, a number of sedimentary interbeds was recovered across the Shatsky Rise (Figure 2.8), which were interpreted to record long periods of volcanic quiescence (Tominaga et al., 2015; Sager et al., 2016).

2.2.5 Paleoelevations and subsidence

The IODP Exp. 324 drilling provided the first extensive sampling of the basement volcanics and evidence for shallow-marine to potentially subaerial emergence of the Shatsky Rise edifices at the time of formation (Sager et al., 2010; 2016). Evidence for shoaling of the three Shatsky Rise summits includes: presence of shallow-water fossils, collected from all three Massifs (Sites U1347, U1348, U1349, U1346); neritic foraminifer assemblage and bedding structures indicative of shoreface environment above wave base at the flank of Tamu Massif (Site U1347); presence of the highly vesicular lavas (up to 75%) at the summits of Ori and Shirshov Massifs (Sites U1349 and U1346); subaerial oxidation and weathering of lavas and volcaniclastic deposits, presence of oolites and potential paleosol (all from Site U1349). In summary, the Exp. 324 preliminary observations suggested the shallow-marine (Shirshov Massif) to subaerial emergence (Ori and Tamu Massifs) for the summits of Shatsky Rise (Sager et al., 2010). However, recent seismic studies by Zhang et al. (2015) do not show extensive wave erosion for any of the Shatsky Rise edifices, providing evidence against significant emergence.

First subsidence values for the Shatsky Rise were estimated by Ito and Clift (1998) on a single succession of sediments recovered from Tamu Massif (DSDP Site 305; Figures 1.2 and 2.6). The resulting values were recognised as anomalously low, widely ranging from 900 to 2700 m as a result of uncertainties in paleodepth

estimations from microfossils analysis (Ito & Clift, 1998). The results from Ito and Clift (1998) are in agreement with recent subsidence estimations by Shimizu et al. (2013) for basaltic lavas from Site U1347 (~2600 m), located within ~150 km from the DSDP Site 305 at Tamu Massif. Nevertheless, Shimizu et al. (2013) demonstrated a significantly greater subsidence for other locations across the Shatsky Rise. Shimizu et al. (2013) suggest that the total subsidence for the central part of the Shatsky Rise is the greatest (~3300 m, Ori Massif) and gets lower towards the southern Tamu Massif (~3000 m for Site U1348 and ~2600 m for Site U1347) and the northern part of this plateau (~2900 m, Shirshov Massif).

2.2.6 Igneous and alteration petrology

Optical microscopy investigations on basalts from the Shatsky Rise edifices were carried out during the ODP Leg 198 and IODP Exp. 324 cruises and post-expedition investigations (Bralower et al., 2002; Koppers et al., 2010; Sager et al., 2010; Delacour & Guillaume, 2013; Husen et al., 2013). My examination of the available thin sections from the IODP Exp. 324 Sites are in agreement with previous investigations.

Pillow lavas and lava flows from Shatsky Rise are aphyric to sparsely phyric tholeiitic basalts, where phenocrysts of plagioclase, clinopyroxene and olivine usually compose less than 3 vol. %. Plagioclase is the most abundant phenocryst and groundmass mineral at all Sites. Clinopyroxene (augite) may be widespread along with plagioclase in some basalts and is absent in the others. Plagioclase-clinopyroxene intergrowths occur within the phenocrysts assemblages (glomerophyres) across Shatsky Rise and, additionally, as ophimottles within the groundmass in basalts from Site U1349. Olivine is rare in basalts from Sites 1213, U1347 and U1350, is relatively more abundant in basalts from U1346 and is more widespread in olivine-rich basalts, limited to Site U1349. Olivine in basalts from Sites U1346 and U1349 often contains chromium spinel. Where present, olivine is completely altered, except for two horizons from Site U1349 at 206.8-207 mbsf (Almeev et al., 2011) and at 236.2-238 mbsf (personal observations). Opaque minerals (e.g., titanomagnetite) are commonly observed within the groundmass. Common alteration mineralogy replacing primary minerals and filling vesicles, voids and veins includes smectite clays, carbonates, zeolites, celadonite, iddingsite, kaolinite, illite, chlorite, sulfides, Fe-oxyhydroxydes and Fe-oxides (Sager et al., 2010; Delacour & Guillaume, 2013; Li et al., 2016).

Glassy margins of pillow lavas and lava flows from Shatsky Rise are usually 1-3 cm thick and contain individual crystals or stellate intergrowths of plagioclase, clinopyroxene and olivine. The amount of glass in basalts decreases inwards from the margins to less than 50 % in pillow lavas across Shatsky Rise and less than 10 % in some of the thick flows from Site U1347. Usually, the interstitial spaces (either glass or fine crystals) between the phenocrysts are entirely altered to clay minerals. Nevertheless, intervals with fresh glass are observed in many localities at Sites U1347 and U1350 and one horizon of U1346 (Sano et al., 2012).

2.2.7 Geochemistry

Geochemical studies on Shatsky Rise were carried out on cored sheet flows and pillow lavas and, to a much lesser extent, on some recovered volcaniclastic material (Mahoney et al., 2005; Sano et al., 2012; Husen et al., 2013; Heydolph et al., 2014; Hanyu et al., 2015). Further analyses were conducted on dredged samples from the Shatsky Rise and nearby seamounts, collected during site survey Cruise TN037 (Tatsumi et al., 1998; Tejada et al., 2016).

Samples from the Shatsky Rise form a trend from less evolved (MgO ~ 12 wt. %) to more evolved (MgO ~ 5 wt. %) compositions (Sano et al., 2012; Husen et al., 2013). Shatsky Rise lavas were subdivided into four magmatic types (Normal, Low-Ti, High-Nb and U1349) by Sano et al. (2012), using the alteration-immobile element ratios of Nb/Ti, Nb/Sc and Zr/Ti (Figure 2.9). Multi element patterns of Normal type basalts are nearly identical to Normal MORB (N-MORB) with slightly greater depletion of Heavy Rare Earth Elements (HREE). Low-Ti type basalts show relatively lower TiO_2 and FeO contents at a given MgO, but their trace element patterns largely overlap with those of the Normal-type. High-Nb samples are somewhat enriched in many incompatible elements (K, Nb, Ta, Zr, Rare Earth Elements, REE), and their multi-element patterns resemble Enriched MORB (E-MORB) or even OIB. Samples from pillow lavas and lava flows at Site U1349, on Ori Massif, appear to be very different from the rest of Shatsky Rise, and their multielement patterns are similar to picrites from Iceland (e.g., Kokfelt et al., 2006). These olivine-phyric basalts of the so called U1349 type are characterised by the highest MgO contents (8-12 wt. %) and the greatest depletion of the more incompatible elements (Almeev et al., 2011), excluding the fluid mobile elements Cs, Rb, Ba that are probably affected by seawater alteration.

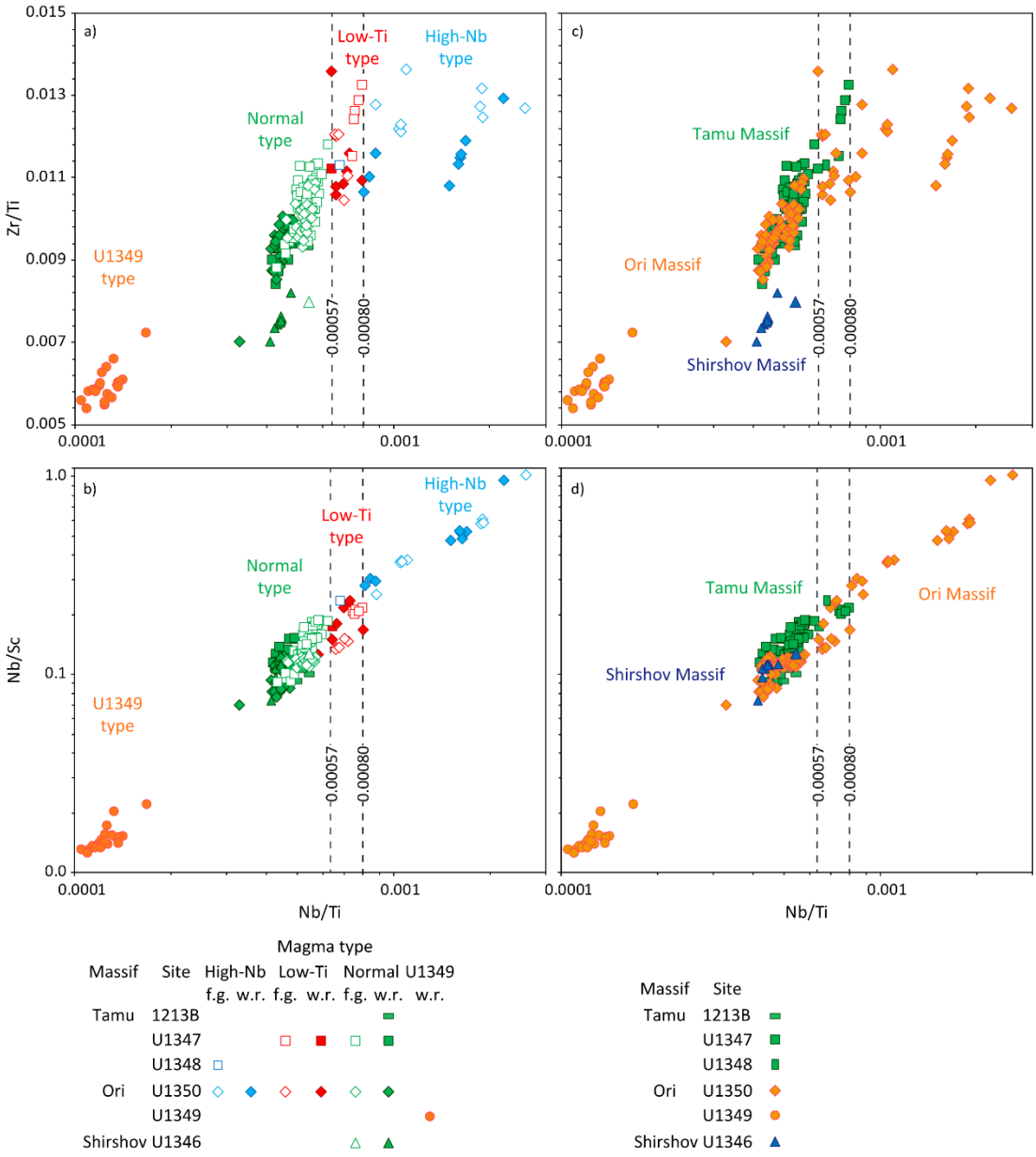

Figure 2.9. Classification of all available compositions from Shatsky Rise on Zr/Ti and Nb/Sc versus Nb/Ti plots, following Sano et al. (2012). Plots a) and b) highlight subdivision of samples into four magmatic types by Sano et al. (2012), whereas colours on c) and d) indicate Massif where samples are located. On a) and b) open symbols indicate the fresh glass compositions and filled symbols correspond to the whole-rock samples. On all plots shapes of symbols refer to drill holes, Sites U1349 (circles), U1350 (diamonds), U1347, U1348 and 1213 (squares) and U1346 (triangles). Data from Sano et al. (2012) and Mahoney et al. (2005).

Lavas from Tamu Massif are overwhelmingly formed by Normal-type magmas, whereas at Ori Massif all four magmatic types are found (Figure 2.9). Only Normal-type lavas were recovered at Shirshov Massif, which potentially belong to the same eruptive unit and may not be representative of composition for this edifice (Sager et

al., 2010). Geochemical modelling suggests that the Normal type lavas were formed by ~15% (Sano et al., 2012) to 20% (Husen et al., 2013) melting of a relatively depleted mantle source in the presence of residual garnet (>85 km). Thermodynamic modelling (Husen et al., 2013) and experimental studies (Husen et al., 2016) on Shatsky Rise fresh glass compositions from the three edifices indicate presence of multi-level plumbing system with fractionation at different crustal levels. The differentiation of the less-evolved magmas (MgO > 8 wt. %) started at ~14 km depth, whereas crystallisation of the most evolved compositions occurred at ~3 km (Husen et al., 2013; 2016).

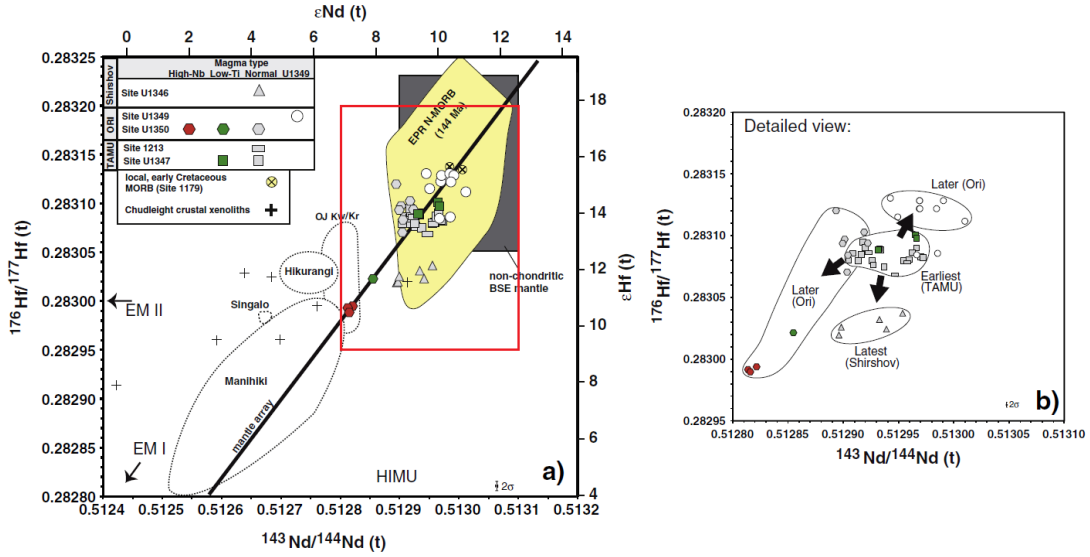

Figure 2.10. On a) initial $^{143}Nd/^{144}Nd_t$ versus $^{176}Hf/^{177}Hf_t$ isotope ratios for data from Shatsky Rise; on b) a detailed view, showing sample allocation in relation to each edifice. Additional data for Manihiki, Hikurangi, Ontong-Java (Singalo and Kwaimbeita (Kw) and Kroenke (Kr)-types) oceanic plateaus are from Tejada et al., (2004), Mahoney et al., (2005), Hoernle et al., (2010), Timm et al., (2011). Also shown compositions of the non-chondritic Bulk Silicate Earth (BSE) mantle (Jackson & Jellinek, 2013), Chudleigh crustal xenoliths (Rudnick & Goldstein, 1990) and modern age-corrected East Pacific Rise N-MORB (Nowell et al., 1998; Salters & White, 1998; Chauvel & Blichert-Toft, 2001). Red box on a) shows the location of diagram b). Source: (Heydolph et al., 2014).

First Pb-Nd-Sr isotopic compositions for samples from Tamu and Ori Massifs, Site 1213 and Cruise TN037, were shown to be indistinguishable from the present day East Pacific Rise (EPR) MORB (Mahoney et al., 2005). Recent Hf-Nd-Pb isotope investigations by Heydolph et al. (2014) on samples from all three edifices suggest

that this depleted EPR-like component was dominant during formation of the Normal and Low-Ti type basalts (Figure 2.10). The U1349 type basalts are more depleted than Normal type basalts (and DMM) but found isotopically identical to contemporaneous ~132 My oceanic crust cored at ODP Site 1179 nearby to Shatsky Rise (Figure 1.2) (Heydolph et al., 2014). Therefore, the U1349 type basalts were interpreted to represent the early Cretaceous depleted upper mantle that was entrained during Shatsky Rise formation and underwent higher degree of melting due to the excess of heat from the Shatsky plume (Heydolph et al., 2014). The High-Nb type basalts show isotopically enriched (EM or HIMU-like) mantle compositions, and were interpreted by Heydolph et al. (2014) to represent the recycled continental material (lower continental crust or subcontinental lithosphere). Presence of the recycled (HIMU) mantle material in the source of Shatsky Rise lavas is consistent with studies of Hanyu et al. (2015), reporting $^{3}He/^{4}He$ isotope signatures for Normal type basalts that are systematically lower than MORB. Additionally, first studies on V isotopes on mafic rocks by Prytulak et al. (2013) reveal deviation of the Shatsky Rise samples from MORB, implying that the mantle source for this LIP could have been different from typical Depleted MORB Mantle. In summary, analysis of the existing geochemical data, mainly from Tamu and Ori Massifs, suggests that Ori Massif is characterised by the largest diversity of magmatic types and heterogeneity of mantle sources among the Shatsky Rise edifices.

Geochemical investigations on Toronto Ridge (D13 and D14), Seamount 6 (D1), Victoria (D2), Cooperation (D11) and Earthwatch (D4) Seamounts (Figures 1.2 and 2.5) were conducted by Tatsumi et al. (1998) and Tejada et al. (2016) on dredged samples collected during the Cruise TN037 of the *R/V Thomas G. Thompson* (Sager et al., 1999). Toronto Ridge is characterised by MORB-like isotope compositions and $^{39}Ar/^{40}Ar$ age ~129 Ma (Heaton & Koppers, 2014), overlapping with these values obtained for basalts from Tamu Massif (131-146 Ma; Mahoney et al., 2005; Geldmacher et al., 2014), and was interpreted as part of prolonged (~15 Ma) magmatism at Tamu Massif (Tejada et al., 2016). Minimum ^{40}Ar-^{39}Ar age estimations for Cooperation seamount are ≥122 Ma (Tejada et al., 2016). The precise age constraints for the other seamounts were not obtained, while their major and trace element and isotope compositions show alkali tholeiitic affinities and the most enriched compositions are associated with the Cooperation Seamount (Tatsumi et al.,

1998; Tejada et al., 2016). As geochemical compositions of basalts from Shatsky Rise are predominantly MORB-like (Mahoney et al., 2005; Sano et al., 2012; Heydolph et al., 2014), the relationship of the Shatsky Rise magmatism to the nearby seamounts, Papanin Ridge and Ojin Rise remains unclear (Tejada et al., 2016).

2.2.8 Alteration assessment

The recovered volcanic successions from Shatsky Rise have undergone slight to complete alteration as a result of seawater-rock interaction and oxidation (Sager et al., 2010; Sano et al., 2012; Delacour & Guillaume, 2013; Li et al., 2014; Miyoshi et al., 2015; Sager et al., 2016). According to these investigations, effusive rocks and volcaniclastic deposits from the summits of Ori and Shirshov Massifs (Sites U1346 and U1349) and high part of Tamu Massif (Site U1348) demonstrate considerably higher degrees of alteration than that observed at the flanks of Tamu and Ori Massifs (Sites 1213, U1347 and U1350). More intense alteration at the high parts of the three Massifs is interpreted as a result of higher permeability of vesicular lavas and volcaniclastic rocks and overall greater hydrothermal circulation (Sager et al., 2010; Delacour & Guillaume, 2013; Li et al., 2014; Miyoshi et al., 2015; Sager et al., 2016).

Basalts from Sites U1347 and U1350 are characterised by light to moderate degrees of low-temperature alteration, resulting in a complete replacement of olivine and glassy mesostasis to smectitic clays and calcite, except for horizons with fresh glass occurrences (Sager et al., 2010; 2016). Among these two locations, the most altered igneous rocks, containing secondary zeolite, are found within the lowermost recovered igneous rocks at Site U1350, which are composed of pillow lavas with intercalated carbonate sediment (stratigraphic unit IV) (Sager et al., 2010).

The volcaniclastic succession at Site U1348 is mainly formed by hyaloclastite fragmentation and contains glassy fragments that are completely altered to secondary palagonite and cemented with zeolite and calcite, except for one interval with fresh glass fragments at 187 mbsf (Sano et al., 2012; Sager et al., 2016). Volcanic successions from the summits of Ori and Shirshov Massifs (Sites U1346 and U1349) have undergone significant alteration at low to elevated temperatures (Li et al., 2014; Miyoshi et al., 2015; Sager et al., 2016). In addition to alteration of glassy mesostasis and replacement of olivine by smectitic clays, carbonates and zeolites (except for a few fresh occurrences, see Chapter 2.2.6), basalts from Sites U1346 and U1349 demonstrate intense alteration of other primary magmatic minerals (pyroxene,

plagioclase, Fe-Ti-oxides) and show presence of secondary celadonite, kaolinite, chlorite and sulfides (Sager et al., 2010; Delacour & Guillaume, 2013). Furthermore, lava flows from Site U1349 have undergone red-brown alteration and contain secondary iddingsite, illite, Fe-oxyhydroxydes and Fe-oxides, interpreted as a result of subaerial oxidation (Sager et al., 2010; Delacour & Guillaume, 2013).

Whole-rock basalts from all sites demonstrate variable uptake of fluid mobile elements, such as K, Cs, Rb, Ba, U and increase in Loss on Ignition (LOI) as a result of low-temperature seawater alteration (Sager et al., 2010; Sano et al., 2012; Miyoshi et al., 2015). These authors indicate that basalts from the summits of Ori and Shirshov show higher LOI and B contents, as compared to the flanks of Tamu and Ori Massifs. The seawater alteration most probably occurred soon after formation of the Massifs, as inferred from studies on carbonate vein precipitation (Li et al., 2014).

2.3 PLUME VERSUS PLATE ORIGIN FOR THE SHATSKY RISE

Previous researchers usually assumed that Shatsky Rise formation was due to a mantle plume (Sager & Han, 1993). Many features of the Shatsky Rise can be explained by the plume head model: with an area of ~4.8 x 10^5 km^2 it is considered one of the largest LIPs, its emplacement rates were high (up to 4.6 km^3/y), its elongated structure with progressively decreasing age resembles plume-head to plume-tail transition (Sager, 2005). The observed thickness of individual lava flows as well as the proportion of sheet flow to pillow lava units decreases from Tamu to Ori and to Shirshov Massifs, implying that the volcanic eruption rates became lower and less effusive during the Shatsky Rise evolution (Sager et al., 2010; 2011; Sano et al., 2012). Paleontological and lithological studies provide evidence for shallow-marine to potentially subaerial environments during plateau formation, suggesting significant volcanic edifice construction (Sager et al., 2010; Shimizu et al., 2013; 2016). Paleoreconstructions indicate that the plateau was formed above the present-day location of the large low shear velocity zone in the south west Pacific referred to as the Pacific Superplume, like many other Pacific oceanic plateau and hotspot tracks (Figure 2.2) (e.g., Tatsumi et al., 1998; Burke et al., 2008; Li & Zhong, 2009).

However, the mantle plume origin for the Shatsky Rise as well as other oceanic plateaus remains controversial (e.g., Anderson, 2005a; Foulger et al., 2005; Foulger, 2010). Despite the existing evidence for Shatsky Rise shoaling in Early Cretaceous,

the estimated paleoelevations and subsidence remain lower than predicted by the mantle plume head model (Korenaga, 2005; Sager et al., 2016). Importantly, like many other plateaus, the Shatsky Rise displays geochemical characteristics that are largely similar to MORB (Mahoney et al., 2005; Sano et al., 2012; Husen et al., 2013; Heydolph et al., 2014). Mid-ocean ridge basalts are widely understood to have been sourced from shallow depths in the upper mantle and by passive decompression melting (Zindler & Hart, 1986; Rampone & Hofmann, 2012; Stracke, 2012). Furthermore, recent studies by Nakanishi et al. (2015a) suggest that the plate boundary reorganizations at the Pacific-Farallon-Izanagi triple junction began several millions of years before the formation of Tamu Massif, implying that the triple junction jumps were not caused by the eruptions at Shatsky Rise. In fact, the formation at a triple junction fits better with the lithospheric model, because it is a low-probability event (~0.4%) that plume activity coincides with an existing ridge-ridge-ridge junction, unless the plumes and triple junctions are related to each other (Sager, 2005; Sager et al., 2010, 2016; Farnetani & Hofmann, 2011).

Non-plume and plume models for the Shatsky Rise formation were proposed by Shimizu et al. (2013) to explain the differences in subsidence degrees for the Tamu and Ori Massifs. The first model does not require thermal anomaly from a mantle plume and suggests formation of the Shatsky Rise from the fertile mantle melting beneath plate extension. In this case, the low subsidence values for Tamu Massif, comparatively to Ori Massif, are interpreted as a result of a large buoyant mass underpinning Tamu Massif that is relatively thinner beneath the Ori Massif (Shimizu et al., 2013). However, such underplating would show a high-velocity lower crustal layer beneath Tamu Massif, which is not observed in the seismic refraction profiles (Korenaga & Sager, 2012). The second model by Shimizu et al. (2013), involving a hot mantle plume origin for the plateau, requires emplacement of the Tamu Massif on a pre-existing ~5 Myr oceanic crust. In this model, the initial total crustal thickness of the plateau is estimated as ~20 km, and the subsequent prolonged crustal growth resulted in the observed ~30 km thickness of the crust (Korenaga & Sager, 2012; Zhang et al., 2016b). In conclusion, current state of knowledge in support of both plume and lithospheric models for Shatsky Rise formation remains contradictory (Sager et al., 2016).

2.4 CONCLUSIONS

Over the past years a number of expeditions was organised to Shatsky Rise, which enabled collection of seismic data and the first drilled and dredged basement samples from this submerged oceanic plateau (Sager et al., 1995; Bralower et al., 2002; Sager et al., 2010; Sager et al., 2016). Current knowledge on mantle sources that contributed to Shatsky Rise magmatism is based on limited geochemical studies of basalts from pillow lavas and lava flows (Mahoney et al., 2005; Sano et al., 2012; Husen et al., 2013; Heydolph et al., 2014). There are no detailed studies on volcaniclastic deposits, despite they compose a significant proportion of the recovered core material at Shatsky Rise (Figure 2.8). Importantly, volcaniclastic deposits of pyroclastic origin were not previously recognised at Shatsky Rise. Such questions as styles of volcanic eruptions and associated paleodepths, geochemical composition of basaltic fragments from volcaniclastic deposits and their alteration were addressed only during preliminary investigations (Sager et al., 2010). This PhD project is attempting to re-investigate the origin of the volcaniclastic deposits from Ori Massif and provide new geochemical data on basaltic fragments from these deposits in order to understand mantle sources and geodynamic settings during formation of this edifice.

Chapter 3: Volcaniclastic deposits from Site U1349, Ori Massif: Implications for a shallow-marine phreatomagmatic volcanism

3.1 INTRODUCTION

Oceanic plateaus are extensive, elevated, magmatically over-thickened regions of seafloor, for which formation processes remain debated (Keith, 2001; Foulger, 2005; Campbell, 2007; Li & Zhong, 2009; Bryan & Ferrari, 2013). Most extant oceanic plateaus were formed in the Mesozoic on young contemporaneous oceanic crust (< 20 Ma at the time of emplacement) with some plateaus appearing to coincide with MOR spreading (Table 3.1) (Sager et al., 2016). Compositionally, oceanic plateaus resemble tholeiitic basaltic crust produced at MORs rather than that of oceanic island basalts (OIBs) (Kerr, 2014 and references therein). Nevertheless, crustal thickness of oceanic plateaus (10-40 km) is up to 6 times greater than that of "normal" oceanic crust (6-7 km) produced at MORs (Carlson et al., 1980; Coffin & Eldholm, 1994b; Kerr, 2014).

Oceanic plateaus represent topographic highs, presently sitting 2-4 km above the surrounding seafloor, and reach water depths of 1-3 km, regardless of the age of oceanic crust that they are built on (Table 3.1) (Korenaga & Korenaga, 2008; Kerr, 2014 and references therein). Such elevated topography contrasts with normal oceanic crust as it ages and undergoes thermal cooling and subsidence, changing in elevation from ~2.5 km below sea level at ridges to up to 11 km below sea level in distant trenches as subduction zones (e.g., Mariana trench; Stein & Stein, 1992; Hillier & Watts, 2005; Korenaga & Korenaga, 2008). The observed elevated topography of oceanic plateaus is principally a result of greatly increased crustal thickness leading to permanent plateau buoyancy (Cloos, 1993).

Shallow lithospheric model suggests that the plateaus grow by volcanic construction to achieve the present-day observed elevations of 2-4 km above the sea floor (Table 3.1), but that the consequence of crustal overthickening resulted in the plateaus having permanent topography (Ito & Clift, 1998; Korenaga, 2005). In

contrast, plume models for oceanic plateau and LIP formation predict significant dynamic topography immediately prior to and during emplacement as a result of the elevated thermal anomaly, higher-degree melting, and greater thermal expansion of the lithosphere at a lower surface area-to-volume ratio (Campbell & Griffiths, 1990; Coffin, 1992; Campbell, 2007; Kerr & Mahoney, 2007). In terms of plume head model, oceanic plateaus are expected to become emergent above sea-level as a consequence of pre-volcanic dynamic uplift and voluminous magmatism (Campbell & Griffiths, 1990; Şengör, 2001; Korenaga, 2005; Rudge et al., 2008; Burov & Gerya, 2014). However, studies on many continental LIPs do not provide any evidence for significant pre-volcanic uplift, or at the very least, the evidence remains highly debated (McHone, 2000; Menzies et al., 2002; Hales et al., 2005; Saunders et al., 2005; Sheth, 2007; Ukstins Peate & Bryan, 2008, 2009; Sun et al., 2010). In contrast to continental settings, oceanic crust is relatively thin and less-complex such that dynamic topography during oceanic LIP formation may be better developed (Richards et al., 1991). The amplitude of plateau paleoelevations, resulting from pre- or syn- eruptive uplift, and the subsequent history of subsidence are the key geological observational constraints on vertical dynamics that can help reconstruct the thermal conditions of the lithosphere during LIP magmatism (Ito & Clift, 1998; Clift, 2005; Korenaga, 2005; Korenaga & Korenaga, 2008).

Importantly, recent studies on the Kerguelen, Wrangellia and the largest known Ontong Java Nui oceanic plateaus have revealed that during their growth and emplacement, the plateaus reached higher than present-day elevations, and were either initially emergent (Kerguelen, Coffin, 1992; Frey et al., 2000; Wrangellia, Greene et al., 2010) or became temporarily emergent during formation (Ontong Java Nui, Coffin & Eldholm, 1994b; Mahoney et al., 2001; Thordarson, 2004; Chandler et al., 2012) (Table 3.1). More persistent evidence for subaerial emergence is preserved on the Kerguelen plateau where subaerially formed pyroclastic units, aa and pahoehoe lavas, various plant fossil remains and terrestrial sediments have been recovered (Frey et al., 2000). However, crustal gneisses were also discovered at Kerguelen, suggesting continental lithospheric underpinning to the plateau and helping to explain the subaerial character to the plateau (Weis et al., 2001; Bénard et al., 2010). The evidence of shoaling from the accreted Wrangellia oceanic plateau (230-225 Ma) includes extensive subaerial effusive and explosive volcanic rocks, conglomerates, and

preservation of shallow-marine fossils (bivalves, ammonites) (Greene et al., 2008; 2010). However, the subaerial character for most of the Wrangellia flood basalts is explained by their formation on top of the Permian volcanic island arc, which is shallower and thicker than "normal" oceanic crust (Richards et al., 1991; Kerr, 2014 and references therein). For the Ontong Java Nui plateau, basaltic accretionary lapilli tuffs from the highest part of the submerged plateau were interpreted to have formed as a result of explosive phreatomagmatic Surtseyan-style activity generated in shallow water (Thordarson, 2004). Importantly, the preservation of the accretionary lapilli tuff requires subaerial deposition as accretionary lapilli are expected to disaggregate if deposited into water (Cas & Wright, 1988; Schumacher & Schmincke, 1995). It therefore remains unclear whether emergence of the Kerguelen, Wrangellia and Ontong Java Nui plateaus is unique and localised to these plateaus because of endemic features such as continental basement (Kerguelen), arc basement (Wrangellia), or the enormity of Ontong Java Nui, or whether shoaling to shallow water depths and potentially brief emergence may in fact be common characteristics of oceanic plateau formation. If it is a common feature of oceanic plateaus and by constraining the timing of the emergence, this may provide important constraints on the mantle plume hypothesis (Coffin & Eldholm, 1994a; Kerr et al., 2000).

The Mesozoic Shatsky Rise oceanic plateau located in the North-western Pacific is known to be emplaced away from continental margins and subduction zones (Nakanishi et al., 1999), and therefore is selected for this study to test whether shoaling or emergence, if any, is associated with its formation. Importantly, results from the IODP Exp. 324 to Shatsky Rise provided several lines of evidence that its summits could have been shallow-marine (Shirshov Massif) to subaerially emergent (Tamu and Ori Massifs) in the Early Cretaceous, but which have subsequently subsided to the current water depths of 2-3 km (Sliter & Brown, 1993; Sager et al., 1999, 2010; Bralower et al., 2002). However, evidence for near sea-level and subaerial emergence of Shatsky Rise edifices remains unverified and is mainly based on preliminary paleontological observations (see details in next section), and is not consistent with seismic observations (Zhang et al., 2015). The purpose of this study is to re-examine the evidence for Shatsky Rise shoaling in more detail, focusing on Ori Massif to contribute to the discussion on whether shoaling +/- brief emergence may be common in oceanic plateau formation.

Table 3.1. Characteristics of existing oceanic plateaus

Oceanic plateau	Location	Age of magmatism (Ma)	Age of oceanic crust upon formation (Ma)	Excess magma volume (10^6 km^3)	Crustal thickness (km)	Current elevation above seafloor (km)	Evidence for shoaling or emergence	Superposed structures / special factors	Post-emplacement rifting	References
Shatsky Rise	N-W Pacific	148-134	148-138	2.5	up to 30	2-4	Highly-vesicular lava flows, littoral and shallow-marine fossils, possibly conglomerate and paleosol (10 m), coral reef fragments	Triple junction of mid-ocean ridges	no	Nakanishi et al. (1999; 2015a); Mahoney et al. (2005); Sager et al. (2010); Geldmacher et al. (2014); Zhang et al. (2015)
Hess Rise	N-W Pacific	110-90	120-90	9.1	15	3.5-4	High vesicularity and red oxidised staining of lavas, weathered trachyte, shallow fossils (< a few hundred m)	Triple junction of mid-ocean ridges?		Vallier (1983); Pringle and Dalrymple (1993); Sager (2005)
Ontong Java	West-Pacific	122-90	140-160	44.4	15-35	2-4.5, partially accreted	Accretionary lapilli tuffs, wood fragments (340 m)	Enormous volume! Collision with Melanesian subduction zone	likely	Thordarson (2004); Ishikawa et al. (2005); Chandler (2015)
Manihiki	West-Pacific	125-115	130-140	8.8	20	3-4 to subaerial	Present-day coral atolls, shallow-marine fossils (bryozoans, echinoderms, bivalves, gastropods) and highly vesicular lava flows	Part of the Ontong Java Nui?	likely	Jenkyns (1976); Beiersdorf et al. (1995); Hoernle et al. (2010); Timm et al. (2011); Nakanishi et al. (2015b)
Hikurangi	West-Pacific	125-120	157-125	2.7	12-15	3-4		Part of the Ontong Java Nui?	likely	Davy (2008)
Magellan Rise	West-Pacific	145-100	157-125	1.8	10	3.5-4		Mid-ocean ridge?		Schlanger et al. (1973)

Table 3.1. Continued

Oceanic plateau	Location	Age of magmatism (Ma)	Age of oceanic crust upon formation (Ma)	Excess magma volume (10^6 km^3)	Crustal thickness (km)	Current elevation above seafloor (km)	Evidence for shoaling or emergence	Superposed structures / special factors	Post-emplacement rifting	References
Caribbean-Colombian	East-Pacific	100, 92–88, 76–72	100-90	4.4	8-20	partially accreted	Shallow-marine fossils, including corals, accretionary lapilli tuffs, ignimbrite, all overlying eroded accreted oceanic plateau basalts	Collision with volcanic arc OR non-oceanic plateau origin (extended continental lithosphere)		Burke (1988); Thompson et al. (2003); James (2009); Wright and Wyld (2011); Hastie et al. (2013)
Wrangellia	N-E Pacific	230-225		1		accreted	Subaerial effusive and explosive volcanics, sedimentary conglomerates, shallow-marine fossils (bivalves, ammonites)	Volcanic arc	no	Richards et al. (1991); Greene et al. (2008; 2010)
Mozambique Ridge	West Indian	140-120	140-122		20-22	2		Mid-ocean ridge	?	König and Jokat (2010); Gohl et al. (2011); Fisher et al. (2017)
Agulhas–Maud Rise–Georgia Rise	West Indian	100-94	100-94	5.2	18-24	2.5		Triple junction of mid-ocean ridges	yes	Ben-Avraham et al. (1995); Parsiegla et al. (2008)
Kerguelen–Broken Ridge	South Indian	118-94	140-120	17.4	20-40	4-0.5, subaerial at present-day hotspot localities	Subaerially formed pyroclastic units, aa and pahoehoe lavas, abundant plant fossil remains and terrestrial sediments, including fluvial conglomerate	Contamination with continental lithosphere. Interaction with present-day hotspot	yes	Bitschene (1992); Charvis et al. (1995); Frey et al. (2000); Weis et al. (2001); Benard et al. (2010)

Table 3.1. Continued

Oceanic plateau	Location	Age of magmatism (Ma)	Age of oceanic crust upon formation (Ma)	Excess magma volume (10^6 km^3)	Crustal thickness (km)	Current elevation above seafloor (km)	Evidence for shoaling or emergence	Superposed structures / special factors	Post-emplacement rifting	References
Madagascar Ridge–Del Cano Rise–Crozet plateau–Conrad Rise	West Indian	90-70	90-70	4.5	20-25	3.5-0.5, subaerial at present-day hotspot localities		Triple junction of mid-ocean ridges. Interaction with present-day hotspot	yes	Sinha et al. (1981); Goslin and Diament (1987); Zhang et al. (2011); Gibbons et al. (2013)
NW Australia (Naturaliste, Wallaby, Exmouth and Scott plateaus, Roo and Joey Rises)	East Indian		<155		10-30	2-3	Shallow-marine shale, deltaic marginal marine and carbonate shoals, volcanic tuffs, subaerial erosion, reefs	Non-oceanic plateau origin? (extended continental shelf / volcanic rifted margin)	yes	von Stackelberg et al. (1980); Colwell et al. (1994); Stagg et al. (2004)
Rio Grande Rise–Walvis Ridge	Atlantic	78-89	78-95		15-30	2-3	Volcaniclastic tuff, shallow-water and reefal fossils, subaerial erosion	Mid-ocean ridge / Contamination with sub-continental lithospheric mantle	yes	Camboa and Rabinowitz (1984); O'Connor and Duncan (1990); Ussami et al. (2013)
Sierra Leone–Ceara Rise	Atlantic	68-84	68-84	2.5	13-17	0.2-3	Fragments of corals	Mid-ocean ridge?	yes	Emelyanov et al. (1990); Jones et al. (2015)

3.2 PREVIOUS KNOWLEDGE ON SHATSKY RISE PALEOELEVATIONS AND THE IMPORTANCE OF VOLCANICLASTIC DEPOSITS FROM SITE U1349

The Shatsky Rise oceanic plateau is outlined by the 5000 m isobath on the surrounding Northwestern Pacific seafloor (Sager et al., 1999). Sediment-corrected depths of igneous basements at the summits of the three main edifices of Shatsky Rise currently sit at water depths of ~2600 m (Tamu Massif, with Toronto Ridge located at ~1950 m), ~3200 m (Ori Massif) and ~3400 m (Shirshov Massif) (Figures 1.2 and 2.6) (Sager et al., 1999; Zhang et al., 2015). The plateau is covered with deep-marine pelagic sediments, showing a generally continuous record from the Lower Cretaceous to the Holocene and indicating that the plateau remained submerged after its formation (Sliter & Brown, 1993; Bralower et al., 2002; Sager et al., 2010). The pelagic sedimentary cap is mostly composed of Cretaceous carbonates, and the observed age unconformities are associated with dissolution of carbonates below the Calcite Compensation Depth (CCD) during plateau subsidence (Pimm et al., 1971; Bralower et al., 2002). However, paleodepths of pelagic sedimentary deposition and the subsidence history for Shatsky Rise during the Cretaceous are still poorly constrained, as a consequence of uncertainties in CCD level (Ito & Clift, 1998; Bralower et al., 2002). During the Cenozoic, the portions of Shatsky Rise shallower than 3 km remained relatively close to the CCD level and the oceanic plateau did not significantly subside further (< 900 m; Ito & Clift, 1998).

The first supporting evidence for shoaling of Shatsky Rise included paleontological and sedimentological observations on the dredged and cored samples from the flanks and summits of the three Shatsky Rise edifices (Sager et al., 1999; 2010). These studies inferred the shallowest paleodepths for the summits of Shatsky Rise, where Tamu Massif was a large island with a summit rising up to ~800 m above sea level, Ori Massif was slightly emergent and the youngest Shirshov Massif may have reached the sea surface (Figure 2.8; Table 3.2). However, glauconite, which was used to indicate shallow water (Sager et al., 2010), has been found to not be depth sensitive and may form over a wide range of water depths (from near sea-level to as deep as 2 km) (Van Houten & Purucker, 1984; Chafetz & Reid, 2000; Baldermann et al., 2013). Furthermore, the observed shallow-marine faunae are sporadic, often occurring as broken fragments and the evidence for *in situ* formation is not well documented. The organisms could have been transported from shallower depths within

Table 3.2. Evidence on shoaling for the Shatsky Rise edifices

Current water depths for the summits from each Massif[1]	Tamu 2600 mbsl[2] (excluding Toronto Ridge)			Ori 3200 mbsl		Shirshov 3400 mbsl
IODP Site	U1347	U1348	D12[3]	U1349	U1350	U1346
Sager et al. (2010):						
Evidence for shoaling	bedding structures indicative of shoaling above the wave baseline, glauconite, neritic benthic foraminifer assemblage	shallow-marine fossil remains (crinoids, gastropods), glauconite, reddish scoria	possible reef fragments (corals and rudist molds)[4]	shallow-marine fossils (echinoderms and bryozoans) (strat. unit[5] IIIa); terrestrial sedimentary conglomerate and possible paleosol (strat. unit IIIb); oolitic limestone, reddened lava flows with highly-vesicular tops (<75%) (strat. unit IV)		highly vesicular lavas (50%), biogenic limestone with epifaunal biota (bivalves, gastropods, echinoderms), shell fragments, echinoids, glauconite, oxidised scoria, possible wood fragments
Current water depths at which the evidence was collected	3530-3600 mbsl	3500-3530 mbsl	3000 mbsl	3270-3300 mbsl		3740-3760 mbsl
Inferred paleodepths for the summits	up to 800 m above sea level	~400 m above sea level	near sea level	~100 m above sea level		near sea level
Shimizu et al. (2013):						
Average eruption depth	943±103 mbsl	381±48 mbsl			767±108 mbsl	781±76 mbsl
Current water depths at which the evidence was collected	3606-3742 mbsl	3551 mbsl			4212-4347 mbsl	3769 mbsl
Inferred subsidence	2585±102 m	2987±48 m			3356±102 m	2917±77 m
Inferred paleodepths for the summits	near sea level	~400 m above sea level			~150 m above sea level	~500 mbsl

[1] Sediment-corrected minimum depth of igneous basement for each summit. [2] mbsl = meters below sea level. [3] Cruise TN037 dredged sample D12 (Figure 2.5a). [4] Undocumented paleontological evidence (Sager et al., 1999). [5] Strat. unit = stratigraphic unit divisions from Sager et al. (2010).

each Massif and buried in deeper waters at the flanks, where most of the paleontological evidence was collected (Table 3.2). Consequently, the paleodepths for the summits of Shatsky Rise could have been shallow-marine and there is no reliable paleontological evidence for subaerial emergence.

Emplacement of volcanics in shallow water depths at the summits of Shatsky Rise is also supported by the recent study of Shimizu et al. (2013), where eruption depths for basalts were estimated based on the measurements of dissolved CO_2 and H_2O in preserved volcanic glasses (Table 3.2). The equilibrium solubility of volatiles is expected at depths of quenching and degassing, and the measured volatile saturation pressures of basaltic glass are considered to be near the vent (Shimizu et al., 2013). Measured water depths vary considerably at each Site, with scatter exceeding 500-1100 m for basalts from the flanks of Tamu (Site U1347) and Ori Massifs (Site U1350), where the overwhelming majority of the fresh glasses was collected (see Figure 2 from Sano et al. (2012)). The reported average volatile saturation depths, after data filtering, imply considerably less intense shoaling for the Shatsky Rise edifices, as compared to the paleontological studies (Table 3.2). According to Shimizu et al. (2013), the summits of Tamu and Ori were near sea level, but not significantly emergent, and the Shirshov Massif was shallow-marine (>500 mbsl).

The critical elements in documenting near-shore and subaerial exposure for Shatsky Rise are observed in the volcanic succession from Site U1349, cored at one of the highest parts of Ori Massif, which represents the shallowest IODP Exp. 324 Site (water depths of 3127 m; Figure 2.8) (Sager et al., 2010). The volcanic succession at Site U1349 was interpreted to record a progressive change upwards in depositional environment from essentially submarine (pillow breccia, Stratigraphic Unit V) to near-shore (reddened lava flows with highly vesicular (40-75%) sponge-like tops and intercalated with oolitic limestone horizons in the upper part, Stratigraphic Unit IV) and to variable depositional conditions from subaerial to shallow-marine (volcaniclastic deposits, Stratigraphic Units III and II) (Sager et al., 2010). The red colour of lavas was interpreted as a result of intense iddingsite alteration of olivine and groundmass in response to subaerial weathering (Sager et al., 2010). However, iddingsite is not exclusively found in subaerial environments (e.g., Clément et al., 2007; Révillon et al., 2007), but is also observed in seafloor basalts ~6 km deep (Talbi & Honnorez, 2003; D'Antonio & Kristensen, 2005). Volcaniclastic deposits contain a

variety of irregular to rounded basaltic fragments, glass shards, crystals and shallow-marine faunae, interpreted as epiclastic shallow-marine debris flow and turbidite deposits and potential paleosol with many clasts sourced from land (Sager et al., 2010). The red and yellow colour of fragments from volcaniclastic deposits (Strat. Units IIIb and II) was interpreted as a consequence of subaerial oxidation of Fe-rich basaltic minerals and used as the main argument for the subaerial exposure of these deposits (Sager et al., 2010). Nevertheless, presence of oolitic limestone (upper Stratigraphic Unit IV) and shallow-marine faunae (including echinoderms and bryozoans, Stratigraphic Unit IIIa) suggest near-shore environments were present at the summit of Ori Massif (Pomar & Hallock, 2008; Sager et al., 2010). In contrast to U1349, Site U1350 from the Eastern flank of Ori Massif was drilled at greater water depths with volcanic basement located about 940 m deeper and does not contain any evidence of shallow-marine deposition (Sager et al., 2010). Importantly, seismic investigations of Zhang et al. (2015) do not support subaerial emergence for any of the Shatsky Rise edifices, because of the lack of evidence for erosional truncation or flattening at the summits of Tamu, Ori and Shirshov Massifs.

In view of conflicting evidence, regarding shoaling and subaerial emergence for the Shatsky Rise edifices, it is important to re-assess the nature of the volcaniclastic deposits from Site U1349, Ori Massif. The purpose of this study is to provide constraints for the origin (pyroclastic versus epiclastic) and paleoelevations upon formation and deposition (subaerial, shallow-marine or deep-marine) for these deposits. Formation by epiclastic processes requires erosion, weathering or reworking of pre-existing rocks from the uppermost portions of Ori Massif and deposition of the newly formed particles by surface processes (e.g., wind, river, ocean currents). Alternatively, in the case of a pyroclastic origin, eruptive styles, including hydromagmatic explosive volcanism, result in in-situ fragmentation and therefore are important water depths indicators. Importantly, high volatile content in magmas, as observed in the highly-vesicular lavas, may trigger explosive volcanic activity (Head & Wilson, 2003; Manville et al., 2009; Graettinger et al., 2013). Pyroclastic activity in subaqueous settings is generally considered to occur shallower than 700-1200 m, depending on volatile content, because the confining pressure of the overlying water column is believed to prevent exsolution of dissolved gas at greater water depths (Head & Wilson, 2003; Manville et al., 2009; Staudigel & Clague, 2010; White et al., 2015).

Surtseyan-style explosive activity generally occurs at water depths of <200 m for basaltic eruptions (Valentine et al., 2014; White et al., 2015). Volcaniclastic deposits are known to record primary volcano-tectonic evolution processes and are particularly important for constraints on paleoelevations and depositional environments in Large Igneous Provinces, including oceanic plateaus (Thordarson, 2004; Ross et al., 2005; Ross & White, 2005; Ukstins Peate & Bryan, 2008; White et al., 2009).

3.3 RESEARCH METHODOLOGY AND MATERIALS

Volcanic successions from the Shatsky Rise were examined at the IODP core repository (College Station, Texas, USA), supplemented with digital photographs of the cores, thin sections, and downhole log data (gamma ray, density, resistivity and concentrations of Uranium and Potassium) (Sager et al., 2010). This study presents new lithostratigraphic descriptions of volcaniclastic deposits from Site U1349, based on detailed examination of samples and thin sections from 22 intervals (at least one thin section per interval; see locations in Figure 3.1). Additional thin sections were produced on nine coarser fragments, separated from the lowermost ~1 m of the deposit. The volcaniclastic succession was examined in terms of components, framework and deposit textures. Clasts in each thin section were classified by type (juvenile, lithic, composite), size, morphology and vesicularity using consistent terminology, as outlined in the next section. Reflected light was particularly useful during microscopic investigations for better textural identification of clasts, especially in the fine-grained or most altered rocks. Quantitative analyses were performed on full thin section scans, where the relative abundance of components, reported in Table 3.3, was determined on a cement-free basis. First, the area occupied by cement was measured using the MagniSci software (http://magnisci.com/) and subtracted from the total thin section area. Then, all clasts over 2 mm long were manually outlined using the ImageJ software (Schneider et al., 2012) and subdivided into clast types. In addition, the total surface area occupied by lithic fragments was measured to evaluate the proportion of juvenile material, including composite clasts.

3.4 TERMINOLOGY

Volcaniclastic rocks are subdivided into two major genetic groups, implying two different mechanisms of particle fragmentation: primary volcaniclastic and epiclastic (White & Houghton, 2006). *Primary volcaniclastic deposits* are composed of

fragments derived and mobilised by explosive or effusive volcanic activity and transported during a single stage (White, 2000; White & Houghton, 2006). Explosive eruptions may be driven solely by exsolution of magmatic volatiles (*magmatic, or "dry", eruptions*), or by interaction of magma with external water (seawater, groundwater, lake water etc.) that evolves into a thermohydraulic explosion (*phreatomagmatic, or "wet", eruptions*) (Morrissey et al., 2000; Cashman & Scheu, 2015; Houghton & Carey, 2015; Zimanowski et al., 2015). Primary volcaniclastic deposits are referred to as *reworked* when unconsolidated fragments of such deposits are re-mobilised (including resizing and reshaping) and/or redeposited by surface processes (e.g., river, wind, landslide, water currents) that can be syn-eruptive or occur after a storage period (Fisher & Schmincke, 1984; White et al., 2009). *Epiclastic deposits* of volcanic heritage are sedimentary rocks, formed by fragmentation (through erosion, reworking or weathering) of lithified volcanic rocks with the material transported and deposited by surface processes (White et al., 2009).

Primary volcaniclastic deposits described in this chapter are classified into tuff, lapilli tuff, tuff breccia and breccia, based on the relative abundance of ash (< 2 mm), lapilli (2-64 mm) and bomb/block (> 64 mm) fragments (Cashman & Scheu, 2015). Component classes of different individual particle types within the primary volcaniclastic deposits include juvenile, lithic and composite clasts (White & Houghton, 2006). *Juvenile* fragments are derived by quenching of magma by contact with water (that for basaltic magmas produces sideromelane or tachylite) and can include *free crystals*, liberated from the erupting magma by the explosions (Cioni et al., 2015; Houghton et al., 2015). *Sideromelane* is brownish to golden glass, characterised by generally fluidal morphology and abundant spherical vesicles, and containing few or no microlites (Taddeucci et al., 2015). In contrast, *tachylite* is opaque glass with abundant microlites, generally larger irregular vesicles and blocky morphology (Taddeucci et al., 2015). Wall-rock *lithic* clasts are derived by fragmentation of the pre-existing comagmatic rocks (*accessory* or *cognate lithics*), or that of the nonvolcanic basement (*accidental lithics*) (Cioni et al., 2015). *Composite* clasts are produced by magma mingling with sediment or lithic debris, e.g. cored juvenile clasts (White & Houghton, 2006).

Classification of vesicularity for glass fragments is adopted from Houghton and Wilson (1989): <5% – non-vesicular; 5-20% – low vesicular; 20-40% – poorly

vesicular; 40-60% – moderately vesicular; 60-80 – highly vesicular; > 80% – extremely vesicular. Here, non- and low vesicular glass fragments (<20% vesicles) are referred to as *dense* clasts; poorly to moderately vesicular glass fragments (20-60% vesicles), characterised by millimetre-sized vesicles and dark reddish to black colour, are referred to as *scoria*; whereas *pumice* represents microvesicular clasts with 60-95% of vesicles. *Reticulite*, highly expanded basaltic foam with ~98% of vesicles (Cashman & Scheu, 2015), was not observed in the studied deposits.

Two types of stratigraphic divisions were implemented to describe volcanic and sedimentary successions, cored from Shatsky Rise during the IODP Exp. 324 (Sager et al., 2010). *Stratigraphic units* from Sager et al. (2010) represent sequences of similar volcanic facies, such as pillow-lava stacks, packages of sheet flows or volcaniclastic successions. Stratigraphic units have been further subdivided into *lithological unit*s, the term particularly applied to effusive rocks, to identify morphologically distinct structures, such as individual pillow lavas and lava flows (Sager et al., 2010). Such preliminary stratigraphic subdivisions do not accurately describe primary volcaniclastic and sedimentary rocks from Shatsky Rise, where many distinct stratigraphic units contain effusive rocks with intercalated sedimentary horizons or combine volcaniclastic rocks of different genesis (e.g., hyaloclastite, sandstone, limestone). Here, the term *Unit* is used to define a section of volcaniclastic deposit that was formed during a single event of continuous deposition and is identified by relative abundance of components, grain-size and textural analysis (Figure 3.1).

3.5 RESULTS

The volcaniclastic deposit from Site U1349 (water depths of 3127 m) is ~30 m thick and located directly above highly vesicular, red-brown flows, with no contacts preserved in the recovered material (Figure 3.1). The deposit is overlayed with pelagic sedimentary rocks. Total core recovery of the volcaniclastic material is ~32%, varying considerably across the core runs (2-92%). No sharp erosional boundaries or truncations within the deposit were recognised. However, internally, subtle layering and grading, variations in grain size, componentry and alteration are observed, as described in the following sections.

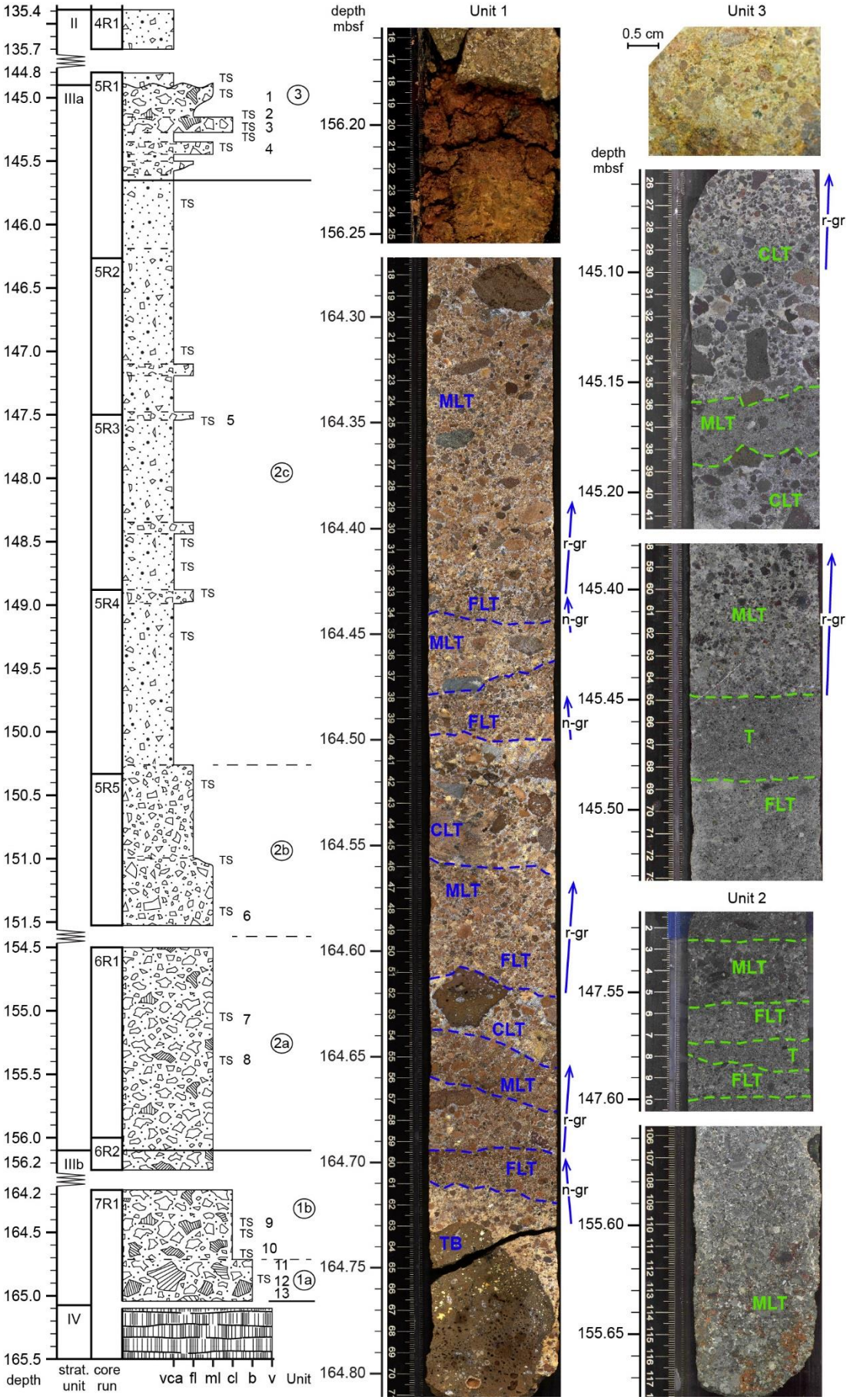
depth
strat. unit
core
run
vca fl ml cl b v
Unit
depth mbsf
Unit 1
Unit 3
Unit 2
0.5 cm
II
IIIa
IIIb
IV
4R1
5R1
5R2
5R3
5R4
5R5
6R1
6R2
7R1
TS
T1
1
2
3
4
5
6
7
8
9
10
11
12
13
1a
1b
2a
2b
2c
3
MLT
FLT
CLT
TB
T
r-gr
n-gr

3.5.1 Volcaniclastic components

The Site U1349 volcaniclastic deposits are composed of fragments that differ in size from very fine (>4 φ) to over 8.5 x 6 cm (<–6 φ) (Table 3.3). Juvenile clasts are dominant (71-100 modal %), whereas lithic and composite clasts are observed less commonly. Lapilli and a single block/bomb-size fragments are set in a matrix of finer ash and cement (Figures 3.1-3.4).

3.5.1.1 Juvenile components

The main proportion of juvenile fragments is composed of quenched pyroclasts (tachylite and sideromelane), whereas free crystals of plagioclase and clinopyroxene are observed sporadically in carbonate and ash matrix (Figures 3.2a, 3.3.c and 3.4a).

Tachylite usually dominates over other pyroclast types. Tachylitic glass is altered to clay minerals, dark-brown to dull black in colour, and is often nearly opaque. Tachylite contains abundant microlites, particularly identifiable under the reflected light, and often comprises blocky phenocrysts of altered plagioclase and olivine (up to 0.5 mm long) (Figures 3.2d and 3.4c, d). Morphologically, tachylite forms poorly-vesicular to moderately vesicular, cauliflower-shaped scoria with irregular clast surfaces (Figures 3.2a, b; 3.3a, c; 3.4c, e). Some denser to poorly-vesicular, tachylite pyroclasts show blocky, angular pyramidal or elongated shapes (Figures 3.2g; 3.3a, b). Vesicles in tachylite scoria demonstrate highly irregular shapes as a result of abundant microlites, some vesicles conglutinate in amoeboid forms (Figures 3.2g and 3.3a).

Figure 3.1 (previous page). Lithological log and representative core section images of mafic volcaniclastic deposit from U1349, Ori Massif. Patterns schematically depict relative clast sizes and their abundances in each Unit, as from this study. Coarse lapilli to block-size clasts are highlighted with dashed lines. Core images are adopted from the IODP Expedition 324 materials and Site U1349 report (Sager et al., 2010), with significant light- and contrast-enhancement. Dashed lines on core images separate layers with different grain-size characteristics. Arrows indicate reverse (r-gr) and normal (n-gr) grading. Stratigraphic units and core run are given according to Sager et al. (2010). Numbers indicate intervals with lapilli fragments used for geochemical analyses (Chapter 4). Numbers in circles indicate Units as from this study. Depth is in meters below sea floor. Abbreviations: TS = thin section, strat. = stratigraphic, vca = very coarse ash, fl = fine lapillus, ml = medium lapillus, cl = coarse lapillus, b = bomb/block, v = volcanic lava, T = tuff, FLT = fine lapilli tuff, MLT = medium lapilli tuff, CLT = coarse lapilli tuff, TB = tuff breccia.

Table 3.3. Component abundances (modal %) as observed in thin sections

Strat. unit	Core run	Interval (cm)	Depth (mbsf)	Unit	Lithology	Grain-size classification (%)		Lapilli components (%) on a cement-free basis				Composite (% from juvenile lapilli)	Tachylite (% from juvenile lapilli)	Relative abundance of components in ash	Total juvenile content
								Juvenile			Lith				
						Ash	Lapilli	Sid	Tach	Cr					
II	5R1	4.5-6	144.85	3	Tuff	77	23	6	63	0	31	0	92	tach, sid, lith, cr	87
IIIa	5R1	13-15	144.93	3	Lap. tuff	48	52	0	52	0	48	3	100	tach, lith, sid, cr	71
IIIa	5R1	30-32	145.10	3	Lap. tuff	39	61	1	76	0	23	13	98	tach, sid, lith, cr	85
IIIa	5R1	41-43	145.21	3	Lap. tuff	66	34	9	53	0	38	28	85	tach, sid, lith, cr	85
IIIa	5R1	46-48	145.26	3	Lap. tuff	73	27	13	39	0	48	21	75	tach, sid, lith, cr	86
IIIa	5R1	58-59	145.38	3	Lap. tuff	50	50	7	39	0	54	6	86	tach, sid, lith, cr	72
IIIa	5R1	58-59	145.38	3	Lap. tuff	58	42	31	58	0	10	20	65	tach, sid, lith, cr	94
IIIa	5R1	102-103	145.82	2	Tuff	100	0	0	100	0	0	0	100	tach, sid, lith, cr	100
IIIa	5R1	103-105	145.83	2	Tuff	97	3	14	86	0	0	39	86	tach, sid, lith, cr	99
IIIa	5R2	72-74	146.99	2	Tuff	91	9	24	76	0	0	6	76	tach, sid, lith, cr	99
IIIa	5R3	3-6	147.53	2	Lap. tuff	56	44	16	84	0	0	64	84	tach, sid, lith, cr	99
IIIa	5R3	95-99	148.45	2	Tuff	78	22	13	82	0	5	1	86	tach, sid, lith, cr	97
IIIa	5R3	118-122	148.68	2	Tuff	82	18	9	82	0	9	9	90	tach, sid, lith, cr	95
IIIa	5R4	3-5	148.90	2	Tuff	79	21	7	88	0	5	2	93	tach, sid, lith, cr	97
IIIa	5R4	36-38	149.23	2	Tuff	86	14	13	83	0	4	14	86	tach, sid, lith, cr	97
IIIa	5R5	8-11	150.40	2	Lap. tuff	75	25	7	69	0	25	16	91	tach, sid, lith, cr	91
IIIa	5R5	70-72	151.02	2	Lap. tuff	71	29	13	75	0	12	53	86	tach, sid, lith, cr	95
IIIa	5R5	110-111	151.42	2	Lap. tuff	63	37	9	87	0	4	38	90	tach, sid, lith	98
IIIa	6R1	56-59	155.06	2	Lap. tuff	62	38	25	72	0	3	9	75	tach, sid, lith, cr	98
IIIa	6R1	88-93	155.38	2	Lap. tuff	63	37	3	91	0	5	28	96	tach, lith, sid	96
IIIb	7R1	32-34	164.42	1	Lap. tuff	41	59	25	45	4	26	22	64	tach, sid, lith, cr	84
IIIb	7R1	59-61	164.70	1	Lap. tuff	69	31	17	29	0	53	0	63	tach, sid, lith, cr	81

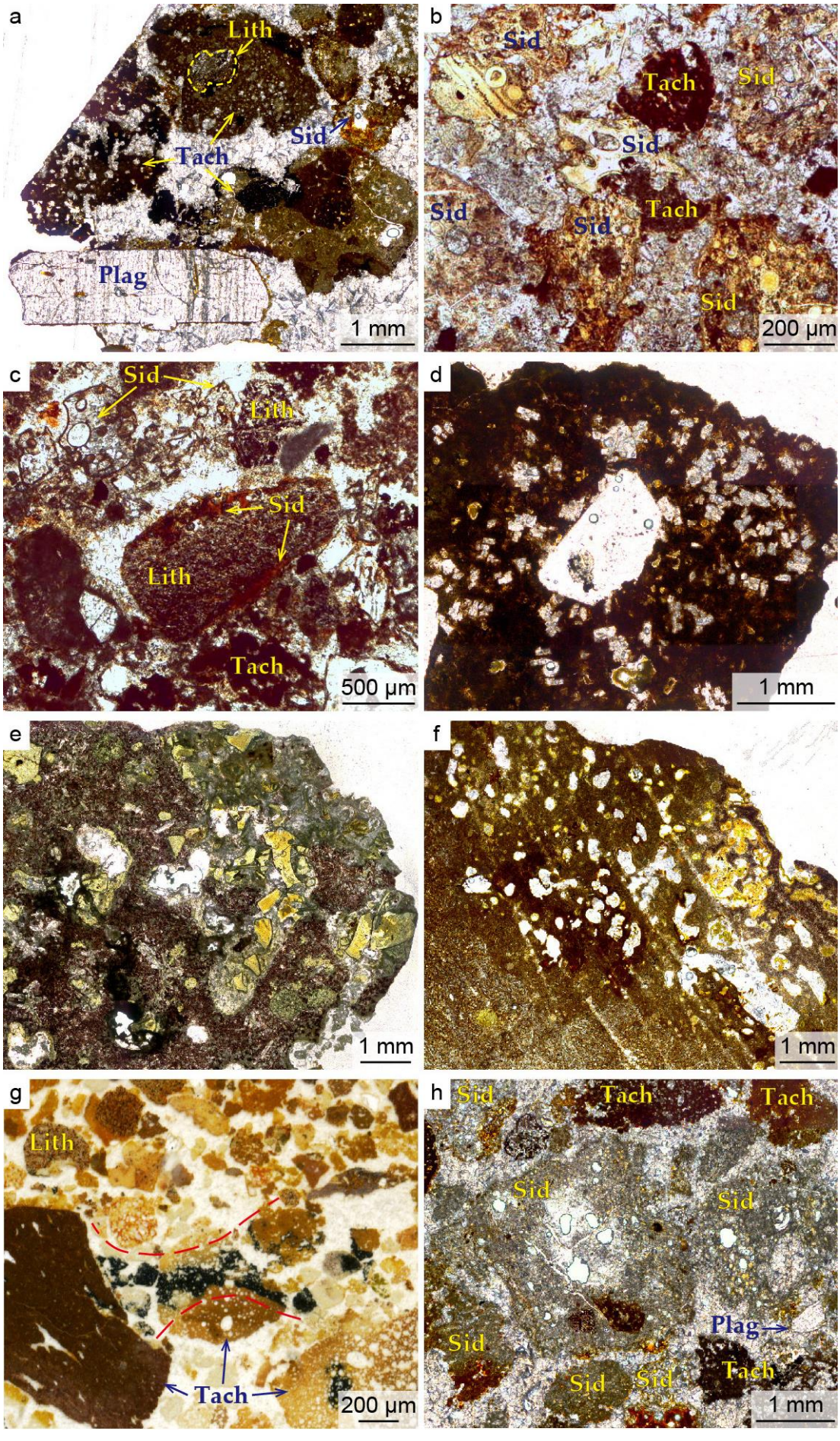
a
Lith
Sid
Tach
Plag
1 mm
b
Sid
Tach
Sid
Sid
Sid
Tach
Sid
200 µm
c
Sid
Lith
Sid
Lith
Tach
500 µm
d
1 mm
e
1 mm
f
1 mm
g
Lith
Tach
200 µm
h
Sid
Tach
Tach
Sid
Sid
Plag
Sid
Sid
Sid
Tach
1 mm

Sideromelane typically occurs within the ash to fine lapilli fraction and is completely replaced with calcite, palagonite or clays (Table 3.3; Figures 3.2b, c, h; 3.3c; 3.4b-f). Despite alteration, the original clast morphology and vesicle textures are still preserved. Larger fragments of sideromelane (up to 4 mm in diameter) typically show bulbous shapes with fluidal and bubble-wall skins (Figures 3.3c and 3.4b, f). Sideromelane fragments vary from poorly-vesicular scoria to highly-vesicular pumice. Vesicles vary from rounded to elongated and arcuate in shape (Figures 3.3c and 3.4b, f). Lapilli-sized sideromelane scoria and pumice often contain poorly vesiculated and highly vesiculated domains or parts that differ in vesicle size and morphology. Sometimes, sideromelane forms rims around tachylite and lithic fragments (Figure 3.2c). Plagioclase phenocrysts in sideromelane are not commonly observed.

Figure 3.2 (previous page). Photomicrographs of thin sections from volcaniclastic deposit, Unit 1, Site U1349. a) Fine lapilli-size plagioclase free crystal, several fine lapilli to ash fragments of low- to moderately vesicular tachylite scoria, and sideromelane ash fragment, cemented with carbonates. Lithic core is outlined within the composite tachylitic lapillus. Central right tachylite lapillus demonstrates zoned alteration from black to light brown. Core section 7R-1 32-34 cm at 164.42 mbsf. b) Yellowish palagonite-altered sideromelane and dark-brown tachylite vesicular ash fragments in carbonate cement, rich in very fine-grained ash. Core section 7R-1 59-61 cm at 164.7 mbsf. c) Coarse ash, composed of accessory lithic clasts (some with sideromelane rims), sideromelane and tachylite scoria, cemented with carbonates. Core section 7R-1 59-61 cm at 164.71 mbsf. d) Coarse lapillus of dark tachylitic glass with abundant tabular plagioclase phenocrysts (Clast 12b, Appendix A). Angular central part of the lapillus was probably occupied with lithic core, which was fallen out. Core section 7R-1 79-81 cm at 164.9 mbsf. e) Accidental lithic coarse lapilli, characterised by high vesiculation and red-brown alteration (Clast 12a). Vesicles are filled with matrix, rich in glassy shards (altered to green clays) in carbonate cement. Core section 7R-1 79-81 cm at 164.9 mbsf. f) Accidental lithic coarse lapilli of broken pillow, showing decreasing crystallinity and increasing vesicularity from pillow interior towards its margin (from left to right). Clast 10b. Core section 7R-1 51-53 cm at 164.62 mbsf. g) Thin section scan from the light-yellow-grey layer of lapilli tuff (IOPD Exp. 324 materials). Area with relatively fresh tachylite is highlighted by red dashed lines. Core section 7R-1 40-46 cm at 164.5 mbsf. h) Sideromelane fragments show two-stage seawater alteration, where secondary yellowish-red palagonite is superimposed with the later grey carbonate alteration. Sideromelane fragments from the middle area of the microphotograph are relatively more intensely altered by second-stage alteration. Core section 7R-1 32-34 cm at 164.42 mbsf. Photomicrographs of thin sections are taken under plane-polarised light. Abbreviations: lith = lithic, tach = tachylite, sid = sideromelane, plag = plagioclase.

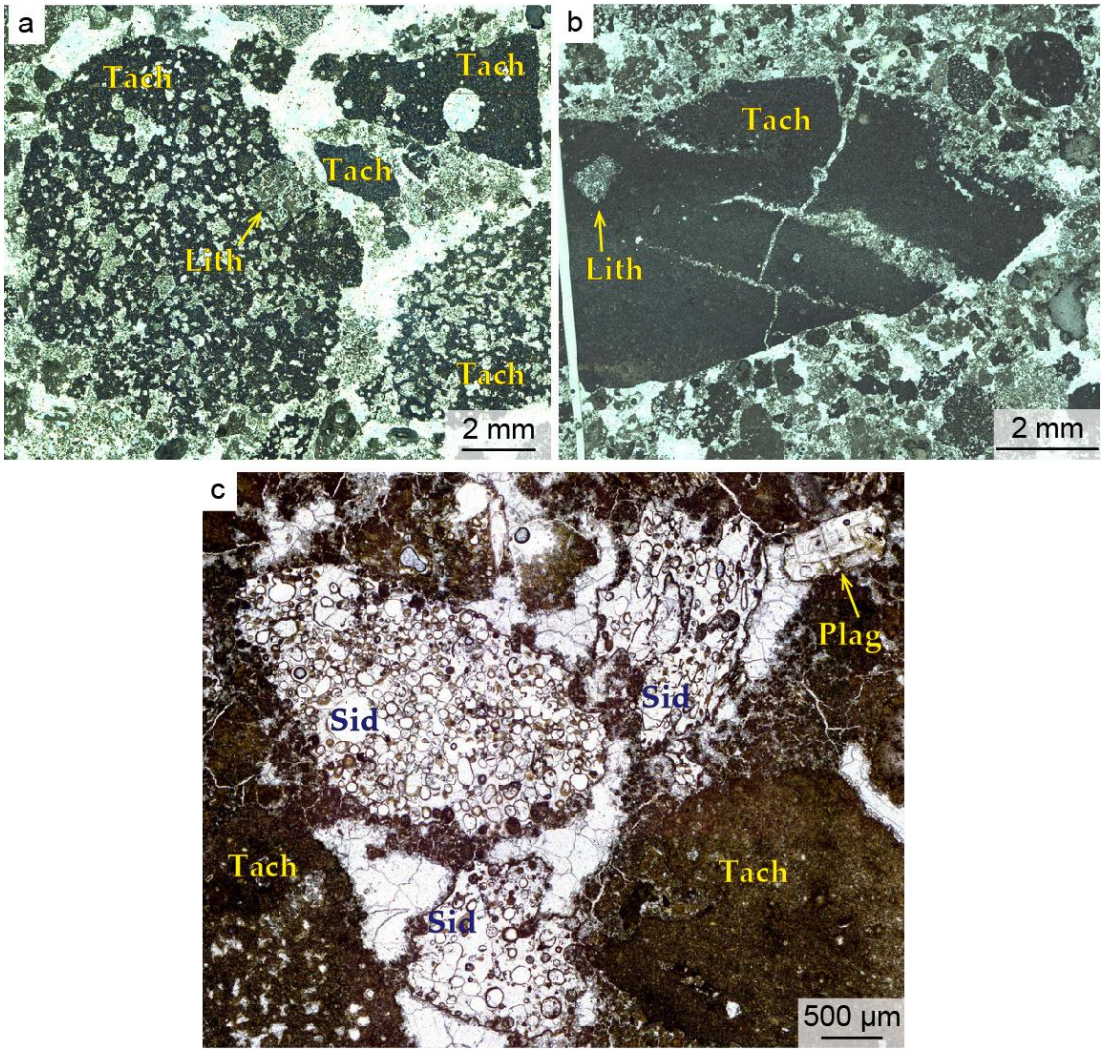

Figure 3.3. Photomicrographs of thin sections from mafic volcaniclastic deposit, Unit 2, Site U1349. a) Medium lapilli of low- and moderately vesicular tachylite scoria in ash and carbonate matrix. Angular fragment of lithic debris inside scoria is also shown. Core section 5R-5 110-111 cm at 151.42 mbsf. b) Medium lapilli of composite clast, where angular lithic core is enclosed within the dense tachylitic exterior. Core section 5R-5 110-111 cm at 151.42 mbsf. c) Fine lapilli of calcite-altered sideromelane pumice with bubble-walls, fine lapilli of tachylite scoria, free crystal of very coarse ash size and very fine-grained ash that surrounds lapilli, all cemented with carbonate. Note that vesicles in pumice differ in shape (rounded, elongated, arcuated) and show bursting (e.g., top right sideromelane fragment). Core section 6R-1 56-59 cm at 155.1 mbsf. Photomicrographs of thin sections are taken under reflected light (a, b) and under plane-polarised light (c). For abbreviations see Figure 3.2.

Free crystals are typically found within the coarse ash fraction, rarely reaching fine lapilli size (Figures 3.2a, 3.3.c and 3.4a). Such crystals are composed of relatively fresh plagioclase (up to 4 mm long), clinopyroxene (up to 1 mm long) or altered olivine (up to 1 mm long). All free crystals are considered here as juvenile, because of

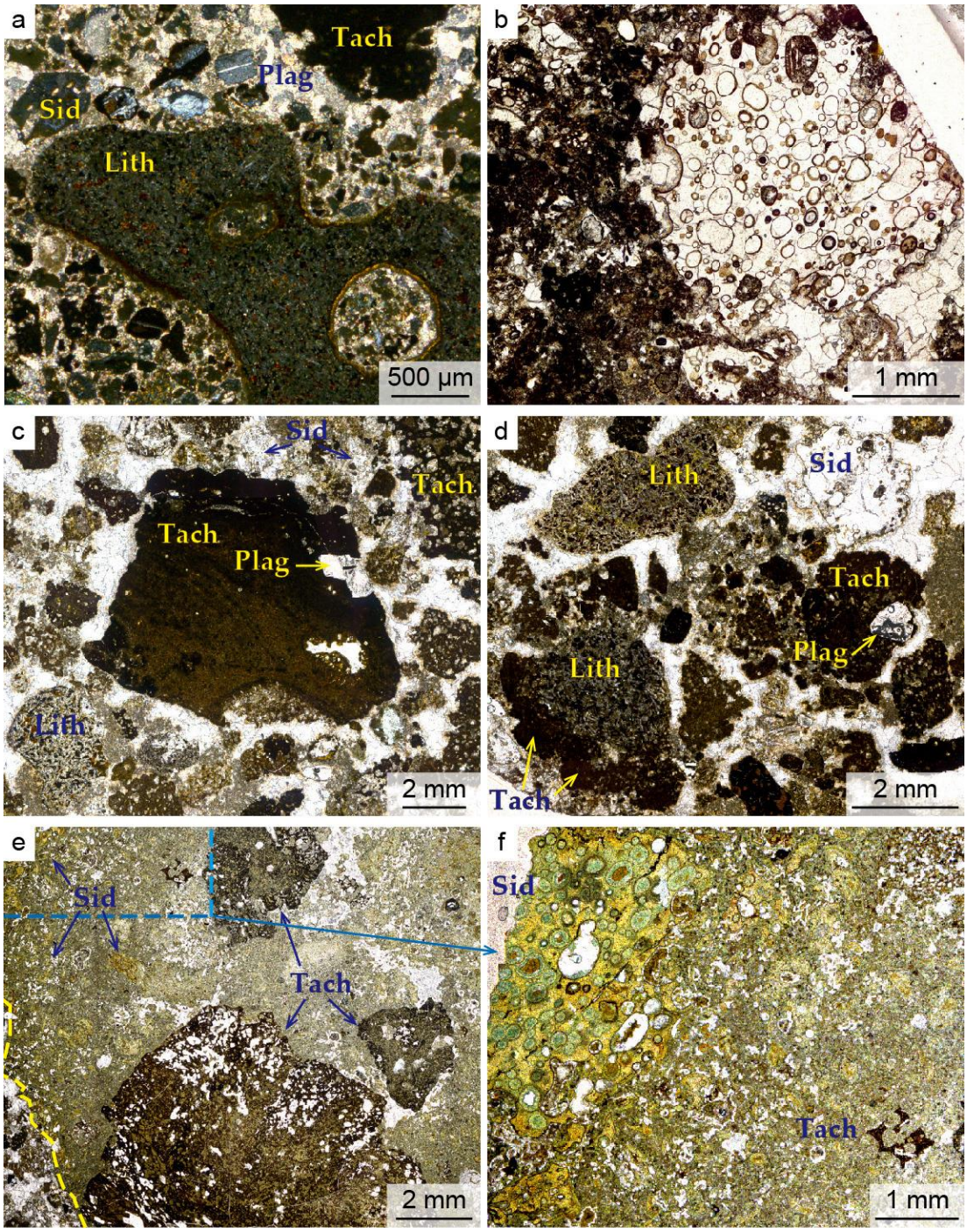

relatively weak alteration and similarity to the phenocrysts that are commonly observed in glass fragments.

3.5.1.2 Lithics

Lithic fragments are of basaltic composition and distributed unevenly throughout the volcaniclastic succession (up to 54 modal % of lapilli) (Table 3.3). Lithics commonly range in size from coarse ash to coarse lapilli, and a single block fragment is found at the bottom of the volcaniclastic deposit (~164.8 mbsf; Figure 3.2).

Observed lithic fragments occur in a variety of irregular angular shapes (Figures 3.1-3.5). Subrounded lithics are observed less frequently and mainly within coarse parts of the deposits (Figures 3.1-3.5).

Accessory lithic fragments are subdivided into two major groups. The most common lithic **(type I)** is represented by non-vesicular holo- and hypo-crystalline basalt with intersertal texture (Figures 3.2c and 3.4c, d). In such clasts, plagioclase, clinopyroxene and opaque minerals are relatively fresh or slightly altered, and the interstitial glass is now completely replaced by clay minerals. Such lithic debris are also found within the composite clasts, usually together with tachylite, and are distributed throughout the entire volcaniclastic section (Figures 3.2a and 3.3a, b). Some composite clasts show partial incorporation of lithics into tachylite (Figure 3.4d), while a glassy selvedge is attached to other lithics (Figure 3.2c).

A second predominant accessory lithic clast **(type II)** includes clasts that significantly vary in degree of vesicularity and colour due to alteration (yellow, pink, light and dark brown, red-brown, green-grey) (Figures 3.1 and 3.5). Such fragments

Figure 3.4 (previous page). Photomicrographs of thin sections from mafic volcaniclastic deposit, Unit 3, Site U1349. a) Fragments of vesicular accidental lithic coarse lapillus and tachylite scoria fine lapillus set in a matrix of fine-medium ash, composed of tachylite, sideromelane and free plagioclase crystals, and cemented with carbonates. Lithic fragment (Clast 3a, Appendix A) shows microcrystalline texture with laths of fresh plagioclase, reddish iddingsite-altered olivine and interstitial glass altered to clays. Vesicles within lithic lapillus are outlined with fibrous saponite. Core section 5R-1 41-43 cm at 145.21 mbsf. b) Example of medium lapilli sideromelane showing bubble-walls and vesicle bursting. Sideromelane is altered to calcite. Vesicles vary in size and shapes within the clast. Core section 5R-1 58-59 cm at 145.38 mbsf. c) Zoned low-vesicular tachylitic medium lapillus with tabular plagioclase phenocrysts and fine lapilli of accessory free lithics and pumiceous tachylite are set in matrix of ash and carbonates. Ash is composed of tachylite, sideromelane and lithics. Core section 5R-1 58-59 cm at 145.38 mbsf. d) Ash to medium lapilli-size fragments of accessory lithics, low-vesicular sideromelane and tachylite, containing plagioclase phenocrysts. Lithic fragment in the left corner is partially enclosed in tachylite scoria. Core section 5R-1 58-59 cm at 145.38 mbsf. e) Accidental lithic fragment composed of pre-existing vitriclastic tuff with abundant sideromelane pumice and tachylite scoria. Yellow dashed line marks boundary of accidental clast. Core section 5R-1 41-43 cm at 145.21 mbsf. f) Magnified area of vitriclastic tuff, outlined with blue box on e). Photomicrographs of thin sections are taken under cross-polarised light (a) and under plane-polarised light (b-f). For abbreviations see Figure 3.2.

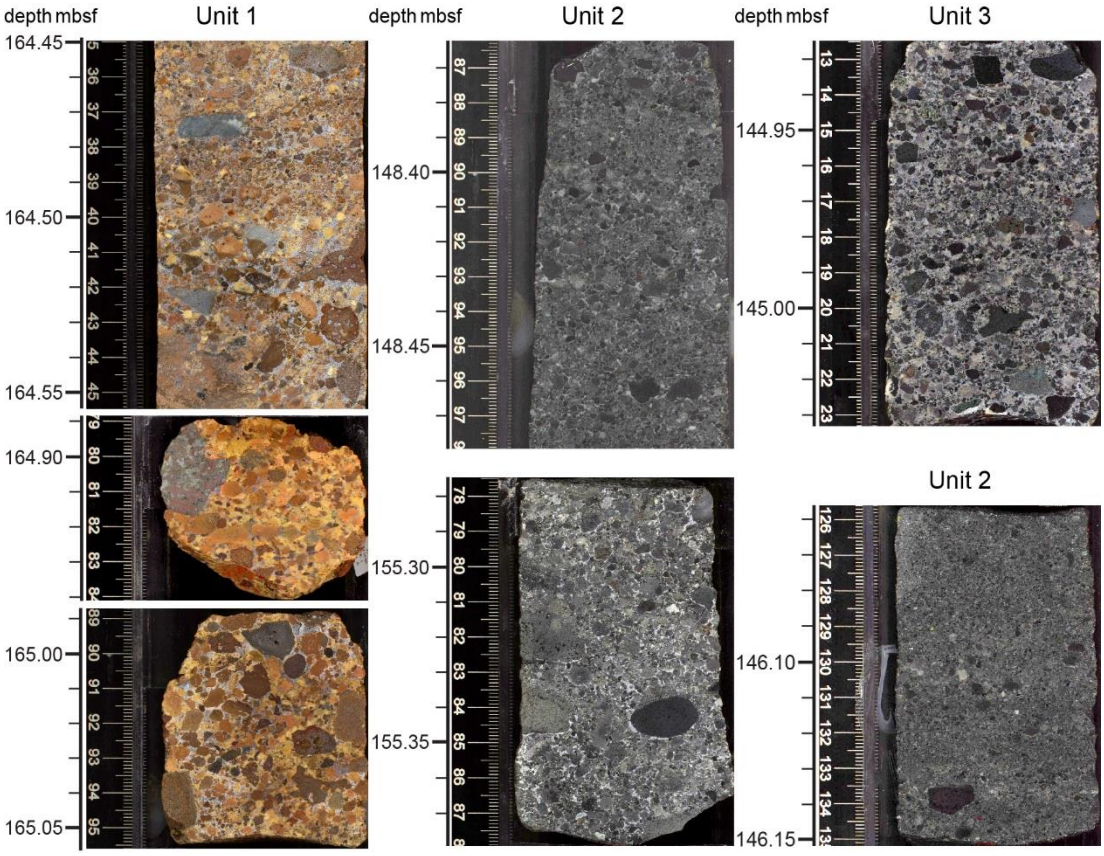

Figure 3.5. Representative core section images of volcaniclastic deposit from Site U1349, showing clast variations in colour, size and angularity. Core images are adopted from the IODP Expedition 324 materials and Site U1349 report (Sager et al., 2010), with significant light- and contrast-enhancement.

are characterised by a microcrystalline texture with plagioclase, clinopyroxene, olivine and opaque minerals, sometimes also containing plagioclase phenocrysts and plagioclase-pyroxene ophimottles (Figures 3.2e, f and 3.4a; also see Figures 21A-B in Chapter "Site U1349" from Sager et al. (2010)). Texturally, type II lithics are similar to basaltic lavas from other cores drilled on Shatsky Rise. Red-brown and light-brown clasts, containing abundant iddingsite-altered olivine, similar to the highly vesicular red-brown lava tops from Unit IV, are relatively rare to the deposits (Figures 3.2e and 3.4a). Brown, dense fragments with glomeroporphyritic texture are similar to basalts from some lava flows observed at Shatsky Rise (Figure 3.2f). Importantly, vesicles from the type II lithic fragments are up to 4-7 mm long (Figures 3.2e, f and 3.4a), which is an order of magnitude greater than the size of vesicles from juvenile clasts (<0.2-0.4 mm in diameter; Figures 3.2b; 3.3c and 3.4b, f). Vesicles in type II lithics are typically filled with calcite or zeolite and are often outlined with fibrous smectite

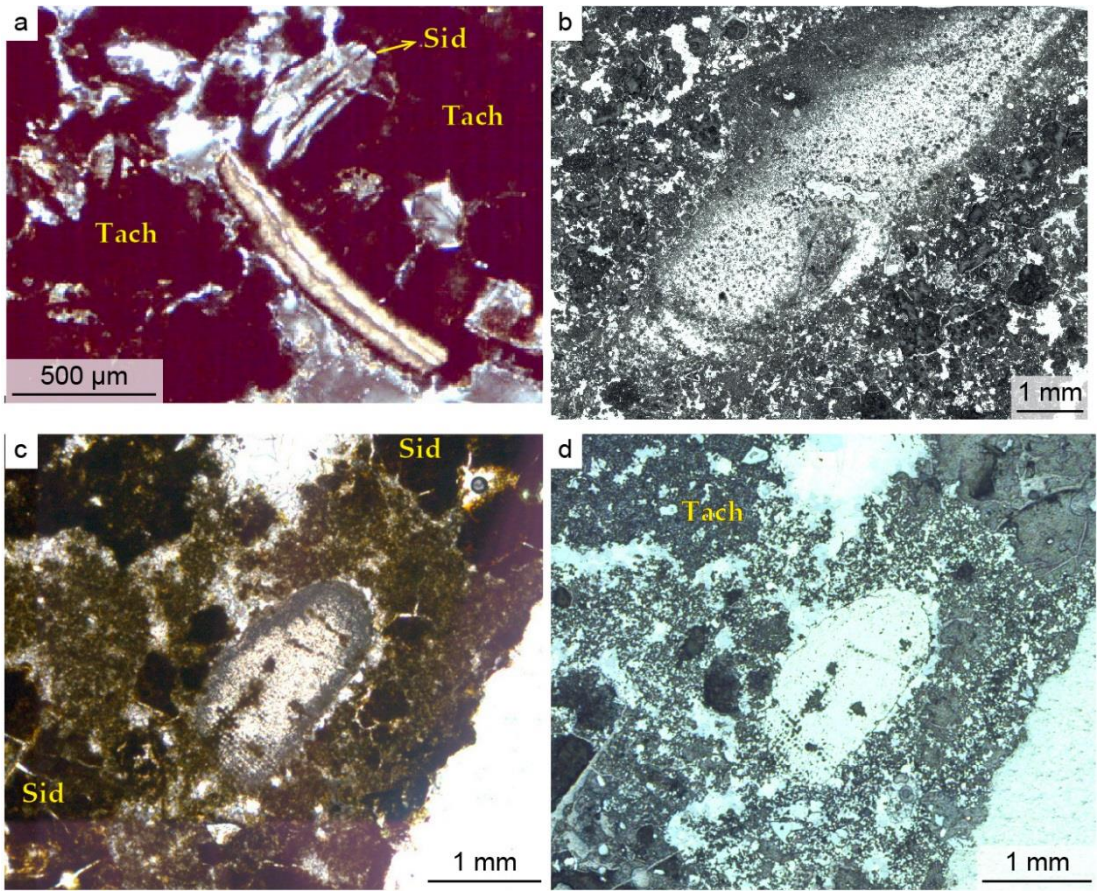

Figure 3.6. Photomicrographs of thin sections from volcaniclastic deposit, Site U1349, showing fragments of shallow-marine fossils: a) mollusc fragment (core section 5R-3 55-58 cm at 148.1 mbsf); b) potential gastropod (core section 5R-5 70-72 cm at 151 mbsf); c) and d) echinoderm bioclast with syn-sedimentary micrite rim alteration surrounded by syntaxial cement (core section 6R-1 88-93 cm at 155.38 mbsf). Photomicrographs of thin sections are taken under cross-polarised light (a), reflected light (b and d) and under plane-polarised light (c). For abbreviations see Figure 3.2.

or opaque minerals (e.g., block fragment from ~164.8 mbsf; Figures 3.1 and 3.2f). Additionally, a single green coarse lapilli fragment of lithified tuff, containing abundant sideromelane pumice and tachylite scoria, is found in thin section from Unit 3 at 145.21 mbsf (Figure 3.4e, f). This clast is subangular in shape with sharp ragged boundaries, which is outlined by fibrous zeolites.

3.5.1.3 Bioclasts

Free, singular marine fossils are observed sporadically throughout the succession. Size of the fossils typically varies from 0.1 to 10 mm. Fossils are preliminary interpreted as shallow-marine bivalves, gastropods and echinoderms (Figure 3.6). This is consistent with previously reported individual broken and rounded

shallow-marine fossils (echinoderms and bryozoans) within the deposits (Sager et al., 2010).

3.5.1.4 Matrix

Matrix is composed of variable proportions of ash fragments and cement. The amount of cement reaches 25% in coarse-grained sections and as little as <5% in the fine-grained portions of the volcaniclastic succession. Ash fragments are predominantly juvenile in composition with minor amounts of relatively coarser lithics. Coarse ash sized fragments are characterised by shapes that are similar to those commonly observed for the lapilli-sized clasts. Finer ash fragments of juvenile composition (< 0.5 mm) are characterised by a variety of shapes, where sideromelane forms irregular fragments with surfaces controlled by vesicle walls or curviplanar fractures, and tachylite is represented by blocky chips and amoeboid-shaped scoria (e.g., Figure 3.2b). Fine ash-sized particles are unevenly distributed within the matrix and often occur as clast-supported moss-like masses that surround larger clasts (Figures 3.3a, c and 3.4b, c). The volcaniclastic succession is completely cemented with carbonates and minor amounts of zeolite minerals.

3.5.2 Descriptions of Units

Based on relative abundance of components, grain-size and textural analysis, the volcaniclastic succession is subdivided into three Units, each representing an event of continuous deposition. Description of the Units is given from bottom to top.

3.5.2.1 Unit 1: yellowish-brown massive tuff breccia and bedded lapilli tuff

The lowermost Unit 1 represents ~1 m of recovered core over a ~9 m interval (Figure 3.1). No contacts of the volcaniclastic deposit with underlying lavas were recovered. Two subunits were recognised in the Unit 1 succession. The lower part is composed of tuff breccia and the upper part of the sequence is made of bedded massive lapilli tuff, where the matrix has a higher content of carbonate.

Subunit 1a: yellowish-brown massive tuff breccia

The tuff breccia is yellowish-brown in colour and is characterised by very poor sorting, clast-supported texture with no structures observed. Tuff breccia contains abundant coarse lapilli (up to 5.5 cm) and a single block-size fragment (at least 8.5 cm long) (~164.8 mbsf; Figure 3.1). Lapilli and block fragments are angular and irregular or rarely subrounded in form and brown, yellow, grey-brown or red-brown in colour

(Figures 3.1 and 3.5). Compositionally, the majority of the clasts are represented by lithics of both types I and II. Juvenile clasts are present as fine and medium sized lapilli, except for the coarse lapillus of tachylitic type only found in this subunit (Figure 3.2d). Juvenile fragments contain abundant tabular plagioclase phenocrysts and are characterised by low vesicularity (up to 10-20%). Vesicles in juvenile clasts are generally irregular or ellipsoidal in shape and filled with carbonates, whereas vesicles within lithic clasts are filled with matrix, containing dense cuspate glassy shards and carbonate cement (Figure 3.2e). All clasts are set in a matrix of finer brown to yellow ash and light-grey carbonate cement.

Subunit 1b: yellowish-brown bedded massive coarse lapilli tuff

The lower contact, separating Subunits 1a and 1b, is diffuse and marked by a 1.5 cm band of moderately sorted fine lapilli tuff at ~164.7 mbsf (Figure 3.1). Lapilli tuff from the Subunit 1b is structureless to medium-bedded and crudely stratified, matrix-supported and mostly poorly-sorted. Both the number of coarse lapilli in lapilli tuff from Subunit 1b and their size (up to 3.7 cm long) are significantly lower than that in tuff breccia from Subunit 1a. Stratification is defined by indistinct layers rich in coarse lapilli, alternating with relatively darker-brown normally and reverse graded fine lapilli tuff (Figure 3.1). The coarse lapilli tuff is light-yellow-grey in colour, fines-poor and shows openwork texture.

Lapilli components within the lapilli tuff vary in the following way: lithics (26-53 modal %), tachylite (29-45 modal %), sideromelane (17-25 modal %), free plagioclase and clinopyroxene crystals (up to modal 4%) (Table 3.3). Lithics of both types I and II are observed within the lapilli tuff. Lithics of type I ash to fine lapilli in size often get incorporated into larger-size tachylite (Figure 3.2a) or into thin sideromelane rims (Figure 3.2c). The main clastic component within the lapilli tuff is juvenile, varying significantly (80-97 modal %) in abundance depending on the presence of coarse lapilli-sized lithic clasts. Individual sideromelane fragments are irregular, sub-angular and cuspate in shape and frequently display cuspate cracks. Tachylite forms angular or cauliflower-shaped scoria and often contains blocky sericite-altered plagioclase phenocrysts (Figure 3.2d). In contrast to the underlying massive tuff breccia, juvenile clasts from the lapilli tuff are characterised by higher vesicularity, ranging from poor to moderate (20-60%).

The quantity of free crystals in thin sections from Subunit 1b is somewhat higher (up to 10 crystals per thin section) than that from the overlying Units (1-2 crystals). Free crystals are coarse ash (0.5-2 mm long) to fine lapilli in size (Figure 3.2a). Throughout the Subunit 1b, broken fragments of free plagioclase crystals are relatively fresh. On the other hand, clinopyroxene crystals have fresh cores and rims altered by clay minerals.

Alteration:

Unit 1 is characterised by significant alteration of clasts, replaced with a variety of secondary minerals (e.g., palagonite, iddingsite, clay, Fe-oxide, zeolite, carbonate). Yellowish colour of the deposits is a result of intense palagonisation of sideromelane clasts and ash fragments. Overall, Subunits 1a and 1b have been affected by a strong oxidative alteration and hydration, producing subtle subparallel layering (Figure 3.1). The light-yellow-grey coarse lapilli tuff layers are distinguished from the darker-brown lapilli tuff by intense alteration of matrix by carbonates. In the light-yellow-grey layers, tachylite is unevenly-altered by clay and carbonate minerals (Figure 3.2a, g) and sideromelane shows a two-stage alteration footprint, where the secondary carbonates partially to almost entirely replace secondary palagonite with corrosion of the primary textures (Figure 3.2h). Lithic fragments demonstrate yellowish-brown alteration of interstitial glass by clay minerals and Fe-oxides (Figure 3.2f) and red-brown iddingsite alteration of olivine and glass (Figure 3.2e), similar to that observed in the underlying lavas.

The uppermost ~20 cm of lapilli tuff (~156.2 mbsf; Figure 3.1) was cored over a distance of ~8 m and contains highly altered red-brown crumbled material that was interpreted as a “possible poorly developed paleosol” (Sager et al., 2010). This soft deposit is relatively fine-gained, but contains abundant ash to lapilli sized volcanic fragments. This material shows similar but more intense alteration to clay minerals and Fe-oxides, as compared to the rest of this Unit (Sager et al., 2010).

Unit 1 is characterised by relatively uniform resistivity and density values, which are somewhat lower as compared to the underlying basalts (Figure 3.7). Gamma Ray values are elevated in Unit 1, as a result of high U and K contents, relative to the underlying lavas and overlying Unit 2 deposits (Figure 3.7). Uranium contents gradually increase towards the upper boundary of Unit 1, where the most altered material is observed.

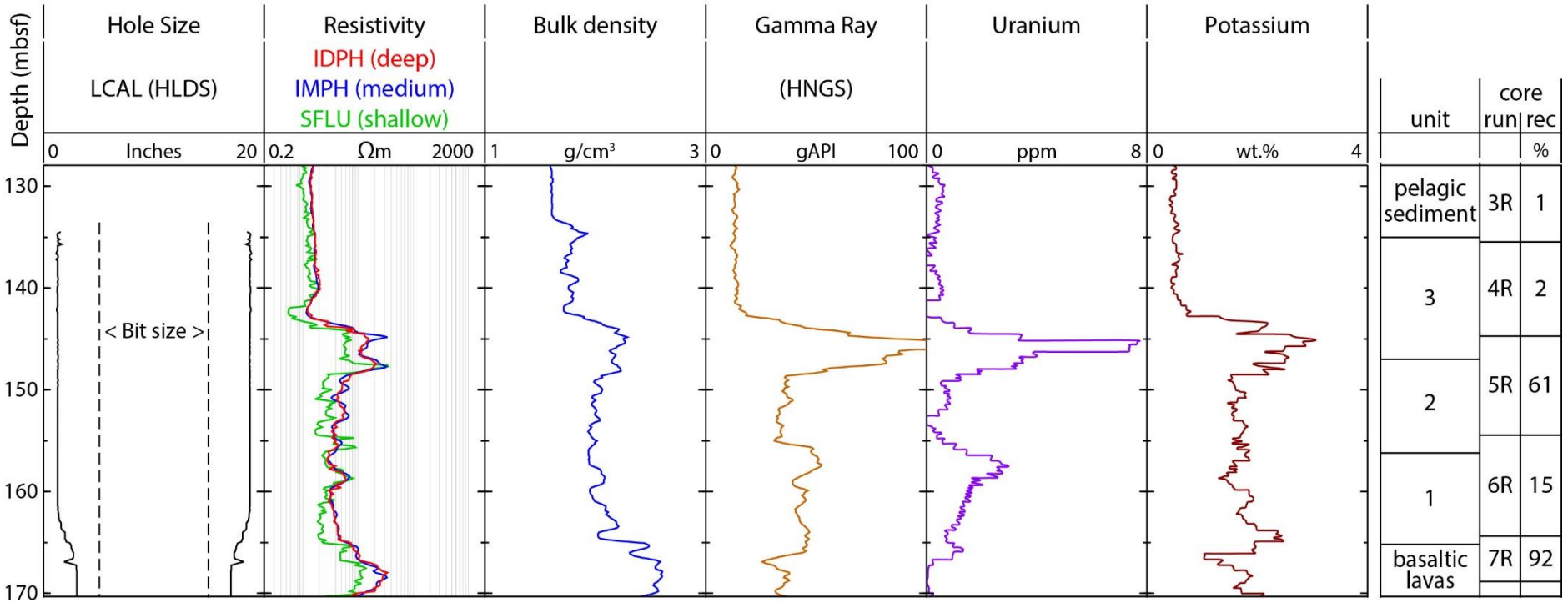

Figure 3.7. Downhole lithostratigraphic correlations for depth interval 130-170 mbsf, Site U1349. Volcaniclastic deposits are distinguished by lower resistivity and density values and higher gamma ray, U and K concentrations relatively to the underlying basalts. Also shown subdivision into three Units as from this study. Log data are from the IODP Exp. 324 materials (Sager et al., 2010). Abbreviations: LCAL = caliper, HLDS = Hostile Environment Litho-Density Sonde, IDPH = deep induction phasor-processed resistivity, IMPH = medium induction phasor-processed resistivity, SFLU = spherically focused resistivity, RHOM = density at medium-mesh boundary, HSGR = gamma ray log, HNGS = Hostile Environment Natural Gamma Ray Sonde, rec = recovery of core runs (drilling reference).

3.5.2.2 Unit 2: graded light-grey lapilli tuff fining upwards to dark-grey tuff

The total recovered thickness of Unit 2 is 7.4 m over a ~10.4 m interval. It is characterised by a light-grey lapilli tuff that gradually fines upwards to a dark-grey tuff (Figure 3.1). Concomitant with the grain size decrease upwards is a decrease in carbonate cementation and increase in ash matrix. Three subunits can be recognised based on grain size differences.

Subunit 2a: massive light-grey medium lapilli tuff with outsized coarse lapilli

Subunit 2a is 1.6 m thick. The lowermost part of Unit 2 (~60 cm) contains core fragments of light-yellow lapilli tuff and light-grey lapilli tuff with reddish-brown alteration staining (~155.65 mbsf; Figure 3.1), representing transitional zone between Units 1 and 2. Above this ~1 m of light-grey lapilli tuff was recovered. Lapilli tuff from Subunit 2a is massive in structure, matrix-supported and poorly sorted with rare coarse lapilli randomly distributed throughout the deposit (Figure 3.5). Plagioclase phenocrysts occur in some tachylite and sideromelane pyroclasts. Lithic clasts of type II are observed mainly within Subunit 2a, where they are angular to subrounded in shape, light-grey to black and red-brown in colour (Figures 3.1 and 3.5).

Subunit 2b: massive dark-grey medium and fine lapilli tuff

About 3 m of drill core was not recovered between Subunits 2a and 2b. Dark-grey massive, poorly sorted medium-fine lapilli tuff (~50 cm thick; Figure 3.3a-b) gradually fines upwards to a fine lapilli tuff with only rare medium lapilli-sized clasts (~70 cm thick). Carbonate cementation within the fine lapilli tuff is still present but only discernible under a microscope. Coarse lapilli are absent from Subunits 2b and 2c.

Subunit 2c: dark-grey stratified tuff

The contact between Subunits 2b and 2c is gradational. Subunit 2c is ~4.6 m thick and represents dark-grey massive, matrix-supported, poorly sorted and mostly ash cemented tuff with rare thin beds of medium-fine lapilli tuff (Figure 3.1). The uppermost ~50 cm of the sequence comprises dark-grey coarse-ash tuff interbedded with layers of moderately sorted lighter-grey fine-ash tuff. Fine and medium lapilli are observed throughout the Subunit 2c (Figure 3.5) and can compose up to 44 modal % within the medium-fine lapilli tuff beds (Table 3.3). Matrix is mostly ash and contains less carbonate, as compared to the underlying subunits.

Overall, Unit 2 deposits show relatively higher juvenile content (91-100 modal %) and lower amounts of lithics (generally <5 modal %) and crystals, as compared to Unit 1 (Table 3.3). The juvenile clasts are predominantly tachylitic in composition and are characterised by irregular, blocky, elongated and generally cuspate shapes. Tachylitic fragments are characterised by low (10-20%) vesicularity with predominantly small, irregular and elongate vesicles. Sideromelane is observed both as lapilli-sized clasts and within the matrix, where it forms poor- to moderately (60%) vesicular scoria. Smaller vesicles within sideromelane are circular or elongated in shape, whereas some of the largest vesicles show complex forms that were likely to be produced by vesicle coalescence (Figure 3.3c). Coarse ash to medium lapilli-sized lithic fragments from the entire Unit 2 are mostly of type I and often occur within glassy tachylite juvenile clasts forming 'composite' clasts (Figure 3.3a, b). Such composite clasts are particularly abundant within the medium and fine lapilli tuff layers.

Alteration:

Deposits from Unit 2 are distinguished of those from Unit 1 by lowered Gamma Ray values and U contents (Figure 3.7), correlating with relatively less intense alteration. Nevertheless, resistivity and density values from the two Units 1 and 2 are similar. Sideromelane is the main juvenile component affected by alteration processes. The sideromelane is replaced by dark-brown and green clay minerals at rims and within vesicles, and the rest is entirely altered by carbonate (Figure 3.3c).

3.5.2.3 Unit 3: dark-grey tuff intercalated with reverse-graded light-grey lapilli tuff

The contact between Units 2 and 3 is gradational and is inferred based on a gradual increase in fragment size, pore space and carbonate cementation. The lowermost part of Unit 3 is ~0.75 m thick and composed of thin beds of dark-grey fine to coarse ash tuff intercalated with up to five layers of reverse-graded light-grey fine to coarse lapilli tuff, each 5-10 cm thick (~145 mbsf; Figures 3.1 and 3.5). Bedding boundaries are parallel and mostly diffuse. Tuff beds are matrix-supported and poorly to moderately sorted, with occasional outsized fragments. Lapilli tuff layers are fines-poor and characterised by an openwork texture. Granularity of lapilli from the lapilli tuff layers increases from fine to coarse upwards. On top of these dark-grey tuff and light-grey lapilli tuff deposits, ~25 cm of highly broken yellow-brown tuff, mixed with pelagic sediments, was collected over a distance of ~9.4 m.

As observed in drill core and in thin sections, fragments within Unit 3 deposits are angular, where forms vary from triangular, polygonal and irregular (~145 mbsf; Figure 3.1). The clasts differ in colour from black to light-grey, red-brown and greenish-grey. Compositionally, the lapilli tuff is characterised by a high amount of lithics (up to 54 modal %), similar to the deposits from Unit 1 with the coarse and medium lapilli-sized clasts being predominantly of lithic type II. These clasts include well- and moderately-crystallised, low to highly vesicular fragments of basaltic pillow lavas or lava flows (Figure 3.4a), often containing glomerocrysts and phenocrysts of plagioclase and clinopyroxene. Greenish-grey fragments of consolidated volcaniclastic deposits are also encountered (Figure 3.4e, f). Additionally, both sideromelane and tachylite from the lapilli tuff are significantly coarser, as compared to the underlying deposits from Subunits 2b-c (Figure 3.4b-d).

Total juvenile content within Unit 3 is reduced to 71-94 modal %, resembling Unit 1 deposits. Furthermore, sideromelane and free crystals are more abundant, relatively to tachylite, which is similar to the deposits from Unit 1, rather than deposits from Unit 2. The juvenile clasts are irregular, blocky, elongate and mostly cuspate in shape and vary from poorly to moderately vesicular with rounded and elongated vesicles. Tachylite from most of the Unit 3 is opaque, dark-brown to black glass, sometimes containing plagioclase phenocrysts, embedded lithics or sideromelane (Figure 3.4c, d). Sideromelane scoria, especially fine and medium lapilli, preserve fluidal and bubble-wall shapes. Free crystals of fresh and altered plagioclase and clinopyroxene are quite common within the matrix. The uppermost portion of the light-grey lapilli tuff is notably different to the rest of this Unit by a significant reduction of fine ash and almost complete absence of sideromelane (Table 3.3).

Alteration:

Alteration of dark-grey tuff and light-grey tuff is generally similar to that of Unit 2. Interstitial glass within the individual lithic debris is replaced with light-, dark-brown or green clay minerals and less frequently with chlorite. Red-brown iddingsite alteration of glass and olivine is also common. Secondary minerals in vesicles include carbonate, zeolite or clay minerals, or a combination of these (e.g., carbonate core and clay rim). Sideromelane is completely replaced by carbonates, less frequently with dark clays, and rarely with light-yellow-red palagonite. Plagioclase and clinopyroxene are altered with clay minerals in some clasts, and are relatively fresh in others.

The yellow-brown tuff is similar to Unit 1 deposits by showing a high degree of alteration. Clasts within the tuff are represented by fine ash to fine- and medium-lapilli, angular and irregular in form, dark- and red-brown to light-grey and green in colour (Figure 3.1). Such fragments are set in the light-yellow matrix that is enriched with carbonates and fine ash. Tachylite is altered to dark-brown and light-yellow clay minerals, whereas sideromelane is replaced with yellowish-red and red palagonite or carbonates. Most of the lithic clasts are of type I or found within the composite tachylitic fragments. Overall, Unit 3 is characterised by elevated resistivity and density and strong increase in Gamma Ray values, high U and K contents, relatively to Units 1 and 2 (Figure 3.7).

3.5.3 Interpretation

The abundance of poorly to moderately vesicular quenched glass fragments and lithics within the volcaniclastic succession from Site U1349 suggests explosive fragmentation of basaltic magma and pre-existing rocks during phreatomagmatic eruptions (Houghton & Wilson, 1989; Sohn & Park, 2004; Sorrentino et al., 2011; Graettinger et al., 2013). Absence of recovered erosional boundaries or sedimentary interbeds within the succession may indicate limited or no repose time between the phreatomagmatic events. Compositional similarity of pyroclastic material from all three Units suggests that it has derived from similar phreatomagmatic events and potentially from the same source. Consequently, the investigated deposits most likely represent one eruptive unit. Intense yellowish and red-brown palagonite alteration of sideromelane is a result of interaction with seawater during phreatomagmatic explosive activity (Ross et al., 2005; Risso et al., 2008; Cashman & Scheu, 2015).

Coarse layers within Units 3 and 1 are lithic-rich and juvenile component is reduced, comparatively to Unit 2, which could reflect transport and depositional processes, where more competent flows are able to transport coarser material further and to the drill hole site, or record change in supply of lithics from the vent, or indicate poorer phreatomagmatic fragmentation efficiency during formation of coarse layers. Deciphering between these possibilities is complicated, as these deposits are collected from one drill core. Abundant coarse lithic fragments of type II within Units 1 and 3 are interpreted as being entrained from the conduit walls in response to the phreatomagmatic explosions at the vent (Cas & Wright, 1988; McPhie et al., 1993). Unit 2 deposits could have formed during the same eruption episode as Unit 1, after a

large proportion of lithics was excavated and juvenile component became more prevalent. Lack of palagonisation in Unit 2 is explained by lower water content and overall "dryer" eruptive conditions (Risso et al., 2008; Graettinger et al., 2013). Tuff fragments, entrained into Unit 3, imply that deposits from this Unit were formed after some underlying deposits consolidated. However, contact between Units 2 and 3 is gradational, suggesting that Unit 3 deposits formed soon after deposition of the underlying Unit 2.

Mainly structureless with gradual fining upwards, non-welded, poorly-sorted and clast- to matrix-supported nature of the deposits from Units 1 and 2 is consistent with transport and deposition by high-concentration mass flow processes during phreatomagmatic eruptions (Sohn & Chough, 1992; White, 1996, 2000; Mulder & Alexander, 2001; Ross & White, 2005; McClintock & White, 2006; Sohn et al., 2008; Portner et al., 2010; Dufek et al., 2015). Layers with normal and reverse grading within Unit 1 suggest traction dominated deposition fed by discrete eruptive pulses (Lowe, 1982; White, 1996). Removal of fines from the light-yellow-grey coarse lapilli tuff layers, Units 1 and 3, could be produced by secondary hydrothermal activity and winnowing by water flushing of finer particles during deposition and transportation (Ross & White, 2005; Befus et al., 2008; Trofimovs et al., 2008). Reverse-graded coarse layers stratified with finer grained tuff carpets from Unit 3 can be produced by high-particle concentration grain flows, where smaller grains sieve through larger grains during grain-to-grain collisions (Cas & Wright, 1988). Such sequences of thin beds of tuff intercalating with lapilli tuff are interpreted as mass flow deposits with traction-dominated deposition (Chough & Sohn, 1990; Gençalioğlu-Kuşcu et al., 2007; Befus et al., 2008; Sohn et al., 2008).

The investigated pyroclastic deposits do not preserve accretionary lapilli or contain evidence for heat retention (e.g., welding) or surge-type deposition, characteristic of subaerial environment (Chough & Sohn, 1990; Bull & Cas, 2000; Thordarson, 2004; McClintock & White, 2006; Gençalioğlu-Kuşcu et al., 2007). Poor sorting of the investigated volcaniclastic deposits, low to high vesicularity of juvenile fragments (up to 60%), localised ash elutriation, grain flow type of deposition, presence of rare broken and rounded non-lithified shallow marine fossil fragments and carbonate-rich matrix suggest deposition processes in shallow subaqueous environment. Preservation of gentle textures and forms of the glass fragments within

the deposits imply relatively limited reworking processes during transportation from the vent, whereas carbonate alteration of sideromelane occurred during lithification and cementation of the deposits.

3.6 DISCUSSION

This study addresses two main questions: 1) whether the volcaniclastic deposits from Site U1349, Ori Massif, formed by pyroclastic or epiclastic processes; and 2) what were the paleodepths at the time of formation and deposition of these deposits, i.e., deep- or shallow-marine, littoral or subaerial? Preliminary interpretations of the volcaniclastic deposits from Ori Massif, Site U1349, suggested an epiclastic origin in shallow-marine to subaerial environments (Sager et al., 2010). Detailed examinations of the U1349 succession, however, provides new evidence for a shallow-marine phreatomagmatic origin.

3.6.1 Evidence for fragmentation by explosive volcanic activity

Assessment of primary-volcaniclastic versus epiclastic processes for the volcaniclastic deposits from U1349, requires an understanding of how the fragments were produced and deposited (White & Houghton, 2006). The volcaniclastic succession from U1349 is largely composed of juvenile fragments (from 70 to 100 modal % on a cement-free basis), whereas accidental lithics are subordinate. The abundant sideromelane and tachylite juvenile fragments are interpreted as products of basaltic melt quenching during phreatomagmatic eruption activity and not derived by fragmentation of chilled glassy margins of pillow lavas or lava flows. This is because opaque tachylitic glass contains abundant microlites, blocky plagioclase and typical diktytaxitic voids (Murtagh & White, 2013) and is texturally different to the chilled margins of effusive units, where spherulitic, variolitic, seriate or hiatal textures are common (see Chapter 5 for comparison). Additionally, juvenile fragments are distinguished by morphological forms (e.g., irregular, fluidal and cauliflower), generally fine vesicle size and vesicle textures (varying vesicularity within fragments, plastic deformation, uniform distribution), which is inconsistent with epiclastic fragmentation of pillow lavas or lava flows (Murtagh & White, 2013). Sideromelane and tachylite demonstrate fluidal or concave and convex (e.g., bubble-wall) surfaces, providing evidence for explosive fragmentation by bubble blasting due to an excess in volatile pressure (Maria & Carey, 2007). This is in contrast to hyaloclastite formation,

where fragments show planar surfaces, produced by quench and chill-shatter non-explosive fragmentation (Cas & Wright, 1988). The volcaniclastic deposits are characterised by high tachylite to sideromelane ratio, which suggests different degrees of microlite crystallisation or devitrification. Abundance of tachylite, relative to sideromelane, implies slower cooling rates, which can be developed within conduits or within the interiors of initially larger clasts (Schipper et al., 2010; Murtagh & White, 2013; Cioni et al., 2014).

Composite clasts of sideromelane and tachylite, are found in many horizons within the investigated volcaniclastic deposits and provide additional evidence for the primary-volcaniclastic origin of juvenile fragments, since none of the surface processes are able to cause embedding of lithic fragments within the juvenile glassy material (White & Houghton, 2006). Lithics, captured by tachylite or sideromelane, are formed by explosive fragmentation of country rocks, including conduit walls and dykes (Cas & Wright, 1988; Houghton et al., 2015). Lithics of type I show similar crystallinity and composition to the lithics found within the composite clasts and therefore are likely of the same origin. Lithics of type II are derived by fragmentation of the country rock material or may be locally incorporated during transportation and deposition, which is commonly observed in other phreatomagmatic deposits (Mattsson & Höskuldsson, 2011; Brown & Andrews, 2015). In conclusion, characteristics of the overwhelming majority of fragments from the investigated volcaniclastic deposits are consistent with pyroclastic origin.

3.6.2 Shallow-marine versus subaerial depositional environments

Assessment of reworking degree for the fragments, produced by primary volcaniclastic processes, is essential, because loose volcaniclastic material can be remobilised prior to lithification (McPhie et al., 1993; White et al., 2009). Sometimes reworking processes cannot be unambiguously differentiated from the primary-volcaniclastic processes (e.g., secondary lahars, Waitt, 2007). This may be particularly problematical for subaqueous settings, where many genuine primary deposits were classified as reworked (White, 2000). Reworking processes, when recognised, remain sensitive indicators of depositional environments and record paleodepth variations. Subaerial storage of tephra during repose time between the eruption events often results in reworking, weathering, erosion or soil development, as in examples of tropical Hawaii Island (Goodfellow et al., 2014), Ambae Island in Vanuatu (Németh

& Cronin, 2009) and Tenerife in Canary Islands (Bryan et al., 1998). Volcaniclastic material from shallow-marine to emergent Surtsey volcano in Iceland was significantly subjected to wave erosion and slumping (Kokelaar & Durant, 1983; Moore, 1985), whereas ocean currents and bioturbation affected deposits from the deep-marine Axial seamount in Pacific (Portner et al., 2015).

Previously, the lower part of the volcaniclastic succession (Unit 1) was interpreted to have formed in a subaerial environment based on the red-yellow alteration colour and rounding of some fragments (Sager et al., 2010). The intense yellow to reddish alteration of Unit 1 was previously interpreted to result from subaerial oxidation (Sager et al., 2010). However, yellow and red-yellow palagonite is also a typical alteration product of metastable sideromelane glass, resulting from interaction with water during phreatomagmatic processes (Ross et al., 2005; Risso et al., 2008; Cashman & Scheu, 2015). Furthermore, two-stage sideromelane alteration and zoned alteration of tachylite indicate higher-temperatures of alteration, resulting from steam moving through pyroclastic debris (Cas & Wright, 1988; McPhie et al., 1993). The reddish colour of some lithic fragments is a result of iddingsite alteration, which is not diagnostic of subaerial environments or exposure and weathering (Talbi & Honnorez, 2003; D'Antonio & Kristensen, 2005).

The interval interpreted as paleosol by Sager et al. (2010) is characterised by very poor recovery (~20 cm over a distance of ~8 m) and cannot be distinguished on the basis of resistivity, density and gamma ray logs from the rest of Unit 1 volcaniclastic deposits (Figure 3.7). Consequently, Unit 1 sequence represents lithologically uniform consolidated deposit, arguing against extensive paleosol development. Furthermore, no plant and root fossil remnants were reported within the volcaniclastic succession (Sager et al., 2010), providing no evidence for subaerial soil development.

Rounding of some clasts within the lowermost volcaniclastic deposits was used as additional evidence for the subaerial origin of clasts and cold transport of volcanic-derived material (Sager et al., 2010). However, rounding is not necessarily diagnostic of coastal or fluvial environments and can be produced during transportation processes and explosive fragmentation in subaqueous environments (Thal et al., 2016), particularly if the flow has glassy, vesiculated juvenile clasts. Scarcity of rounded clasts, absence of profound hydraulic sorting, erosional contacts, cross-beds and lenses

within the deposits do not support fluvial origin (Bull & Cas, 2000; Ross & White, 2005). Importantly, this study demonstrates that the majority of fragments are angular and the roundness is more characteristic of juvenile clasts. The examined deposits contain a high juvenile content, and sideromelane is widespread and preserved gentle forms and vesicle textures, providing evidence against reworking. Furthermore, basaltic glass, especially sideromelane, is known as the most friable component of volcaniclastic rocks and therefore is most susceptible for disintegration during processes of primary deposition and transportation as well as reworking (Fisher & Schmincke, 1984). Rounding of some lithics could be associated with in-vent abrasion during phreatomagmatic eruption and subsequent transportation, and some of the lithics could have been reworked prior to eruption (Fisher & Schmincke, 1984; Cas & Wright, 1988; Sohn & Park, 2004; Cioni et al., 2014; Thal et al., 2016).

The recovered core material of volcaniclastic deposits does not provide evidence for erosional processes or contain any interbedded sedimentary layers. Marine fossils are present only in small quantities within the deposits and did not record any colonisation during hiatuses, which is in contrast to many other locations at Shatsky Rise demonstrating substantial biogenic marine colonisation during volcanic tranquillity (Figure 2.8) (Sager et al., 2010). This implies a limited repose time between the phreatomagmatic events.

Poor sorting and marine fossils, identified in all Units, imply that the deposition processes occurred within the subaqueous environment (Sohn & Park, 2004). Accretionary lapilli, ash aggregates and armoured lapilli are commonly observed in subaerial phreatomagmatic deposits (Moore, 1985; Thordarson, 2004; Risso et al., 2008; Sohn et al., 2008), but are absent in the investigated deposits potentially as a result of subaqueous deposition (Schumacher & Schmincke, 1995; Houghton et al., 2015). Abundant carbonate and minor zeolite cementation and alteration of sideromelane across the volcaniclastic succession is also consistent with subaqueous deposition and lithification. Additionally, observed elevated U and K concentrations are associated with carbonatisation during seawater hydrothermal alteration of oceanic crust (Kelley et al., 2003) (also see Chapter 5).

3.6.3 Implications for the emergence of Ori Massif

A shallow-marine to near sea-level depositional environment for the phreatomagmatic deposits from Site U1349 is supported by a combination of the following factors: presence of shallow-marine fossils, relatively high vesicularity of juvenile fragments, as well as high-vesicularity (up to 75%) of the underlying lavas and traces of oolites within the limestone (Sager et al., 2010). However, absence of sedimentary structures (e.g., symmetrical ripples, hummocky cross-stratification) within the deposits favours primary volcaniclastic depositional processes below wave base. It is also possible that loose tephra of phreatomagmatic origin was remobilised by slumping from a shallow-marine subaqueous tuff cone and redeposited by mass flows at water depths below the wave base. Such shallow-marine to near sea-level phreatomagmatic activity is commonly referred to as Surtseyan style volcanism (Kokelaar & Durant, 1983; Thordarson & Larsen, 2007; Murtagh & White, 2013; Houghton et al., 2015; White et al., 2015).

The location of the phreatomagmatic deposits from Site U1349 at one of the highest parts of the current day Ori Massif (Zhang et al., 2015) suggests that they could represent the later stages of formation for this edifice. This study supports the idea that the shallow-marine to near sea-level Surtseyan style phreatomagmatic eruptions at the summit of Ori Massif were responsible for producing the volcaniclastic material from Site U1349. Results from this study and critical reexamination of previous knowledge on Ori Massif provide no evidence that could support subaerial emergence of Ori Massif unambiguously, implying that Ori Massif might never have been subaerial. This is also consistent with recent studies of Shimizu et al. (2013) and Zhang et al. (2015), supporting a largely submarine nature of the Ori Massif.

3.7 SUMMARY OF THE KEY FINDINGS

This study has re-assessed the formation of volcaniclastic deposits at Site U1349, cored near the summit of Ori Massif, and the evidence for shoaling and subaerial emergence for this edifice. Results from this study demonstrate that:

- The overwhelming majority of fragments from the volcaniclastic deposits at Site U1349 was produced by Surtseyan style phreatomagmatic activity.
- Most of the volcaniclastic succession represents one eruptive unit.
- The particles were transported by high-concentration mass flows and grain flows.

- Deposition of the entire volcaniclastic succession was likely syn-eruptive and involved minimal reworking.
- Depositional processes occurred in subaqueous environment and below wave base.
- The summit of Ori Massif was shallow-marine to near sea-level.
- There is no unambiguous evidence to support subaerial emergence for Ori Massif.

Chapter 4: Differentiating magma sources at Ori Massif: Evidence from basaltic fragments within the volcaniclastic deposits, Site U1349

4.1 INTRODUCTION

Oceanic crust varies in topography, thickness and geochemical composition, and comprises relatively thin "normal" oceanic crust (up to 6-7 km thick), produced at MORs, as well as numerous isolated volcanic islands and seamounts and over-thickened regions of oceanic plateaus (10-40 km thick), which usually form in intraplate tectonic settings and cannot be directly related to spreading at MORs (Carlson et al., 1980; Coffin & Eldholm, 1993; Korenaga & Korenaga, 2008; Koppers & Watts, 2010; Kim & Wessel, 2011; Kerr, 2014). Such intraplate oceanic features are largely associated with chemical heterogeneities in magmatic sources, as opposed to the "normal" oceanic crust, characterised by relatively uniform chemical compositions and which formation is related to melting of the fairly homogeneous upper mantle source (Nowell et al., 1998; Sims et al., 2002; Ito & Mahoney, 2005; Stracke, 2012). Geochemically, OIBs are the most remarkable examples of oceanic intraplate magmatism, characterised by large variability in petrological (alkali basalts, hawaiites etc), petrochemical (high alkalis, enriched Nb, Ta and La/Yb ratio) and isotope compositions (low, unradiogenic Nd and Hf, high radiogenic Sr and Pb isotope ratios, high $^{3}He/^{4}He$ ratios) that require existence a number of long-term isolated reservoirs in the deep mantle (Kurz et al., 1982; Zindler & Hart, 1986; Hart et al., 1992; Hofmann, 2003; Stracke, 2012). Compared to the much less voluminous oceanic islands and seamount chains, oceanic plateaus generally show only limited variations in their magma geochemistry, often having transitional compositions between MORB and OIB (Geldmacher et al., 2003; Thompson et al., 2003; Castillo, 2004; Roberge et al., 2004; Shafer et al., 2004; Tejada et al., 2004; White et al., 2004; Kerr & Mahoney, 2007; Hastie & Kerr, 2010; Hoernle et al., 2010; Timm et al., 2011; Tejada et al., 2013; Kerr, 2014). The widely accepted mantle plume model explains the formation of

oceanic plateaus and island chains by melting of thermochemical mantle plume, which form voluminous heads (triggering plateau volcanism) followed by narrow tails while ascending from the lower mantle (Griffiths & Campbell, 1990; Campbell, 2007). Consequently, it is suggested that the lower mantle material within the plumes differs from the ambient (upper) mantle by both higher temperatures and commonly enriched chemistry (Lin & van Keken, 2005; Putirka, 2008; Collerson et al., 2010).

Oceanic plateaus, other LIPs and hotspots are traditionally regarded as intraplate magmatic outpourings and their emplacement is considered as independent of plate tectonic boundaries (Coffin & Eldholm, 1993, 1994b; Bryan & Ernst, 2008; Bryan & Ferrari, 2013). Nevertheless, global plate tectonic reconstructions reveal that a number of oceanic plateaus (e.g., Rio Grande Rise, Agulhas plateau, Shatsky Rise; Table 3.1) and hotspot islands (e.g., Crozet, Tristan da Cunha, Iceland, Galapagos) formed at or near existing mid-oceanic spreading ridges, including triple junctions (Sager, 2005; Li & Zhong, 2009; Farnetani & Hofmann, 2011; O'Connor et al., 2012; Seton et al., 2012; Gibbons et al., 2013; Whittaker et al., 2015). Iceland in the North Atlantic is one of the most prominent and best-investigated examples of a modern hotspot located at an active MOR. In Iceland, presence of geochemically depleted MORB-like material and enriched components (potentially from recycled oceanic slabs or subcontinental lithosphere) in the magma source have long been recognised and is attributed to intense interaction of a mantle plume with an active spreading system (Hanan & Schilling, 1997; Kempton et al., 2000; Thirlwall et al., 2004; Kokfelt et al., 2006; Peate et al., 2009; Koornneef et al., 2012). Consequently, if mantle plumes are involved in the formation of LIPs, oceanic plateaus emplaced at an active (or recently active) MOR are expected to geochemically differ from those formed well away from MORs.

Shatsky Rise is one of the largest oceanic plateaus known to be emplaced at an active triple junction of oceanic spreading ridges (Nakanishi et al., 1999; Sager, 2005; Sager et al., 2016). Previous investigations on basalts from the three large edifices at Shatsky Rise revealed predominantly MORB-like compositions with variations ranging from distinctly depleted MORB to slightly more enriched (OIB-like), implying presence of the mantle plume derived material in the source of some Shatsky Rise lavas (Mahoney et al., 2005; Sano et al., 2012; Heydolph et al., 2014). The central Shatsky Rise edifice, Ori Massif, is characterised by the greatest variations in magmatic compositions for this oceanic plateau (Figures 2.9 and 4.1).

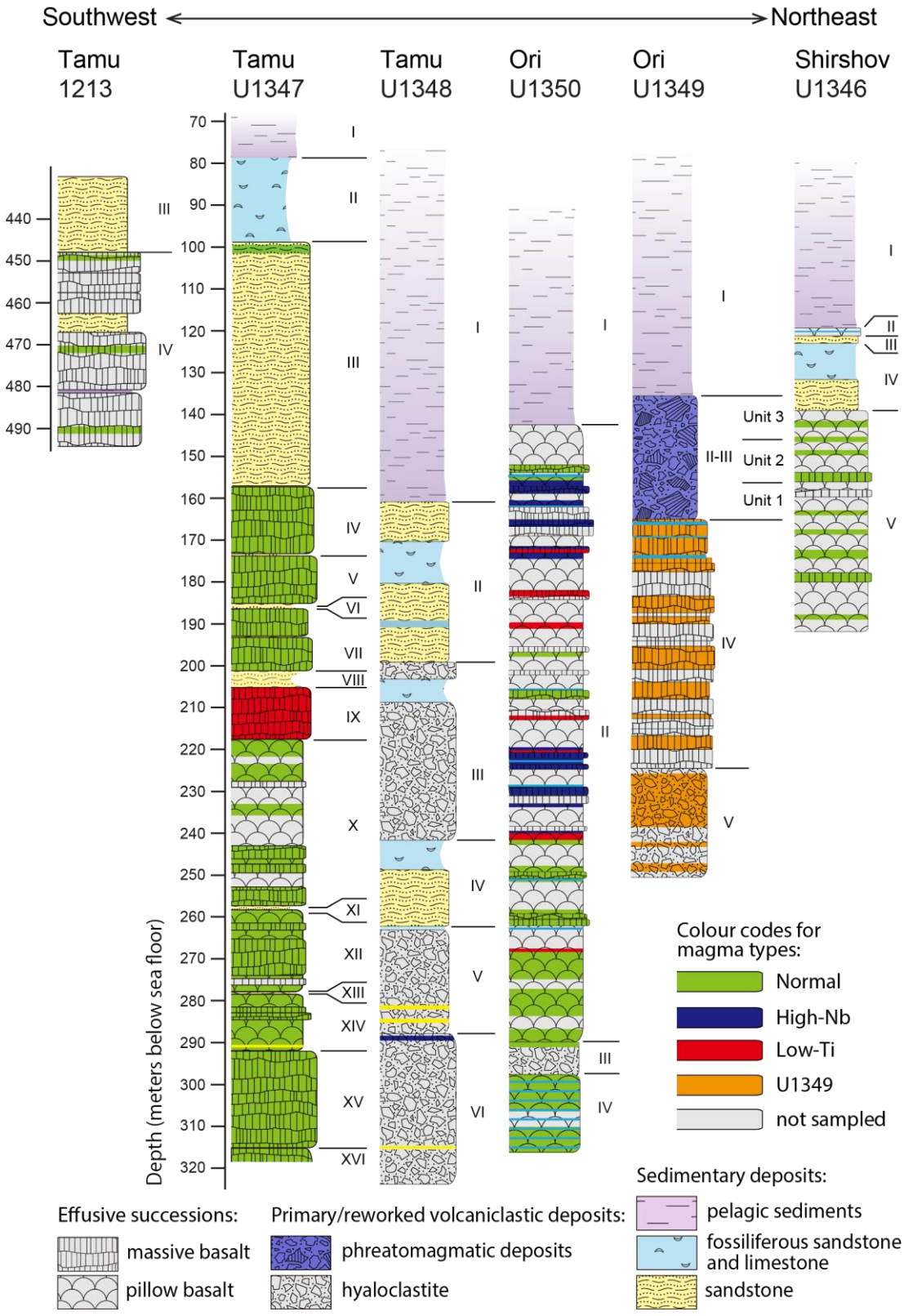

Figure 4.1. Lithologic summary of cores drilled on Shatsky Rise, modified from Figure 2.8 and Koppers et al. (2010) by showing distribution of magma types after Sano et al. (2012). Geochemical data on fresh glass and whole-rock samples are from Mahoney et al. (2005) and Sano et al. (2012). Roman numbers indicate stratigraphic units as from Sager et al. (2010).

Importantly, basalts from a number of nearby seamounts, potentially representing subsequent plume-tail magmatism as a continuation of the Shatsky Rise emplacement, demonstrate alkali basaltic affinities and enriched OIB-like isotopic compositions (Tatsumi et al., 1998; Tejada et al., 2016). However, the relationship of OIB magmatism to the main plateau building stage remains unclear, because geochemically enriched basalts are rare at Shatsky Rise and the ages of seamounts are not well-constrained (Heydolph et al., 2014; Tejada et al., 2016). Therefore, a better understanding of late stage volcanism at Shatsky Rise, at the end of the plateau-building stage at Ori Massif is desirable.

This study specifically investigates basaltic fragments from volcaniclastic deposits, representing the late building stage of the Ori Massif. The fragments were formed by explosive fragmentation of juvenile magma and wall-rock material during phreatomagmatic activity and, therefore, may represent a wide sampling of basalts with potentially distinct magmatic chemistry. New major element, trace element and Nd-Hf isotope data for basaltic fragments from Ori Massif are presented in this study and discussed in terms of compositional heterogeneity of Ori Massif.

4.2 SAMPLES AND ANALYTICAL TECHNIQUES

4.2.1 Samples

Major and trace element along with Nd-Hf isotope geochemical investigations were conducted on basaltic fragments from volcaniclastic deposits, located at the top of the igneous basement at Site U1349 between lava flows and the pelagic sedimentary cap (Figure 4.1). Forty-two of the largest fragments, with sizes ranging from medium to coarse lapilli, were selected from 13 intervals of the volcaniclastic succession, representing all three Units, as identified in Chapter 3 (see sample location on Figure 3.1). Due to generally small size of the fragments, usually less than 1 cm in diameter, only nine petrographic thin sections for the biggest fragments (3a, 4a, 10a, 10b, 10c, 11, 12a, 12b, 13) were produced. For geochemical analyses, samples were ground on a non-reusable corundum paper and washed with Ultrapure (18 MΩ cm) H_2O in order to remove any adherent matrix and contamination from the rock saw. All samples were air-dried, photographed and examined using a binocular microscope. Afterwards, each fragment was powdered by hand in an agate mortar.

4.2.2 Loss on ignition

Loss on Ignition (LOI) was performed at QUT for 39 samples. Depending on availability of powders, 0.08 to 1 g of each sample was used for LOI analysis, including seven samples that weigh less than 0.1 g (2b, 2d, 3b, 3c, 3h, 3i, 8b). To calculate the moisture content, each sample was placed into porcelain crucibles and heated at 105º C overnight. Before the LOI analysis, platinum crucibles were washed in Ultrapure H_2O and dried in the oven at 950º C for 1 hour. To calculate the LOI, the powders were placed into the platinum crucibles and heated in the oven at 950º C for 1 hour. The powders were weighted before and after the ignition.

4.2.3 Major elements

Major element compositions were determined for 40 samples by using Perkin Elmer Optima 8300DV Inductively Coupled Plasma Optical Emission Spectroscopy (ICP-OES) at QUT. Before the analysis, sample powders were dried at 105º C for 2 hours to reduce any moisture. Approximately 0.08 g of each powder was mixed with ~0.6 g of lithium metaborate to prepare glass beads by fusion on Katanax. The glass beads were completely dissolved in ~50 ml of 5% HNO_3 in an ultrasonic bath and the aliquots of these solutions were taken for measurements. Procedural blanks, duplicates and geochemical reference materials (W1, G2, BCR1, AGV1) were analysed together with the samples. The instrument tubes were washed by 5% HNO_3 solution between the measurements to remove any remaining solution. Monitors were prepared by mixing representative samples and run every few analyses to detect memory effects and correct for the instrument drift.

4.2.4 Multivariate analysis

To assess major element variations, multivariate methods (Hierarchical Cluster Analysis, HCA, and Principal Component Analysis, PCA) on 40 major element compositions, normalised to anhydrous, were applied. Q-mode HCA, using the Ward linkage method and the Squared Euclidean distance, were first performed to describe groups (clusters) of the major element values. Following this, listwise PCA was performed on z-standardised data to explain variability in the major element values using the Kaiser criterion (only principal components with eigenvalues >1 are valid). Component loadings for each principal component (PC) were used to calculate a score for each major element value; these component scores were used to investigate the

variability for each major element value within and between both clusters, according to each principal component.

All multivariate statistical analyses were processed using the software STATGRAPHICS Centurion XVII (StatPoint technologies, Inc. Version 17.1.12). The principles of hierarchical cluster and principal component analyses are summarised in Kaiser (1960), Stetzenbach et al. (1999), Hair, et al. (2006), Templ, et al. (2008).

4.2.5 Trace elements

The trace element data were acquired for 40 samples in Class 1000 clean room at QUT. Chemical preparation of the samples was modified from digestion methods (Eggins et al., 1997; Yu et al., 2001) as follows to avoid fluoride or nitride precipitation. About 50 mg of each sample was weighed in 15 ml Savillex beakers and digested at 110-125º C for 12 hours by using a mixture of 1.5 ml HCl, 0.5 ml HNO_3 and 0.3-0.5 ml HF, all acids are double distilled. Afterwards, the samples were dried down by halves at 80º C, mixed with 2 ml HCl and dried down by halves at 80º C again. The other 3 ml of HCl were added to the samples; the beakers were capped and placed for 12 hours at 100º C. After that, the solutions were dried down at 100º C to incipient dryness, mixed with 1 ml HNO_3 and 1 ml Ultrapure H_2O and dried down completely. The last two steps were repeated for four times. For the final solution ready for the analysis, the samples were mixed with 4.8 ml Ultrapure H_2O and 0.2 ml HNO_3, left overnight to reflux at 100º C. The samples were removed to centrifuge tubes and centrifuged at 3500 RPM for 15 minutes. The trace element measurements were carried out on Agilent 8800 Triple Quadrupole Inductively Coupled Plasma Mass Spectrometer (ICP-MS). Procedural blanks and reference materials (W-2, BIR-1, AGV-2) were analysed together with the samples. Blanks and monitors (representative samples) were used every few samples to detect memory effects and correct for instrument drift.

4.2.6 Hf-Nd isotope geochemistry

Eleven samples were selected to represent different trace element compositions from all three Units. Nd and Hf chemistry was carried out in Class 1000 clean rooms at GEOMAR Helmholtz Centre for Ocean Reseach Kiel (Germany). Isotope analysis at GEOMAR used a Thermo Finnigan TRITON TIMS for Nd and a NU Plasma multiple collector ICP-MS for Hf Both instruments operated in static multi-collection

mode. About 100 mg of fine-grained sample powder for each isotope analysis were digested. Hf chromatography followed the methods described by Blichert-Toft and Albarede (1997) and Heydolph et al. (2014) while the procedures for Nd followed those of Hoernle et al. (2008). Within-run mass bias correction used $^{146}Nd/^{144}Nd$ = 0.7219 and $^{179}Hf/^{177}Hf$ = 0.7325 and applied exponential mass fractionation. 2σ within run errors shown in Tables 4.2 and 4.3 are $2\sigma / \sqrt{n - 1}$ (n = numbers of scans passing the outlier test). External errors reported for the standards below are 2σ standard deviation (2SD) of the mean of multiple analysis measured along with the samples. La Jolla gave $^{143}Nd/^{144}Nd$ = 0.511850 ± 0.000004 (n=11) and the standard bracketing normalized value for the in-house Hf monitor solution SPEX was $^{176}Hf/^{177}Hf$ = 0.282167 ± 9 (n = 24). This value corresponds to $^{176}Hf/^{177}Hf$ = 0.282160 for JMC 475 (Vervoort & Blichert-Toft, 1999). The initial epsilon values were calculated using the decay constants of 1.867×10^{-11} (εHf) and 6.539×10^{-12} (εNd), and the CHUR values from Bouvier et al. (2008).

4.3 RESULTS

4.3.1 Petrography

Basaltic fragments from the volcaniclastic deposits were classified into lithic and juvenile types, representing wall-rock and quenched basalt magma fragments, respectively (Appendix A). Analysis of the available petrographic thin sections shows that eight out of nine fragments are lithics (Figures 3.2e, f and 3.4a) and one fragment is juvenile (Figure 3.2d). Additionally, fragments with clear crystalline textures were identified as lithics after examination using binocular microscope.

As observed in thin sections, all lithic clasts are accessory, corresponding to type II (see Chapter 3). Lithic fragments vary in colour (yellow, pink, light and dark brown, red-brown, green-grey), are dense to vesicular and range in crystallinity from hypo- to almost holo-crystalline. Primary magmatic minerals include fresh and slightly altered plagioclase and opaque minerals, as well as entirely altered clinopyroxene, olivine and interstitial glass. Secondary minerals comprise clay minerals, carbonates, iddingsite, celadonite and zeolites, in order of predominance.

Juvenile fragments used for this study are entirely composed of microcrystalline tachylitic glass. Sideromelane glass were not selected because it is entirely replaced with carbonate minerals and palagonite. Tachylite may contain phenocrysts of blocky

plagioclase (Figure 3.2d) and multiple microlites of plagioclase and clinopyroxene, well recognised under the reflected light. Glassy mesostasis in the studied juvenile fragments is completely replaced with clay minerals. As observed in thin sections, juvenile (tachylite) fragments differ from the lithic clasts by darker-brown colour, shapes with more irregular and ragged surfaces, and relatively smaller and arcuate vesicles.

4.3.2 Major element geochemistry

The selected samples show wide variations in major element compositions and high volatile contents, with the majority of samples having LOI values ranging from 5 to 15 wt.% (Appendix A). In particular, contents of K_2O reach up to 10.5 wt.% (Figure 4.2a), with only three samples having less than 1 wt.% of K_2O. Contents of MgO and CaO broadly vary from 0.88 to 9.89 wt.% and from 1.56 to 21.5 wt.%, respectively (Figure 4.2b). Wide compositional range in major element geochemistry of the selected samples and intense secondary mineralisation prevent from reliable magmatic classification by using the conventional major element diagrams (e.g., TAS, Figure 4.2a; AFM; binary plots, Figure 4.2b).

Petrogenetic affinities of the samples are examined by using TiO_2, Al_2O_3 and P_2O_5, which are considered as the least mobile major element oxides during seawater alteration of basalts (Figure 4.3). Basaltic fragments are characterised by Al_2O_3 compositions varying within 12.1-18.6 wt.%, excluding three samples with relatively lower Al_2O_3 (9.9-10.6 wt.%) and also very high LOI (9.8-15.3 wt.%) (Appendix A). Concentrations of P_2O_5 in all studied samples are under 1 wt. % (usually lower than 0.5 wt.%). All samples from the volcaniclastic deposits are characterised by high TiO_2 (1.42-4.10 wt.%) with over half of sample population showing TiO_2 > 2.5 wt. %. Investigated samples show Al_2O_3/TiO_2 values varying from 4 to 10.1 (Figure 4.3).

4.3.3 Geochemical groupings

Statistical approach was applied to evaluate the compositional variation in major elements across the three Units. Based on similarity in major element compositions, all samples were subdivided into six subclusters, by using the Hierarchical Cluster Analysis (HCA) (Figure 4.4a). Principal component analysis (PCA) was used to explain variability of data in combination with HCA. Four valid principal components (PC) with eigenvalues >1 were identified, explaining ~78 % of variability. Binary plots

show vectors for each major element oxide contributing to the two major PC 1 and 2 (Figure 4.4b) and the corresponding scores of these PC for all samples (Figure 4.4c-e). These two PC explain 28.3 % (PC1) and 22.5 % (PC2) of the dataset variability.

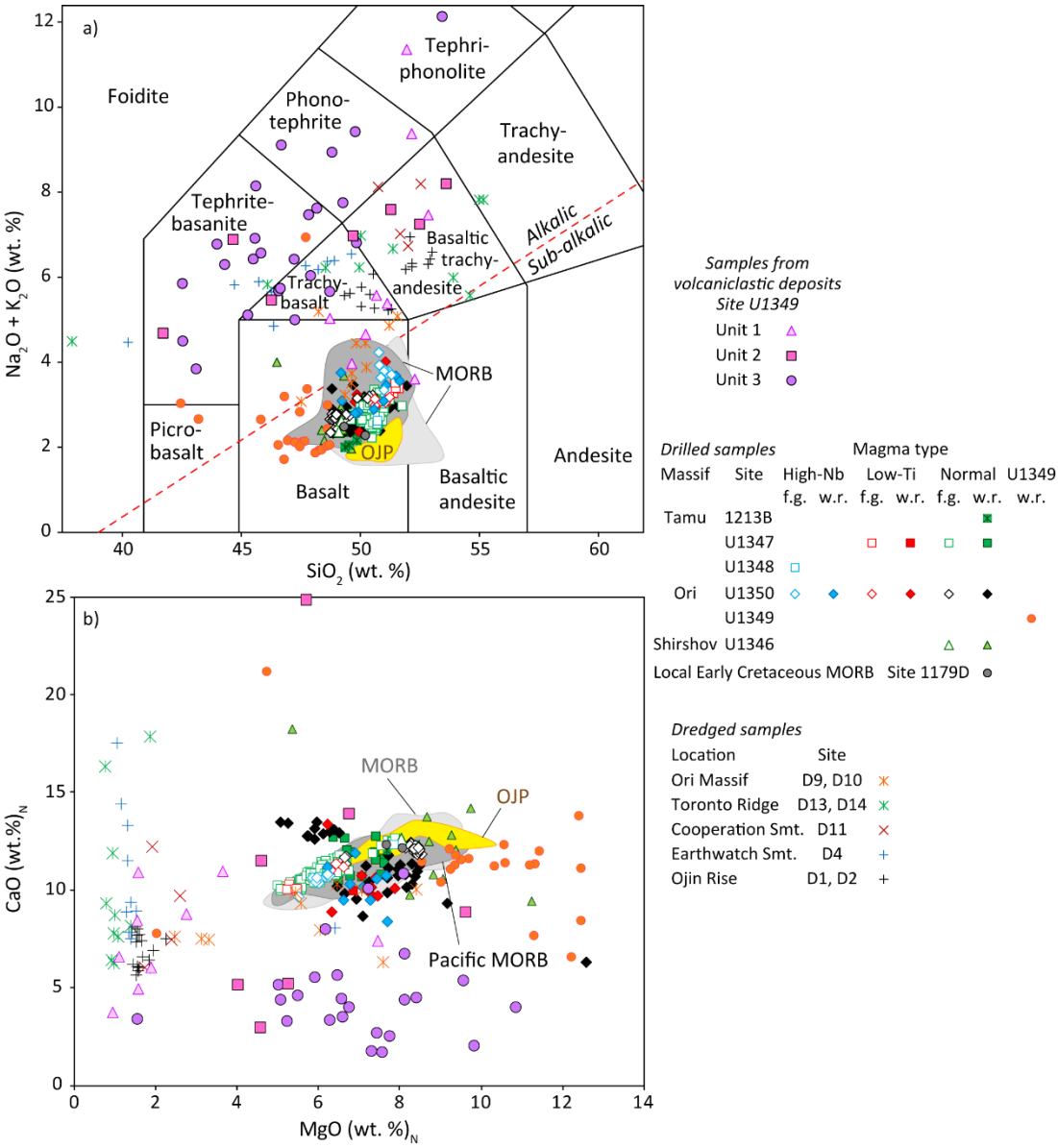

Figure 4.2. On (a) Total Alkali versus Silica (TAS) classification diagram, after Le Maitre (2002), on (b) CaO (wt. %) versus MgO (wt. %) binary plot, showing major element compositions for samples from this study. Available data for samples from Shatsky Rise (Sano et al., 2012; Husen et al., 2013), TN037 dredges (Tatsumi et al., 1998) and local MORB samples from Site 1179D (Mahoney et al., 2005) are plotted for comparison. Also shown fields for fresh glass compositions from the Ontong Java Plateau (Roberge et al., 2004; Sano & Yamashita, 2004) and mid-ocean ridges (Jenner & O'Neill, 2012). All data are normalised to anhydrous. Line dividing between alkaline and subalkaline series on TAS is after Irvine and Baragar (1971).

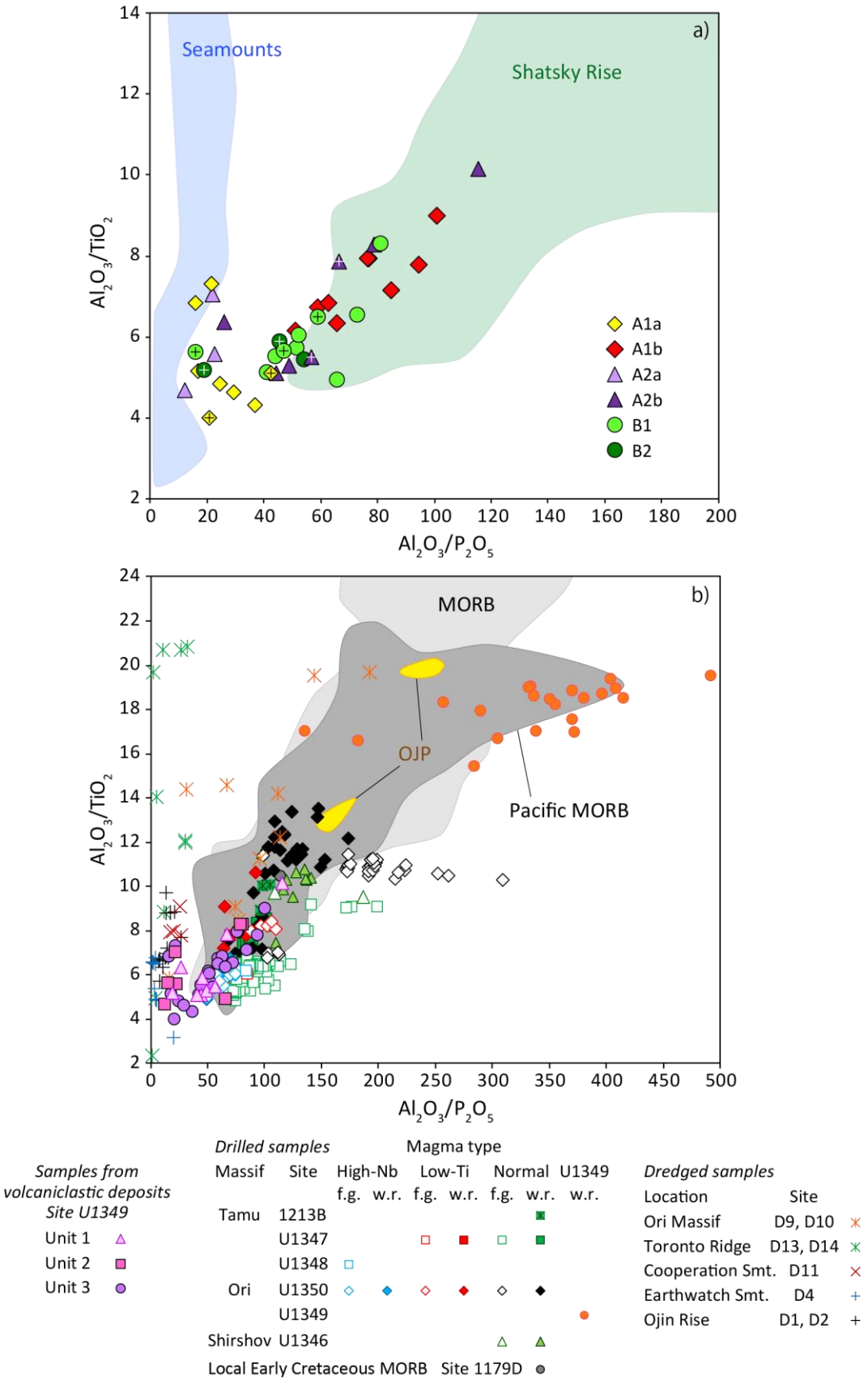

Figure 4.3. Al_2O_3/TiO_2 versus Al_2O_3/P_2O_5 binary plots, showing major element compositions for samples from this study. Subdivisions on plot a) according to cluster analysis, crosses indicate samples for Hf-Nd studies. Additional data as in Figure 4.2.

Samples from four of the six subclusters largely correspond to three designated Units. Subclusters A1a and A1b are entirely represented by fragments from Unit 3, subcluster A2a consists of samples from Unit 2, whereas subcluster A2b mainly contains samples from Unit 1 (Figure 4.4a, d). Samples from the two remaining subclusters, B1 and B2, form larger cluster B and represent all three Units with half of the samples from Unit 3. Samples from each subcluster are distinguished from other subclusters by geochemical and petrographical properties as described below (see also Table 4.1; Figure 4.4; Appendix A):

Samples from subcluster A1a are characterised by the greatest contents for TiO_2, Fe_2O_3, Na_2O and P_2O_5, high concentrations of Al_2O_3 and MgO, relatively low K_2O and the lowermost CaO. Fragments from A1a are dark-brown to dark-grey in colour and are dense to low-vesicular.

Samples from subcluster A1b show the highest Al_2O_3 and MgO and the lowermost P_2O_5. These basalts are relatively lighter-brown in colour and contain larger plagioclase grains within the groundmass, comparatively to samples from subcluster A1a. All fragments from A1b are low-vesicular lithics, with vesicles up to 2-3 mm long and filled with carbonates, zeolites and clay minerals. Petrographic investigations of thin sections reveal entire replacement of the primary pyroxene, olivine and the interstitial glass by clay minerals and iddingsite (Figure 3.4a).

Samples from subcluster A2a are characterised by the highest contents of CaO and LOI, high concentrations of MgO and P_2O_5, and also the lowermost contents of Al_2O_3 TiO_2 and SiO_2. Such basaltic fragments are dark-grey to brown in colour and contain small vesicles, filled with carbonate minerals.

Samples from subcluster A2b contain the lowermost K_2O and generally low MgO, TiO_2 and P_2O_5 contents, whereas MnO contents are relatively high. This group comprises one dark-grey vesicular fragment from Unit 2 and several yellow-brown and red-brown vesicular lithic clasts from Unit 1. As observed in thin sections, lithics are hypocrystalline, with abundant groundmass plagioclase set in glassy matrix replaced by reddish-brown iddingsite. Vesicles in basalts are occupied by yellowish carbonate and clay minerals (Unit 1) or by light-grey carbonate minerals (Unit 2).

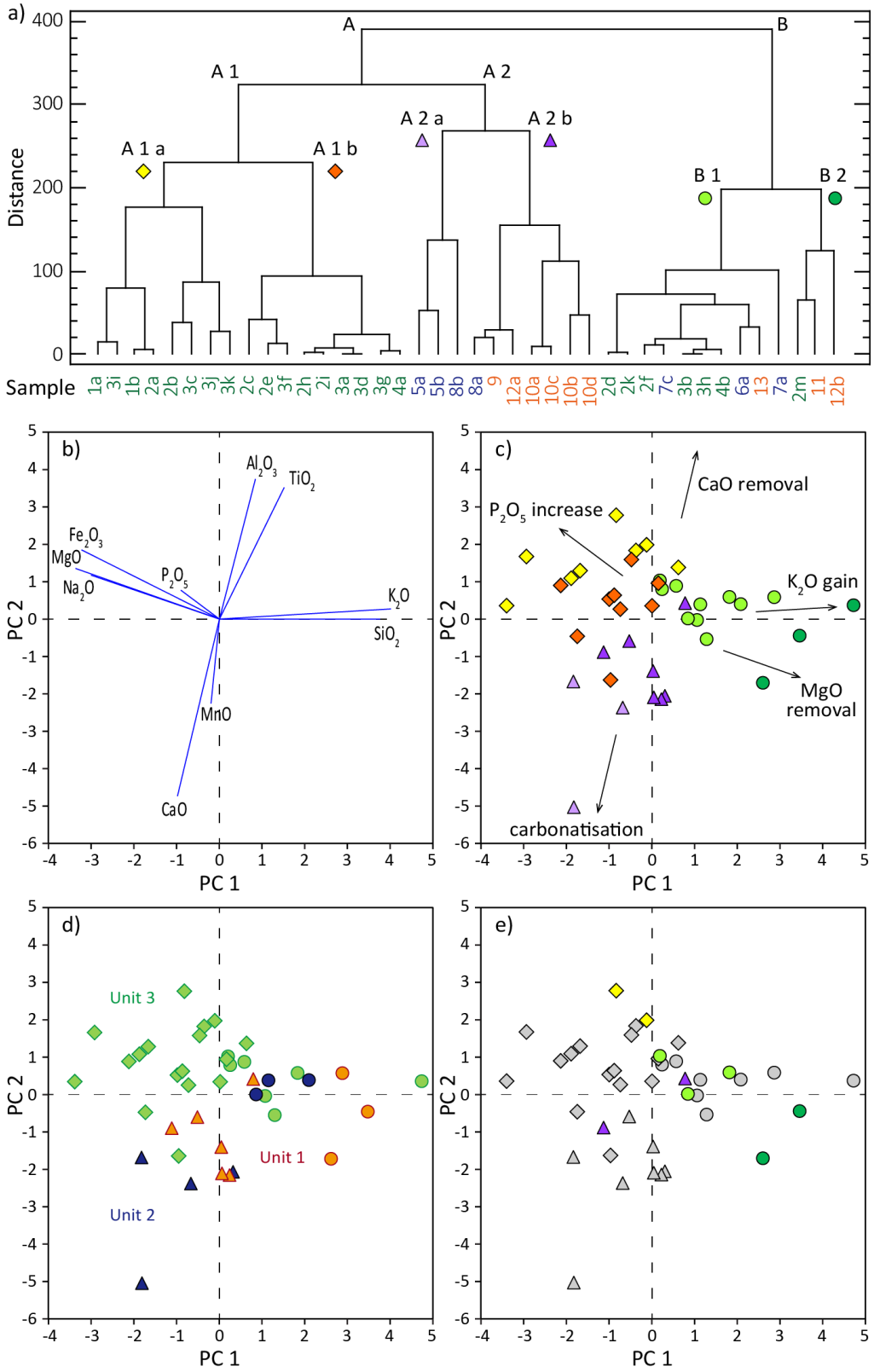

Figure 4.4. Hierarchical cluster analysis dendrogram for basaltic fragments (a). Sample names are coloured according to the Units, identified in Chapter 3 (see colour code on d). Images b-e display binary plots for two major principal components (PC1 and PC2) relative to: b) vectors of the component weights for each variable (major element oxide); c) subcluster divisions (see legend on a); d) Unit membership; e) samples used for the Hf-Nd isotope analysis (coloured).

Table 4.1. Major element compositional range for six subclusters. All data are normalised to anhydrous. Maximum and minimum average values are highlighted.

Subcluster		SiO_2	TiO_2	Al_2O_3	Fe_2O_3	MnO	MgO	CaO	Na_2O	K_2O	P_2O_5	Alkalis	LOI
A1a	max	47.8	4.1	19.9	19.9	0.15	9.7	5.5	4.8	6.0	1.06	7.4	11.8
	min	41.7	2.1	15.2	15.0	0.06	5.0	1.7	1.4	0.7	0.47	4.9	0.0
	mean	45.5	***3.3***	16.8	***17.0***	0.11	7.1	***3.5***	***3.3***	2.7	***0.70***	6.0	5.5
A1b	max	47.2	2.9	19.7	18.3	0.22	10.7	10.7	2.5	5.8	0.33	8.0	9.1
	min	41.9	1.8	16.5	12.6	0.09	4.9	2.5	1.9	1.9	0.16	3.8	5.1
	mean	44.5	2.5	***17.8***	15.4	0.13	***7.7***	5.9	2.3	3.5	***0.25***	5.9	7.2
A2a	max	45.4	2.5	11.7	17.7	0.16	9.4	24.6	2.5	5.2	0.96	6.8	15.3
	min	41.3	1.6	10.8	10.1	0.10	5.6	8.7	1.6	2.1	0.48	4.6	9.8
	mean	***43.6***	***2.0***	***11.4***	13.7	0.14	7.2	***15.7***	2.0	3.6	0.65	5.6	***12.5***
A2b	max	51.7	3.3	18.3	19.5	0.50	7.4	11.4	3.0	4.0	0.55	6.9	9.9
	min	48.0	1.7	14.3	11.1	0.11	1.1	6.0	2.5	0.8	0.15	3.6	2.8
	mean	49.6	2.4	15.8	14.7	***0.25***	3.2	8.8	2.8	***2.2***	0.30	***5.0***	5.7
B1	max	53.0	3.4	18.3	16.6	0.16	6.7	7.9	2.8	7.4	0.94	9.3	9.7
	min	46.2	2.2	14.8	10.6	0.04	1.6	3.0	1.4	4.3	0.23	6.7	2.1
	mean	49.6	2.8	16.8	12.6	***0.08***	5.2	4.5	2.3	5.8	0.37	8.1	***4.8***
B2	max	53.0	3.4	18.7	14.8	0.26	1.5	8.4	1.4	10.7	0.83	12.0	9.4
	min	51.3	2.3	13.3	7.3	0.05	0.9	3.4	0.1	7.2	0.29	7.4	2.0
	mean	***52.1***	2.9	15.9	***11.7***	0.16	***1.3***	5.1	***0.7***	***9.5***	0.49	***10.2***	5.3

Samples from subcluster B1 are distinguished by the lowest MnO contents, relatively low LOI and Fe_2O_3 and elevated K_2O and TiO_2. Fragments from Unit 3 are characterised by grey-brown colour and are rich in small vesicles, filled with carbonate and clay minerals. Lithic fragments from Units 2 and 3, are mainly grey and light-brown in colour, dense to low-vesicular. A single yellow-brown clast from Unit 1 is characterised by brown smectitic alteration of glassy groundmass, which is different to the iddingsite reddish-brown alteration, observed in Unit 1 fragments from subcluster A2b.

Samples from subcluster B2 contain the highest K_2O and SiO_2 concentrations, elevated TiO_2 contents and the lowermost contents of MgO, Na_2O and Fe_2O_3. These samples comprise one dark-grey low-vesicular basalt from Unit 3 and two dark-red-brown fragments from Unit 1, lithic and juvenile in composition (Figure 3d). Lithic clast from Unit 1 contains a number of large vesicles (up to several mm), filled with light-grey carbonates and yellow-brown clay minerals.

4.3.4 Trace element geochemistry

Primitive mantle normalised trace element patterns for samples from the volcaniclastic deposits are shown in Figures 4.5 and 4.6. Absolute trace element concentrations in the studied samples are distinctly higher than those in the U1349-type lavas that underlie the volcaniclastic deposits at Site U1349 (Sano et al., 2012). Trace element patterns for samples from this study lay in the field between average compositions for N-MORB and Earthwatch seamount. Samples show positive anomalies in Rb, U, Cs and Ba and negative anomalies in Pb and Sr. Europium anomaly is either not observed or slightly negative (0.71-1.09), as in the previously published data from Shatsky Rise (Sano et al., 2012). Exceptions include sample 12a with positive spikes in Sr and Eu and sample 12b with positive anomalies in Pb as well as Zr, Hf and Ti.

Most of the samples, representing all three Units and subclusters A1b, A2b, B2 and partly B1, are very similar to the Normal type trace element compositions from Shatsky Rise. Normal type samples from this study show reasonably flat trace element patterns with $(Gd/Lu)_N$ = 1.07-1.73 (subscript N denotes primitive mantle normalisation after Sun and McDonough (1989)), and their absolute REE concentrations total 47-116 ppm. Most of the Normal type compositions display positive spikes in Ti, Zr and Hf, comparatively to the Light REE (LREE).

The remaining samples correspond to all three Units and subclusters A1a, A2a and B1. These samples are distinguished by relatively steeper slopes in the HREE, $(Gd/Lu)_N$ = 1.53-2.67, demonstrate larger variations in the total REE contents (50-192 ppm) along with Y (29-130 ppm), P_2O_5 (0.2-1 wt.%) and TiO_2 (1.4-3.9 wt.%), which is consistent with compositions from the Earthwatch Seamount and Seamount 6 (Tejada et al., 2016). Overall, such compositions are relatively more fractionated, as compared to the Normal type and show slightly humped-back patterns and usually possess negative Ti anomalies. A small number of samples, mainly from subcluster A2a, are distinguished by elevated REE, including Y, and relatively lower Ba, Th, Nb, Ta, Zr, Hf and Ti contents that overlap with the Normal-type field (Figure 4.6a).

Samples from the volcaniclastic deposit demonstrate wide variations in Zr/Ti (0.007-0.018), Nb/Ti (0.0002-0.0007) and Nb/Sc (0.05-0.45). Most of the samples from this study plot within the field between the Normal and U1349 types on classification diagrams from Sano et al. (2012) (Figure 4.7a and b).

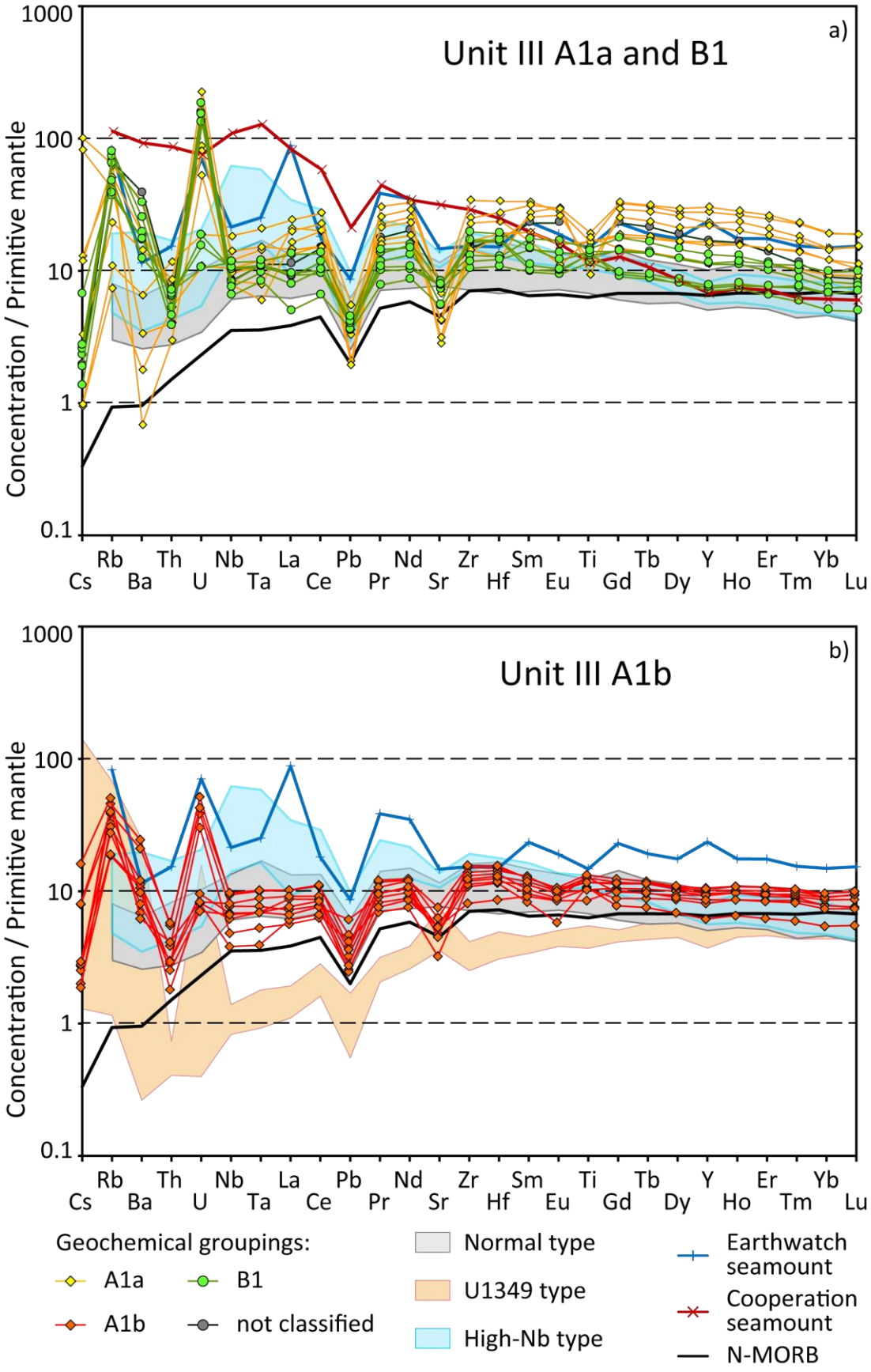

Figure 4.5. Primitive-mantle-normalised incompatible trace element concentrations for fragments from Unit III.

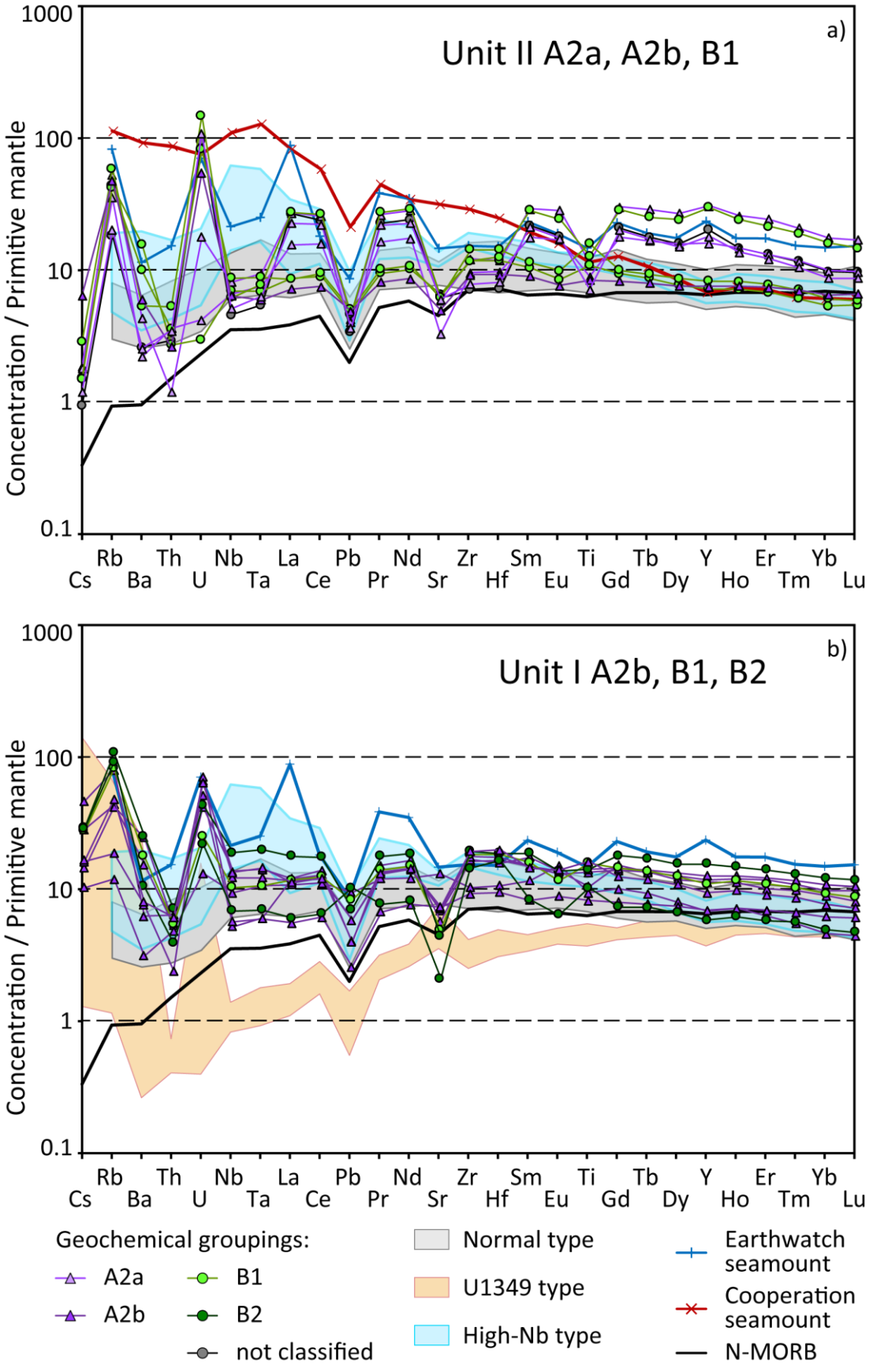

Figure 4.6. Primitive-mantle-normalised incompatible trace element concentrations for fragments from Units II (a) and I (b).

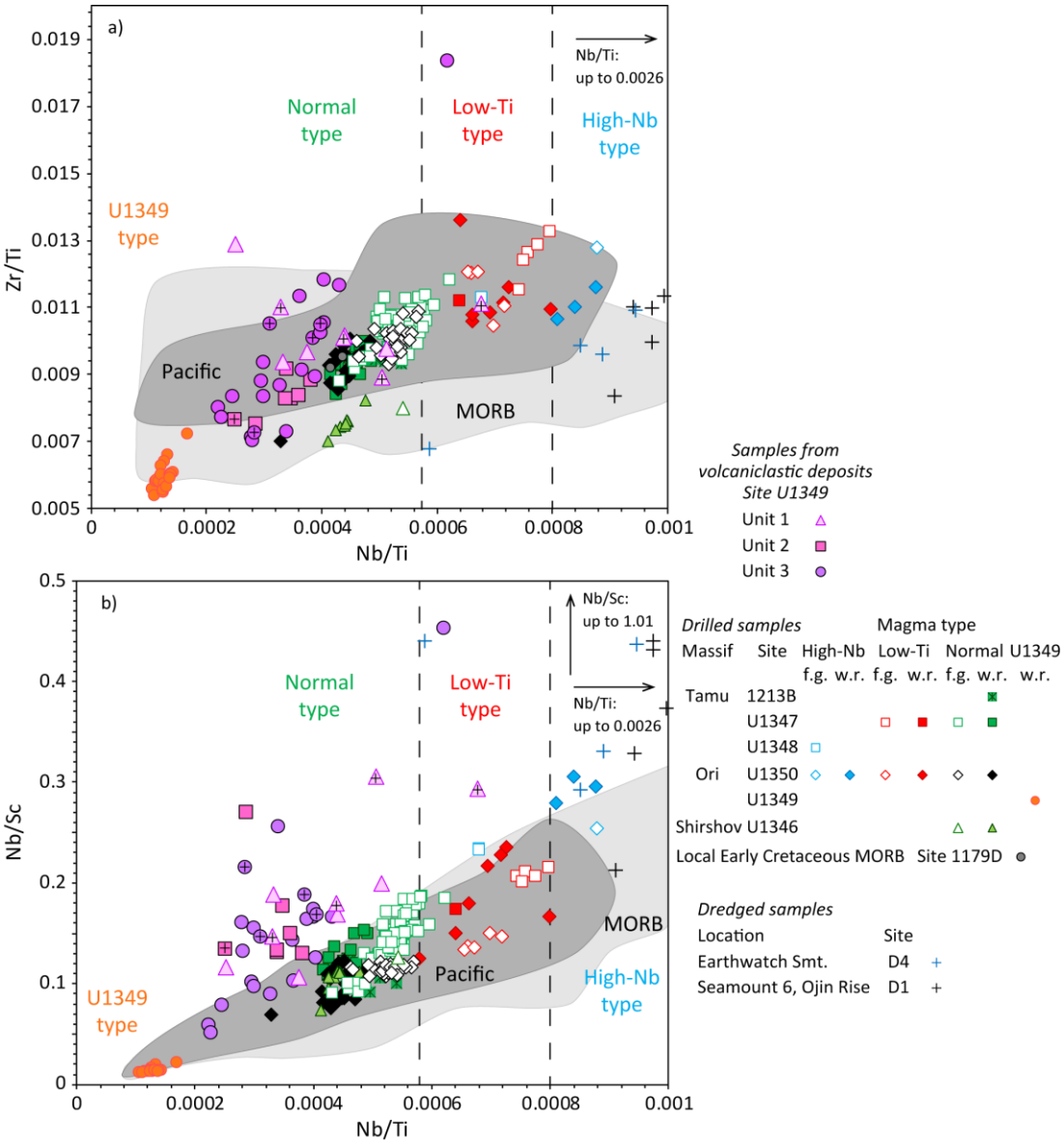

Figure 4.7. Trace element compositions from this study on classification plots from Sano et al. (2012). Samples used for Hf-Nd studies are marked with crosses. Samples from Cooperation seamount plot outside of the diagram boundaries, with compositions ranging for Nb/Ti from 0.004 to 0.007, for Nb/Sc from 2.5 to 3.5, for Zr/Ti from 0.18 to 0.3. Additional data as in Figure 4.2.

Notes to Figures 4.5 and 4.6 (previous pages). Samples are compared to compositions from N-MORB (Sun & McDonough, 1989) and average compositions from Earthwatch and Cooperation seamounts (Tejada et al., 2016). Average trace element compositions from Seamount 6, Ojin Rise, are almost indistinguishable from Earthwatch seamount. Also shown are fields for magma types from Shatsky Rise after Sano et al. (2012): Normal and High-Nb (both are based on fresh glass data) and U1349 (based on whole-rock data). Trace element patterns for Low-Ti fresh glass compositions from Sano et al. (2012) are subparallel to those of the Normal type and not included in these Figures.

4.3.5 Nd and Hf isotope geochemistry

Nd and Hf isotope data for the selected basaltic fragments, representing all three Units, are reported in Tables 4.2 and 4.3. Basalts, excluding sample 12a from Unit 1, show a restricted range of Nd-Hf isotope compositions (εHf_t = 16.9-18; εNd_t = 10.2-10.8) and plot within the mantle array and the most radiogenic compositions for MORB from Pacific (Figure 4.8). Such εHf_t values are the most radiogenic (depleted) compositions among samples from Shatsky Rise, where εHf_t varies from 10.5 to 15.7 (Mahoney et al., 2005; Heydolph et al., 2014). Meanwhile, εNd_t values for samples from this study overlap with those for the U1349 type lavas from Shatsky Rise and the local, Early Cretaceous MORB from Site 1179. One sample (12a) is characterised by relatively lower εHf_t 13.3 and εNd_t 8.9, plotting in the field of Normal type basalts from Tamu and Ori Massifs.

Table 4.2. New measured and age corrected to 140 Ma Nd isotopic compositions.

Sample	Group	Core section	Depth (mbsf)	Sm (ppm)	Nd (ppm)	$^{147}Sm/^{144}Nd$	$^{143}Nd/^{144}Nd_m$	±2σ	$^{143}Nd/^{144}Nd$ (140 Ma)	εNd (140 Ma)
1a	A1a	5R1 13-15	144.95	6.69	20.5	0.205	0.513173	(3)	0.512985	10.4
2a	A1a	5R1 30-32	145.12	12.6	36.0	0.222	0.513204	(2)	0.513001	10.8
2d	B1	5R1 30-32	145.12	7.01	19.5	0.226	0.513193	(3)	0.512986	10.4
2j		5R1 30-32	145.12	9.30	25.3	0.231	0.513185	(2)	0.512973	10.2
3b	B1	5R1 41-42	145.23	4.08	12.8	0.201	0.513165	(3)	0.512981	10.3
7a	B1	6R1 56-59	155.06	11.4	35.7	0.201	0.513168	(3)	0.512984	10.4
8c		6R1 88-93	155.38	8.69	29.6	0.185	0.513163	(3)	0.512994	10.6
10d	A2b	7R1 51-53	164.61	5.91	17.9	0.208	0.513188	(3)	0.512997	10.7
11	B2	7R1 65-68	164.75	7.60	23.3	0.205	0.513165	(3)	0.512977	10.3
11*	B2	7R1 65-68	164.75	7.60	23.3	0.205	0.513154	(3)	0.512966	10.1
12a	A2b	7R1 80-83	164.90	4.75	15.2	0.197	0.513088	(3)	0.512908	8.9
12b	B2	7R1 80-83	164.90	3.40	10.2	0.210	0.513186	(2)	0.512994	10.6

Table 4.3. New measured and age corrected to 140 Ma Hf isotopic compositions.

Sample	Group	Core section	Depth (mbsf)	Lu (ppm)	Hf (ppm)	$^{176}Lu/^{177}Hf$	$^{176}Lu/^{177}Hf_m$	±2σ	$^{176}Lu/^{177}Hf$ (140 Ma)	εHf (140 Ma)
1a	A1a	5R1 13-15	144.95	0.61	6.6	0.013	0.283210	(6)	0.283176	17.0
2a	A1a	5R1 30-32	145.12	1.26	7.7	0.023	0.283246	(6)	0.283187	17.3
2d	B1	5R1 30-32	145.12	0.54	3.6	0.021	0.283230	(8)	0.283176	16.9
2j		5R1 30-32	145.12	0.58	5.0	0.016	0.283236	(6)	0.283194	17.6
3b	B1	5R1 41-42	145.23	0.47	4.7	0.014	0.283225	(8)	0.283188	17.4
7a	B1	6R1 56-59	155.06	0.98	3.5	0.039	0.283284	(6)	0.283183	17.2
10d	A2b	7R1 51-53	164.61	0.49	5.6	0.012	0.283229	(6)	0.283197	17.7
11	B2	7R1 65-68	164.75	0.79	5.3	0.021	0.283236	(6)	0.283182	17.1
11*	B2	7R1 65-68	164.75	0.79	5.3	0.021	0.283234	(8)	0.283180	17.1
12a	A2b	7R1 80-83	164.90	0.30	3.0	0.014	0.283110	(7)	0.283074	13.3
12b	B2	7R1 80-83	164.90	0.32	4.7	0.009	0.283231	(6)	0.283206	18.0

*duplicate analyses

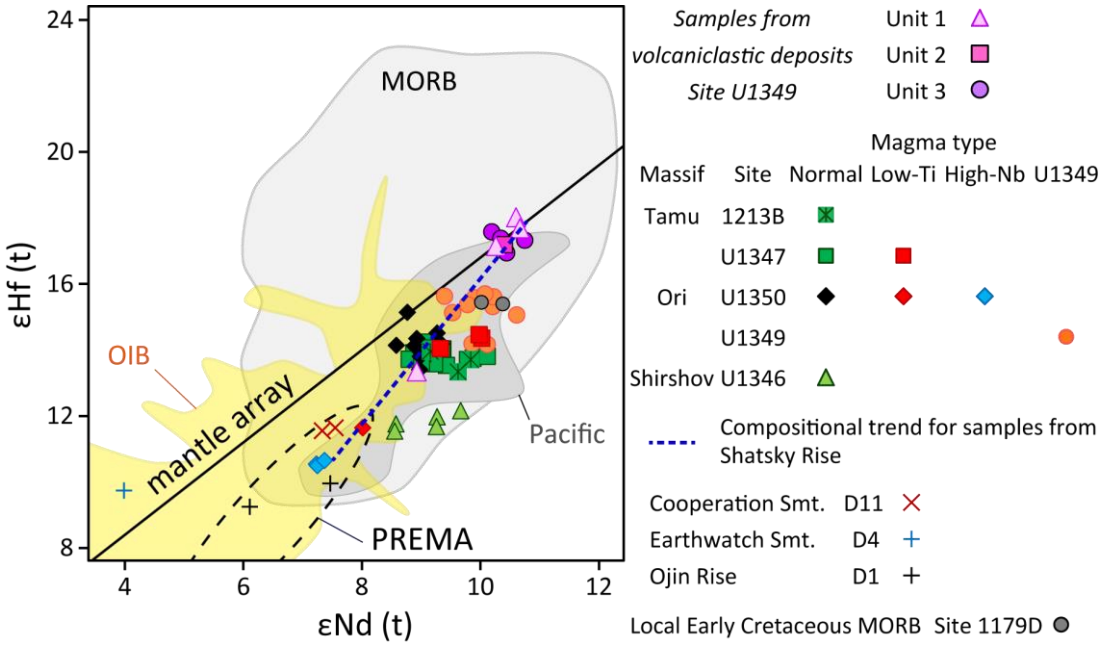

Figure 4.8. Plots of initial εNd(t) vs. initial εHf(t) for basalts from volcaniclastic deposits, Ori Massif. Additional compositions for Shatsky Rise, Seamount 6 (Ojin Rise), Earthwatch and Cooperation seamounts are from Mahoney et al., (2005), Heydolph et al., (2014), Tejada et al. (2016). All data were recalculated according to the inferred time of emplacement, as in the data source: Shatsky Rise (140 Ma), Seamount 6 (120 Ma), Earthwatch (120 Ma) and Cooperation (122 Ma) seamounts. Compositions for the local MORB, Site 1179, are from (Mahoney et al., 2005; Heydolph et al., 2014) and recalculated to 129 Ma. Data for MORB and OIB are plotted using data compilation after Stracke (2012), excluding MORB data from transform faults and MORB mixed with enriched material. Also shown PREMA (FOZO) field after Stracke et al. (2005). Fields for MORB, OIB and PREMA have been corrected for radiogenic ingrowth over 140 Ma assuming $^{147}Sm/^{144}Nd = 0.25$ and $^{176}Lu/^{177}Hf = 0.04$ (MORB), $^{147}Sm/^{144}Nd = 0.2$ and $^{176}Lu/^{177}Hf = 0.03$ (OIB), $^{147}Sm/^{144}Nd = 0.1$ and $^{176}Lu/^{177}Hf = 0.005$ (PREMA). Mantle array is defined by $\varepsilon Hf = 1.4\varepsilon Nd + 2.8$ (Geldmacher et al., 2003). Blue dashed line identifies trend for Shatsky Rise compositions.

4.4 DISCUSSION

4.4.1 Influence of seawater alteration and primary magmatic signatures

Petrographical and geochemical investigations reveal significant alteration of basaltic samples from volcaniclastic deposits, Ori Massif. Alteration affected the colour of basaltic fragments and resulted in replacement of glass and primary minerals by secondary minerals, including clay minerals, carbonates, iddingsite, celadonite and zeolites. Geochemically, the alteration caused elevated LOI, broad variations in major element compositions and uptake of the fluid-mobile trace elements (LILE: Rb, U, Cs

and Ba), which is typical to seawater-related alteration of basalts from oceanic crust (Alt & Teagle, 2003; Bach et al., 2003; Schramm et al., 2005; Zhang & Smith-Duque, 2014). Nevertheless, the intensity of seawater alteration on basalts from this study is considerably higher than that observed in the magmatic rocks from pillow lavas and lava flows at Shatsky Rise (Chapter 5; Sager et al., 2010; Sano et al., 2012). Such intense alteration is interpreted as a result of interaction of steaming seawater with quenched juvenile and wall-rock fragments during phreatomagmatic activity and subsequent cementation of volcaniclastic material in subaqueous environments.

4.5.1.1 Major element chemistry

High potassium enrichments in samples from this study are associated with the development of secondary K-enriched phyllosilicates, such as celadonite (Alt & Teagle, 2003; Benzerara et al., 2007), iddingsite and illite, observed in the underlying lavas (Delacour & Guillaume, 2013). Most of the basaltic fragments experienced leaching of CaO, which most probably entered the crystal structure of carbonate minerals during carbonate cementation of the volcaniclastic deposits. Removal of CaO in some samples, containing unaltered plagioclase, was less intense. Gain of CaO is observed in samples from Unit 2 and is explained by the presence of secondary carbonates in the alteration haloes.

Despite high variability in most of the major element concentrations from investigated samples, concentrations of immobile major element oxides, TiO_2, Al_2O_3 and P_2O_5 are considered as relatively unaltered. Measured P_2O_5 contents are significantly lower than those in the dredged samples from Shatsky Rise and seamounts obtained during Cruise TN037, where P_2O_5 reaches several wt.% as a result of intense secondary phosphorization (Tatsumi et al., 1998). Contents of Al_2O_3 and P_2O_5 in the investigated samples are typical to the igneous rocks from Shatsky Rise (Sano et al., 2012; Husen et al., 2013). Nevertheless, TiO_2 contents in the basaltic fragments are generally higher than those from other parts of Shatsky Rise (Sano et al., 2012; Husen et al., 2013), but are comparable to basalts from seamounts nearby this oceanic plateau (Tatsumi et al., 1998). On Al_2O_3/TiO_2 versus Al_2O_3/ P_2O_5 plot, basalts from the volcaniclastic deposits form a trend (Figure 4.3), starting from relatively evolved compositions of Low-Ti, High-Nb and Normal magma types at Ori Massif (Sano et al., 2012; Husen et al., 2013), within the MORB field, and continuing towards the most evolved compositions, represented by Cooperation, Earthwatch and

Victoria Seamounts, Seamount 6 and Toronto Ridge, located within the boundaries of Shatsky Rise (Tatsumi et al., 1998).

4.5.1.1 Trace element chemistry

Trace element compositions for samples from this study show rather weak correlation with major element mobility, apart from TiO_2 and P_2O_5. Multielement patterns for most of the investigated basalts, excluding LILE, are indistinguishable from previously documented Normal type trace element compositions of fresh glasses from Shatsky Rise (Sano et al., 2012) (Figures 4.5 and 4.6). Therefore, the Normal type trace element compositions, excluding fluid-mobile elements, are considered as unaltered. Only one sample from B2 subcluster stands apart by positive spikes in Pb, Zr, Hf and Ti as well as higher K_2O contents, which is interpreted as a result of more intense hydrothermal alteration involving REE leaching and probably supply of metal components (Figure 4.6b).

The remaining samples show variable enrichments of REE, Y, P_2O_5 and TiO_2. High concentrations of P_2O_5, REE and Y in basalts from oceanic crust, including oceanic islands, seamounts and oceanic plateaus, are often related to precipitation of Mn-rich Fe-oxyhydroxides, palagonisation, phosphorisation, carbonatisation and zeolitisation (Bienvenu et al., 1990; Cotten et al., 1995; Pichler et al., 1999; Tejada et al., 2001; Wheat et al., 2002; Shafer et al., 2004; Kruber et al., 2008; Vanderkluysen et al., 2014; Tejada et al., 2016). Concentrations of REE in seawater are 10^4-10^6 times lower, than in basalts (Fleet, 1984), and therefore simple basalt-seawater interaction cannot lead to the REE enrichments in basalts. To explain the elevated REE, it was suggested that basalts may absorb some REE from seawater at low temperatures, provided the REE are bound into water-soluble carbonate complexes (Cantrell & Byrne, 1987; Pichler et al., 1999). Meanwhile, Cotten et al. (1995) recognised the REE and Y enrichments in subaerial basalts through formation of the rhabdophane-type REE-Y-phosphates. Seawater-related alteration processes involve preferential enrichment of LREE over HREE in the altered rocks, along with anomalous behaviour for Ce and Eu: Ce (IV) is selectively absorbed during formation of Fe-Mn oxyhydroxides (Hein et al., 1993; Pichler et al., 1999; Hein et al., 2012), whereas phosphorisation and carbonatisation show relative depletion in Ce and Eu, due to insolubility of oxidised Ce (IV) and Eu (III) in seawater and meteoric water (Piper, 1974; Ludden & Thompson, 1979; Owen & Olivarez, 1988; Cotten et al., 1995; Wheat

et al., 2002). However, basalts from this study do not show any significant Ce and Eu anomalies, along with LREE enrichments over HREE, whereas concentrations of CaO, MnO, Fe_2O_3 and P_2O_5, are comparable or lower than those in the fresh basaltic glasses from Shatsky Rise (Sano et al., 2012) along with the dredged samples from this plateau (Tatsumi et al., 1998) and Pacific seamounts (e.g., Hikurangi seamounts, Hoernle et al., 2010; Louisville Seamount Chain, Vanderkluysen et al., 2014; Earthwatch Seamount and Seamount 6, Tejada et al., 2016). Furthermore, analysis of trace element data from these seamounts does not reveal strong proportional increase of the REE and Y with P_2O_5 or CaO contents, implying a combination of the alteration and primary-magmatic processes.

Hafnium and Neodymium isotopes represent the most alteration-resistant systems and also provide the greatest potential for detecting mantle sources (Salters & White, 1998; Pearce et al., 1999; Kempton et al., 2002; Thompson et al., 2008). Considering the Hf-Nd isotope compositions for samples from this study fall in a tight range, the Sm-Nd and Lu-Hf systematics were unlikely affected by alteration and the REE enrichments in basalts may be of primary-magmatic genesis. The elevated concentrations of REE, Y and P_2O_5, along with variable enrichments in Ba, Th, Nb, Ta, Zr, Hf, Ti, Na and relatively steeper HREE slopes in basalts from volcaniclastic deposits are probably related to a complex interplay of variable degrees of partial melting and fractional crystallisation with melting started in the presence of garnet.

4.4.2 Geochemical variety of basalts from volcaniclastic deposits

Samples from volcaniclastic deposits demonstrate Zr/Ti, Nb/Ti and Nb/Sc ratios that are transitional between the Normal and U1349 types (Figure 4.7a and b). Samples, especially from subclusters A1b and A2b, are brown and red-brown in colour and show iddingsite alteration, similar to the underlying U1349 type lavas (Sager et al., 2010; Delacour & Guillaume, 2013). In such samples, ratios of Al_2O_3/TiO_2 and Al_2O_3/ P_2O_5 are higher (Figures 4.3a) and Zr/Ti, Nb/Ti and Nb/Sc are somewhat lower, relatively to the rest of the investigated samples, and closer towards the compositional field of the U1349 type lavas. Nevertheless, the compositional range of Al_2O_3/TiO_2 and Al_2O_3/ P_2O_5 and the multielement patterns for all samples are more consistent with the Normal type.

Presence of clasts from different compositional subclusters and with variable fractionation degrees within the same intervals of the volcaniclastic succession from

Site U1349 (Figure 4.4a and Figure 3.1 for sample location) suggests fragmentation of compositionally heterogeneous parts of a volcanic vent and juvenile magma during phreatomagmatic activity. Despite phreatomagmatic deposits are immediately underlain by ~90 m of basalts from the depleted U1349 type (Figure 4.1), no fragments with apparent U1349 type affinities were analysed in this study. Presence of fragments from Normal and intermediate U1349-Normal types in the deposits and absence of clear U1349 type basalts, indicate that the location of volcanic vent, where explosive eruptions took place, was at some distance from Site U1349. The underlying lavas and the basaltic fragments could have been produced by volcanic activities from different vents or some Normal-type lavas erupted in between the effusive and phreatomagmatic events. Nevertheless, no sedimentary layers are recovered in between the lavas and the volcaniclastic deposits at Site U1349, indicating that the explosive activity occurred soon after the effusive eruptions.

4.4.3 Geochemical variety of magmas at Ori Massif

New data provide evidence for chemical heterogeneities of magmatic sources during the late stages of Ori Massif construction. Previously, only U1349 type lavas were recognised at Site U1349 (Sager et al., 2010; Sano et al., 2012; Heydolph et al., 2014), and volcaniclastic deposits demonstrate a significant contribution of the Normal type and transitional Normal-U1349 type basalts at this Site. Alternation of magmatic rocks with different geochemistry and variable fractionation degree is also observed in other part of Ori Massif (Figure 4.1). At Site U1350, the High-Nb type lavas intercalate with basalts from the Low-Ti and Normal types (Sano et al., 2012). Such alternation provides evidence for changes in chemistry of magmas from “enriched” to “depleted” melts during Ori Massif formation. The successive magmatic cycles with possible magma mingling were previously suggested for Shatsky Rise and Ontong Java plateau (Michael, 1999; Husen et al., 2013). Husen et al. (2013; 2016) assumed that two interconnected magma chambers (deep, at 14 km, and shallow, at 3 km) are present at Ori Massif, which allowed significant fractional crystallization processes and magma mingling during replenishing of magmas.

Overall, basalts from Ori Massif demonstrate a wide range in major and trace element compositions from the most depleted MORB compositions, defined by depleted olivine-rich basalts of U1349 type, to the most evolved and enriched compositions of High-Nb type. The compositional heterogeneities are also suggested

from isotope geochemistry. The majority of the new Hf-Nd isotope data shows systematically higher εHf_t and εNd_t, in comparison to the previously published data for basalts from Ori Massif (Heydolph et al., 2014), indicating presence of either a more depleted MORB mantle component or a depleted plume component in the source chemistry of Ori magmas than previously thought (Figure 4.8). The difference in the Hf-Nd isotope geochemistry between the Normal type and transitional Normal-U1349 type basalts from this study and the previously documented Normal and U1349 type basalts indicate the existence of similar melting conditions for mantle regions with variable isotopic signatures. The new data are consistent with compositional trend for basalts from Ori Massif, extending from the most depleted Pacific MORB compositions towards more enriched values within the PREvalent MAntle (PREMA) field. These results imply variable mixing degrees of magmas from the common depleted MORB source with minor enriched component, potentially PREMA (or HIMU; Heydolph et al., 2014), during formation of the Ori Massif.

4.5 SUMMARY OF THE KEY FINDINGS

This study investigated basaltic fragments from the volcaniclastic deposits from Site U1349, located near the summit of Ori Massif. Results from this study enlarge our understanding into mantle source heterogeneities at Ori Massif.

- Basaltic fragments from the volcaniclastic deposits are variably altered due to intense interaction with steamed seawater during phreatomagmatic activity and subsequent cementation of volcaniclastic material in subaqueous conditions.
- Most of the basaltic fragments show considerable CaO leaching and gain of fluid-mobile elements (K_2O, Rb, Cs, U, Ba), but despite seawater alteration Al_2O_3, TiO_2, P_2O_5 and most of the trace elements remain relatively unaltered.
- Basaltic fragments demonstrate Normal-type and transitional Normal-U1349 type affinities.
- No fragments with apparent U1349 type affinities were identified, indicating change in chemical composition of magma during final stages of Ori Massif formation.
- The Hf-Nd isotope compositions of basalts from this study indicate a relatively more depleted Pacific MORB component in the compositional variety of volcanic products from Ori Massif.

Chapter 5: Quantitative evaluation of element mobility during seawater alteration of basalts from Ori and Tamu Massifs

5.1 INTRODUCTION

The physical and chemical properties of oceanic crust are significantly affected by hydrothermal processes, seawater and marine microbial life that result in element migration and redistribution (Staudigel et al., 1996; Wheat et al., 2002; Alt & Teagle, 2003; Schramm et al., 2005; Santelli et al., 2009; Bach & Früh-Green, 2010). Element enrichment and depletion within the oceanic crust have relevance to compositional changes in the mantle and related systems. The subducting oceanic crust devolatilizes, fluxing hydrophyllic and incompatible elements into the overlying mantle wedge and into the ocean (Seyfried et al., 1978; Staudigel, 2003; Bach & Früh-Green, 2010; Guillot & Hattori, 2013).

Chemical modification can occur soon after crust formation as a result of hydrothermal activity at MORs with fluid contributions principally from seawater and supplemented by exsolved magmatic fluids (Alt, 1995). Cold seawater can percolate through the newly generated, still-warm but jointed oceanic crust, heating up at depth, chemically reacting with basaltic glass and minerals susceptible to fluid alteration and then rises producing exhalative vents on the seafloor, and sometimes black smokers rich in ore minerals (German & Von Damm, 2003; Staudigel et al., 2004; McCaig et al., 2007). This high-temperature (up to 400ºC), but relatively short-lived alteration contrasts with protracted cool-temperature (<100ºC) seawater-driven alteration of the uppermost crust while in transit from the MOR to the trench (Stein & Stein, 1994; Alt, 1995). Many studies have revealed that the upper oceanic crust becomes oxidized and hydrated with age, where the crust becomes enriched in fluid mobile elements such as K, Rb, Cs, Ba, Li, B, U, while a substantial redistribution of major elements (Mg, Ca, Fe, Mn, Na, Si) also occurs (Seyfried & Mottl, 1982; Alt, 1995; Staudigel et al., 1996; Gillis et al., 2001; Alt & Teagle, 2003; Staudigel, 2003; Walton et al., 2005). Despite this chemical modification, the bulk composition of oceanic crust remains basaltic.

Oceanic plateaus have been a key target for geochemical studies aiming to constrain mantle source regions, mantle dynamics and potential plume origins for LIPs (Richards et al., 1989; Ernst & Buchan, 2003; Campbell, 2005; Kerr & Mahoney, 2007; Bryan & Ferrari, 2013). However, comparatively few studies have detailed alteration of basalts from these volcanic structures (Clayton & Pearce, 2000; Banerjee et al., 2004; Benzerara et al., 2007), largely because drilling on oceanic plateaus is limited and the focus on unaltered samples for petrogenetic and mantle source investigations. In terms of hydrothermal alteration of oceanic crust, these forms of intraplate magmatism may provide additional mechanisms to drive high-temperature hydrothermal alteration of oceanic crust and submarine basaltic rocks.

Shatsky Rise is a strategically significant place to study, because it is the oldest non-accreted oceanic plateau (~145 Ma) residing in the north west Pacific, and therefore has the potential to record a protracted alteration history. Importantly, previous investigations revealed a significant variation in alteration style and intensity in basalts (Chapter 2.2.8) and volcaniclastic deposits (Chapter 4) from Shatsky Rise. This study investigated the nature and degree of alteration and element mobility in two volcanic successions (IODP Sites U1347 and U1350) recovered from flanks of the two largest Tamu and Ori Massifs at Shatsky Rise. These two successions preserved fresh glass fragments at multiple horizons (see Figure 2 from Sano et al. (2012) and, therefore, allow for a quantitative geochemical comparison with the altered pillow and sheet flow interiors from the same eruptive units. Basaltic material from Sites U1347 and U1350 shows variation in magma types, thereby allowing a test of whether the original composition has an influence on chemistry of alteration.

5.2 SAMPLE CHARACTERISATION

5.2.1 Stratigraphy

Among the six drill cores available at Shatsky Rise, Sites U1347 and U1350 represent the thickest basaltic successions (159.9-172.7 m; Figure 5.1) and are where the freshest basaltic material was also recovered (Sano et al., 2012). Sites U1347 and U1350 are located on the flanks of the Tamu and Ori Massifs, respectively. Sheet flow and pillow lava units at Sites U1347 and U1350 often display well-preserved upper and lower chilled contact zones as well as flow top, core and basal sections with characteristic vesicularity downgrading towards the cores (Sager et al., 2010).

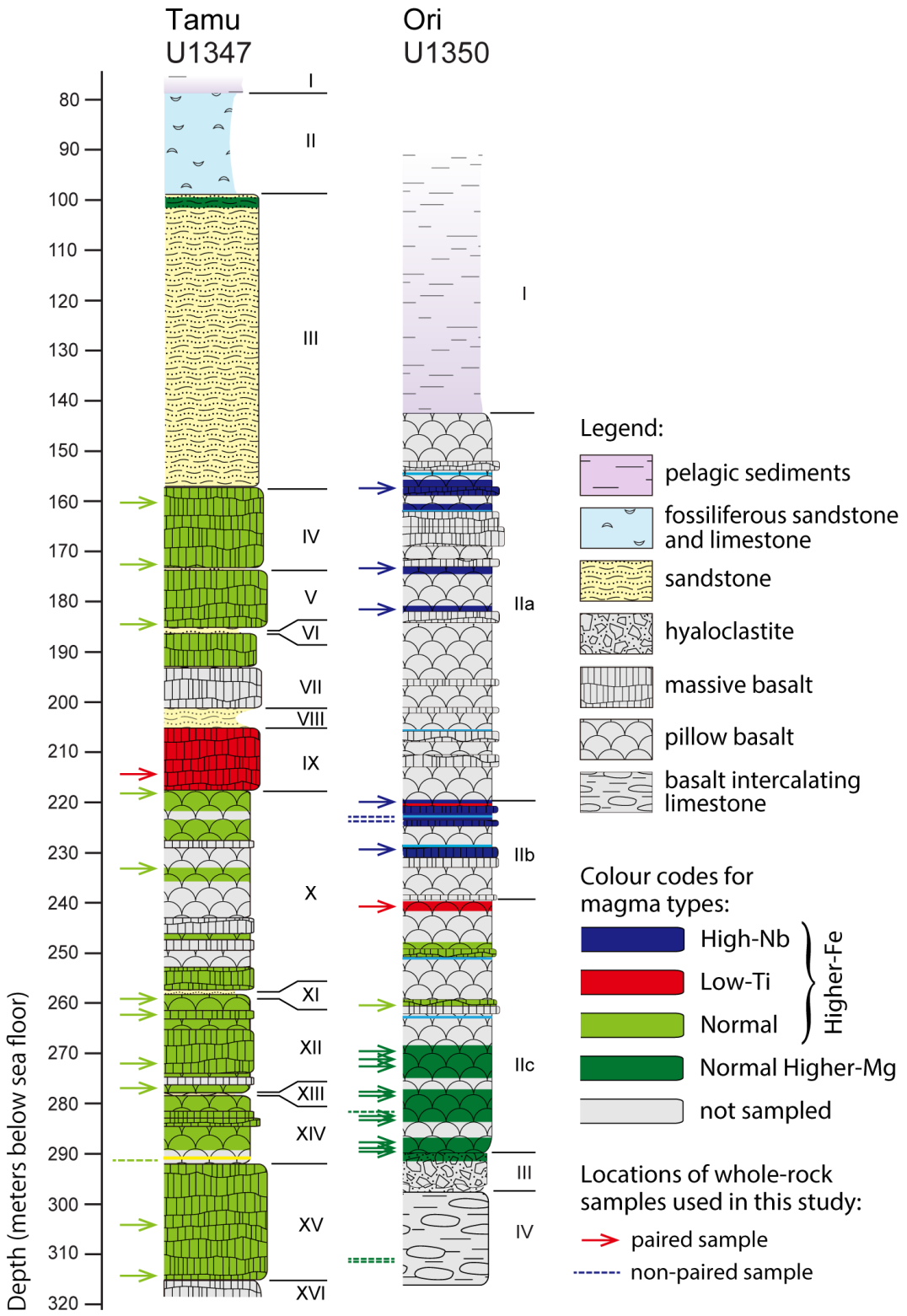

Figure 5.1. Stratigraphic summary of Sites U1347 and U1350 with locations of whole-rock samples from this study. “Paired” samples are found within lithological units that contain fresh glass, and “non-paired” samples are from those units with no fresh glass analysed. Individual lava flows and pillow lavas containing fresh glass are colored according to magma types after Sano et al. (2012) with subdivision into Higher-Fe and Higher-Mg tholeiites. Roman numbers indicate stratigraphic units as from Sager et al. (2010). Modified from Figure 4.1. See Appendices B and C for more details.

The volcanic succession at Site U1350 is largely formed by pillow lavas, with occasional thin sheet lava flows (Figure 5.1). The lowermost recovered igneous rocks at Site U1350 are composed of brecciated and calcite cemented pillow basalt (stratigraphic unit III) and pillow lavas with intercalated carbonate sediment (stratigraphic unit IV). The observed thickness (up to 22 m) of individual lava flows at Site U1347 is higher than that at Site U1350 as well as the proportion of sheet flow to pillow lava units.

Basalts from Sites U1347 and U1350 are tholeiitic, varying in grain size, phenocryst shape and crystallinity. Phenocrysts, if present, comprise plagioclase, clinopyroxene and olivine. Olivine is rare and where present, is completely replaced with clay minerals or calcite. Groundmass mineralogy includes plagioclase, clinopyroxene and titanomagnetite. Common alteration mineralogy replacing primary minerals and filling vesicles, voids and veins are smectite clays, calcite, opaque minerals (e.g., Fe-oxyhydroxydes, pyrite) as well as zeolites and rare chlorite. Usually, the groundmass glass is entirely altered to clay. Fresh glass is observed in multiple sections from both U1347 and U1350 cores, though no fresh glass was recovered from stratigraphic unit IV at U1350. Overall, samples from Sites U1347 and U1350 are low to moderately altered (Sager et al., 2010).

5.2.2 Geochemistry

Samples from Site U1347 are mostly formed by Normal-type magmas with a minor addition of Low-Ti types, whereas samples from Site U1350 represent a range of Normal, Low-Ti and High-Nb lava types (Figures 5.1-5.3). In addition to magmatic types introduced by Sano et al. (2012), lava flows can be subdivided based on their degree of fractionation (Husen et al., 2013; Husen et al., 2016). The most primitive fresh glass compositions form a tight cluster with elevated MgO (8.06-8.56 wt. %) and are High-Mg olivine tholeiites of Normal-type found within the lower ~20 meters of stratigraphic unit IIc in U1350 (Figures 5.1-5.3). The rest of the fresh glass samples recovered from pillow or sheet flow margins from the Ori and Tamu Massifs are High-Fe quartz tholeiites and represent more evolved basaltic compositions (5.43-6.81 wt. % MgO). The change from least to most evolved compositions is accompanied by gradual decrease in MgO, CaO, Al_2O_3 and Sr and an increase in FeO and trace element contents (Figures 4.2, 5.2 and 5.3) (Husen et al., 2013). This represents differences in the fractionating assemblages and conditions from spinel-olivine- plagioclase-

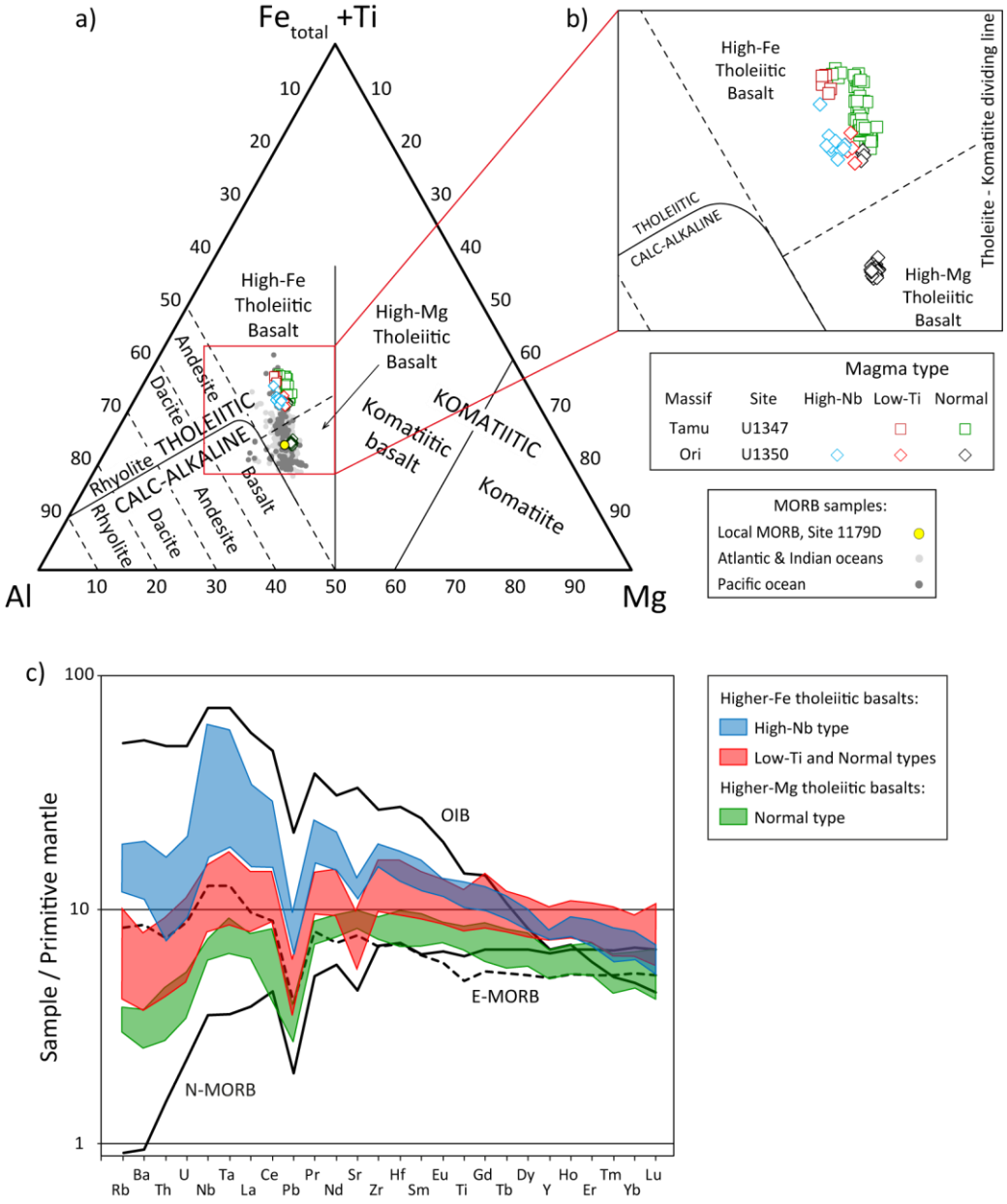

Figure 5.2. Shatsky Rise fresh glass compositions from pillow and sheet flow margins at Sites U1347 and U1350; data source: Sano et al. (2012). On a) Jensen Cation Plot, after Jensen and Pyke (1982), including fresh glass MORB compositions (only spreading ridge samples, 497 in total: Atlantic (276), Indian (37), Pacific (184), data from Jenner and O'Neill (2012)), and local MORB sample from Site 1179D, data from Mahoney et al. (2005); on b) expanded area of Jensen plot with sample subdivision into High-Fe and High-Mg tholeiite basalt groups; on c) multielement plot with comparison to average N-MORB, E-MORB and OIB compositions, after Sun and McDonough (1989); samples are normalised to primitive mantle compositions, after McDonough and Sun (1995). On a and b images, Shatsky Rise fresh glass data are labelled according to their magma type division (Normal, Low-Ti, High-Nb) as in Sano et al. (2012). On plot c) three compositional groups are shown: Higher-Fe tholeiite basalts of High-Nb type, Higher-Fe tholeiite basalts of Low-Ti and Normal types, and Higher-Mg tholeiite basalts of Normal type.

dominant to higher degrees of fractional crystallization (Arndt et al., 1993) with a greater proportion of plagioclase and clinopyroxene within the different plumbing systems associated with these groups (Husen et al., 2013). Hereafter, High- and Low-MgO Normal types are referred to as Higher-Mg and Higher-Fe tholeiites, respectively, to avoid confusion with High-Mg basalts (e.g., picrites). Therefore, three major compositional groups are identified: Higher-Fe tholeiite basalts of High-Nb type, Higher-Fe tholeiite basalts of Low-Ti and Normal types, and Higher-Mg tholeiite basalts of Normal type (Figure 5.2).

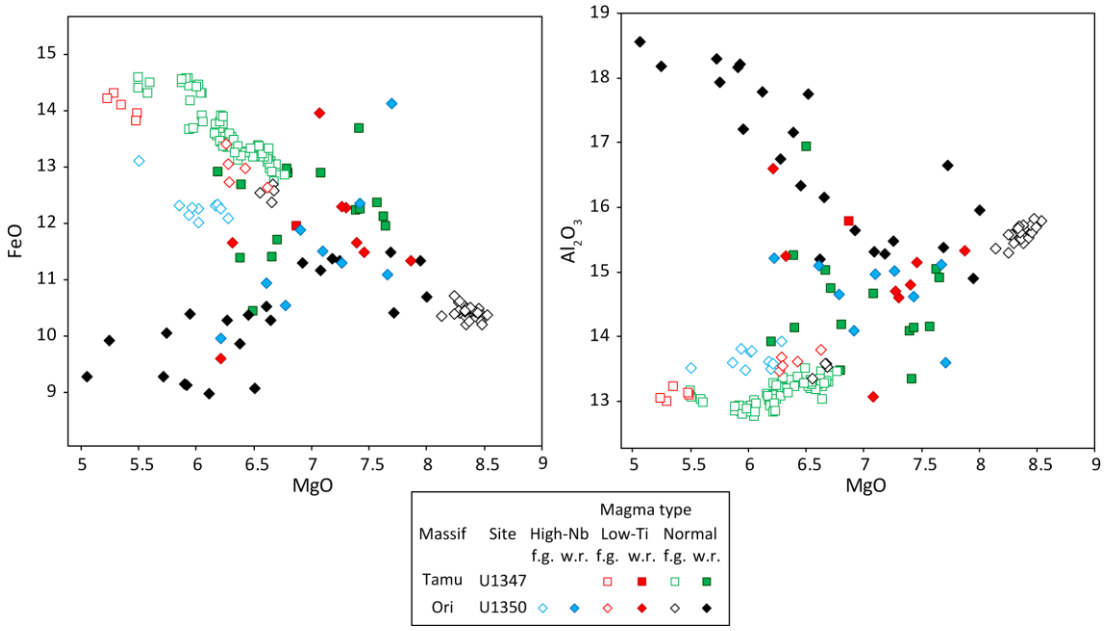

Figure 5.3. Plots of FeO and Al_2O_3 versus MgO for compositions from Sites U1347 and U1350, data source: Sano et al. (2012). Dataset represents stratigraphic units where both the fresh glass and whole rock compositions are available. This removes the samples from Unit III of U1347 and Unit IV of U1350.

The fresh glass samples are distributed throughout almost the entire stratigraphy of both U1347 and U1350 (Figure 5.1, also see Figure 2 from Sano et al. (2012)). The coherent geochemical trends obsevered in the fresh glass analysis are here interpreted to represent the full extent of magmatic geochemical variation in the pillow lava and sheet flow units from U1347 and U1350 that contain fresh glass, which excludes Unit IV of U1350 (Figure 5.3). The equivalent whole rock analyses from these units, however, do not demonstrate comparable geochemical trends. For example, the fresh glass samples from U1350 demonstrate a positive relationship between MgO and Al_2O_3 and a negative relationship between MgO and FeO, while the whole-rock

samples show the reverse relationship (Figure 5.3). This major discrepancy between the fresh glass analyses and the whole-rock analyses must relate to variation due to alteration. The alternative explanation, that the whole rock samples underwent very different magmatic fractionation to the fresh glass, is problematic.

5.3 RESEARCH METHODOLOGY AND ANALYTICAL TECHNIQUES

5.3.1 Data sources

This study examines fresh glass and whole-rock samples from Sites U1347 and U1350 drilled during IODP Exp. 324 and presents new petrographic and mineralogical data on the whole-rock samples (N=29) acquired by X-Ray Diffraction (XRD) for mineral and clay analyses. The geochemical data used here consist of major and trace element analyses published in Sano et al. (2012). Sano et al. (2012) used the freshest rocks from Shatsky Rise in their study to discuss the origin of the source. Fresh glass and whole-rock geochemical data are integrated with optical microscopy and XRD mineralogical analysis on the same altered whole-rock samples that were analysed in Sano et al. (2012) to assess the chemical effects of alteration on major and trace elements in the submarine basaltic rocks.

5.3.2 Whole-rock – fresh glass pair

To evaluate the chemical effect of seawater alteration on basaltic rocks and to quantify element mobility during alteration, an understanding of the primary composition prior to alteration is required. This is achieved by the preservation of fresh basaltic glass material at Shatsky Rise. One of a number of approaches developed in studies on basaltic alteration is a comparative analysis of fresh versus altered parts of individual samples or flows, i.e., lithological units (Humphris & Thompson, 1978; Bienvenu et al., 1990; Schramm et al., 2005; Walton et al., 2005; Zhang & Smith-Duque, 2014). Fresh glasses from Sites U1347 and U1350 represent quenched lava from the chilled margins of pillow lavas or sheet lavas. These glasses are used to represent original magmatic compositions for altered pillow and sheet flow interiors sampled as bulk rock. Importantly, the phenocryst abundances in both glass and whole-rock samples are very low, usually comprising less than 3 vol. % (Sager et al., 2010; Sano et al., 2012).

Sano et al. (2012) presented 125 analyses of fresh basaltic glass determined by electron microprobe (EPMA and LA-ICP-MS) and 99 analyses of whole-rock samples

measured by X-ray fluorescence and ICP-MS methods. Each sample location was reassessed using core images and descriptions from the IODP Exp. 324 database, from which I have identified 29 whole-rock – fresh-glass pairs from U1347 and U1350 where sampling was within 20 metres of each other and that they have been sampled from the same lithological unit. These pairs include both Higher-Mg and Higher-Fe tholeiites (Appendices B, C and Figure 5.1). Fresh glass and whole-rock sample pairs at U1350 (17 in total) are usually located within 50 cm from each other, because of the recovered core is mostly built by thin flows of less than 1 m thickness. In U1347, six pairs out of 12 are of thick lava flows where sample pairs may be several meters away from each other. Therefore, this study allows evaluating any influence of crystallinity, grain size and primary magmatic type on chemistry of alteration, examining alteration of interstitial glass versus primary minerals, assessing pillow lava versus sheet lava flow alteration, and comparing the alteration on Early-Cretaceous oceanic crust between the two largest Massifs at Shatsky Rise.

5.3.3 X-Ray Diffraction analyses

5.3.3.1 Mineral XRD analysis and quantitative phase assessment

X-Ray Diffraction (XRD) analysis was undertaken to identify secondary phases and also to assess the relative proportion of primary igneous and secondary alteration phases. Introduction of an internal standard (corundum) permits determination of the exact concentrations of each phase and the relative amount of non-diffracting phases (residue) (Chipera & Bish, 2013). Possible contributors to the residue are background, amorphous material such as fresh glass and disordered phases, organic material, unidentified phases in small quantities and clays. Fresh glass is found only in fragments from the lava flow or pillow margins and is not preserved in the interiors of lava flows or pillows. Organic material is not observed petrologically in the whole-rock basaltic samples (Sager et al., 2010). Here, most of the non-diffracting residual material in the whole-rock samples is considered as clay. Unfortunately, it is difficult to evaluate the concentrations of clay minerals precisely using the XRD due to the wide variations in structure and composition of these minerals. Consequently, the amount of clays is often under-estimated. Here, the amounts of clays are approximately estimated by subtraction of the other mineral phases from 100 wt.%.

Twenty-nine samples used by Sano et al. (2012) were analysed here for quantitative XRD phase analysis. This includes whole-rock powders from 23 paired

samples and, additionally, one sample from U1347 and five samples from U1350 were analysed to reveal more detailed alteration variation along the cores. One to two grams of powdered samples were mixed with ~10% of corundum internal standard. The mixtures of spiked rock powder were micronized with ethanol in agate mill for 6 minutes. XRD analysis was carried out using PANalytical X'Pert (MPD) diffractometer at QUT with a CuKα radiation. Phase identification was performed using X'Pert Highscore Plus (V3.0.5, PANalytical). Quantitative phase analysis was performed using TOPAS (V4.2, Bruker) with Rietveld refinement where the X-ray diffraction pattern is modelled by means of the crystal structures of the identified phases. The closest matches in the American Mineralogist reference pattern database were used to identify mineral species (Downs & Hall-Wallace, 2003).

5.3.3.2 Clay XRD analysis

A few grams of each sample were disintegrated manually in a mortar to prevent over-crushing. The derived mixture of rock fragments and powder was placed into sonicating bath in deionised water for 10 minutes. A drop of ammonia was added to the obtained solutions, and left for 5 minutes to settle. Afterwards, the upper layer was taken by pipette and placed on silicon glass slides to dry overnight. Oriented clay mounts were scanned following USGS clay identification procedures. The samples were analysed twice (air-dried and ethylene glycolated) on PANalytical X'Pert (MPD) diffractometer at Queensland University of Technology with a CoKα radiation. Clay identification included peak and d-spacing verification of both air dried and glycolated samples.

5.3.4 Defining a relative alteration metric

To quantify differences between fresh and altered samples, studies on metasomatic and metamorphic mass-volume balance changes commonly use Gresens (1967) equations and its modified version of isocon analysis, a graphic method introduced by Grant (2005). However, this method involves calculations of mass changes, which requires an assumption that some elements were immobile during alteration (for example, Al, Ti) and that the alteration was pervasive. In addition, problems associated with volume changes in basalts, such as lack of space, can be ignored, because of generally high porosity in basalts and fractures occurring after cooling.

Here I introduce a relative alteration (RA) parameter, which reflects the difference between each altered whole-rock sample and its fresh glass pair. Importantly, RA does not depend on either the magmatic type or the effect of fractional crystallisation. The parameter is calculated this way:

$RA_i = WR_i \times 100 / FG_i,$

where WR_i is the concentration of a component i in the altered rock; FG_i is the concentration of a component i in the fresh glass pair. The RA parameters (in %) are calculated for selected elements in each of the 29 whole-rock – fresh-glass pairs and used as a dataset for multivariate statistical analysis. Only those elements that were analysed in every sample pair are used: Si, Ti, Al, Fe, Mn, Mg, Ca, Na, K, P, V, Sc, Rb, Sr, Y, Zr, Nb, Ba, REE, Hf, Ta, Pb, Th, U.

5.3.5 Multivariate analysis

To assess seawater alteration-related element mobility, multivariate methods on the RA value for each element in the whole-rock – fresh-glass pairs were performed. All multivariate statistical analyses were processed using the software STATGRAPHICS Centurion XVI (StatPoint technologies, Inc. Version 16.2.04). Details on the method procedures are described in Chapter 4.2.4.

5.4 RESULTS

5.4.1 Igneous petrology

Investigated samples vary in crystallinity from almost holohyaline to holocrystalline (Figure 5.4; Appendices B and D). For the purpose of this study, the term “crystallinity” refers to the proportion of primary magmatic minerals both phenocrysts and groundmass to glass. Glassy margins of pillows or lavas are usually 1-3 cm thick, sparsely phyric and contain individual crystals or stellate intergrowths of plagioclase and clinopyroxene that increase in abundance inwards from the margins (Fig. 4a, Sager et al., 2010). Four major textural types are recognised in investigated samples from cores of lithological units, where types 1 and 2 are found only in Higher-Mg tholeiitic basalts with normative olivine (Site U1350 at depths below ~ 270 mbsf):

1. Textural type 1 samples are found within ~ 5 cm of pillow lava and massive lava sheet margins. These samples contain plagioclase and rare olivine phenocrysts set

in hypocrystalline felty-textured groundmass of plagioclase microlites (10-20 vol.%) (Figure 5.4b and c). Total crystallinity ranges between 50 to 60 vol.%.

2. Textural type 2 samples are sparsely plagioclase and olivine phyric and preserve well-crystallised, almost holocrystalline textures (>90 vol.% crystallinity). Individual phenocrysts and glomerocrysts are set in a network of plagioclase laths, dendritic subophitic clinopyroxene, euhedral olivine and interstitial Fe-Ti-oxides (Figure 5.4d and e). Least altered samples contain high amounts of clinopyroxene (28-37 wt.%) and the largest amounts of plagioclase (60-67 wt.%) as indicated by XRD analysis (Appendix B).

3. Textural type 3 samples occur within ~ 50 cm of pillow lava and massive lava sheet margins. Samples show well-preserved seriate or hiatal inequigranular texture and contain a large proportion of glomerocrysts (15-25 vol.%), where plagioclase and clinopyroxene show subophitic or radiate intergrowths and where present olivine is euhedral. Devitrified glass demonstrates variolitic texture, where the finest groundmass phases of plagioclase, clinopyroxene and titanomagnetite form bow-tie spherulites and dendrites (Figure 5.4f). Total crystallinity ranges from 75-90 vol.% in samples from U1347 and is 60 vol.% in samples from U1350. Samples from U1347 are distinct from the rest of the dataset by relatively higher proportions of clinopyroxene (31-40 wt.%) in their XRD compositions (Appendix B).

4. Textural type 4 samples are sparsely phyric quartz tholeiitic basalt from massive flow interiors showing intergranular to subophitic and intersertal textures. Samples from U1347 are located > 1 m away from margins and contain coarser groundmass minerals (Figure 5.4g). Both grain size of groundmass minerals and crystallinity (65-75 vol.%) increase towards lower contacts of each lithological unit. Samples from U1350 are generally finer grained and show lower total crystallinity (60-75 vol.%) (Figure 5.4h). Phenocryst assemblage comprises plagioclase, clinopyroxene and rare olivine. Space between slightly elongated plagioclase, euhedral pyroxene and octahedral titanomagnetite is occupied by dark grey-brown partly devitrified glass, where sometimes it is possible to distinguish microlites of plagioclase and opaque minerals.

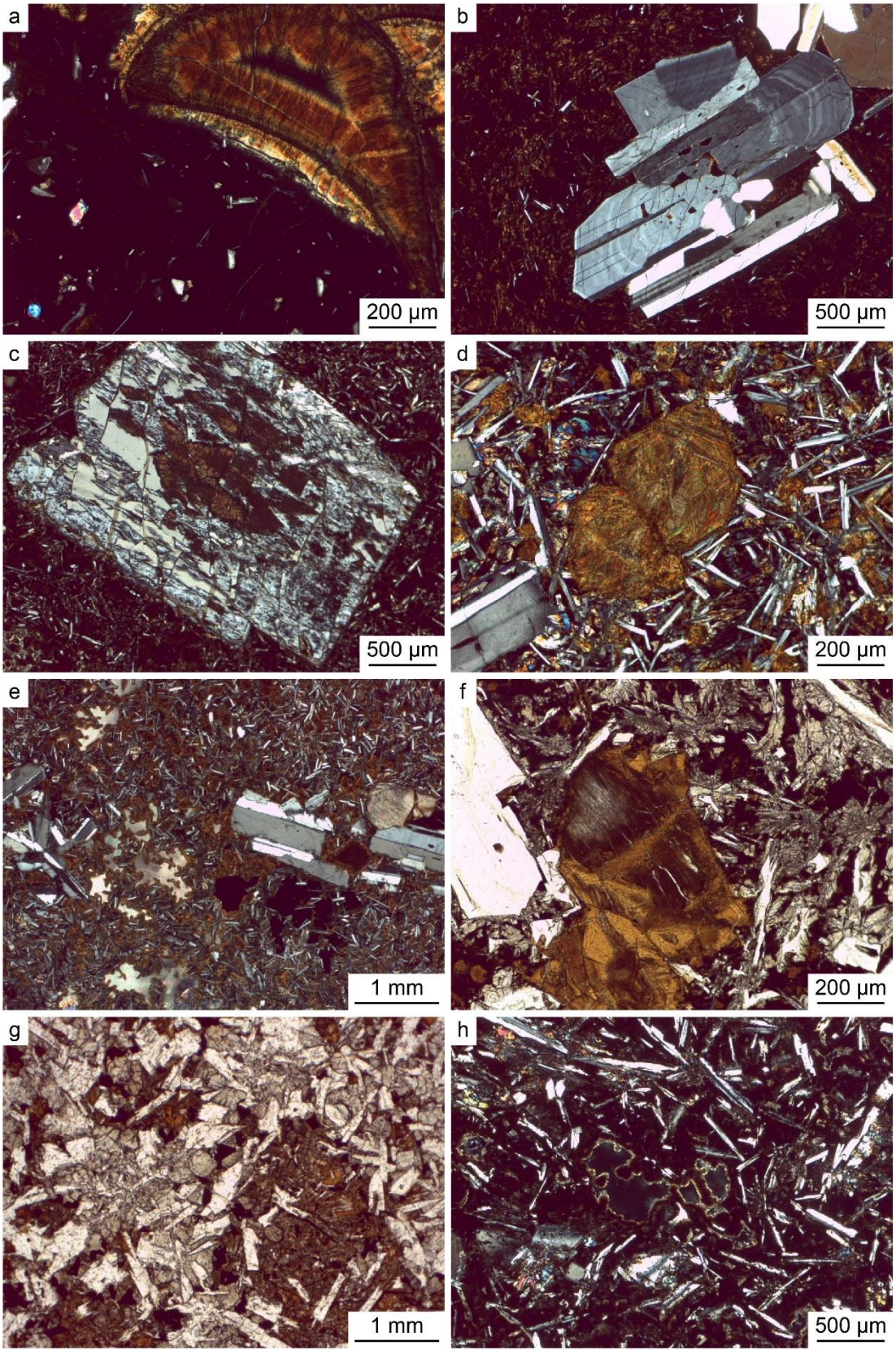
a
200 µm
b
500 µm
c
500 µm
d
200 µm
e
1 mm
f
200 µm
g
1 mm
h
500 µm

5.4.2 Alteration petrology

Fresh glass is preserved only at margins of pillows or lava flows and samples from interiors of lithological units show complete replacement of fresh glass and olivine (where present). As observed in thin sections, alteration of basaltic glass starts with formation of orangey-bronze fibrous birefringent saponite along fractures and alteration continues to form brown micaceous, platy clays, often in a patchy pattern (Figure 5.4a). Green clays replacing glassy metastasis are found in minor amounts, mostly in U1350 samples, especially from stratigraphic unit IV. Calcite alteration of glass is much less significant compared with clay minerals (Figure 5.4e).

The sequence of olivine alteration is: (1) formation of orangey-bronze fibrous birefringent saponite along fractures in the olivine, and (2) subsequent alteration of inner parts of the olivine with either the same clay or brown micaceous platy clay or calcite (Figures 5.4d-f). Individual samples often show similar clay mineralogy

Figure 5.4 (previous page). Photomicrographs of representative basaltic samples: a) saponite-altered (bright orange) and fresh (black) glass with plagioclase, clinopyroxene and olivine microphenocrysts, U1350 24R3 15 (pair 17); b) vitrophyric texture with large fresh plagioclase glomerocrysts and microlites set in altered glassy matrix, U1350 22R5 42-46 (pair 10); c) felty texture with plagioclase phenocryst moderately altered to K-feldspar and brown clays set in a very fine grained network of plagioclase. Clinopyroxene and glass are altered to brown clays and minor calcite, U1350 26R4 100-101 (unit IV); d) intergranular and subophitic textures with phenocrysts of saponite-altered olivine and fresh plagioclase set in a network of plagioclase laths, dendritic subophitic clinopyroxene, saponite-altered olivine microphenocrysts and interstitial Fe-Ti-oxides, U1350 23R5 34-38 (pair 14); e) intergranular and diktytaxitic textures, cavities are filled with calcite (pastel), brown clays and ore minerals (black). Glomerocrysts of fresh plagioclase and calcite-altered olivine are present, U1350 23R5 34-38; f) hiatal texture with olivine, altered to saponite and calcite, and fresh plagioclase phenocrysts set in groundmass of bow-tie plagioclase laths, variolitic clinopyroxene dendrites (all fresh), ore minerals and glass altered to orangey clays, U1347 18R4 24-28 (pair 22); g) intergranular, subophitic and intersertal texture with elongated plagioclase, euhedral pyroxene, octahedral titanomagnetite. Grey-brown domains of partly devitrified glass contain elongated microlites of white plagioclase, black opaque minerals and orangey clays, U1347 28R4 75-92 (pair 28); h) intersertal, intergranular and diktytaxitic textures with slightly altered plagioclase to sericite and brown clays, moderately altered subophitic clinopyroxene in cryptocrystalline clayey matrix, U1350 8R2 118-121 (pair 1). Microphotographs a-e and h are taken under cross-polarised light, f and g are under plane-polarised light.

replacing basaltic glass and olivine. In the olivine tholeiites altered olivine as phenocrysts and groundmass minerals is distinguished from altered glass occupying interstitial spaces by euhedral granular shapes (Figure 5.4d).

Clinopyroxene alteration to brown clays varies from insignificant to moderate (Figure 5.4h). The most stable primary mineral is plagioclase, which remains unaltered in some samples, but in other samples is partially replaced with brown clays and rare sericite (Figure 5.4h). Five samples reveal small amounts of K-feldspar (3-6 wt.%), likely microcline in their XRD patterns, which is replacing primary plagioclase (Figure 5.4c). Sanidine was previously identified as a secondary mineral replacing plagioclase in a plagioclase-phyric pillow succession of unit IV, Site U1350 (Sager et al., 2010).

Microlites often show a brown clay coating, which makes them difficult to discern under an optical microscope. Consequently, the observed crystallinity in thin sections may be underestimated for some very fine grained samples as well as samples containing altered phases (olivine, clinopyroxene), especially those from Site U1350, and potentially is more accurately calculated by the XRD method (Appendix B).

Investigated samples from cores of lithological units at Sites U1347 and U1350 are generally poorly vesicular. Vesicles may remain empty, but are often filled with fibrous and platy clays and / or calcite, with clays usually forming rims and calcite occupying the inner parts. Diktytaxitic textures are common to many investigated samples, especially those of textural type 4. Voids of irregular shapes with or without piercing groundmass minerals, usually plagioclase, are empty or more often they are filled with calcite, brown clays, or opaque minerals (Figure 5.4e and h).

5.4.3 Clay variations

X-ray diffraction patterns obtained on all 29 samples indicate the presence of basal reflections within 15.2-12.5 Å in the air-dried state, which expand to 17-17.5 Å on glycolation (Appendices B and E). This is a “swelling” property, which characterises the smectite group and vermiculite. Ethylene glycol saturated state for the studied samples is consistently >17 Å, corresponding to 2 glycol layers, which is typical for smectites with low interlayer charge (0.3) and not for vermiculites (Meunier, 2005). Glycolated profiles show 3.4 Å peak (005 plane) of greater intensity than 8.5 Å peak (002 plane), and very low intensity of 5.7 Å peak (003 plane), while the position of 060 peak is near 1.53 Å in all of the air-dried samples (Appendices D

and E). These parameters are indicative of a trioctahedral character of smectite minerals, that are common in altered seafloor basalts (Robinson et al., 1993; Meunier, 2005). The structure of trioctahedral smectites implies the presence of divalent cations in octahedral layers, such as Mg^{2+}, Fe^{2+}, Mn^{2+} (Meunier, 2005).

Expandable clays are often mixed-layered with 0, 1 or 2 polar molecule interlayer sheets (Meunier, 2005). The expandability of layers is lost with K^+ saturation. One water layer hydration state is usually associated with a Na^+ exchangeable cation, whereas a two water hydration state could be related to Na^+, Ca^{2+} or Mg^{2+} in trioctahedral smectites, such as saponite (Velde & Meunier, 2008). Samples from Sites U1347 and U1350, located within the lowermost 10 m of the recovered stratigraphic unit IIc, show only one peak at ~15 Å (Appendix E d), which is attributed to non-layered smectites in a 2 water layer hydration state. Petrographically, this trioctahedral smectite is brown or orangey-bronze saponite. The majority of samples from Site U1350 display 2 peaks at ~15 Å and ~13 Å for the 001 plane in the air-dried state (Appendices B and E a-c), associated with the presence of 2 and 1 water layers in the clay structure, respectively (Velde & Meunier, 2008). Both brown and green clays are present in thin sections from most Site U1350 samples, with dominant clay being brown saponite. The green smectitic clay is likely to be nontronite (dioctahedral Na-Fe-smectite), previously reported in samples from Shatsky Rise and other altered basalts from oceanic crust (Alt & Honnorez, 1984; Clayton & Pearce, 2000; Drief & Schiffman, 2004; Sager et al., 2010; Delacour & Guillaume, 2013; Miyoshi et al., 2015).

Three samples from Site U1350 reveal a minor phase with reflections at 10 and 3.33 Å in the air-dried state, which do not change when glycolated (Appendices B and E a). This K-bearing phase could be either mica or illite, and both are common minerals that form mixed-layered minerals with smectites. The three samples show sericite alteration of plagioclase in thin sections. Therefore, this phase is likely to be mica. Two of the mica-containing samples (pairs 5 and 7) also show a “shoulder” at 13.6 Å or so-called “partial swelling” in the ethylene glycol state indicating the presence of non-expanding layers, most probably related to hydroxy-interlayered smectites (Fig. 6a, Velde & Meunier, 2008) (Velde & Meunier, 2008).

Three samples from Site U1350 (pairs 6, 9, 10) that contain microcline and large proportions of residue (35-50%) are not characterised by a significant increase in peaks

at ~14, 4.6, 1.53 Å (Appendices D e and E b), compared to samples with high clay amounts (~30-45%) (Appendix D b, c and f). These samples also show an increased background at ~3.10 Å and high general background especially at low angles (Appendices D e and E b). This indicates a large proportion of amorphous material, such as unaltered basaltic glass. The fresh glass is observed in the whole-rock sample of pair 10. All three samples are located less than 3 cm away from upper or lower margin of pillow lavas.

5.4.4 Downhole variations in major element composition

An examination of the available fresh glass and whole-rock geochemical data, including non-paired samples, demonstrated variation in certain major elements between fresh glass – whole-rock pairs relative to the commonly used immobile element Ti, Nb/Lu ratios as well as Natural Gamma Radiation (NGR) along the U1347 and U1350 cores (Figures 5.5-5.7). Natural Gamma Radiation is produced by radioactive decay from K, U and Th. Values for NGR are relatively low in both drill cores (<5 cps), but are markedly elevated in the upper part of stratigraphic unit IIa, where High-Nb samples were cored, and also in stratigraphic unit IV, all from Site U1350 (Sager et al., 2010).

Fresh glass and whole-rock samples from Site U1347 show quite uniform compositions (including MORB-like Nb/Lu ratios, Figure 5.6). Most of the paired whole-rock samples demonstrate enriched SiO_2/TiO_2, Al_2O_3/TiO_2, CaO/TiO_2, MgO/TiO_2 and depleted K_2O/TiO_2, relative to their fresh glass equivalent (Figures 5.5-5.6). In contrast, samples from Site U1350 show much wider compositional variations and are roughly divided into two groups by depth at ~270 mbsf (Figures 5.5 and 5.7). Whole-rock samples above this depth are Higher-Fe tholeiites of High-Nb, Low-Ti and Normal-types and demonstrate lower SiO_2/TiO_2, CaO/TiO_2, FeO/TiO_2 and K_2O/TiO_2, relative to their fresh glass pair. Similar to U1347, the altered samples from this group show MgO-enrichment (Figure 5.5). Most of the whole-rock samples from ~270-290 mbsf are of Higher-Mg-type and demonstrate significant depletion in MgO and FeO contents. The remaining two samples from this horizon do not show these depletions, but an increase in K_2O and other alkalis contents. The whole-rock major element and Nb/Lu ratios from the lowermost stratigraphic unit IV (U1350) are similar to these two K-enriched compositions (Figure 5.7).

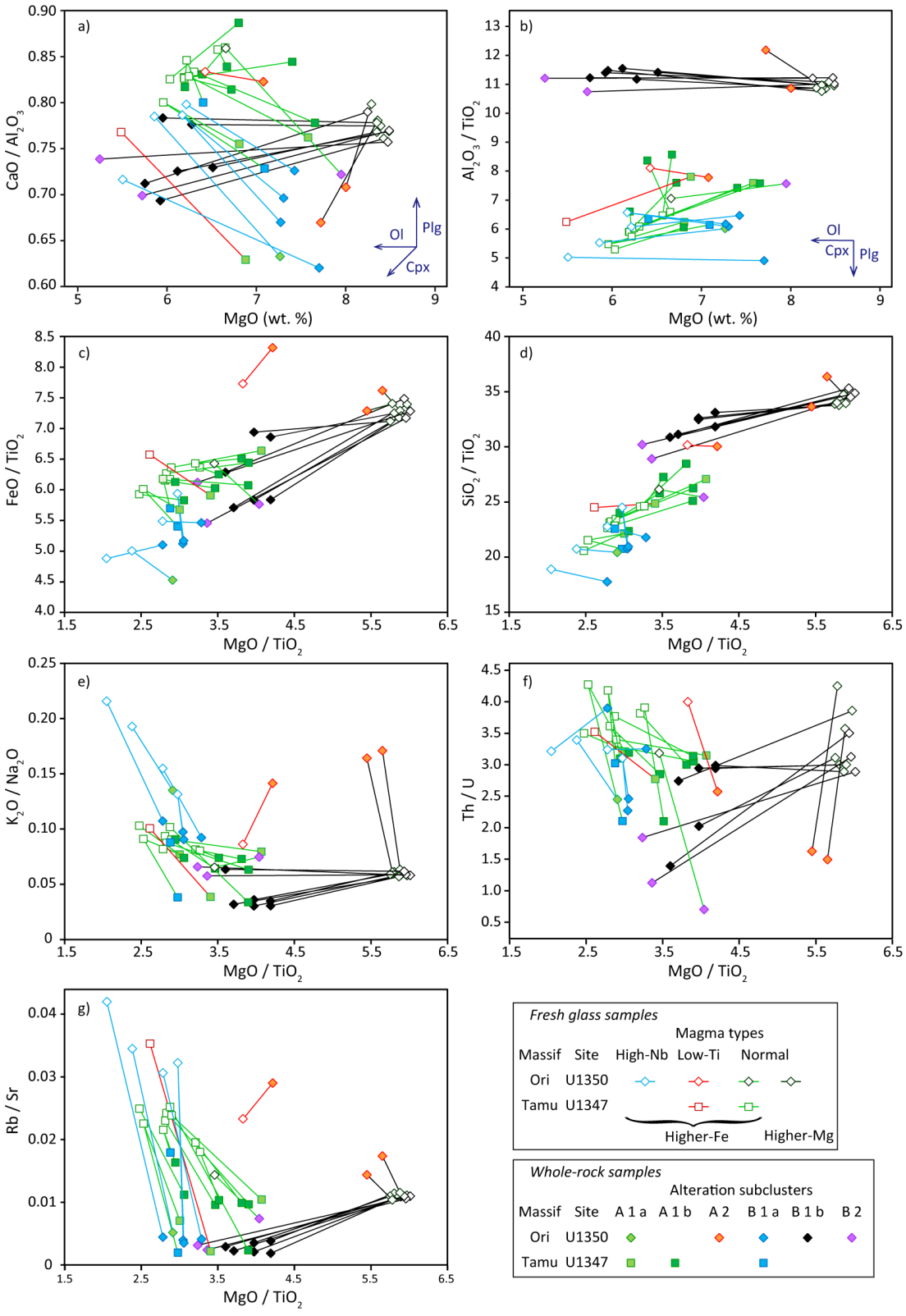

Figure 5.5. Variations of major and trace element concentrations and ratios in the examined pairs (connected with lines) versus MgO (wt.%, normalised to anhydrous) or MgO/TiO_2. Arrows in (a) and (b) plots indicate plagioclase (Plg), clinopyroxene (Cpx), and olivine (Ol) fractional crystallisation vectors, resulting in lowering of MgO (Ol, Cpx), CaO (Cpx, Plg), and Al_2O_3 (Plg), which explain evolution of the primitive magma.

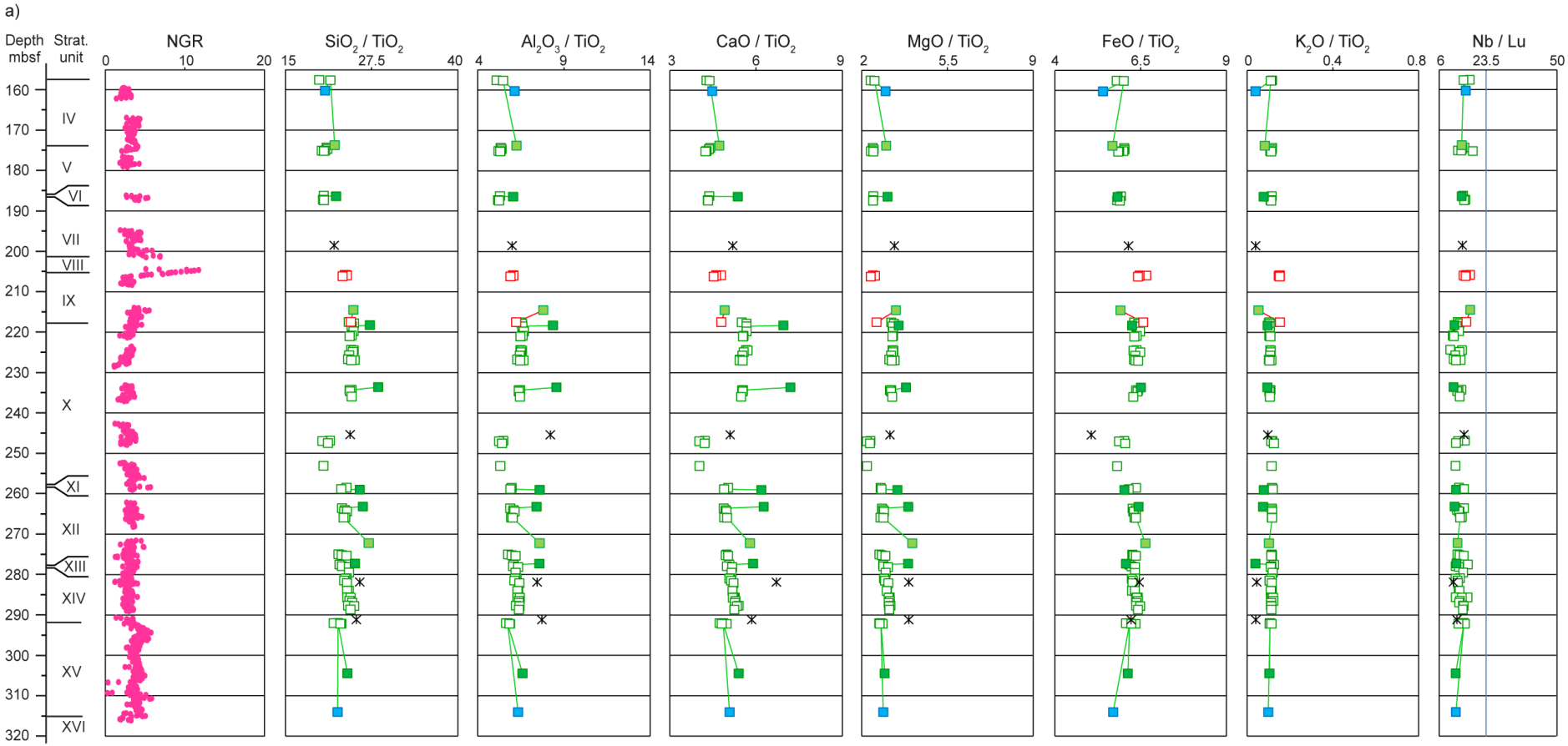

Figure 5.6. Downhole variations of NGR, major element oxide compositions relatively to TiO_2, and Nb/Lu ratios for all available geochemical dataset from Site U1347, data from (Sano et al., 2012). Average Nb/Lu ratios for N-MORB, E-MORB and OIB are 5, 23.5 (shown as blue vertical line), and 160, correspondingly after Sun and McDonough (1989). Fresh glass symbols are hollow and the whole-rock symbols are filled. Stars indicate whole-rock samples from lithological units with no fresh glass present or analysed. For more details see legend on Figure 5.5.

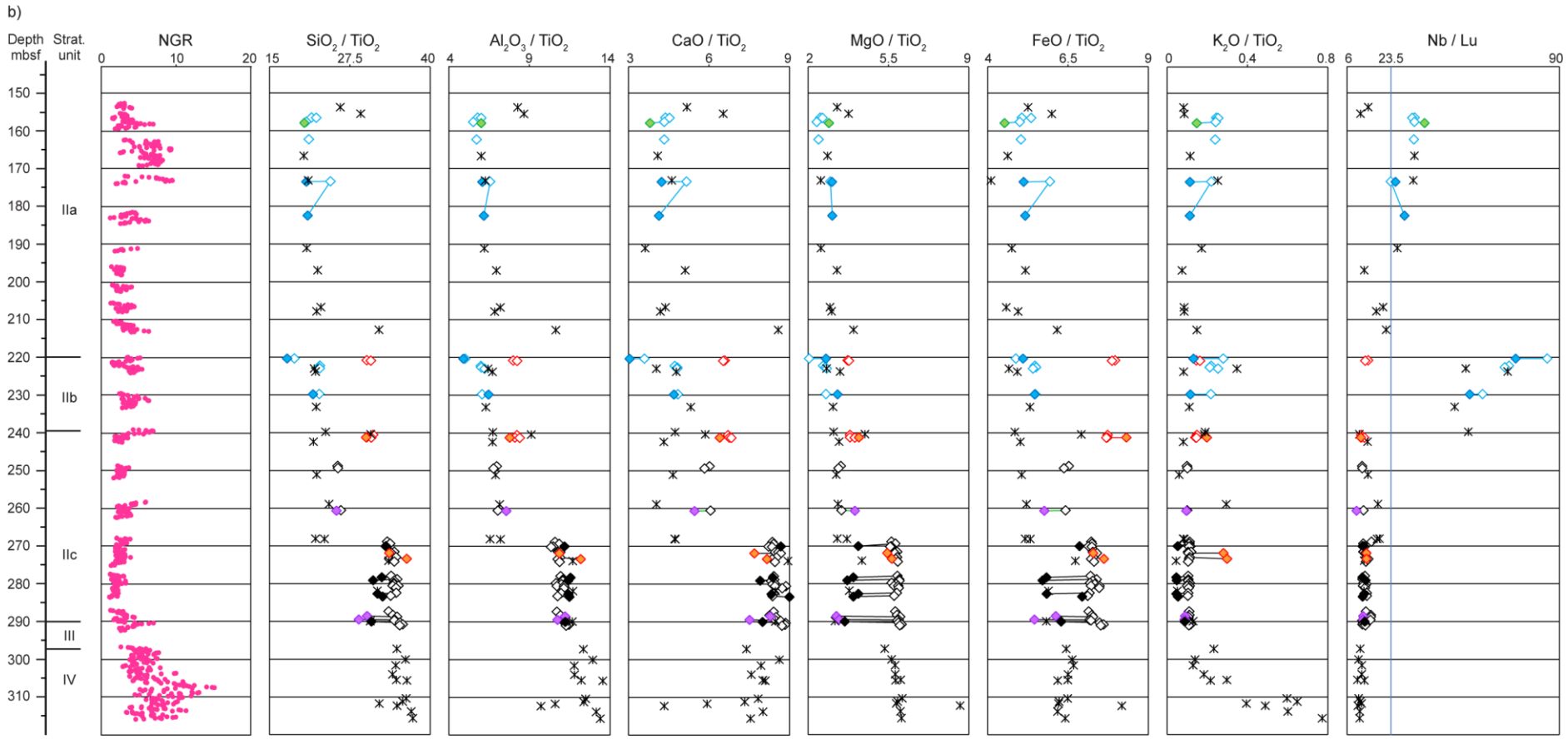

Figure 5.7. Downhole variations of NGR, major element oxide compositions relatively to TiO_2, and Nb/Lu ratios for all available geochemical dataset from Site U1350, data from (Sano et al., 2012). Average Nb/Lu ratios for N-MORB, E-MORB and OIB are 5, 23.5 (shown as blue vertical line), and 160, correspondingly after Sun and McDonough (1989). Fresh glass symbols are hollow and the whole-rock symbols are filled. Stars indicate whole-rock samples from lithological units with no fresh glass present or analysed. For more details see legend on Figure 5.5.

Most of the trace elements vary systematically within each paired whole-rock sample, so that their multi-element patterns are generally parallel to each other (Figure 5.8). Samples are usually characterised by depletions in Mn, Fe and alkalis including Rb, Ba and K, while they are largely enriched in U and P. On the other hand, Si and Sr concentrations are relatively unchanged in all of the altered samples in Figure 5.8.

5.4.5 Alteration groupings within the identified sample pairs

Hierarchical cluster analysis (HCA) identified six subclusters of samples with similar RA values (Figure 5.9; Table 5.1). Principal component analysis (PCA) was used to explain variability of data in combination with HCA. Three major principal components (PC) explain over 76% of variability of the dataset, with PC1 accounting for 55% of variability, and PC2 and PC3 accounting for ~11% each (see table in Figure 5.10). Component loadings for the RA of each element are shown in Figures 5.10a-c: the larger the amplitude of a component loading, the greater its influence on a particular PC. Binary plots in Figure 5.11 show vectors for each chemical element contributing to the principal components and plot the corresponding component score for each RA value of each element for all samples.

Analysis of PC1 displays a strong negative correlation of RA(Mg) with RA of almost all of the trace elements as well as some major elements (Ti, P, Na), but positive correlation with RA(Rb) (Figure 5.10a). Samples from Site U1347 generally fall into cluster A1, characterised by enrichment in RA of Mg and the lowest RA for fluid immobile trace elements, compared to the other subclusters (Figures 5.11a and b). Higher-Fe tholeiite basalts of High-Nb type from Site U1350 form subcluster B1a with one sample falling into subcluster A1a. They show a similar alteration petrology and mineral phase proportions identified using XRD to the most altered U1347 samples. Higher-Mg tholeiites fall into subclusters B1b, B2 and A2, and are largely characterised by a decrease in RA of Mg (Figure 5.11a and b). The positive loading for RA(Mg) for PC1 and the high percentage of explained variability for PC1 (~55%) (Figure 5.10a and Appendix F) indicate that a large proportion of relative alteration in the Shatsky Rise basalts can be explained by either Mg gain or loss.

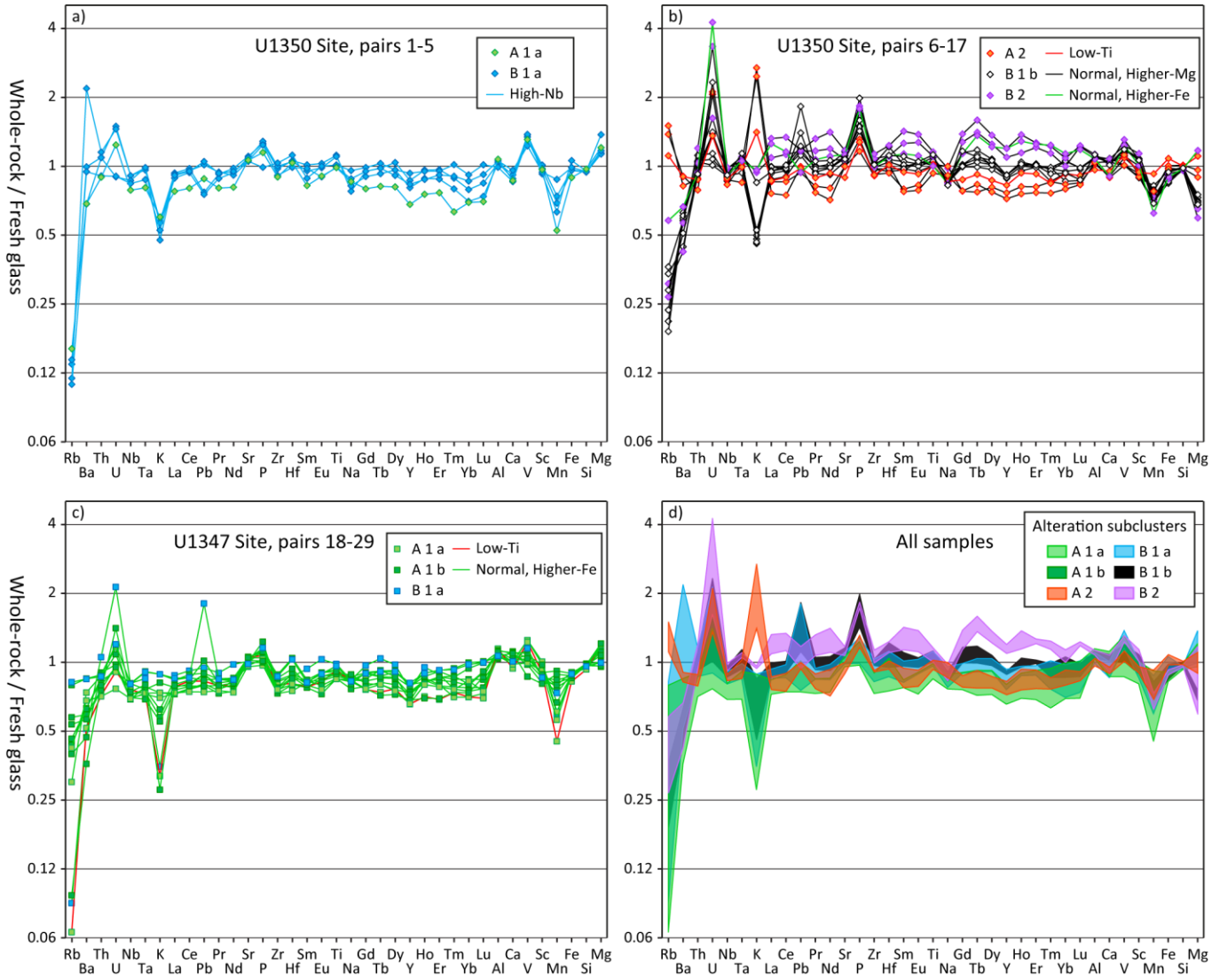

Figure 5.8. Relative changes in chemical compositions of whole-rock samples as compared to fresh glasses for each representative pair.

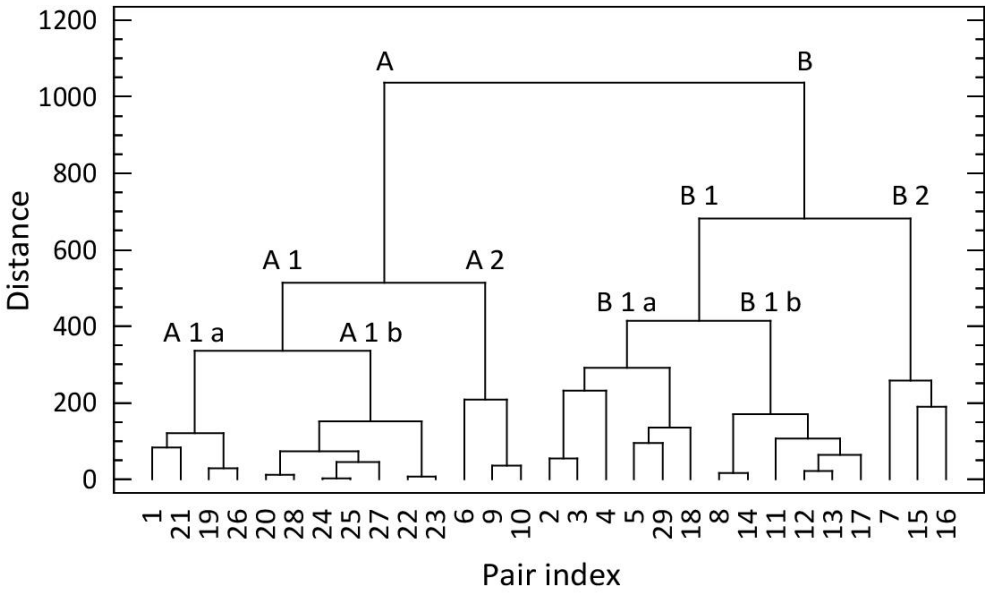

Figure 5.9. Hierarchical cluster analysis dendrogram for the identified whole rock – fresh glass sample pairs.

PC2 and PC3 show the explained variability in all major and some trace elements in the absence of the dominating influence of Mg loss/gain highlighted by PC1, but the percentage of this explained variability is relatively lower than of PC1, being 11% and 10.6% for PC2 and PC3, respectively (Figure 5.10b and c). Three samples from Site U1350 fall into subcluster A2 and show negative values for PC2. These samples are characterised by minor changes in Mg composition, but significant additions of K, Rb, Ba, Na as compared to the rest of the U1350 core (Figures 5.8d and 5.11; Appendix F). These samples have distinct petrography, characterised by higher proportion of glass, which is now partly altered to clay minerals with randomly oriented mixed-layer structures, and containing secondary K-feldspar replacing plagioclase (Appendix B).

Samples that demonstrate petrographically alteration in primary plagioclase and/or clinopyroxene show high values for PC3 (Figure 5.11). Samples from A1a and B1a with clinopyroxene alteration demonstrate high RA of Mg, Sc, V, Th and Ti, but low RA in heavy REE, Y, Mn, Pb, Ca, Al and Si. In contrast, samples from the B2 subcluster, with altered clinopyroxene and plagioclase, show PC2 and PC3 values close to B1b, the least altered whole-rock samples from Higher-Mg type (Figure 5.11e). As compared to B1b, these samples from B2 demonstrate relatively higher contents for many of the trace elements, in response to larger MgO additions.

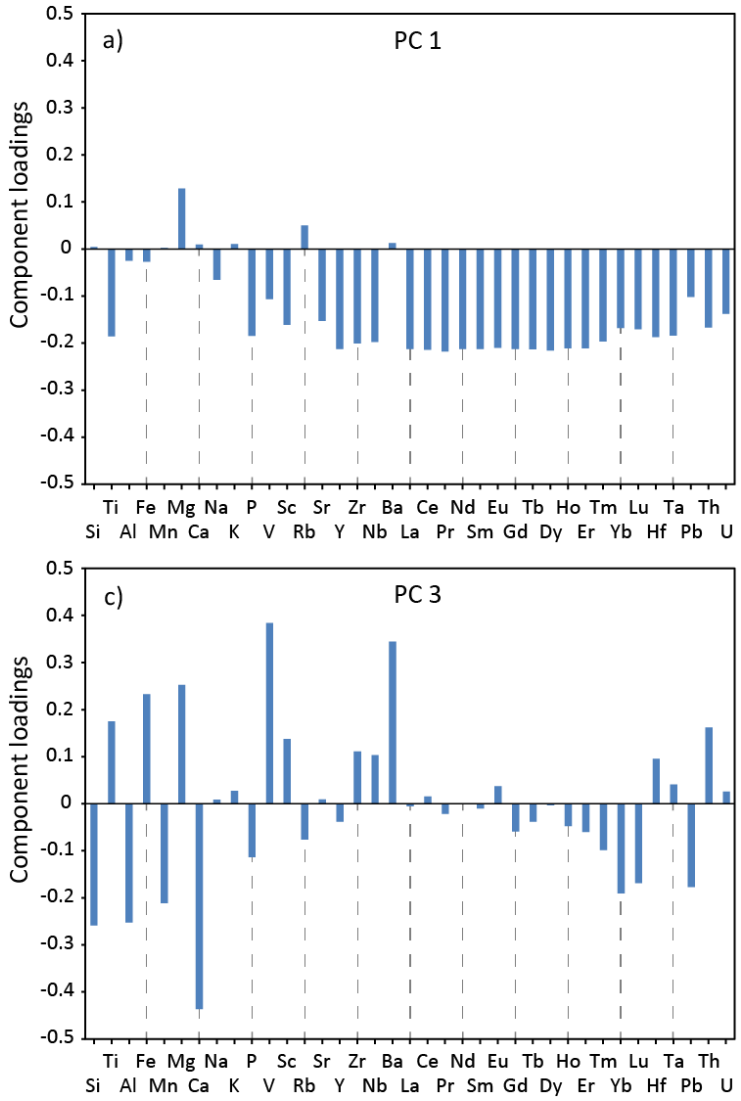

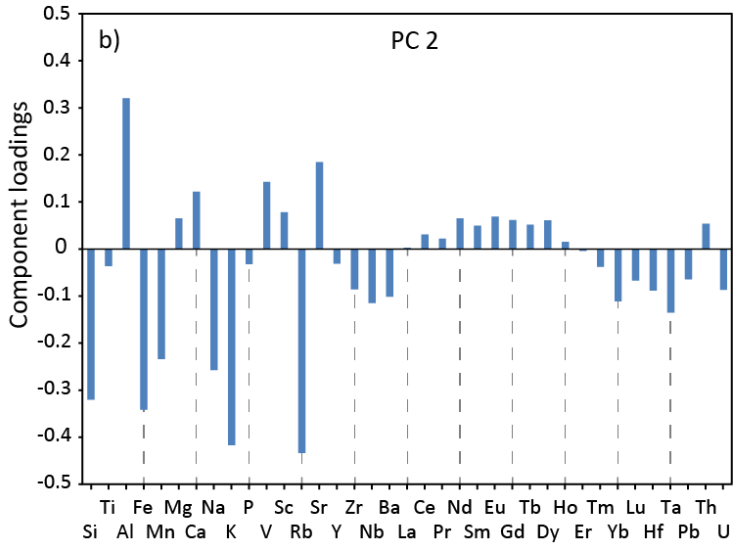

Figure 5.10. Loadings for three major principal components that explain most of the variance (a-c). Also provided is a table with eigenvalues and percentages of explained variance for principal components with eigenvalues larger than 1.

Principal components	PC 1	PC 2	PC 3	PC 4	PC 5	PC 6
Eigenvalue	20.35	4.08	3.92	1.74	1.62	1.01
Percentage of explained variance	55.01	11.01	10.58	4.69	4.38	2.72
Cumulative percentage of explained variance	55.0	66.0	76.6	81.3	85.7	88.4

Table 5.1. Summary of alteration groupings

Alteration subcluster	IODP Site	Tholeiitic group	Magma types	Pair №	Textural type	Crystal-linity %	Altered primary phases	Dominant secondary minerals	Chemical change
A 1 a	U1347 & U1350	Higher-Fe	Normal, Low-Ti, High-Nb	1, 19, 21, 26	4	60-73	glass and olivine (complete); cpx and plag (slight to moderate)	brown and orange clays, calcite	Mg-gain
A 1 b	U1347	Higher-Fe	Normal	20, 22-25, 27, 28	3	75-90	glass and olivine (complete)	brown and orange clays, calcite	Ca- and Mg-gain
A 2	U1350	Higher-Fe Higher-Mg	Low-Ti Normal	6 9, 10	1	50	glass (local); olivine (complete); plag (slight)	brown, orange, green clays, calcite	Ca-loss, alkali-enrichment
B 1 a	U1347 & U1350	Higher-Fe	Normal, High-Nb	2-5, 18, 29	4	60-74	glass and olivine (complete); cpx and plag (slight to moderate)	green, brown and orange clays, calcite, sericite	Mg-gain, Ca-loss
B 1 b	U1350	Higher-Mg	Normal	8, 11-14, 17	2	90-95	glass and olivine (complete)	brown and orange clays, calcite	Mg-loss, Ca-gain
B 2	U1350	Higher-Fe Higher-Mg	Normal Normal	7 15, 16	2 4	75 95	glass and olivine (complete); cpx and plag (moderate)	brown clays, calcite	Mg-gain, Ca-loss Mg-loss, Ca-gain

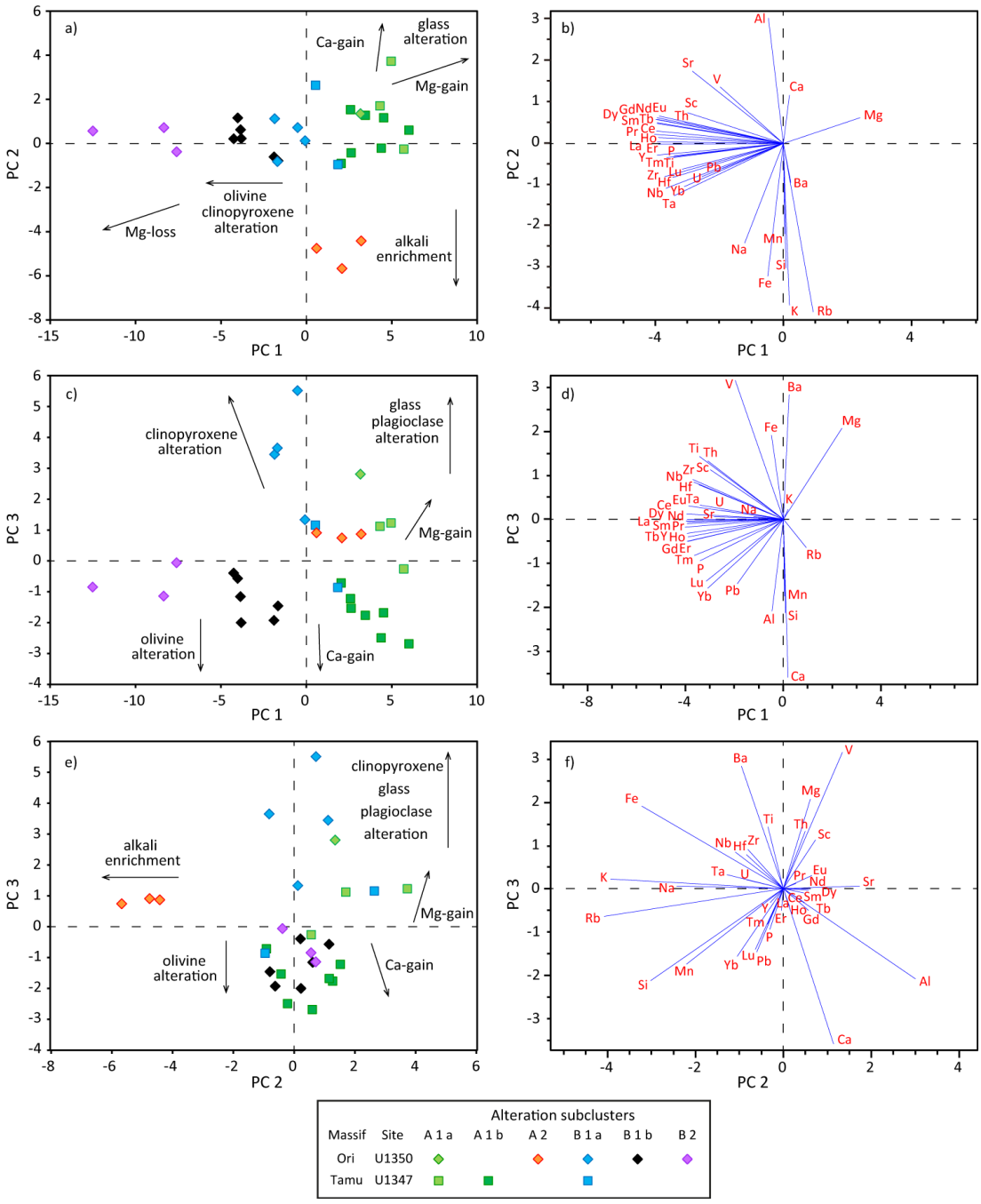

Figure 5.11. Left images show six subclusters distinguished using three major principal components (PC), right images display vectors (weights) for each variable (chemical element) in each of the binary systems. The scale proportions among each of the left and right plots are maintained.

5.5 DISCUSSION

Basalts examined in this study from the flanks of Tamu and Ori Massifs are normative olivine and quartz tholeiites, varying in magmatic type from Normal (MORB-like) to High-Nb (OIB-like). Whole-rock – fresh-glass pair analysis allows differentiating groups of samples with similar degrees and nature of alteration. In this section, the controls on element mobility produced during seawater alteration of submarine basalts from Shatsky Rise are discussed.

5.5.1 Controls on Magnesium variations

Results from numerous investigations on seawater alteration of upper oceanic crust have demonstrated that a significant chemical exchange occured between the crust and seawater that results in alteration of basaltic glass and primary minerals and formation of secondary minerals (Bienvenu et al., 1990; Staudigel et al., 1996; Stroncik & Schmincke, 2002; Staudigel, 2003; Pauly et al., 2011). Major element oxides of Si, Al, Fe, Ca, Mg reflect changes in their abundances of up to 15% between the fresh glass – whole-rock pairs, except for MgO that shows up to 40% of gain/loss.

Low-temperature seawater alteration of basalts leads to high Mg mobility, usually associated with its fixation in the crust (e.g., Mottl, 1983; Alt, 1995; Clayton & Pearce, 2000; Staudigel, 2003; Bach & Früh-Green, 2010; Pauly et al., 2011). Olivine, clinopyroxene and basaltic glass are Mg-bearing phases that compose significant proportions of whole-rock samples from Sites U1347 and U1350. This paired study confirms that Mg is substantially mobilised during seawater alteration, which involves destruction of primary phases and formation of Mg-bearing smectites and low-Mg secondary minerals (nontronite, calcite). Possible controls on MgO gain and loss are: 1) primary basaltic characteristics including crystallinity, primary mineral susceptibility to alteration, chemical variations of original fresh glass and crystals, and 2) fluid characteristics including fluid temperature, chemistry, alkalinity, oxidative conditions. Below I discuss how the primary basaltic characteristics relate to MgO mobility based on the whole-rock – fresh glass pair analysis.

5.5.1.1 Importance of initial crystallinity and stability of primary minerals to alteration

Basaltic glass is the most susceptible to alteration, and thus the proportion of glass versus crystalline components (phenocrysts and microlites) has a significant effect on the degree of alteration and Mg mobility. Analysis of MgO change (δMgO

wt.% = $MgO_{whole\text{-}rock} - MgO_{fresh\ glass}$) versus clay content in the whole-rock samples reveals two major groups of alteration. The first group, corresponding to the Higher-Fe tholeiitic type lavas based on relatively lower MgO contents in glass (5.43-6.81 wt. %), experienced Mg-gain, producing a weak positive correlation with increasing clay content (Figure 5.12a). Total amount of clays in Higher-Fe tholeiites increases from A1b to A1a and B1a subclusters (Appendix B). Therefore, fixation of Mg in these samples may be related to the formation of clays. Higher degrees of alteration relate to larger proportions of glass replaced by clays and alteration of clinopyroxene and plagioclase.

A second group showing Mg-depletion (negative δMgO) represents the more primitive Higher-Mg tholeiitic type lavas (Figure 5.12a). These lavas are normative olivine tholeiites containing abundant olivine (Figure 5.4d and Appendix B). However, normative olivine is significantly reduced in chemical compositions of altered samples from 7-10 vol.% in fresh glass to absent in the whole-rock (Appendix B). Most investigated Higher-Mg tholeiites are almost entirely crystalline, based on petrological and XRD phase observations (Appendix B). Magnesium depletion as a result of olivine alteration was previously reported for both upper and lower oceanic crust (e.g., Alt & Honnorez, 1984; Bach et al., 2001; Nozaka et al., 2008) as well as for mantle peridotites (Ligi et al., 2013). Subsequent alteration of clinopyroxene to clays observed in samples from subcluster B2 leads to further decrease in δMgO (Figure 5.12a).

Two samples of Higher-Mg tholeiite basalts and one of Higher-Fe, which were combined into subcluster A2, are located near or at pillow boundaries and demonstrate vitrophyric textures. These samples distinct by less significant Mg mobility and comparatively larger proportion of glass partly replaced with clays (orange diamonds in Figures 5.8b and 5.12a). The low Mg mobility in these samples is related to presence of unaltered glass and limited amounts of olivine due to lower overall crystallinity.

5.5.1.2 Magnesium – Calcium relationships

Magnesium-fixation in the rocks through smectitic clay formation is often associated with Ca release from the rocks, and considered as one of the major alteration processes of basaltic rocks (Mottl & Holland, 1978; Seyfried et al., 1978; Seyfried & Mottl, 1982; Mottl, 1983; Alt, 1995; Scholz et al., 2013). Well-crystallised samples from both Higher-Fe and Higher-Mg tholeiitic basalt groups show a gain in CaO contents relative to fresh glass compositions (Figure 5.12b). Calcium enrichments are

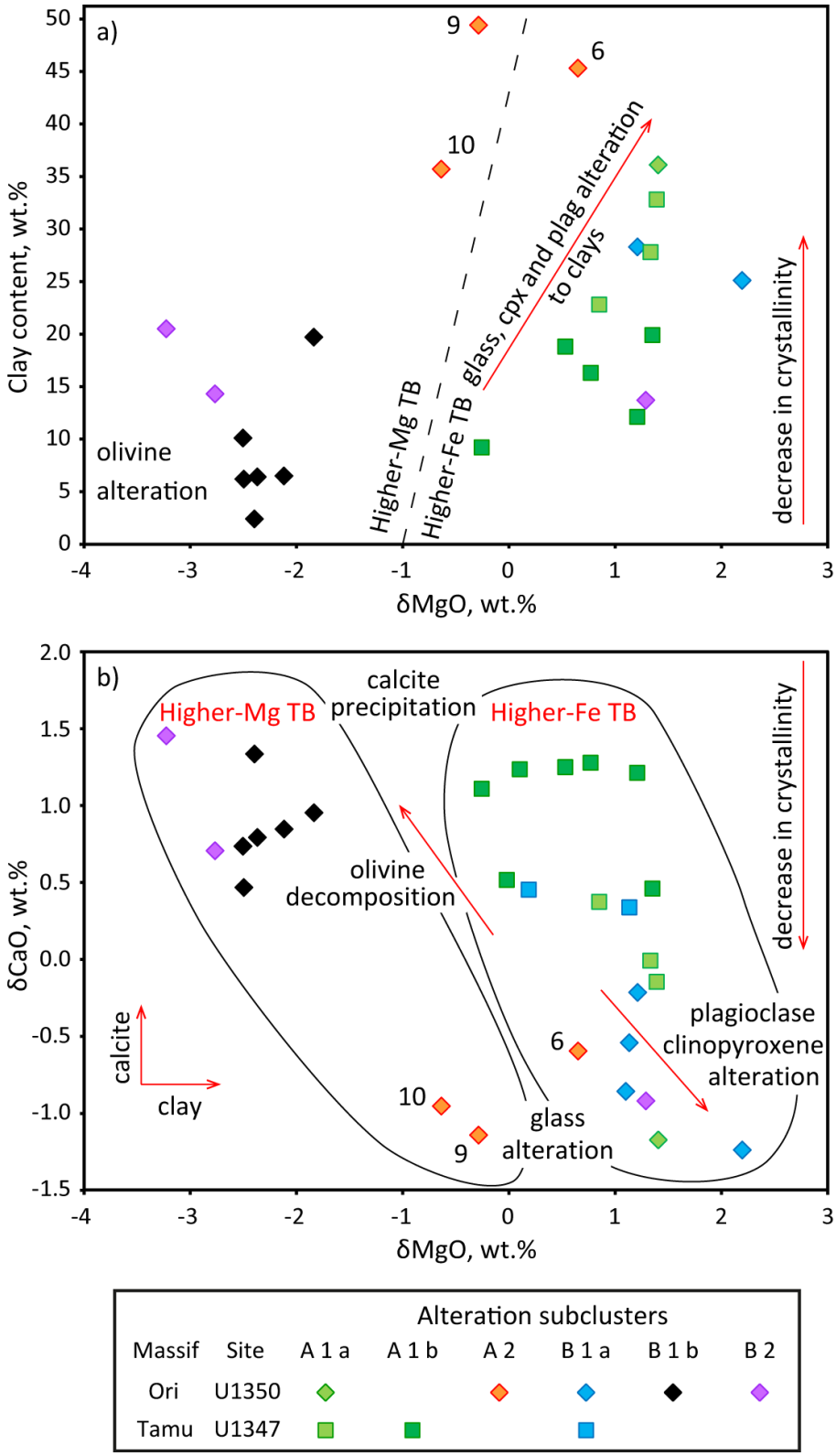

Figure 5.12. Illustrations showing dependence of δMgO on clay content (on a) and on δCaO (b) in paired whole-rock samples. $\delta MgO = MgO_{whole\text{-}rock} - MgO_{fresh\ glass}$, $\delta CaO = CaO_{whole\text{-}rock} - CaO_{fresh\ glass}$, all in wt.%. Higher-Mg and Higher-Fe tholeiitic basalts (TB) show two compositionally different alteration groups. Clay amounts in samples from subcluster A2 (numbers indicate pair indices) are overestimated due to presence of fresh glass.

related to secondary calcite alteration of olivine, in addition to clays, and precipitation in vesicles and veins. Decrease in crystallinity in Higher-Fe tholeiites is associated with MgO-gain and CaO-loss.

Higher-Mg tholeiites, containing olivine pseudomorphs, show Mg-removal and relative Ca-enrichment, which is indicated by olivine decomposition to clays and calcite precipitation. Two vitrophyric Higher-Mg samples (subcluster A2) had limited olivine alteration and also intense glass alteration, which resulted in limited loss of MgO and significant decrease of CaO contents. In the case of Higher-Fe tholeiitic basalts, the largest δCaO (>1 wt.%) (δCaO wt.% = $CaO_{whole\text{-}rock} - CaO_{fresh\ glass}$) occurs in the least altered samples, all from Site U1347, showing relatively larger proportion of phenocrysts including olivine. Sparsely phyric Higher-Fe tholeiites from U1347 show limited CaO-gain (<0.5 wt.%), which decrease with increasing δMgO (due to clay formation).

Higher-Fe tholeiites from Site U1350 contain a larger proportion of secondary calcite, filling vesicles and replacing glass, than the rest of the paired samples (Appendix B). Despite this, these U1350 samples demonstrate negative δCaO, which is likely caused by more intense alteration of primary plagioclase and clinopyroxene to calcite and clays leading to CaO redistribution and its loss (Figure 5.12b). A weak trend with decreasing δCaO and increasing δMgO is consistent with clay formation as a result of basaltic glass alteration.

5.5.1.3 Magnesium relationships with other major elements

Whole-rock samples from studied pairs show an increase in P_2O_5 and Al_2O_3 contents and a decrease in MnO and FeO relative to their fresh glass counterparts (Figures 5.6-5.8). This implies that these elements get accumulated (Al, P) or diluted (Mn, Fe) regardless of primary chemical composition of tholeiitic basalt (Higher-Mg versus Higher-Fe) or its mineralogy. Therefore, such element behaviour is a result of open system seawater-rock interaction, which is mainly observed as glass decomposition and smectite formation. Slight change in concentrations of SiO_2 and TiO_2 negatively correlate with MgO mobility indicating conservative behaviour.

5.5.2 Fluid-mobile elements

Element variations among the whole-rock – fresh glass pairs are the most profound for fluid mobile elements such as U, Rb, Ba, and K (Figure 5.8). Uranium is

enriched in most of the studied samples, suggesting fixation of U from oxidised seawater (Alt, 1995; Zhang & Smith-Duque, 2014). Although Sr is often regarded as a fluid mobile element, no significant changes in Sr concentrations have been recognised within the pairs. Data from PCA show that Sr mobility often differs from that of the other trace elements (Figures 5.8, 5.10 and 5.11). Some researchers suggest that this element may be redistributed locally, within the rocks, without significant migration to or from seawater (Staudigel et al., 1996; Walton et al., 2005; Zhang & Smith-Duque, 2014).

Generally, for the studied samples, RA of Rb, Ba and K elements are <100, implying alkali loss. Caesium shows very low concentrations in the whole-rock samples from both Sites U1347 and U1350 (Sano et al., 2012), but it is not included into our pair comparison study due to lack of fresh glass data. A few samples from Site U1350 show presence of mica (in sericite-altered plagioclase), indicating K-availability (Meunier, 2005). Two of these samples are of High-Nb magmatic type, which is characterised by relatively higher initial K contents (Figure 5.5e). Despite mica formation in the High-Nb samples, they still show low RA for K, Na and Rb. Site U1350 samples from subcluster A2 and stratigraphic unit IV show alkali enrichment and microcline in their XRD patterns (Appendices D and E; Figure 5.5). The fluid-mobile elements are likely to enter clay and/or K-feldspar structure, which is common for the upper oceanic crust during low-temperature alteration (Pertsev & Boronikhin, 1983; Alt, 1995; Von Damm, 2013).

Mafic rocks usually consume alkalis to form low-temperature secondary minerals during seawater alteration under 100-150ºC (Alt, 1995; Staudigel, 2003; Von Damm, 2013). However, investigated samples from the interiors of pillow lavas and sheet lava flows show predominantly alkali loss. Nevertheless, samples from Shatsky Rise are characterised by non-pervasive predominantly smectitic alteration with minor calcite, zeolite and rare chlorite (Sager et al., 2010), which corresponds to zeolite facies, the lowermost (diagenetic) grades of metamorphism, well below 300ºC (Wilson, 2013).

5.5.3 Immobile elements

Using a multivariate analysis permits groups of elements with similar behaviour to be differentiated within the entire sample selection and each subcluster independently. Elements within such groups are thus immobile relative to each other

during seawater alteration processes. Negative correlation of RA(Mg) with most trace elements in our samples indicates that the trace elements get passively accumulated or diluted depending on Mg mobility (Figure 5.10a). Passive accumulation of trace elements is consistent with olivine alteration, because the trace element abundances, included in the multivariate analysis, do not partition into olivine. On the other hand, these elements are passively diluted during Mg fixation into clays, and potentially insignificantly participate in seawater alteration of basaltic glass. However, differences in trace element alteration behaviour are recognised when plagioclase and clinopyroxene get altered. The trace elements Eu, Sr, Ba are compatible in plagioclase, and Sc, V, Mn, Y, Ti, heavy and middle REE are compatible in clinopyroxene (Severs et al., 2009). Studied samples with clinopyroxene alteration (subclusters A1a and B1a) show significant element migration. Specifics of the element migration are likely to be dependent on chemistry and duration of hydrothermal activity.

High-field strength elements are susceptible to a much smaller degree of alteration-related mobility (Figure 5.11). Traditionally regarded as immobile elements, Hf, Zr, Nb and Ta, similarly respond to alteration in all samples, and can be used for immobile element ratios (e.g., Nb/Zr). Titanium can be used together with these elements in samples free of clinopyroxene alteration. REE patterns of the whole-rock samples normalised to fresh glass compositions are generally flat and parallel to each other (Figure 5.8). This means REE are relatively unaltered in relation to each other, especially in the clinopyroxene-fresh samples, and can be used for geochemical classifications.

One of the main tendencies in studies of basalts from OIBs and LIPs is to determine proportions of OIB versus MORB components (Ernst & Buchan, 2003; Kerr, 2014). This could be done by using Nb/Lu ratio, because OIB- and MORB-like samples show steep and flat slopes in multielement diagrams, respectively. Average Nb/Lu ratios for OIB, E-MORB and N-MORB are 160, 23.5, and 5, respectively (after Sun & McDonough, 1989). Most of the studied whole-rock samples paired to fresh glass compositions demonstrate no significant changes in Nb/Lu ratios (Figures 5.6 and 5.7). The exceptions are High-Nb whole-rock samples, demonstrating slight deviations from the unaltered pairs. These whole-rock samples were subjected to more intense clinopyroxene alteration.

5.5.4 Comparison of alteration characteristics in basalts from flanks of the Tamu and Ori Massifs

Investigated samples from Sites U1347 and U1350 are located at the flanks of Tamu and Ori Massifs. Whole-rock samples from Site U1350 show variability in alteration degree from low to moderate and less intense alteration is observed in samples from Site U1347. Proportions of glass and/or olivine, which are very susceptible to alteration, are directly proportional to degree of alteration. The amount of glass in a rock is largely dependent on cooling rates. Thin pillow lavas, which dominate the stratigraphy of Site U1350, cool faster and have a greater proportion of glass than the thick massive flows, which dominate the stratigraphy of Site U1347 (Figure 5.1). The amount of olivine in a rock is dependent on petrogenesis including degrees of partial melting and fractional crystallisation.

Pillow lavas and thin lava flows are common to both Sites U1347 and U1350, whereas thick lava flows are found only in U1347. A variety of textures is found at U1350 from vitrophyric in sections close to pillow boundaries, hypocrystalline varieties (subophitic, intersertal) to almost holocrystalline textures in the inner parts of pillows (e.g., lower stratigraphic unit IIc). All of these are associated with a generally smaller size of phenocryst and groundmass minerals compared to U1347. This study shows that close to pillow lava boundaries, with fast cooling, low crystallinity vitrophyric textures form. Less rapid cooling of more internal parts of pillows and flows leads to formation of variolitic textures in the groundmass, which increases crystallinity in these basaltic sections. Slower cooling of the inner parts of pillows and flows results in increase in grain size and development of subophitic and intergranular textures. Samples from U1347 demonstrate that the crystallinity in the inner parts of sheet flows is lower that than in the parts with variolitic groundmass, but it increases with increasing grain size. In conclusion, at Site U1350, the cooling rates were supposedly higher as a result of thinner pillowed lava units and, likely, lower emplacement rates, compared to Site U1347. This resulted in generally lower crystallinity of the rocks from Site U1350, which in turn made these glassy rocks more susceptible to seawater alteration.

Larger variability in alteration chemistry in volcanic succession from Site U1350, as compared to Site U1347, is associated with both a higher diversity of magmatic compositions and the predominance of pillow lavas over sheet flows in

U1350. Only Higher-Fe tholeiitic basalts are found in Site U1347, whereas both Higher-Mg and Higher-Fe tholeiitic basalts occur at Site U1350. This research demonstrates that the timing of seawater alteration on these two groups of basalts results in differences in element migration, especially noticeable for Mg. Subdivisions within the Higher-Fe group to Normal, Low-Ti and High-Nb types show little or no significance to alteration character.

5.6 SUMMARY OF THE KEY FINDINGS

This study was focused on element mobility during seawater alteration of basalts from the flanks of Ori and Tamu Massifs. Results from this study demonstrate that:

- Alteration-induced element mobility in basalts from the flanks of Ori and Tamu massifs is largely associated with smectitic clay formation due to decomposition of basaltic glass and primary minerals (olivine, plagioclase and clinopyroxene).
- Glass and olivine are the most susceptible phases in basalts to seawater alteration, and therefore the degree of seawater alteration in submarine basalts is primarily dependent on magma chemistry and cooling rates.
- Higher-Mg and Higher-Fe tholeiitic basalts show two compositionally different alteration types.
- Most Higher-Mg tholeiitic basalt pillow flow interiors are composed of almost entirely crystalline (<10% glass), olivine-bearing rocks, which underwent MgO-loss (2-3 wt.%) during olivine alteration.
- High-crystalline (<10% glass) Higher-Fe tholeiitic basalt pillow and sheet flow interiors show no significant change in MgO composition (±0.2 wt.%).
- A decrease in crystallinity in both groups is associated with increased smectitic clay formation and correlated with relatively higher Mg and lower Ca.
- Subdivisions within the Higher-Fe group to Normal, Low-Ti and High-Nb types show little or no significance to alteration character.
- Variations in Mg due to olivine and glass alteration are accompanied by passive accumulation or dilution of many trace elements, excluding the fluid-mobile elements U, Rb, Ba, and K that are the most variable elements during seawater alteration. Usually, P, Al and U are enriched, whereas alkalis, Mn and Fe are depleted in most cases. Elements Hf, Zr, Nb and Ta remain immobile in respect to each other.

- Clinopyroxene alteration results in an increase in Mg concentrations due to progressive clay formation, whereas elements compatible in clinopyroxene (V, Sc, Mn, Y, Ti, heavy and middle REE, Th, Pb, Si, Ca, Al) are subject to element migration or redistribution within the rocks.

Chapter 6: Synthesis

6.1 INTRODUCTION

Research from this thesis has been focused on Ori Massif, the second largest and oldest edifice from the central part of the Shatsky Rise oceanic plateau. Ori Massif is significant in terms of understanding the origin and evolution of the Shatsky Rise, because: 1) it was drilled both at the summit and on the flanks and, therefore, the IODP drilling provided an opportunity to examine evidence for shoaling and/or subaerial emergence for this edifice, 2) it is known as the most heterogeneous in composition across the Shatsky Rise, 3) it contains previously uninvestigated basaltic material from volcaniclastic deposits, allowing for further investigations into potential magma compositional and mantle source heterogeneities for this edifice, and 4) it preserves fresh glass fragments at multiple core intervals and, therefore, allows for a comprehensive mineralogical and geochemical assessment of seawater alteration at this edifice by comparison of fresh and altered parts of the same eruptive units. The aims of this thesis were to determine: 1) the paleoelevations upon formation for Ori Massif, 2) the extent of compositional heterogeneity of mantle sources contributing to magmatism at Ori Massif, and 3) the extent and controls on element mobility during seawater alteration following edifice construction. Each of these aims was addressed in a separate research project, which altogether enable a better understanding of the formation of the Ori Massif.

In this Chapter, results from this thesis are further discussed in terms of physical volcanology, mantle source geochemistry and alteration of the Shatsky Rise. This Chapter contributes to the debates on the deep mantle plume versus shallow lithospheric controls on the vertical dynamics, on the nature of mantle sources at Shatsky Rise and provides implications for the origin of oceanic plateaus and LIPs in general.

6.2 IMPLICATIONS FOR THE FORMATION AND EVOLUTION OF SHATSKY RISE

6.2.1 Pyroclastic rocks: an undervalued component of Shatsky Rise?

Re-examination of the volcaniclastic deposits from Ori Massif and interpretation as being phreatomagmatic in origin (Chapter 3) provided the first evidence for explosive volcanic activity during formation of Ori Massif and overall Shatsky Rise. The recovered material from Ori Massif (Sites U1349 and U1350) includes both effusive volcanic products, including pillow lavas, sheet flows and pillow breccia, and explosive volcanic products with minor amounts of epiclastic fossiliferous limestone and a thin horizon of potentially redeposited hyaloclastite, observed as relatively thin interbeds between the eruptive units (Figures 2.8 and 6.1).

Volcaniclastic deposits are also present in the recovered stratigraphy of the Tamu and Shirshov Massifs from Shatsky Rise, where they were initially interpreted as sedimentary epiclastic (e.g., sandstone, siltstone, claystone) and primary/reworked hyaloclastite deposits based on the preliminary IODP Exp. 324 observations (Figure 2.8; Sager et al., 2010). Unlike the phreatomagmatic deposits from Site U1349, the volcaniclastic deposits from Sites U1347, 1213 and U1346 are considerably finer grained, contain variable amounts of fossils and show abundant bioturbation (e.g., burrows), clast rounding, fine lamination, flame structures and bedding (Bralower et al., 2002; Sager et al., 2010). The presence of such sedimentary structures and bioclastic material implies reworking (reshaping and resizing) of volcanic clasts, variable depositional rates and processes as well as episodes of volcanic tranquillity that allow substantial biogenic marine colonisation. However, the initial fragmentation mechanism for the volcanic material from deposits at Sites U1347, 1213 and U1346 was not necessarily epiclastic (i.e., through surface erosion or weathering) and re-investigation is required to assess the nature of primary fragmentation mechanism (e.g., initially fragmented during explosive volcanic activity (pyroclastic origin) or by contact with water during effusive volcanism (hyaloclastite origin) but subsequently reworked and/or redeposited).

The volcanic succession from Site U1348, Tamu Massif, was initially interpreted as hyaloclastite and sandstone deposits with variable amounts of biogenic material (Sager et al., 2010). Volcanic clasts from Site U1348 are almost exclusively composed of altered glass, presumably sideromelane, with minor addition of crystalline basaltic

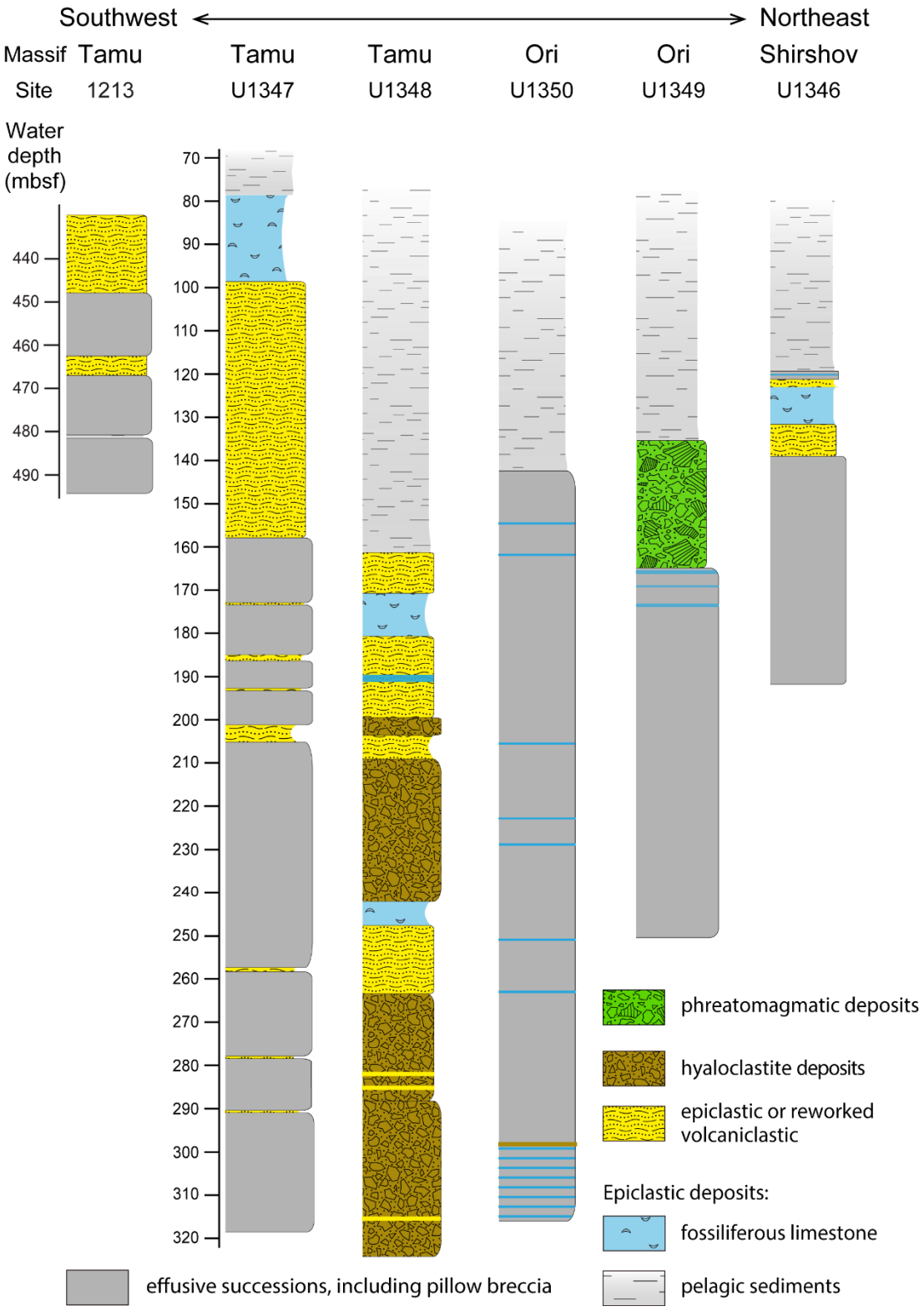

Figure 6.1. Lithologic summary of cores drilled on Shatsky Rise, modified from Figure 2.8 and Koppers et al. (2010). Effusive successions, including pillow breccia, and pelagic sediments are in dull grey colouring. Here, fossiliferous deposits are considered as epiclastic, based on their light grey to light brown colour and very high amounts of fossils with only minor additions of volcanic material. Volcaniclastic deposits are coloured, according to their inferred origin.

material (Sager et al., 2010), which makes this succession different to the mixed juvenile and lithic nature of the pyroclastic deposits from Site U1349. A hyaloclastite origin for stratigraphic units III, V and VI from Site U1348 (Figures 2.8 and 6.1) is suggested by Sager et al. (2010), because of the angularity and low vesicularity of the glassy basalts. Nevertheless, highly vesiculated fragments are also recognised in some parts of the deposits from U1348, which could be indicative of pyroclastic activity at the flank of Tamu Massif (Sager et al., 2010; personal observations). The rest of the volcaniclastic succession from Site U1348 contains abundant biogenic components and preserves evidence for reworking of the volcaniclastic material (Figure 6.1; Sager et al., 2010), making the initial fragmentation processes difficult to discern without detailed petrological investigation.

In conclusion, pyroclastic rocks and in particular phreatomagmatic deposits could be unique to Site U1349 and Ori Massif. Currently, there are no detailed studies and componentry analyses for the volcaniclastic deposits from Tamu and Shirshov Massifs, apart from the preliminary IODP Exp. 324 investigations (Sager et al., 2010). Further investigations are required on volcaniclastic deposits from Tamu and Shirshov Massifs to provide evidence for mechanisms of particle fragmentation (epiclastic, effusive/quench, explosive) along with transport and deposition processes.

6.2.2 Did any edifice from Shatsky Rise shoal to emergence?

Analysis of the new and existing evidence for shoaling and subaerial emergence for Ori Massif (Chapter 3) has found no unequivocal validation for the subaerial emergence of this edifice. Investigations from Chapter 3 suggest a submarine, potentially below wave base, depositional environment for the volcaniclastic deposits from Site U1349, drilled near the summit of Ori Massif. Currently, traces of oolites within the limestone that underlie the volcaniclastic deposits and shallow-marine faunae found within the volcaniclastic deposits remain the main evidence for Ori Massif reaching the near-shore depths upon formation (Sager et al., 2010), as oolites typically form within the shoreface (Pomar & Hallock, 2008). As Site U1349 is located at one of the highest parts of the Ori Massif summit (Zhang et al., 2015), only some very limited portions of this edifice could have reached the sea level.

Investigations on shoaling for Shirshov Massif are based on volcanic and sedimentary material, cored near the summit of this youngest Shatsky Rise edifice (Table 3.2; Chapter 3.2). Presently, the evidence from Shirshov Massif on water depth

that includes epifaunal biota (Sager et al., 2010), recently estimated shallow-marine (~500 m) eruption depths for basaltic glass from this edifice (Shimizu et al., 2013) and an absence of erosion (Zhang et al., 2015) indicate the edifice reached shallow-marine depths but was not emergent.

Geological evidence used to evaluate paleoelevations for Tamu Massif is limited to the flanks of this edifice and remains contradictory (Table 3.2; Chapter 3.2). Based on estimations of eruption depths for basalts from the flanks of Tamu Massif (Shimizu et al., 2013), two different paleoelevation values for the summit of Tamu Massif can be extrapolated: ~400 m above sea level and near sea level (Table 3.2). Shimizu et al. (2013) explained the existing discrepancy as a consequence of different initial uplift and subsidence, which were greater at the elongated northern flank of Tamu Massif, relative to its central part (Figure 1.2). Therefore, Shimizu et al. (2013) concluded that the summit of Tamu Massif was near sea level, which is largely consistent with the absence of erosional flattening on seismic profiles that would suggest subaerial emergence (Zhang et al., 2015). Nevertheless, the narrow Toronto Ridge, interpreted as part of prolonged (~15 Ma) magmatism at Tamu Massif (Tejada et al., 2016), sits ~0.6-1 km shallower than the summit of Tamu (Figure 2.5a), (Zhang et al., 2015). Consequently, the Toronto Ridge is interpreted to have been subaerial, unless the summit of Tamu Massif subsided by at least 1 km within the first 15 Myr after the culmination of the main construction phase (Sager et al., 2016).

Preliminary paleontological and sedimentological studies by Sager et al. (2010) are consistent with paleodepth estimations for the northern part of Tamu Massif by Shimizu et al. (2013), but suggest significantly greater shoaling for the eastern flank of this edifice (< 200 m deep) and overall significant subaerial emergence for Tamu's summit (Table 3.2). Such extensive shoaling and emergence for the summit of Tamu Massif could reconcile the existing discrepancy in uplift and subsidence across this largest edifice of the Shatsky Rise. Younger seamount volcanism on top of Tamu Massif (Sager et al., 1999; Zhang et al., 2015; 2016a) could potentially disguise any erosional flattening for this summit.

In conclusion, investigations from Chapter 3 and recent studies of Shimizu et al. (2013) and Zhang et al. (2015) suggest that all three Shatsky Rise edifices were largely submarine and not significantly emergent. However, detailed paleontological studies

are required to provide more precise depth estimations for the summits of the three large Massifs within the Shatsky Rise.

6.2.3 What is the compositional and temporal variation across the Shatsky Rise and associated seamounts?

New major, trace and Hf-Nd isotope data for Ori Massif reveal more heterogeneities in geochemical composition of basalts from this edifice than previously recognised (Chapter 4). Such compositional variability of magmas from Ori Massif is the greatest across the Shatsky Rise (Mahoney et al., 2005; Sano et al., 2012; Husen et al., 2013; Heydolph et al., 2014). Basalts from the summit Site U1349 of Ori Massif are the most depleted picrite-like and transitional to N-MORB-like, whereas N-MORB-like and the most enriched OIB-like compositions are associated with the flank Site U1350 (Figures 4.1; 6.2 and 6.3). The High-Nb basalts represent only a minor stratigraphic component of Shatsky Rise (Figure 4.1) and, therefore, no strong alkaline signatures or isotopic enrichments, characteristic of oceanic islands (Zindler & Hart, 1986; Hart et al., 1992; Hofmann, 2003; Stracke et al., 2005; Stracke, 2012), are observed during construction of this oceanic plateau. Nevertheless, younger magmatism from local seamounts demonstrates alkali tholeiitic affinities (Figures 6.2 and 6.3) and may be related to the Shatsky Rise formation (Tatsumi et al., 1998; Tejada et al., 2016).

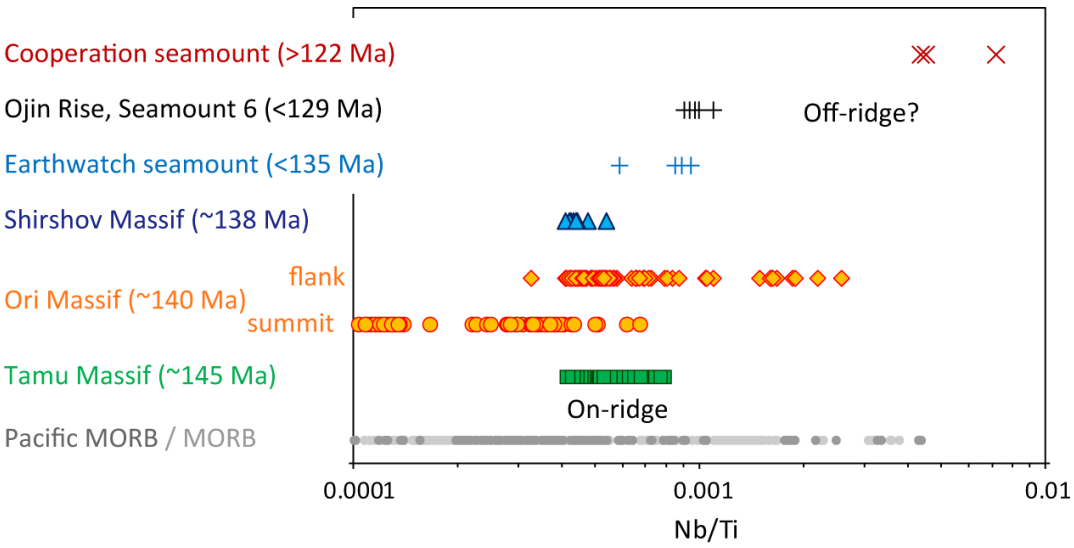

Figure 6.2. Plot illustrating temporal-compositional variation across the Shatsky Rise and local seamounts. Ages are inferred from magnetic lineations and available ^{40}Ar-^{39}Ar dating (see Chapters 2.2.3 and 2.2.7). Data are from this study, Mahoney et al., (2005), Jenner and O'Neill (2012), Sano et al. (2012), Heydolph et al., (2014) and Tejada et al. (2016).

The available Hf-Nd isotope compositions from Shatsky Rise form a trend, mainly set by compositions from Ori Massif (Figures 4.8 and 6.3). The trend starts from the most depleted end of the Pacific MORB field, intersecting mantle array, and continues towards the more enriched compositions within the PREvalent MAntle (PREMA) field. In the PREMA field, the trend goes through the Low-Ti and High-Nb type samples from Ori Massif, close to the data from Cooperation seamount and Seamount 6 from Ojin Rise, and may be continued to the more enriched compositions from Hess Rise (see maps on Figures 1.2, 2.4 and 2.5). Importantly, Pb isotope compositions from the most enriched High-Nb basalts from Ori Massif along with that from Cooperation seamount and Seamount 6, Ojin Rise and Hess Rise indicate influence of the High-μ (HIMU) component (Heydolph et al., 2014; Tejada et al., 2016). Such coincidence favours existence of a common source for the Shatsky Rise (~148-130 Ma) and younger Ojin Rise (<135 Ma), the Cooperation Seamount (>122 Ma) and Hess Rise (>90 Ma) (Figure 2.4; Pringle & Dalrymple, 1993; Sager et al., 1999; Tejada et al., 2016). It appears that mantle sources became more heterogeneous with time, during formation of Tamu and Ori Massifs and the seamounts from Shatsky Rise. However, the youngest Shirshov Massif demonstrates limited, although somewhat isotopically enriched, compositional range, similar to Tamu Massif (Heydolph et al., 2014).

Presently, the available ^{40}Ar-^{39}Ar ages for the Shatsky Rise are limited to the largest and oldest Tamu Massif (Mahoney et al., 2005; Geldmacher et al., 2014). The age estimations for the younger and smaller Ori and Shirshov Massifs as well as for seamounts in continuation of Shatsky Rise remain imprecise and are mainly based on paleomagnetic constraints from the magnetic lineations on oceanic crust (see Chapters 2.2.3 and 2.2.7). Consequently, geochronological studies are necessary for understanding the temporal relationships between the Massifs and seamounts from Shatsky Rise as well as their association with seafloor spreading. Furthermore, compositional variability of igneous rocks from the youngest Shirshov Massif is poorly understood, because the investigated lavas are limited to one eruptive unit and may not be representative of this Massif (Sager et al., 2010). Therefore, more sampling is required from the Shirshov edifice.

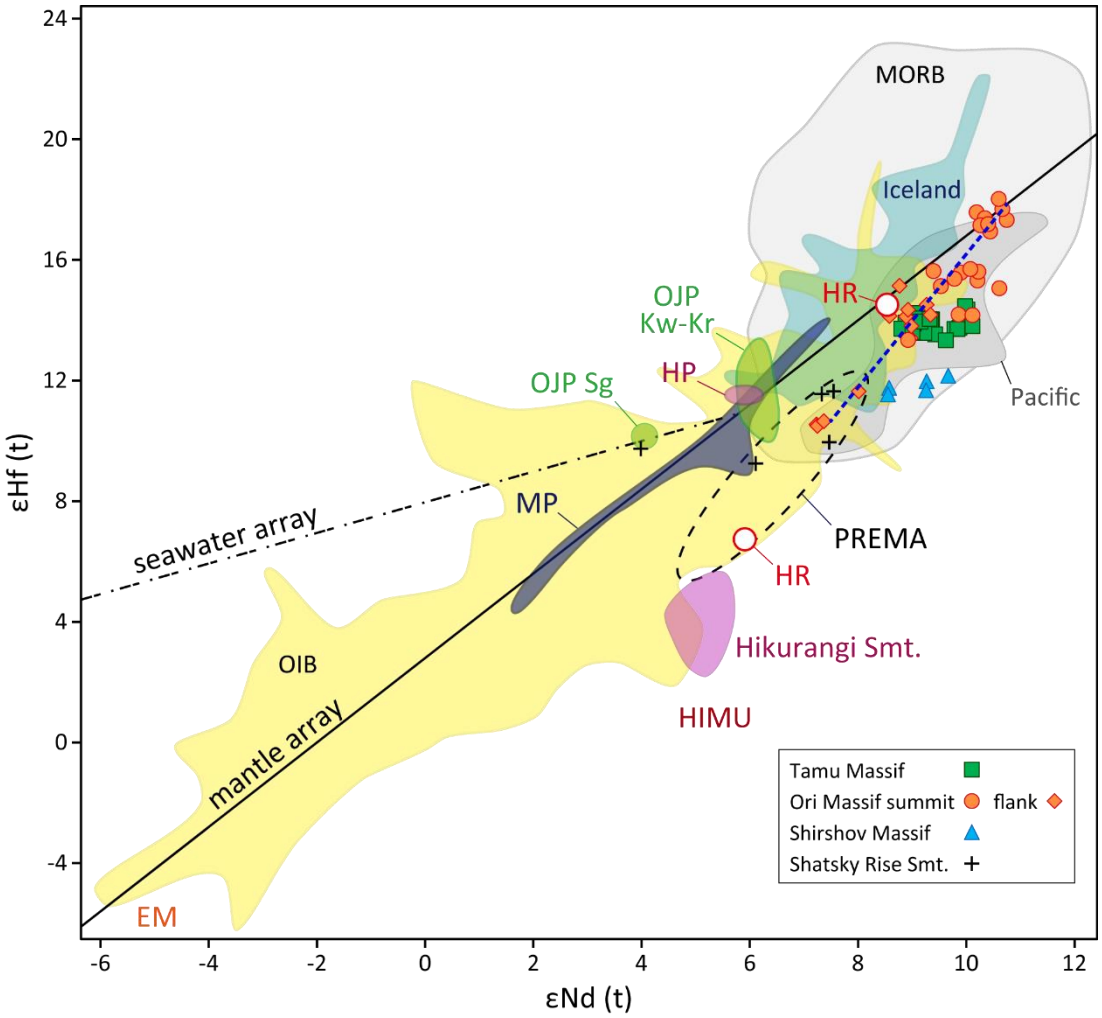

Figure 6.3. Plots of initial εNd(t) vs. initial εHf(t) for basalts from Shatsky Rise, Hess Rise (HR), Manihiki (MP), Hikurangi (HP), Ontong-Java (OJP; Singalo (Sg), Kroenke (Kr) and Kwaimbeita (Kw)-types) oceanic plateaus and seamounts from Shatsky Rise and Hikurangi. Data sources: this study, Tejada et al., (2004), Mahoney et al., (2005), Hoernle et al., (2010), Timm et al., (2011), Heydolph et al., (2014), Tejada et al. (2016). All data were recalculated according to the inferred time of emplacement, as in the data source: Shatsky Rise (140 Ma), HR (110 Ma), MP (125-117 Ma), HP (118-96 Ma), OJP (120 Ma), Seamount 6 (120 Ma), Earthwatch (120 Ma), Cooperation (122 Ma), Hikurangi (99-67 Ma) seamounts. Data for MORB and OIB (Hawaii, Galapagos, Society Islands, Samoa, Kerguelen-Heard, Pitcairn, Walvis Ridge, Comores, Azores, Cape Verdes, St. Helena, Ascension, Gough, Tristan da Cunha, Iceland, Austral-Cook) are plotted using data compilation after Stracke (2012), excluding MORB data from transform faults and MORB mixed with enriched material. Also shown PREMA (FOZO) field after Stracke et al. (2005). Fields for MORB, OIB and PREMA have been corrected for radiogenic ingrowth over 140 Ma assuming $^{147}Sm/^{144}Nd = 0.25$ and $^{176}Lu/^{177}Hf = 0.04$ (MORB), $^{147}Sm/^{144}Nd = 0.2$ and $^{176}Lu/^{177}Hf = 0.03$ (OIB), $^{147}Sm/^{144}Nd = 0.1$ and $^{176}Lu/^{177}Hf = 0.005$ (PREMA). Mantle array is defined by $\varepsilon Hf = 1.4\varepsilon Nd + 2.8$ (Geldmacher et al., 2003). Seawater array is from Goldstein and Hemming (2003). Blue dashed line identifies trend for Shatsky Rise compositions.

6.2.4 Can any spatial-temporal-compositional variations inform us about the source regions and drivers (plume or plate tectonics) for Shatsky Rise magmatism?

Investigations from Chapter 3 and recent studies of Shimizu et al. (2013) and Zhang et al. (2015) provide evidence against extensive subaerial emergence for the Shatsky Rise edifices, which is inconsistent with classical plume head model, where significant elevated topography is predicted (Korenaga, 2005). However, more recent plume models suggest both thermal and compositional differences of the plume material, relative to the surrounding mantle, which accounts for "insufficient" buoyancy and helps to explain absence of surface uplift during LIP emplacement (Dannberg & Sobolev, 2015). Nevertheless, Shatsky Rise represents a superimposed structure over a propagating triple junction of active spreading ridges, adding complexity towards an understanding of the mechanisms of its formation (Nakanishi et al., 1999; Sager, 2005; Nakanishi et al., 2015a; Sager et al., 2016). Such formation at spreading ridges on young buoyant oceanic crust is common to a number of other oceanic plateaus and hotspots, and their paleoelevations vary significantly, relative to the surrounding seafloor (Table 3.1) (Sager, 2005; O'Connor et al., 2012; Whittaker et al., 2015; Sager et al., 2016). It remains unclear if superposition on the active spreading ridge provided sufficient thermal buoyancy to elevate the Oceanic Plateau to shallow waters and/or whether dynamic uplift was driven by plume processes.

Results from Chapter 4 and studies of Mahoney et al., (2005), Sano et al. (2012), Husen et al. (2013) and Heydolph et al. (2014) demonstrate a significant contribution of the depleted MORB source during formation of the Shatsky Rise. Predominantly depleted compositions of basalts from oceanic plateaus can be explained by decompression melting of uppermost mantle beneath a spreading ridge (e.g., Anderson, 2005a; Foulger et al., 2005; Foulger, 2010). Alternatively, such compositions can be a result of heterogeneity of the mantle plume, containing enriched and depleted blobs, and surrounded by a depleted mantle sheath along with an intensive mixing of the plume material with an ambient mantle during an ascent of the plume (Griffiths & Campbell, 1990; Duncan & Richards, 1991; Kempton et al., 2000; Farnetani et al., 2002; Campbell, 2007). Such mixing with the upper mantle material is consistent with the isotope and geochemical data from Shatsky Rise and the estimated temperature anomalies that are ~50ºC higher than MORB but lower than expected for a hot mantle plume (Korenaga, 2005; Campbell, 2007; Kerr & Mahoney,

2007; Sager et al., 2016). In case of a mantle plume origin, the formation of the Shatsky Rise oceanic plateau may be explained in terms of plume head magmatism (Richards et al., 1989; Campbell, 2007). The OIB-like magmatism, observed in Cooperation and Earthwatch seamounts and Ojin Rise, commonly postdates the main plateau-building stage by ~20 Ma and is often interpreted as an ascending plume tail (Hoernle et al., 2010; Timm et al., 2011; Vanderkluysen et al., 2014; Tejada et al., 2016).

Although it is difficult to rule out which one of the two models, deep mantle plume or shallow lithospheric processes, was dominant during the formation of Shatsky Rise, it is also possible that both plume and plate drivers were active during formation of this oceanic plateau (Sager et al., 2016). Indeed, the evidence from magnetic lineations (Sager et al., 1988; Nakanishi et al., 1999; Sager, 2005; Nakanishi et al., 2015a; Sager et al., 2015), seismic studies (Sager et al., 2013; Zhang et al., 2015), age dating (Mahoney et al., 2005; Geldmacher et al., 2014) and studies on orientation of joints and veins in the drill cores (Li et al., 2016) suggest that the largest and oldest Tamu Massif was emplaced at an active triple junction of oceanic spreading ridges and formation of this edifice was closely associated with the triple junction development. However, the Shatsky Rise structure is geometrically asymmetrical (Figure 2.6), and it is debated whether Ori Massif formation was slightly off MOR axis (Li et al., 2016). Consequently, it is possible that formation of the Tamu Massif and potentially Shirshov Massif was influenced by an active spreading ridge system, whereas construction of the Ori Massif and the younger local seamounts was slightly to considerably away from MOR. Such off-MOR formation of the Ori Massif could potentially explain the greater range in vertical dynamics (Chapter 2.2.5) and compositional heterogeneity at Ori Massif (Figures 6.2 and 6.3), relative to Tamu Massif, as a result of more intense involvement of a mantle plume during construction of this edifice.

6.2.5 How did seawater alteration change the initial chemical composition of igneous and volcaniclastic rocks from Shatsky Rise?

Investigations on basalts from the flanks of Ori and Tamu Massifs (Chapter 5) demonstrated considerable element mobility during seawater alteration in the two least altered successions from Shatsky Rise. Seawater alteration of basalts from these two locations resulted in a significant disturbance of concentrations for major elements, especially Mg, and fluid-mobile elements (U, Rb, Ba, K), whereas other trace elements

usually correlate with MgO mobility indicating conservative behaviour. Both olivine-poor and olivine-phyric basalts, varying in crystallinity, present in the pillow-dominated succession from Site U1350, whereas moderately to highly crystalline olivine-poor basalts are observed in the massive flow-dominated stratigraphy of Site U1347 (Figure 5.1). Glass and olivine are found to be the most susceptible phases in basalts to seawater alteration, therefore, larger variability in alteration degree and generally more intense alteration are associated with basalts from Site U1350, Ori Massif (Figure 6.4), relative to basalts from Site U1347, Tamu Massif.

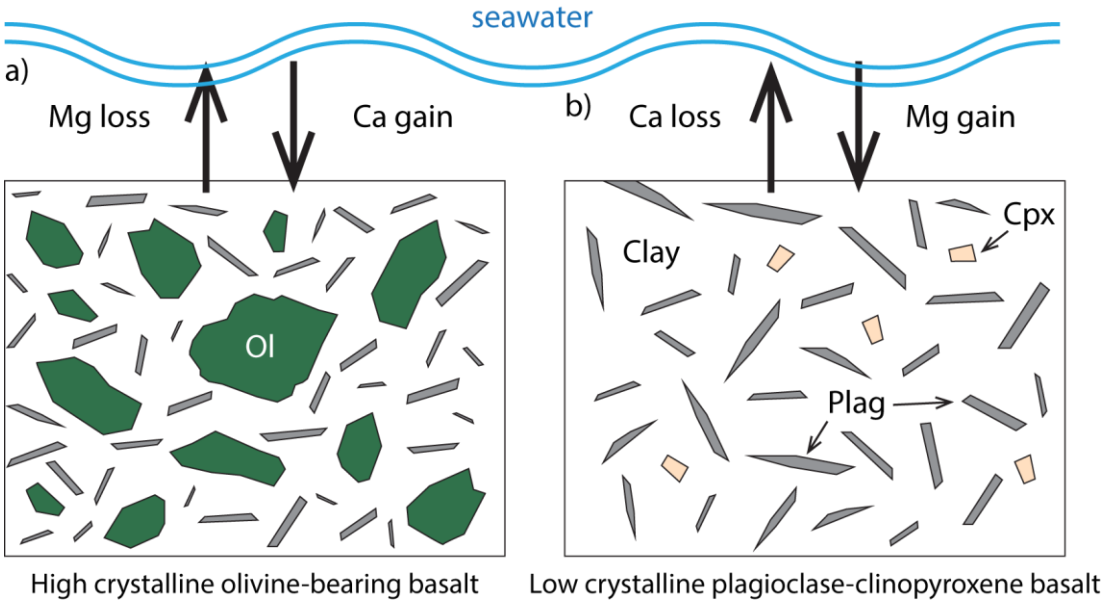

Figure 6.4. Illustrations showing seawater alteration in the two end-member types of basalt from this study. The highly crystalline olivine-bearing Higher-Mg tholeiitic basalts from Site U1350 show the largest Mg loss and Ca gain, as a result of olivine decomposition to clay minerals and calcite precipitation (a). The low crystalline olivine-poor Higher-Fe tholeiitic basalts from Site U1350 demonstrate the greatest Mg gain and Ca loss, associated with basaltic glass alteration to clay minerals (b). Abbreviations: ol, olivine; plag, plagioclase; cpx, clinopyroxene; clay, clay minerals.

Quantitative and qualitative comparison between the fresh glass and the altered whole-rock samples from other drill cores across the Shatsky Rise is complicated, because the horizons with fresh glass fragments are almost absent from these locations (Sager et al., 2010; Sano et al., 2012). Nevertheless, the alteration assessment of basalts from the flanks of Ori and Tamu Massifs (Chapter 5) allows for some assumptions on compositional change during seawater alteration of basalts from Sites U1346, Shirshov Massif, and U1349, Ori Massif, summarised below.

Thin pillow lavas, potentially from the same eruptive unit, dominate the stratigraphy of Site U1346, Shirshov Massif (Figure 2.8), and are composed of low to moderately microcrystalline basalts with variably altered plagioclase, clinopyroxene and olivine (personal observations; Sager et al., 2010). Basalts from Site U1346 demonstrate carbonate replacement of olivine and clinopyroxene, where present, and therefore have potentially lost some Mg and gained Ca (Figure 6.4a). However, significant amounts of secondary minerals are observed in these basalts (60-80%), with clay minerals replacing glassy mesostasis, plagioclase and pyroxene (Sager et al., 2010; personal observations), suggesting Mg gain and Ca loss (Figure 6.4b). Comparison of major element compositions from the whole-rock basalts with those from the unique fresh glass horizon at Site U1346, available from Sano et al. (2012), also support Mg fixation and Ca release during alteration of basalts from the Shirshov summit.

Presently, no fresh glass fragments are observed in the recovered material from Site U1349, Ori Massif, and therefore the initial magmatic composition of basalts from U1349 type, unique to this location, remains poorly understood. Furthermore, a wide assemblage of secondary minerals is observed in these basalts (Chapter 2.2.8), indicating that there could be additional mechanisms of element mobility, relative to basalts from the flanks of Ori and Tamu Massifs. Nevertheless, effusive rocks from Site U1349 are characterised by higher contents of olivine, relative to Higher-Mg tholeiite basalts from Site U1350, suggesting Mg loss and Ca gain (Figure 6.4a). Strong Mg release to seawater in effusive basalts from Site U1349 is consistent with major element compositional difference between these picrite-like basalts (Sano et al., 2012) and picrites from Iceland, where MgO elevates up to 30 wt. % (Kokfelt et al., 2006; Peate et al., 2009). Chemical change during olivine alteration in the U1349 type basalts could be evaluated by comparing compositions of the olivine alteration products and fresh olivine found in the two horizons within the U1349 succession (personal observations; Almeev et al., 2011).

Basalts from volcaniclastic deposits demonstrate the greatest degrees of alteration across the Shatsky Rise (Chapters 2.2.8 and 4; Figure 6.1). Fragments of volcanic glass, now completely replaced with carbonates, palagonite and clay minerals, compose most of the volcaniclastic successions from Sites U1349 (Table 3.3) and U1348 (Sager et al., 2010; Sano et al., 2012; Sager et al., 2016). Consequently,

the primary magmatic compositions along with element mobility during alteration for such fragments are not possible to deduce. Lithic fragments from phreatomagmatic deposits at Site U1349, Ori Massif, are highly altered as well, showing the greatest variability of major element compositions in crystalline basalts across the Shatsky Rise (Chapter 4; Figure 4.2).

In conclusion, the degree of seawater alteration in Shatsky Rise volcanic complex is largely dependent on basement stratigraphy (lava flows, pillow lava, volcaniclastic rocks), cooling rates, affecting crystallinity and grain size, and magma chemistry, particularly the amount of olivine.

6.3 IMPLICATIONS FOR THE FORMATION AND EVOLUTION OF OCEANIC PLATEAUS AND LIPS IN GENERAL

6.3.1 Mafic volcaniclastic deposits in LIPs

Volcaniclastic deposits have been increasingly recognised as an important stratigraphic component in many LIPs (Ross et al., 2005; Thordarson et al., 2009; White et al., 2009; Bryan et al., 2010; Bryan & Ferrari, 2013). Volcaniclastic products contribute significant thicknesses and volumes of most continental LIPs, including Ferrar-Karoo (Ross & White, 2005; McClintock & White, 2006; Elliot & Fleming, 2008), Emeishan (Ukstins Peate & Bryan, 2008), Siberia (Black et al., 2015; Jerram et al., 2016). Many of the volcaniclastic deposits from continental LIPs are of phreatomagmatic origin and are associated with the beginning of continental flood basalt volcanism (Ross et al., 2005; Thordarson et al., 2009; White et al., 2009). In subaqueous environments, volcaniclastic rocks of phreatomagmatic origin commonly intercalate with hyaloclastite deposits and marine sedimentary units, as suggested from studies on continental LIPs (Ross et al., 2005).

Volcaniclastic deposits are also observed in oceanic plateaus (e.g., Ontong Java Plateau, Caribbean-Colombian, Walvis Ridge; Table 3.1) and are potentially an important component contributing to oceanic LIP construction. Volcaniclastic rocks from oceanic plateaus are commonly associated with hyaloclastite (e.g., Shatsky Rise (Figures 2.8 and 6.1); Manihiki (Jenkyns, 1976); Wrangellia (Greene et al., 2010); Caribbean-Colombian (Kerr, 2014)), formed by fragmentation of effusive lava during chilling from contact with water (White & Houghton, 2006). Currently, only a small number of studies, focusing on the origin (pyroclastic versus epiclastic) of

volcaniclastic deposits from oceanic plateaus, provide evidence for explosive volcanic activity to take place on oceanic LIPs (Shatsky Rise (Chapter 3); Ontong Java Plateau (Thordarson, 2004); Kerguelen (Bitschene et al., 1992; Frey et al., 2003); Caribbean-Colombian (Wright & Wyld, 2011); Table 3.1). Studies from the Ontong Java Plateau and Kerguelen oceanic plateaus suggest that subaerial phreatoplinian eruptions were responsible for formation of hundreds of meters thick phreatomagmatic deposits during late stages of construction of these two largest oceanic plateaus (Bitschene et al., 1992; Thordarson, 2004). Investigations from Chapter 3 demonstrate that shallow-marine phreatomagmatic deposits may be an important component of the Shatsky Rise stratigraphy. In contrast, studies from Wrangellia (Greene et al., 2010) suggest only minor amounts of subaerial pyroclastic rocks in the volcanic stratigraphy of this accreted oceanic plateau. In conclusion, late-stage phreatomagmatic activity in shallow-marine to subaerial environments is potentially a common scenario during oceanic plateau formation.

6.3.2 Implications for oceanic plateau formation at an active triple junction of oceanic spreading ridges

Formation of Shatsky Rise at an active triple junction of oceanic spreading ridges has potentially influenced both vertical dynamics and magmatic composition of this oceanic plateau. It is suggested that the plateau construction at an active spreading ridge system leads to decrease in paleoelevations and subsidence, potentially as a result of more intense magma delivery to the surface and lateral growth of the volcanic construction. The latter is consistent with new evidence on anomalously low slopes for the Tamu Massif edifice (Sager et al., 2013) and prolonged duration of its magmatism (Geldmacher et al., 2014; Tejada et al., 2016).

Shatsky Rise differs from other oceanic plateaus by two key compositional features: it is dominated by depleted to highly depleted DMM end-member Nd and Hf isotopic compositions (Chapters 2.2.7 and 4) and, while all samples analysed to date from the Shatsky Rise plot in the MORB field, this plateau has a wider scatter of Hf-Nd isotope compositions compared with other oceanic plateaus (Figure 6.3). Similar Hf-Nd isotope compositions and variability are observed in basalts from Iceland, which has slightly more radiogenic εHf for a given εNd relative to Shatsky Rise within the field for Atlantic MORB (Figure 6.3). Importantly, the Hf-Nd isotope compositions from Icelandic basalts are the most depleted, relative to basalts from other hotspots

(Koornneef et al., 2012; Stracke, 2012). Both Shatsky Rise and Iceland are characterised by an intense interaction with an active spreading ridge system upon emplacement (Smallwood et al., 1995; Nakanishi et al., 1999; Sager, 2005). Consequently, a significant contamination by depleted mantle material at these oceanic structures may be associated with more intense entrainment of the upper mantle substrate, as a result of superposition of an ascending upper-mantle convective flow on an emerging deep-mantle plume. The observed variations in petrological, geochemical and isotope compositions in basalts from Shatsky Rise and Iceland are also likely related to the plume-ridge interaction, where melt extraction from different mantle components and a large range of depths with incomplete melt mixing takes place (Thirlwall et al., 2004; Stracke & Bourdon, 2009; Peate et al., 2010; Koornneef et al., 2012; Stracke, 2012; Sager et al., 2016).

6.3.3 Enriched and depleted source components in oceanic plateaus

Results from this study (Chapter 4) and investigations by Heydolph et al. (2014) demonstrate a significant contribution of the depleted MORB source during formation of the Shatsky Rise, which is inconsistent with data from other oceanic plateaus (Geldmacher et al., 2003; Thompson et al., 2003; Shafer et al., 2004; Tejada et al., 2004; White et al., 2004; Kerr & Mahoney, 2007; Hastie & Kerr, 2010; Hoernle et al., 2010; Timm et al., 2011; Tejada et al., 2013; Kerr, 2014). Importantly, the Hf-Nd isotope compositions from Shatsky Rise, Hess Rise and seamounts connecting these two oceanic plateaus lie distinctively below the mantle array, whereas the Hf-Nd isotope data from the Ontong Java, Manihiki and Hikurangi oceanic plateaus tend to plot on and above the mantle array (Figure 6.3). This compositional discrepancy between the two groups of Cretaceous oceanic plateaus is probably related to slight chemical variations between the Indian and Pacific MORB source mantle domains (Pearce et al., 1999; Vlastélic et al., 1999; Kempton et al., 2002; Pearce et al., 2007), which is in agreement with recent geodynamic reconstructions for locations of these LIPs at the moment of their formation (Figures 2.2 and 6.5) (Nakanishi et al., 1999; Kuz'min et al., 2003; Sager, 2005; Taylor, 2006; Torsvik et al., 2006; Davy et al., 2008; Li & Zhong, 2009; Chandler et al., 2012; Chandler et al., 2015; Miyazaki et al., 2015). Accordingly, Shatsky Rise and, likely, later Hess Rise were emplaced at a triple junction of the Pacific, Izanagi and Farallon oceanic plates at the northern margin of the Pacific Large Low-Velocity Province (LLVP) under the influence of the Pacific

MORB source mantle domain. The greater Ontong Java Nui, comprising Ontong Java, Manihiki and Hikurangi oceanic plateaus, was formed on young Pacific oceanic crust (up to 40 Ma; Ishikawa et al., 2005) at the southern margin of the Pacific LLVP and above the Indian MORB source mantle domain.

Minor amounts of isotopically enriched components are found in the two groups of Pacific oceanic plateaus and potentially highlight an input from the South Pacific Isotopic and Thermal Anomaly (SOPITA). The SOPITA is interpreted as a persistent zone of upwelling from the lower mantle, which has been active and stable at least since the Cretaceous, and also separates the two large mantle domains, Indian and Pacific, with their own convection histories (Staudigel et al., 1991; Vlastélic et al., 1999). SOPITA is associated with the large-scale (>6000 km) seismically slow anomaly of LLVP below Pacific, which is proposed as a region of upwelling of deep mantle material rising from the core-mantle boundary, commonly referred to as the Pacific "superplume", potentially responsible for formation of many Pacific LIPs and OIBs since the Cretaceous (Figure 6.5) (Koppers et al., 1995; Romanowicz & Gung, 2002; Torsvik et al., 2006; Li & Zhong, 2009; Miyazaki et al., 2015).

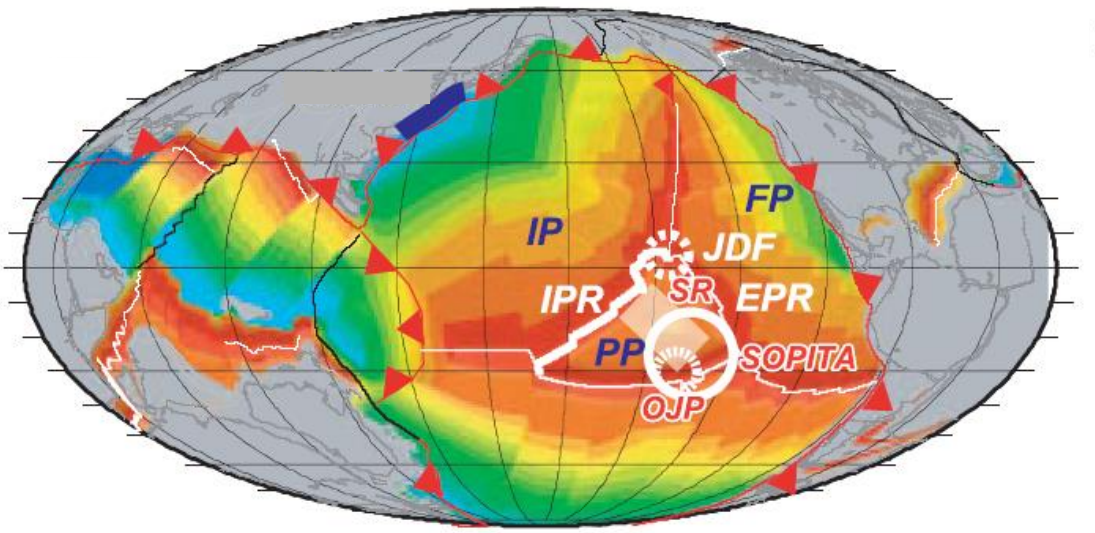

Figure 6.5. Plate tectonic reconstruction for the 140 Ma timeframe, illustrating the emplacement of Shatsky Rise (SR) at a triple junction of Pacific (PP), Farallon (FP) and Izanagi (IP) plates. Also shown are the locations of the Ontong Java Plateau (OJP), emplaced on ~10-20 My Pacific crust at 120 Ma. Abbreviations: IPR, Izanagi Pacific Ridge; JDF, Juan de Fuca Ridge; EPR, East Pacific Rise; SOPITA, South Pacific Thermal and Isotopic Anomaly. Source: (Miyazaki et al., 2015).

6.3.4 Implications for alteration of oceanic plateaus

Basaltic lavas from the flanks of the submarine Shatsky Rise oceanic plateau show predominantly non-pervasive smectitic alteration with slight to considerable element mobility as a result of low-temperature alteration processes (zeolite facies, below 300ºC; Chapter 5). This is similar to off-axis seawater alteration processes occurring during MORB ageing and that on the other submarine plateaus and oceanic islands (e.g., Alt, 1995; Clayton & Pearce, 2000; Stroncik & Schmincke, 2002; Banerjee et al., 2004; Drief & Schiffman, 2004; Schramm et al., 2005; Marks et al., 2010). Despite this similarity, the change of oceanic plateau chemistry *en masse* during seawater alteration may differ from that on MORB. LIPs, including oceanic plateaus, are often associated with thicker lava flows and higher temperatures upon formation (Bryan & Ernst, 2008; White et al., 2009; Kerr, 2014), and may lead to comparatively slower cooling rates, resulting in higher crystallinity and lower alteration degree. This is particularly the case for the largest and oldest Tamu Massif, which stratigraphy is dominated by thick lava flows (Figure 4.1). On the other hand, volcaniclastic deposits potentially compose a significant proportion of the Shatsky Rise (Figures 2.8 and 6.1), as well as other oceanic LIPs (Table 3.1; Bitschene et al., 1992; Frey et al., 2003; Shafer et al., 2004; Thordarson, 2004; Ross et al., 2005; White et al., 2009; Wright & Wyld, 2011), and are subjected to an intense alteration in seawater-rich environment (Chapters 4 and 6.2.5).

6.3.5 Implications for Mg mobility within oceanic crust, seawater and related systems

There are two key implications for Mg mobility. The first is on oceanic crust in general. This research identified that during low temperature seawater alteration Higher-Fe tholeiitic basalts consume Mg from seawater through smectite formation, whereas Higher-Mg tholeiitic basalts containing normative olivine provide additional Mg to seawater. This Mg contribution to seawater is in addition to the generally considered Mg sources of weathered continental crust and seawater-altered olivine-rich rocks from lower oceanic crust and mantle peridotites exposed at slow spreading ridges (Albarède & Michard, 1986; Snow & Dick, 1995; Bach et al., 2001; Ligi et al., 2013). This means that the relative proportion of altered olivine-phyric versus olivine-poor rocks in the oceanic crust significantly impacts on the Mg cycle in the oceans along with the continental crust weathering rates. This could indicate a greater Mg

redistribution within the oceanic crust rather than an element migration to or from the oceanic crust.

The second key implication for Mg mobility is that the alteration of rocks from oceanic LIPs and OIB events provides an additional source of Mg for seawater during olivine alteration, because LIPs and OIBs contain a larger proportion of olivine-bearing rocks, such as olivine tholeiites and alkaline olivine basalts, picrites and other Mg-rich rocks, in comparison to MORB (Campbell, 2005; Kerr & Mahoney, 2007; Bryan & Ernst, 2008; Kerr, 2014). Because of their areal extent, greater lithospheric thickness and buoyancy relative to typical oceanic crust, oceanic plateaus are more likely to contribute to continental crust growth rather than return back to mantle (e.g., Ben-Avraham et al., 1981; Cloos, 1993; Saunders et al., 1996; Kamber, 2010; Kerr, 2014). The chemical composition of altered oceanic plateaus is therefore of global importance for geochemical mass balance estimations between continental crust and mantle.

6.4 SUMMARY POINTS

Research from this study has enabled a better understanding of the physical volcanology, magmatic composition and controls on element mobility during seawater alteration of Ori Massif and provided new insights into the origin and evolution of the Shatsky Rise oceanic plateau. The following contributions have been made:

- Shallow-marine to near sea-level Surtseyan phreatomagmatic eruptions mark the late stage of Ori Massif construction.
- Ori Massif was largely submarine and might never been subaerially emergent, similar to other edifices from Shatsky Rise.
- Late-stage phreatomagmatic activity in shallow-marine to subaerial environments is potentially a common scenario during oceanic plateau formation.
- Pyroclastic deposits are potentially an important stratigraphic component of the Shatsky Rise as well as other oceanic plateaus.
- Compositional variability of magmas from Ori Massif is the greatest across the Shatsky Rise. Basalts from the summit of Ori Massif are the most depleted picrite-like and transitional to N-MORB-like, whereas N-MORB-like and the most enriched OIB-like compositions are associated with the flank of Ori edifice.

- The Hf-Nd isotope compositions of basalts from this study indicate a relatively more depleted Pacific MORB component in the compositional variety of volcanic products from Ori Massif.
- The Hf-Nd isotope compositions from Shatsky Rise, Hess Rise, Ojin Rise and Cooperation seamount follow a common compositional trend, suggesting mixing of a common depleted Pacific MORB source mantle with an enriched component, such as PREMA or HIMU. The compositional difference between these oceanic structures and the greatest Cretaceous Ontong Java Nui, comprising Ontong Java, Manihiki and Hikurangi oceanic plateaus, is probably related to slight chemical variations between the Pacific and Indian MORB source mantle domains.
- Emplacement of the Shatsky Rise oceanic plateau at an active triple junction of oceanic spreading ridges has significantly affected geochemical composition of the plateau basalts, similarly to basalts from the ridge-centred Iceland hotspot. Shatsky Rise shows more depleted Hf-Nd isotope compositions and more variety within the MORB field, comparatively to other oceanic plateaus that were formed independently from ridge tectonics.
- Greater range in vertical dynamics and compositional heterogeneity in Ori Massif, relative to Tamu Massif, could be explained by Ori Massif formation slightly off-MOR axis, allowing for a more intense involvement of a mantle plume during construction of this Shatsky Rise edifice.
- The degree of seawater alteration in Shatsky Rise volcanic complex is largely dependent on stratigraphy (lava flows, pillow lava, volcaniclastic rocks), cooling rates, affecting crystallinity and grain size, and magma chemistry, particularly the amount of olivine.
- Two compositionally different alteration types of basalt are found in Ori Massif, olivine-bearing Higher-Mg tholeiitic basalts and olivine-free Higher-Fe tholeiitic basalts. Only Higher-Fe tholeiitic basalts are found in Tamu Massif.
- Seawater alteration of high-crystalline (<10% glass) olivine-bearing Higher-Mg tholeiitic basalts releases significant soluble Mg^{2+} (2-3 wt.% of MgO), whereas high-crystalline olivine-free Higher-Fe tholeiitic basalts show no significant change in MgO composition. A decrease in crystallinity in both groups is associated with increased smectitic clay formation and correlated with relatively higher Mg and lower Ca.

- Variations in Mg due to olivine and glass alteration in basalts are accompanied by passive accumulation or dilution of many trace elements, excluding the fluid-mobile elements U, Rb, Ba, and K that are usually enriched in the altered rocks from Shatsky Rise.
- Alteration of Higher-Mg rocks from oceanic LIPs may provide an additional source of Mg for seawater.
- Estimations on relative proportion of seawater-altered olivine-phyric versus olivine-poor rocks in the oceanic crust will give insight on Mg mobility in seawater-oceanic crust system.

Appendices

Appendix A. Major and trace element compositions for basalts from volcaniclastic deposits, Site U1349, Ori Massif.

Appendix B. Optical microscopy observations and mineral compositions for samples from Sites U1350 and U1347, Ori and Tamu Massifs, respectively.

Appendix C. Major and trace element compositions for whole-rock and fresh glass sample pairs from Sites U1350 (Ori Massif) and U1347 (Tamu Massif). Data from Sano et al. (2012).

Appendix D. Mineral XRD patterns for samples from Sites U1350 and U1347, Ori and Tamu Massifs, respectively.

Appendix E. Clay XRD patterns for samples from Sites U1350 and U1347, Ori and Tamu Massifs, respectively.

Appendix F. Median values for variables within each subcluster after hierarchical cluster analysis, samples from Sites U1350 and U1347, Ori and Tamu Massifs, respectively.

APPENDIX A. MAJOR AND TRACE ELEMENT COMPOSITIONS FOR BASALTS FROM VOLCANICLASTIC DEPOSITS, ORI MASSIF

Sample	1a	1b	2a	2b	2c	2d	2e	2f	2h	2i	2j
Core section	5R1	5R1	5R1	5R1	5R1	5R1	5R1	5R1	5R1	5R1	5R1
Interval (cm)	13-15	13-15	30-32	30-32	30-32	30-32	30-32	30-32	30-32	30-32	30-32
Depth (mbsf)	144.95	144.95	145.12	145.12	145.12	145.12	145.12	145.12	145.12	145.12	145.12
Unit	3	3	3	3	3	3	3	3	3	3	3
Composition	lithic	lithic			lithic		lithic		lithic	lithic	
ICPOES (wt. %)		n=2	n=2				n=2				
SiO_2	40.6	44.4	42.3	41.3	39.3	45.7	38.8	45.1	41.5	40.9	
TiO_2	3.56	3.27	3.87	2.30	2.19	2.95	2.13	2.30	2.38	2.58	
Al_2O_3	18.2	15.8	15.4	15.7	17.0	16.6	16.9	15.1	16.0	15.8	
Fe_2O_3	15.5	14.7	16.1	15.3	16.9	10.5	14.6	10.3	13.7	14.6	
MnO	0.10	0.14	0.09	0.11	0.15	0.11	0.17	0.11	0.09	0.10	
MgO	6.80	6.78	6.89	8.91	9.89	6.33	6.59	5.95	5.87	7.54	
CaO	1.56	1.64	2.51	1.85	3.67	3.77	9.21	4.05	5.17	6.29	
Na_2O	2.40	1.29	1.56	4.32	1.74	1.34	2.33	2.52	2.06	1.88	
K_2O	2.19	5.64	4.86	1.51	1.77	7.03	1.78	6.02	5.34	4.42	
P_2O_5	0.43	0.65	0.75	0.98	0.18	0.35	0.22	0.21	0.27	0.31	
LOI	7.11	5.48	5.17	8.07	6.72	2.05	9.15	8.90	6.95	7.06	
Total	98.44	99.79	99.54	100.33	99.57	96.78	101.90	100.58	99.22	101.49	
ICPMS (ppm)			n=2								
Li	84.5	57.5	72.7	66.4	57.7	54.3	46.8	38.8	55.9	63.0	77.3
Sc	49.0	41.1	53.3	38.8	54.8	24.9	49.8	26.6	37.8	39.5	53.9
V	730	607	639	433	462	533	456	441	440	428	545
Cr	75.8	220	39.3	42.8	337	59.8	115	43.5	55.2	54.1	75.7
Co	45.4	57.9	127	43.8	55.9	81.8	56.4	58.4	39.8	44.0	79.2
Ni	89.4	112	84.0	78.2	100	103	78.5	96.4	62.1	81.1	81.1
Cu	50.5	274	70.5	68.2	51.8	138	193	108	143	134	127
Zn	502	640	650	94.9	336	288	83.3	236	60.1	45.5	365
Rb	13.7	37.2	30.4	24.7	11.3	38.7	11.6	43.7	28.0	23.5	39.7
Sr	85.3	135	149	62.7	64.8	165	110	107	152	127	164
Y	48.5	71.0	130	94.1	26.9	56.7	35.2	30.3	44.1	42.0	72.0
Zr	239	175	262	172	115	136	127	109	160	148	157
Nb	9.17	6.35	7.79	5.54	3.21	5.37	5.13	4.26	6.27	6.48	5.49
Cs	0.069	0.249	0.269	1.71	0.043	0.048	0.058	0.054	0.054	0.059	0.041
Ba	94.8	218	124	21.9	70.9	213	75.3	129	164	141	255
La	9.41	9.23	12.9	13.5	3.70	5.81	4.75	3.23	6.70	6.70	7.25
Ce	25.0	25.8	37.7	33.6	10.7	19.6	13.2	10.9	18.6	18.9	24.8
Pr	4.00	4.28	6.52	5.38	1.79	3.44	2.11	1.97	3.02	3.11	4.49
Nd	20.5	23.1	36.0	28.9	9.57	19.5	11.2	10.8	15.4	15.8	25.3
Sm	6.69	7.83	12.6	10.2	3.41	7.01	3.94	3.98	5.23	5.35	9.30
Eu	1.69	2.42	4.53	4.02	0.906	2.58	1.35	1.45	1.65	1.58	3.54
Gd	7.92	10.2	17.8	13.7	4.29	9.57	4.86	5.16	6.27	6.46	12.5
Tb	1.36	1.80	3.09	2.34	0.756	1.62	0.886	0.880	1.14	1.15	2.11
Dy	8.42	11.2	19.9	14.2	4.69	9.72	5.91	5.37	7.27	7.12	12.6
Ho	1.75	2.31	4.21	2.98	0.989	1.91	1.30	1.08	1.54	1.47	2.44
Er	4.89	6.48	11.4	8.02	2.76	5.00	3.78	2.84	4.47	4.07	6.04
Tm	0.699	0.933	1.56	1.13	0.411	0.677	0.587	0.399	0.691	0.619	0.776
Yb	4.08	5.34	8.49	6.35	2.43	3.59	3.51	2.22	4.05	3.48	3.95
Lu	0.615	0.762	1.26	1.03	0.377	0.538	0.516	0.335	0.639	0.520	0.580
Hf	6.64	5.44	7.75	4.64	3.31	3.61	3.57	3.04	4.30	4.12	4.99
Ta	0.561	0.394	0.532	0.293	0.198	0.412	0.288	0.307	0.376	0.382	0.411
Tl	0.047	0.174	0.413	0.630	0.384	0.207	0.643	0.215	0.299	0.230	0.126
Pb	0.541	0.605	0.826	0.632	0.389	0.554	0.374	0.529	0.713	0.581	0.536
Th	0.684	0.424	0.592	0.319	0.228	0.418	0.312	0.307	0.445	0.465	0.497
U	1.62	1.78	4.53	2.82	0.62	3.69	0.795	2.65	1.07	0.880	3.17

Thin sections are available for samples marked with stars (*). Abbreviations: juv = juvenile; mbsf = meters below sea floor; n = number of analyses, where more than 1.

Appendix A. Continued

Sample	2k	2m	3a	3b	3c	3d	3f	3g	3h	3i	3j
Core section	5R1	5R1	5R1	5R1	5R1	5R1	5R1	5R1	5R1	5R1	5R1
Interval (cm)	30-32	30-32	41-42	41-42	41-42	41-42	41-42	41-42	41-42	41-42	41-42
Depth (mbsf)	145.12	145.12	145.23	145.23	145.23	145.23	145.23	145.23	145.23	145.23	145.23
Unit	3	3	3	3	3	3	3	3	3	3	3
Composition			lithic*	lithic		lithic	lithic	lithic	lithic		lithic
ICPOES (wt. %)	n=2										
SiO_2	41.5	51.9	43.7	47.2	37.4	42.1	41.2	43.5	46.1	46.8	48.6
TiO_2	2.61	3.36	2.38	2.71	1.86	2.09	1.73	2.61	2.68	4.10	3.33
Al_2O_3	14.9	18.3	16.2	17.6	13.6	16.6	15.6	18.6	16.2	17.7	17.2
Fe_2O_3	9.73	7.18	16.1	14.1	17.8	13.9	11.9	14.8	13.2	15.1	17.6
MnO	0.14	0.16	0.11	0.05	0.12	0.09	0.20	0.10	0.06	0.10	0.06
MgO	5.50	1.50	7.75	6.47	8.41	7.61	7.54	7.24	5.89	5.45	6.08
CaO	7.13	3.32	4.20	3.45	4.74	4.08	10.1	2.36	3.18	4.57	5.74
Na_2O	1.54	1.32	2.43	2.67	3.21	2.33	2.28	2.30	2.36	3.55	3.94
K_2O	6.57	10.4	3.84	4.80	1.94	2.81	3.58	3.06	4.90	2.82	1.20
P_2O_5	0.29	0.34	0.26	0.30	0.63	0.22	0.15	0.22	0.31	0.48	0.97
LOI	9.66	2.05	5.14	2.40	11.8	7.14	8.76	6.79	3.90	0.00	
Total	99.61	99.81	102.08	101.84	101.49	99.01	102.97	101.60	98.89	100.71	104.69
ICPMS (ppm)											
Li	46.4		43.4	33.4	61.4	53.3	38.3	53.8	30.9		23.0
Sc	37.5		43.6	40.0	40.9	50.9	49.4	52.6	39.7		26.6
V	509		455	470	333	416	486	458	467		290
Cr	50.5		90.1	89.6	31.2	38.8	234	194	88.3		15.4
Co	70.1		38.4	27.2	41.9	32.7	93.1	44.8	27.8		53.0
Ni	89.7		51.5	41.3	62.8	47.5	129	65.1	40.6		49.0
Cu	119		145	154	48.1	109	179	256	155		23.7
Zn	300		281	301	72.5	67.1	48.5	406	351		70
Rb	47.5		24.3	22.0	37.5	19.8	18.7	16.8	23.1		6.47
Sr	144		108	153	56.3	96.0	108	96.4	155		145
Y	48.0		45.6	32.0	99.1	40.4	40.6	37.5	33.0		119
Zr	123		131	174	150	120	86	139	179		356
Nb	4.95		4.43	6.74	5.15	4.55	2.54	4.12	6.88		12.0
Cs	0.058		0.171	0.028	2.11	0.169	0.040	0.063	0.040		0.020
Ba	164		65.4	113	4.55	45.9	80.8	53.8	113		43.4
La	5.11		5.01	5.96	10.5	5.73	3.98	4.37	6.15		15.6
Ce	17.0		14.3	15.9	33.2	14.8	11.3	12.9	16.9		45.5
Pr	2.97		2.46	2.53	5.69	2.51	1.95	2.31	2.70		7.69
Nd	16.5		13.6	12.8	31.5	13.2	10.9	12.4	13.5		41.0
Sm	5.89		4.89	4.08	11.1	4.62	3.76	4.27	4.47		13.5
Eu	2.10		1.57	1.53	4.60	1.51	1.32	1.38	1.57		4.26
Gd	7.73		6.37	4.90	15.8	5.80	5.60	5.44	5.27		17.4
Tb	1.36		1.15	0.861	2.78	1.04	0.964	0.979	0.924		3.00
Dy	8.23		7.51	5.39	17.3	6.84	6.37	6.12	5.76		18.4
Ho	1.66		1.64	1.14	3.47	1.47	1.47	1.30	1.19		3.92
Er	4.35		4.75	3.27	9.07	4.29	4.19	3.72	3.31		10.7
Tm	0.597		0.715	0.500	1.23	0.629	0.654	0.564	0.518		1.53
Yb	3.26		4.31	2.95	6.49	3.84	4.00	3.29	2.96		8.40
Lu	0.512		0.683	0.473	1.01	0.593	0.647	0.504	0.473		1.27
Hf	3.44		3.72	4.67	3.58	3.39	2.47	3.90	4.78		9.49
Ta	0.359		0.259	0.393	0.220	0.260	0.147	0.260	0.405		0.768
Tl	0.154		0.067	0.096	0.176	0.083	0.692	0.241	0.095		0.065
Pb	0.542		0.417	0.592	0.293	0.492	0.635	0.930	0.617		0.312
Th	0.361		0.204	0.506	0.236	0.240	0.145	0.237	0.523		0.929
U	3.04		0.145	0.374	1.061	0.197	0.167	0.168	0.310		0.380

Appendix A. Continued

Sample	3k	4a	4b	5a	5b	6a	7a	7c	8a	8b	8c
Core section	5R1	5R1	5R1	5R3	5R3	5R5	6R1	6R1	6R1	6R1	6R1
Interval (cm)	41-42	58-59	58-59	3-5	3-5	110-111	56-59	56-59	88-93	88-93	88-93
Depth (mbsf)	145.23	145.40	145.40	147.54	147.54	151.45	155.06	155.06	155.38	155.38	155.38
Unit	3	3	3	2	2	2	2	2	2	2	2
Composition	lithic	lithic*	lithic			lithic	lithic	lithic			lithic
ICPOES (wt. %)	n=2							n=2			
SiO_2	47.8	43.5	47.5	39.6	41.5	52.1	49.9	48.9	45.7	36.0	
TiO_2	3.30	2.71	2.80	2.25	1.77	2.17	2.53	3.15	1.67	1.42	
Al_2O_3	15.3	17.2	15.5	10.6	9.9	18.0	14.2	15.5	13.8	10.0	
Fe_2O_3	18.0	13.6	16.1	12.0	16.1	10.4	11.7	12.7	10.3	8.77	
MnO	0.14	0.08	0.07	0.15	0.09	0.04	0.04	0.09	0.10	0.14	
MgO	4.97	4.54	4.99	5.98	8.61	4.44	4.99	3.85	4.23	4.92	
CaO	4.32	4.70	3.15	12.4	7.97	2.91	4.96	4.94	10.6	21.5	
Na_2O	4.84	2.34	2.29	1.44	1.69	2.30	2.41	2.73	2.72	2.20	
K_2O	0.71	3.14	4.19	4.67	3.21	5.68	4.48	4.51	3.69	1.84	
P_2O_5	0.52	0.26	0.35	0.87	0.44	0.22	0.90	0.24	0.18	0.46	
LOI	1.02	7.29	5.32	12.5	9.76	3.80	3.36	3.22	9.89	15.3	
Total	100.92	99.36	102.19	102.32	101.03	102.10	99.51	99.91	102.90	102.56	
ICPMS (ppm)		n=7	n=2					n=2	n=2		
Li	35.5	46.8	34.8	42.6	46.3	46.0	26.3	18.9	21.4	25.2	20.0
Sc	26.9	55.2	45.8	29.9	28.7	34.7	29.9	21.1	32.3	25.2	24.5
V	460	543	525	376	322	408	410	520	320	260	237
Cr	19.3	137	121	47.0	35.0	130	51.5	70.6	35.5	26.5	24.5
Co	54.6	18.4	39.2	33.4	58.6	18.3	158	56.9	33.3	34.3	31.2
Ni	60.4	37.8	41.6	32.7	45.6	22.9	311	55.9	36.3	33.7	29.6
Cu	42.0	180	72.1	110	87.5	176	126	322	187	67.4	58.4
Zn	86	58	79	411	109	90	166	74	433	189	182
Rb	4.44	30.8	28.4	31.2	21.0	25.8	34.8	25.0	28.0	12.0	10.8
Sr	83.0	90.8	110	116	65.0	130	125	122	98.6	119	122
Y	66.7	46.1	48.8	130	67.8	30.6	126	35.1	32.0	76.2	85.2
Zr	147	167	205	126	99	122	122	149	96	82	74
Nb	6.88	5.38	7.61	5.29	4.29	4.54	4.01	5.67	4.18	3.34	2.98
Cs	0.020	0.343	0.140	0.039	0.038	0.032	0.060	0.031	0.134	0.025	0.020
Ba	11.7	41.5	81.5	28.6	14.5	102	35.0	64.9	39.1	16.8	17.0
La	8.57	6.01	8.63	17.4	9.99	5.55	17.4	5.50	4.61	14.6	17.1
Ce	25.8	15.6	22.6	42.1	26.2	14.7	43.6	15.7	12.5	36.5	39.2
Pr	4.32	2.76	3.64	6.55	4.12	2.39	6.85	2.56	2.04	5.51	5.68
Nd	23.1	15.2	18.6	35.0	21.5	12.5	35.7	13.4	10.7	28.0	29.6
Sm	7.95	5.16	6.03	11.6	7.11	4.18	11.4	4.58	3.62	8.50	8.69
Eu	2.41	1.66	1.84	4.29	2.57	1.29	3.70	1.50	1.17	2.65	2.75
Gd	9.87	6.84	7.58	16.2	9.56	5.07	15.3	5.36	4.45	10.8	11.2
Tb	1.73	1.19	1.33	2.82	1.63	0.850	2.46	0.914	0.782	1.67	1.73
Dy	11.1	7.44	8.30	17.9	10.5	5.17	16.0	5.77	5.08	9.99	10.5
Ho	2.35	1.65	1.75	3.79	2.16	1.06	3.54	1.21	1.12	2.02	2.17
Er	6.42	4.75	4.88	10.5	5.69	2.95	9.21	3.38	3.21	5.25	5.69
Tm	0.961	0.685	0.740	1.40	0.788	0.409	1.28	0.476	0.472	0.704	0.781
Yb	5.31	4.30	4.32	7.65	4.33	2.34	6.97	2.65	2.83	3.81	4.24
Lu	0.693	0.679	0.665	1.13	0.647	0.364	0.978	0.393	0.444	0.581	0.645
Hf	5.22	4.47	5.36	3.31	2.72	3.31	3.52	3.99	2.58	2.28	2.04
Ta	0.443	0.332	0.437	0.345	0.274	0.252	0.285	0.324	0.219	0.231	0.198
Tl	1.76	0.086	0.043	0.072	0.060	0.084	0.084	0.097	0.103	0.068	0.061
Pb	0.491	0.551	0.673	0.637	0.598	0.707	0.688	0.750	0.731	0.543	0.510
Th	0.420	0.333	0.563	0.095	0.287	0.214	0.417	0.283	0.207	0.275	0.232
U	0.220	0.171	0.212	0.358	0.085	0.060	2.94	1.63	1.09	2.18	1.89

Appendix A. Continued

Sample	9	10a	10b	10c	10d	11	12a	12b	13
Core section	7R1	7R1	7R1	7R1	7R1	7R1	7R1	7R1	7R1
Interval (cm)	32-34	51-53	51-53	51-53	51-53	65-68	80-83	80-83	85-87
Depth (mbsf)	164.42	164.61	164.61	164.61	164.61	164.75	164.90	164.90	164.95
Unit	1	1	1	1	1	1	1	1	1
Composition	lithic	lithic*	lithic*	lithic*	lithic	lithic*	lithic*	juv*	lithic*
ICPOES (wt. %)									
SiO_2	51.6	45.3	47.1	46.8	48.9	48.1	46.2	47.5	48.7
TiO_2	1.65	2.85	2.11	2.72	3.26	2.84	1.90	2.06	3.18
Al_2O_3	16.8	14.5	13.4	14.4	17.9	14.8	14.9	12.1	16.3
Fe_2O_3	11.5	14.7	18.4	15.1	14.5	12.2	13.5	13.5	11.1
MnO	0.23	0.47	0.15	0.34	0.19	0.24	0.17	0.04	0.05
MgO	3.60	1.45	1.75	2.56	1.05	0.88	6.96	1.38	1.47
CaO	10.8	10.2	5.60	8.20	6.39	3.47	6.93	7.62	4.61
Na_2O	2.79	2.38	2.65	2.35	2.95	0.64	2.86	0.10	1.76
K_2O	0.77	2.30	2.30	1.99	2.43	9.88	0.84	6.61	7.00
P_2O_5	0.15	0.33	0.51	0.29	0.32	0.78	0.22	0.27	0.40
LOI	2.75	7.25	5.39	5.01	3.21	4.34	6.18	9.41	5.32
Total	102.66	101.72	99.40	99.65	101.14	98.20	100.67	100.62	99.78
ICPMS (ppm)	n=3	n=5				n=3		n=2	n=3
Li	28.5	46.9	23.1	52.4	47.3	17.3	16.0	19.3	24.6
Sc	35.2	47.7	29.5	44.9	49.2	42.3	20.1	30.7	35.9
V	403	571	296	501	596	558	351	339	417
Cr	62.6	107	43.9	175	225	88.6	858	326	377
Co	85.3	152	35.8	122	290	55.8	51.1	23.8	17.6
Ni	81.2	85.7	49.9	73.0	58.0	123	174	37.7	34.9
Cu	104	156	79.6	157	87.5	169	46.2	158	157
Zn	99	378	95	487	660	205	169	89	489
Rb	11.3	25.3	48.3	26.5	29.0	65.4	7.18	55.6	49.9
Sr	145	142	113	137	146	87.7	261	41.6	97.9
Y	29.8	54.7	48.7	50.9	40.3	67.1	29.5	25.0	47.3
Zr	97	186	177	171	204	204	109	151	192
Nb	3.76	8.06	3.45	8.98	8.87	12.4	6.17	4.52	6.78
Cs	0.342	0.305	0.981	0.598	0.350	0.618	0.216	0.608	0.585
Ba	50.3	163	41.2	102	53.0	167	20.7	69.2	118
La	3.59	7.53	7.91	7.75	7.28	11.6	7.02	3.91	7.61
Ce	10.3	20.2	23.3	21.6	20.3	29.5	18.6	10.9	20.9
Pr	1.72	3.32	3.86	3.46	3.36	4.52	3.06	1.97	3.57
Nd	9.56	17.8	20.9	18.2	17.9	23.3	15.2	10.2	18.8
Sm	3.36	6.12	7.14	6.10	5.91	7.60	4.75	3.40	6.48
Eu	1.36	2.12	2.13	2.01	2.16	2.12	2.34	0.990	1.80
Gd	4.36	7.85	8.29	7.60	6.81	9.76	5.48	4.00	7.88
Tb	0.766	1.39	1.33	1.34	1.17	1.69	0.915	0.721	1.36
Dy	4.99	8.90	7.99	8.50	7.31	10.5	5.41	4.47	8.44
Ho	1.07	1.89	1.68	1.80	1.46	2.21	1.07	0.925	1.73
Er	3.03	5.32	4.41	5.13	3.99	6.16	2.75	2.54	4.79
Tm	0.449	0.790	0.669	0.735	0.585	0.884	0.375	0.385	0.697
Yb	2.73	4.80	3.93	4.32	3.39	5.35	2.03	2.17	4.07
Lu	0.412	0.711	0.546	0.658	0.488	0.792	0.300	0.319	0.587
Hf	2.68	4.96	4.49	4.68	5.63	5.30	3.04	4.69	5.16
Ta	0.221	0.452	0.223	0.526	0.538	0.739	0.396	0.258	0.392
Tl	0.011	0.066	0.041	0.027	0.013	0.342	0.088	0.103	0.053
Pb	0.386	0.874	0.598	0.606	0.872	1.06	1.42	1.53	1.24
Th	0.191	0.438	0.509	0.424	0.490	0.565	0.385	0.311	0.435
U	1.45	1.36	1.06	0.859	1.30	0.886	0.269	0.447	0.513

APPENDIX B. OPTICAL MICROSCOPY OBSERVATIONS AND MINERAL COMPOSITIONS FOR SAMPLES FROM ORI AND TAMU MASSIFS

№ Stat.	Rock type	Core section	Interval (cm)	Depth (mbsf)	Strat. unit	Lith. unit	Morpho-logy	Magma type	Texture			Mineral phases (relative abundance)		Alteration				Vesicularity		Mineral composition, wt.%						Clay d-spacing, Å			CIPW	
									Type	Description	Cryst. %	Phen. (max size and vol. %)	GM, average size of plag	Glass	Olivine	Cpx	Plag	%	Infill	Plag	Mcl	Cpx	Mgt	Cal	Clay	2-w	1-w	0-w	Rock type	Olivine content vol. %
Site U1350, Ori Massif																														
1	A1a	w.r.	8R2	118-121	158.0	IIa	7	Lava flow	4	Hypocrystalline, microglome-rophyric, subophitic	60	aphyric	plag (0.3 mm), cpx, glass, opaque	brown clays, calcite		brown clays (moderate)	brown clays, sericite (initial)	15	green & brown clays, calcite, partly empty	43.8		17.7	2.5		36.1	**15.1**	13	10	Qtz Th.	
		f.g.	8R2	88-89	157.7			High-Nb High-Fe																					Qtz Th.	
2	B1a	w.r.	10R2	18-22	173.5	IIa	12	Lava flow																					Qtz Th.	
		f.g.	10R2	8-10	173.4			High-Nb High-Fe																					Ol Th.	3.4
3	B1a	w.r.	11R1	98-101	182.5	IIa	12	Lava flow																					Ol Th.	0.3
		f.g.	10R2	8-10	173.4			High-Nb High-Fe																					Ol Th.	3.4
4	B1a	w.r.	17R1	45-47	220.4	IIb	29	Pillow lava												46.5		24.4	4		25.1	+	12.8		Ol Th.	6.1
		f.g.	17R1	43-47	220.3			High-Nb High-Fe																					Qtz Th.	
		w.r.	17R3	24-27	223.0	IIb	34	Lava flow	4	Hypocrystalline, inter-granular, intersertal	65	<3%, plag (1x0.5 mm), cpx (0.2x0.3 mm), ol (0.5x0.3 mm)	plag (0.3 mm), cpx, glass, opaque	brown, orange clays, calcite	brown, orange clays, calcite	brown clays (moderate)	brown clays (initial)	<5	green & brown clays, calcite, partly empty	47.6		24.3	2.1	1	24.9	15.2	+		Qtz Th.	
		w.r.	17R3	103-105	223.8			High-Nb High-Fe												46.4		19.7	2.4	1.3	30.3	15	**12.8**		Qtz Th.	
		f.g.	17R3	19-21	223.0																								Qtz Th.	
5	B1a	w.r.	18R1	33-36	229.8	IIb	36	Lava flow	3	Hypocrystalline, diktytaxitic, variolitic	60	7%, plag (0.5 mm), cpx (0.1 mm)	microlites and crystallites of plag, cpx, opaque in glass	brown, orange clays, calcite		brown clays (moderate)	brown clays, sericite (initial)	10	green & brown clays, calcite, partly empty	42.3		24.7	2.7	2.1	28.3	14.9	13	10	Ol Th.	3.3
		f.g.	18R1	25-28	229.8			High-Nb High-Fe																					Qtz Th.	
6	A2	w.r.	19R2	72-74	241.3	IIc	43	Pillow lava												7.4	6.4	35.9		5	45.3			*	Qtz Th.	
		f.g.	19R2	71-73	241.2			Low-Ti High-Fe																					Qtz Th.	
7	B2	w.r.	21R2	87-89	260.7	IIc	53	Lava flow	4	Hypocrystalline, intergranular, intersertal	75	<3%, plag (1x0.5 mm), cpx (0.2x0.3 mm), ol (0.5x0.3 mm)	plag (0.2 mm), cpx, glass, opaque	brown clays	brown clays	brown clays (moderate)	brown clays, sericite (initial)	<5	green clays, calcite, partly empty	52.9		28.7	3.3	1.4	13.7	14.9	13.1	10	Qtz Th.	
		f.g.	21R2	77-79	260.6			Normal High-Fe																					Ol Th.	1
8	B1b	w.r.	22R2	117-120	270.0	IIc	59	Pillow lava	2	Holocrystalline, subophitic, intersertal	95	<3%, plag (1.5x0.5 mm), ol (0.7x0.4 mm)	plag (0.2 mm), cpx, olivine, opaque, glass	orange clays, calcite	orange clays	brown clays (initial)	fresh	<5	calcite	62.7		29.8	1.1		6.5			*	Qtz Th.	
		f.g.	22R2	53-55	269.4			Normal High-Mg																					Ol Th.	10
9	A2	w.r.	22R4	31-35	271.9	IIc	63	Pillow lava												23.3	6.3	18.2		2.8	49.4			*	Ol Th.	5.8
		f.g.	22R4	33-35	271.9			Normal High-Mg																					Ol Th.	9.2
10	A2	w.r.	22R5	42-46	273.4	IIc	67	Pillow lava	1	Vitrophyric, felty	50	15%, plag (1.8x0.7 mm), ol (0.4x0.3 mm)	microlites and crystallites of plag, cpx, opaque in glass	brown, orange clays	orange clays		brown clays (initial)	5	green clays, calcite, partly empty	36.8	4.9	21.3		1.2	35.7	15.2	13.6		Ol Th.	2.8
		f.g.	22R5	2-4	273.0			Normal High-Mg																					Ol Th.	7

Optical microscopy observations and XRD data were obtained for whole-rock samples. Pair № refers to identification number of pair as used in statistics. Subdivision on magma types (Normal, Low-Ti, High-Nb) is based on fresh glass compositions where available, following Sano et al. (2012). Fresh glass samples are subdivided into two tholeiite basalt groups, Higher-Fe and Higher-Mg, is as from this study. Assessment of crystallinity and phenocryst amounts that are identifiable under optical microscope were quantifyed using MagniSci (http://magnisci.com/) and ImageJ (Schneider et al., 2012) softwares, respectively. Alteration of groundmass glass and olivine in whole-rock samples from this study is complete. Degree of alteration in clinopyroxene and plagioclase is as stated. Mineral compositions were quantified in whole-rock samples using XRD analysis. Clay amounts account for all of the residual material. Clay d-spacings show most intensive peaks for 2 water (2-w), 1 water (1-w) and 0 water (0-w) layer hydration states. Bold numbers for 2-w and 1-w correspond to those peaks that display higher intensity, all 10 Å peaks are of much lower intensity, comparatively. Those peaks that show a wide slope of lower intensity than the main peak are marked with plus (+). Air-dried clay analyses where 001 plane peak is less than 1000 cps are marked with a star (*). The CIPW normative compositions are given for both whole-rock and fresh glass type samples and are calculated according to method described in Best (2003). Fresh glass compositions from pairs 28 and 29 are used as an average of the two compositions from the same interval. Abbreviations: stat. = statistical group, mbsf = meters below seafloor, strat. = stratigraphic, lith. = lithological, cryst. = crystallinity prior to alteration, phen. = phenocryst, GM = groundmass, plag = plagioclase, cpx = clinopyroxene, ol = olivine, mgt = magnetite, mcl = microcline, cal = calcite, tr = traces identified through XRD clay analysis, vol. = volume (%), wt. = weight (%), Qtz Th. = quartz tholeiite, Ol Th. = olivine tholeiite, w.r. = whole-rock, f.g. = fresh glass.

Appendix B. Continued

№ Stat.	Rock type	Core section	Interval (cm)	Depth (mbsf)	Strat. unit	Lith. unit	Morpho-logy	Magma type	Texture			Mineral phases (relative abundance)		Alteration				Vesicularity		Mineral composition, wt.%						Clay d-spacing, Å			CIPW	
									Type	Description	Cryst. %	Phen. (max size and vol. %)	GM, average size of plag	Glass	Olivine	Cpx	Plag	%	Infill	Plag	Mcl	Cpx	Mgt	Cal	Clay	2-w	1-w	0-w	Rock type	Olivine content vol. %
11 B1b	w.r.	23R1	90-92	278.3	IIc	72	Pillow lava	Normal High-Mg	2	Holocrystalline, subophitic, intersertal	95	<3%, plag (1.6x0.4 mm), ol (0.4x0.4 mm)	plag (0.3 mm), cpx, olivine, opaque, glass	orange clays, calcite	orange clays	brown clays (initial)	fresh	5	calcite, brown clays	64.2		28.1	1.3		6.4	15		+	Qtz Th.	
	f.g.	23R1	53-55	277.9																									Ol Th.	9.5
12 B1b	w.r.	23R2	29-31	279.1	IIc	73	Pillow lava	Normal High-Mg	2	Hypocrystalline, subophitic, intersertal	90	<3%, plag (0.7x 0.2 mm), ol (0.2x 0.2 mm)	plag (0.3 mm), cpx, olivine, opaque, glass	brown, orange clays, calcite	orange clays	brown clays (initial)	fresh	<5	calcite	62.8		25.5	1.6		10.1	15.1	**13**		Qtz Th.	
	f.g.	23R2	0-3	278.8																									Ol Th.	7.7
	w.r.	23R4	20-22	281.9	IIc	79	Pillow lava	Normal High-Mg	2	Holocrystalline, subophitic, intersertal	95	<3%, plag (1.7x 0.3 mm), ol (0.7x 0.6 mm)	plag (0.3 mm), cpx, olivine, opaque, glass	brown, orange clays, calcite	orange clays	fresh	fresh	<5	calcite	67.4		28.8	1.7		2.1	14.9		+	Qtz Th.	
13 B1b	w.r.	23R4	99-102	282.7	IIc	81	Pillow lava	Normal High-Mg												53.9		23.3	1.6	1.6	19.7	14.8			Qtz Th.	
	f.g.	23R4	76-80	282.4																									Ol Th.	7.4
14 B1b	w.r.	23R5	34-38	283.4	IIc	82	Pillow lava	Normal High-Mg	2	Holocrystalline, subophitic, intersertal	95	<3%, plag (1.2x0.6 mm), ol (0.5x0.4 mm)	plag (0.2 mm), cpx, olivine, opaque, glass	brown, orange clays, calcite	orange clays	fresh	fresh	<5	brown clays, calcite, opaques	60.6		36.7	0.3	tr	2.4	15.2			Ol Th.	0.6
	f.g.	23R5	14-18	283.2																									Ol Th.	7.5
15 B2	w.r.	24R2	8-10	288.6	IIc	86	Pillow lava	Normal High-Mg												49.4		27.7	1.4	1	20.5	15.1			Qtz Th.	
	f.g.	24R2	31-33	288.8																									Ol Th.	8.2
16 B2	w.r.	24R2	101-104	289.5	IIc	88	Pillow lava	Normal High-Mg	2	Holocrystalline, subophitic, intersertal	95	<3%, plag (0.5x0.2 mm)	plag (0.2 mm), cpx, opaque, glass	brown clays	brown clays	brown clays (advanced)	brown clays (moder)	<5	green clays, calcite, partly empty	59.2		25.2	1.3		14.3	**15**	12.8		Ol Th.	1.1
	f.g.	24R2	110-113	289.6																									Ol Th.	7.9
17 B1b	w.r.	24R3	15-18	290.0	IIc	90	Pillow lava	Normal High-Mg												61.1		31.1	1.6		6.2	15.2		*	Qtz Th.	
	f.g.	24R3	44-47	290.3																									Ol Th.	9
	w.r.	26R4	97-100	311.2	IV	159	Pillow lava	Normal High-Mg	1	Vitrophyric, felty	60	10%, plag (2.6x2 mm), ol (1x0.5 mm)	plag (0.1 mm), cpx, glass, opaque	brown, green clays, calcite	calcite, brown clays		brown clays, KFSp (advanc)	<5	brown clays, calcite	40.2	5.1	19.4	1.6	3.5	30.2	**14.8**	12.9		Ol Th.	2.1
	w.r.	26R5	22-25	311.8	IV	160	Pillow lava	Normal High-Mg	1	Vitrophyric, felty	50	20%, plag (2.6x2 mm), ol (1x0.5 mm)	microlites and crystallites of plag, cpx in glass	brown, green clays, calcite	calcite, brown clays		brown clays, KFSp (advanc)	<5	brown clays, calcite	35.9	3.5	10.2	1.8	3.2	45.3	15.1	**12.6**		Qtz Th.	
Site U1347, Tamu Massif																														
18 B1a	w.r.	12R1	63-65	160.2	IV	4	Lava flow	Normal High-Fe	4	Hypocrystalline, intergranular, intersertal	65	<3%, plag (1.5x0.3 mm), cpx (1x0.6 mm), ol (0.8x0.6 mm)	plag (0.5 mm), cpx, glass, opaque	brown, orange clays, calcite	calcite, brown clays	brown clays (initial)	brown clays (initial)	20	brown clays, calcite, rarely empty										Qtz Th.	
	f.g.	11R1	24-26	157.6																									Qtz Th.	
19 A1a	w.r.	13R6	91-93	173.7	IV	4	Lava flow	Normal High-Fe	4	Hypocrystalline, intergranular, intersertal	66-73	<3%, plag (2.5x0.3 mm), cpx (1.1x0.7 mm), ol (1x0.6 mm)	plag (1 mm), cpx, glass, opaque	brown, orange clays, calcite	calcite, brown clays	brown clays (initial)	brown clays (initial)	<5	brown clays, calcite, rarely empty	45.6		27.2	4.4		22.8	14.8			Qtz Th.	
	f.g.	11R1	24-26	157.6																									Qtz Th.	
20 A1b	w.r.	15R1	20-23	186.4	V	5	Lava flow	Normal High-Fe	3	Hypocrystalline, glomerophyric, seriate, variolitic	80	20%, plag (0.6x0.5 mm), cpx (0.5x0.6 mm), ol (0.5x0.3 mm)	plag (0.3 mm), cpx, glass, opaque	brown, orange clays, calcite	calcite, brown clays	fresh	fresh	<5	brown clays, calcite, rarely empty	42.7		37.8	3.2	tr	16.3	14.9		*	Qtz Th.	
	f.g.	15R1	5-7	186.3																									Qtz Th.	

Appendix B. Continued

№ Stat.	Rock type	Core section	Interval (cm)	Depth (mbsf)	Strat. unit	Lith. unit	Morpho-logy	Magma type	Texture			Mineral phases (relative abundance)		Alteration				Vesicularity		Mineral composition, wt.%						Clay d-spacing, Å			CIPW	
									Type	Description	Cryst. %	Phen. (max size and vol. %)	GM, average size of plag	Glass	Olivine	Cpx	Plag	%	Infill	Plag	Mcl	Cpx	Mgt	Cal	Clay	2-w	1-w	0-w	Rock type	Olivine content vol. %
21 A1a	w.r.	18R1	51-54	214.5	IX	11	Lava flow	Low-Ti High-Fe	3-4	Hypocrystalline, seriate, intersertal, diktytaxitic	71	20%, plag (1.8x0.8 mm), cpx (0.6x0.5 mm), ol (0.5x0.3 mm)	plag (0.3 mm), cpx, glass, opaque	brown clays, calcite	calcite, brown clays	brown clays (moderate)	brown clays (initial)	<5	brown clays, calcite	46.4		17.3	3.4		32.8	15			Qtz Th.	
	f.g.	18R3	89-91	217.5																								Qtz Th.	
22 A1b	w.r.	18R4	24-28	218.3	X	13	Pillow lava	Normal High-Fe	3	Hypocrystalline, glomerophyric, seriate, variolitic	90	20%, plag (1.4x0.5 mm), cpx (0.7x0.6 mm), ol (1x0.7 mm)	plag (0.2 mm), cpx, glass, opaque	brown clays	orange clays, calcite	fresh	fresh	<5	calcite	48.9		39.8	2		9.2			*	Qtz Th.	
	f.g.	18R4	44-46	218.5																								Qtz Th.	
23 A1b	w.r.	20R1	43-47	233.6	X	30	Pillow lava	Normal High-Fe	3	Hypocrystalline, glomerophyric, seriate, variolitic	88	20%, plag (1.4x0.5 mm), cpx (0.7x0.6 mm), ol (1x0.7 mm)	plag (0.1 mm), cpx, glass, opaque	brown, orange clays	orange clays, calcite	fresh	fresh	10	calcite										Qtz Th.	
	f.g.	20R1	110-112	234.3																								Qtz Th.	
24 A1b	w.r.	22R5	94-99	259	XII	46	Pillow lava	Normal High-Fe	3	Hypocrystalline, glomerophyric, seriate, variolitic	80	25%, plag (1.9x0.7 mm), cpx (0.9x0.5 mm), ol (0.6x0.4 mm)	plag (0.1 mm), cpx, glass, opaque	brown, orange clays	orange clays, calcite	fresh	fresh	<5	calcite	42.4		36	2.7	tr	18.8	14.8			Qtz Th.	
	f.g.	22R5	73-76	258.8																								Qtz Th.	
25 A1b	w.r.	23R2	97-100	263.2	XII	48	Lava flow	Normal High-Fe	3	Hypocrystalline, glomerophyric, seriate, variolitic	75	25%, plag (1.3x0.5 mm), cpx (0.6x0.5 mm), ol (0.5x0.5 mm)	plag (0.3 mm), cpx, glass, opaque	brown, orange clays	orange clays, calcite	fresh	fresh	<5	calcite	48.3		37	2.5		12.1	14.7		*	Qtz Th.	
	f.g.	23R2	138-141	263.6																								Qtz Th.	
26 A1a	w.r.	24R1	63-66	272.2	XII	53	Lava flow	Normal High-Fe	4	Hypocrystalline, subophitic, intersertal	70	<3%, plag (1.4x0.8 mm), cpx (0.5x0.3 mm)	plag (0.7 mm), cpx, glass, opaque	brown, orange clays, calcite		brown clays (initial)	fresh	<5	calcite	43.8		24.8	3.6		27.8	14.7			Qtz Th.	
	f.g.	23R4	90-92	266																								Qtz Th.	
27 A1b	w.r.	24R5	32-35	277.3	XII	57	Pillow lava	Normal High-Fe	3	Hypocrystalline, glomerophyric, seriate, variolitic	75	20%, plag (0.9x0.2 mm), cpx (0.5x0.4 mm), ol (0.2x0.3 mm)	plag (0.3 mm), cpx, glass, opaque	brown, orange clays	calcite, orange clays	fresh	fresh	<5	calcite	46.5		31.1	2.6		19.9	14.9			Qtz Th.	
	f.g.	24R5	57-58	277.5																								Qtz Th.	
	w.r.	26R1	48-50	291.2	XIV	79	Pillow lava	Normal High-Fe	4	Hypocrystalline, intergranular, intersertal	67	10%, plag (1xx1 mm), cpx (0.2x0.3 mm), ol (0.5x0.2 mm)	plag (0.3 mm), cpx, glass, opaque	brown, orange clays	calcite, orange clays	fresh	fresh	10	brown clays, calcite	47.6		29.4	2.8		20.2	14.8			Qtz Th.	
28 A1b	w.r.	28R4	47-50	304.5	XV	81	Lava flow	Normal High-Fe	4	Hypocrystalline, intergranular, intersertal	90	<3%, plag (1.6x0.8 mm), cpx (1x0.6 mm), ol (0.8x0.4 mm)	plag (0.7 mm), cpx, glass, opaque	brown, orange clays, calcite	calcite, orange clays	fresh	fresh	<5	calcite										Qtz Th.	
	f.g.	26R2	0-2	292.2																								Qtz Th.	
29 B1a	w.r.	29R4	41-45	314.1	XV	81	Lava flow	Normal High-Fe	4	Hypocrystalline, intergranular, intersertal	74	<3%, plag (1.5x0.7 mm), cpx (0.5x0.3 mm), ol (0.6x0.3 mm)	plag (1 mm), cpx, glass, opaque	brown, orange clays, calcite	calcite, orange clays	brown clays (initial)	brown clays (initial)	<5	calcite										Qtz Th.	
	f.g.	26R2	0-2	292.2																								Qtz Th.	

APPENDIX C. MAJOR AND TRACE ELEMENT COMPOSITIONS FOR WHOLE-ROCK AND FRESH GLASS SAMPLE PAIRS FROM ORI AND TAMU MASSIFS, DATA FROM SANO ET AL. (2012)

Pair №	1		2		3		4		5	
Stat. group	A 1 a		B 1 a		B 1 a		B 1 a		B 1 a	
Sample type	w.r.	f.g.	w.r.	f.g.	w.r.	f.g.	w.r.	f.g.	w.r.	f.g.
Site	U1350		U1350		U1350		U1350		U1350	
Core section	8R-2	8R-2	10R-2	10R-2	11R-1	10R-2	17R-1	17R-1	18R-1	18R-1
Interval (cm)	118-121	88-89	18-22	8-10	98-101	8-10	45-47	43-47	33-36	25-28
Depth (mbsf)	157.95	157.65	173.53	173.43	182.48	173.43	220.35	220.33	229.83	229.75
Strat. unit	IIa	IIa	IIa	IIa	IIa	IIa	IIb	IIb	IIb	IIb
Lith. unit	7	7	12	12	12	12	29	29	36	36
Morphology	Lava flow		Lava flow		Lava flow		Pillow lava		Pillow lava	
Magma type	High-Nb		High-Nb		High-Nb		High-Nb		High-Nb	
Compos. group	Higher-Fe		Higher-Fe		Higher-Fe		Higher-Fe		Higher-Fe	
XRF (whole-rock), EPMA (fresh glass), wt. %										
SiO_2	49.13	50.58	48.39	51.21	48.21	51.21	47.65	50.08	47.46	50.09
TiO_2	2.41	2.44	2.33	2.09	2.30	2.09	2.68	2.65	2.18	2.20
Al_2O_3	14.5	13.5	14.2	13.7	14.2	13.7	13.2	13.3	14.1	13.4
FeO	10.9	12.2	11.9	12.4	11.9	12.4	13.7	12.9	11.9	12.1
MnO	0.11	0.21	0.15	0.20	0.14	0.20	0.15	0.23	0.18	0.20
MgO	7.00	5.81	7.10	6.22	7.03	6.22	7.46	5.43	7.16	6.12
CaO	9.15	10.6	9.88	10.8	9.52	10.8	8.17	9.54	10.2	10.7
Na_2O	2.62	3.06	2.72	3.50	2.87	3.50	3.28	3.43	2.73	3.10
K_2O	0.35	0.59	0.27	0.46	0.26	0.46	0.35	0.74	0.25	0.48
P_2O_5	0.24	0.21	0.24	0.19	0.24	0.19	0.27	0.27	0.22	0.18
LOI	1.85		1.21		1.33		1.47		1.71	
Total	98.21	99.17	98.41	100.79	98.01	100.79	98.33	98.62	98.11	98.46
ICP-MS (whole-rock), LA-ICP-MS (fresh glass), ppm										
Sc	39.6	41.0	43.8	43.3	42.3	43.3	37.4	40.4	40.8	43.3
V	464	355	461	344	471	344	492	358	425	347
Rb	1.37	8.60	0.982	7.20	0.853	7.20	1.28	11.5	1.07	7.50
Sr	265	250	247	224	243	224	288	274	259	245
Y	23.0	33.8	29.9	34.5	27.8	34.5	32.9	35.3	27.6	33.1
Zr	159	177	156	160	160	160	208	202	150	165
Nb	12.1	15.4	10.0	11.0	10.0	11.0	35.5	41.0	21.1	25.1
Ba	75.1	110	74.5	75.0	164	75.0	89.0	130	69.6	73.6
La	9.50	12.2	9.30	9.96	8.84	9.96	20.6	22.4	12.7	13.9
Ce	24.9	31.1	25.0	25.6	24.0	25.6	46.7	48.9	30.7	32.3
Pr	3.58	4.46	3.73	4.04	3.57	4.04	5.83	6.19	4.07	4.37
Nd	17.0	21.0	18.3	18.7	17.5	18.7	24.7	27.0	18.1	19.1
Sm	4.58	5.57	5.29	5.22	4.98	5.22	5.88	6.64	4.81	4.92
Eu	1.62	1.79	1.87	1.82	1.79	1.82	2.00	2.00	1.67	1.86
Gd	5.10	6.40	6.32	6.65	5.99	6.65	6.77	6.86	5.56	5.85
Tb	0.833	1.02	1.04	1.06	0.983	1.06	1.08	1.05	0.930	0.950
Dy	4.96	6.11	6.34	6.11	5.88	6.11	6.56	6.81	5.64	6.19
Ho	0.965	1.28	1.25	1.30	1.15	1.30	1.33	1.40	1.12	1.28
Er	2.67	3.49	3.42	3.54	3.11	3.54	3.78	3.97	3.13	3.42
Tm	0.360	0.570	0.452	0.510	0.406	0.510	0.518	0.510	0.425	0.470
Yb	2.29	3.30	2.76	3.49	2.45	3.49	3.28	3.58	2.6	3.02
Lu	0.329	0.470	0.396	0.470	0.347	0.470	0.487	0.480	0.386	0.420
Hf	4.26	4.12	4.34	4.11	4.31	4.11	5.42	4.85	4.04	4.09
Ta	0.781	0.970	0.679	0.690	0.664	0.690	2.14	2.17	1.24	1.42
Pb	1.19	1.35	0.785	1.02	0.768	1.02	1.49	1.47	1.09	1.04
Th	0.698	0.780	0.645	0.590	0.679	0.590	1.47	1.35	0.735	0.810
U	0.285	0.230	0.284	0.190	0.276	0.190	0.377	0.42	0.226	0.250

Total iron as FeO for the fresh glass samples, and that for the whole-rock samples is recalculated from Fe_2O_3. For abbreviations see Appendix B.

Appendix C. Continued

Pair №	6		7		8		9		10	
Stat. group	A 2		B 2		B 1 b		A 2		A 2	
Sample type	w.r.	f.g.	w.r.	f.g.	w.r.	f.g.	w.r.	f.g.	w.r.	f.g.
Site	U1350		U1350		U1350		U1350		U1350	
Core section	19R-2	19R-2	21R-2	21R-2	22R-2	22R-2	22R-4	22R-4	22R-5	22R-5
Interval (cm)	72-74	71-73	87-89	77-79	117-120	53-55	31-35	33-35	42-46	2-4
Depth (mbsf)	241.25	241.24	260.67	260.57	270.03	269.40	271.88	271.89	273.40	273.00
Strat. unit	IIc	IIc	IIc	IIc	IIc	IIc	IIc	IIc	IIc	IIc
Lith. unit	43	43	53	53	59	59	63	63	67	67
Morphology	Pillow lava		Lava flow		Pillow lava		Pillow lava		Pillow lava	
Magma type	Low-Ti		Normal		Normal		Normal		Normal	
Compos. group	Higher-Fe		Higher-Fe		Higher-Mg		Higher-Mg		Higher-Mg	
XRF (whole-rock), EPMA (fresh glass), wt. %										
SiO_2	49.23	49.15	48.46	49.63	48.20	48.63	48.47	47.92	48.14	49.26
TiO_2	1.64	1.63	1.91	1.90	1.46	1.44	1.44	1.41	1.32	1.42
Al_2O_3	12.8	13.2	14.4	13.4	16.3	15.6	15.7	15.3	16.1	15.5
FeO	13.6	12.6	11.0	12.2	10.0	10.4	10.5	10.4	10.1	10.4
MnO	0.20	0.22	0.13	0.21	0.14	0.17	0.14	0.18	0.12	0.18
MgO	6.91	6.24	7.70	6.57	6.10	8.36	7.85	8.15	7.48	8.35
CaO	10.5	11.0	10.4	11.5	12.6	12.1	11.1	12.2	10.8	12.1
Na_2O	2.29	2.67	2.45	2.91	2.21	2.61	2.46	2.46	2.31	2.53
K_2O	0.32	0.23	0.18	0.19	0.08	0.16	0.40	0.15	0.40	0.16
P_2O_5	0.15	0.12	0.21	0.12	0.14	0.09	0.11	0.08	0.09	0.08
LOI	0.48		1.59		1.29		0.49		1.60	
Total	98.10	97.08	98.45	98.65	98.50	99.62	98.59	98.34	98.48	99.91
ICP-MS (whole-rock), LA-ICP-MS (fresh glass), ppm										
Sc	45.0	47.8	46.7	46.3	37.0	41.5	37.7	39.4	35.1	39.0
V	394	351	464	376	295	293	306	281	295	292
Rb	3.45	3.10	1.45	2.50	0.764	2.10	2.76	2.00	3.16	2.10
Sr	119	133	196	174	199	184	192	193	182	182
Y	28.5	34.5	38.1	31.8	21.6	24.4	18.9	24.7	16.1	22.3
Zr	108	118	108	109	83.9	86.7	84.7	91.9	74.6	82.1
Nb	5.67	6.40	4.87	5.30	4.10	4.50	4.19	4.80	3.66	4.40
Ba	33.9	37.6	16.5	24.8	13.4	23.1	20.9	23.1	17.9	21.8
La	5.26	6.08	6.59	5.25	4.05	4.35	3.71	4.33	3.06	4.02
Ce	14.5	16.2	17.3	14.9	11.7	12.2	10.5	12.3	8.68	11.6
Pr	2.27	2.55	2.71	2.53	1.85	1.96	1.67	2.04	1.39	1.81
Nd	11.4	12.2	14.4	13.0	9.67	9.84	8.72	10.9	7.29	10.2
Sm	3.53	3.74	4.65	4.10	3.07	3.19	2.76	3.47	2.35	3.03
Eu	1.24	1.34	1.68	1.51	1.16	1.11	1.06	1.28	0.904	1.15
Gd	4.60	5.26	6.26	5.51	3.92	3.94	3.52	4.52	2.97	3.80
Tb	0.839	0.910	1.09	0.80	0.675	0.680	0.610	0.790	0.525	0.630
Dy	5.42	6.24	7.02	5.77	4.23	4.37	3.86	4.76	3.26	4.22
Ho	1.15	1.23	1.48	1.15	0.869	0.91	0.791	0.970	0.675	0.890
Er	3.42	3.69	4.18	3.35	2.5	2.52	2.27	2.79	1.95	2.54
Tm	0.497	0.590	0.557	0.450	0.344	0.400	0.317	0.370	0.275	0.360
Yb	3.23	3.49	3.45	3.04	2.21	2.37	2.06	2.47	1.79	2.25
Lu	0.492	0.540	0.497	0.420	0.327	0.360	0.305	0.360	0.266	0.320
Hf	3.09	3.05	3.08	2.79	2.37	2.49	2.43	2.60	2.16	2.13
Ta	0.377	0.380	0.338	0.320	0.281	0.300	0.289	0.340	0.257	0.250
Pb	0.559	0.570	0.536	0.570	0.616	0.440	0.535	0.570	0.529	0.530
Th	0.350	0.400	0.328	0.350	0.253	0.240	0.268	0.340	0.221	0.250
U	0.136	0.100	0.468	0.110	0.086	0.080	0.165	0.080	0.148	0.070

Appendix C. Continued

Pair №	11		12		13		14		15	
Stat. group	B 1 b		B 1 b		B 1 b		B 1 b		B 2	
Sample type	w.r.	f.g.	w.r.	f.g.	w.r.	f.g.	w.r.	f.g.	w.r.	f.g.
Site	U1350		U1350		U1350		U1350		U1350	
Core section	23R-1	23R-1	23R-2	23R-2	23R-4	23R-4	23R-5	23R-5	24R-2	24R-2
Interval (cm)	90-92	53-55	29-31	0-3	99-102	76-80	34-38	14-18	8-10	31-33
Depth (mbsf)	278.30	277.93	279.11	278.82	282.67	282.44	283.41	283.21	288.56	288.78
Strat. unit	IIc	IIc	IIc	IIc	IIc	IIc	IIc	IIc	IIc	IIc
Lith. unit	72	72	73	73	81	81	82	82	86	86
Morphology	Pillow lava		Pillow lava		Pillow lava		Pillow lava		Pillow lava	
Magma type	Normal		Normal		Normal		Normal		Normal	
Compos. group	Higher-Mg		Higher-Mg		Higher-Mg		Higher-Mg		Higher-Mg	
XRF (whole-rock), EPMA (fresh glass), wt. %										
SiO_2	48.65	48.54	48.28	49.53	47.92	49.65	47.61	49.12	47.41	49.50
TiO_2	1.50	1.43	1.55	1.42	1.51	1.43	1.46	1.45	1.57	1.42
Al_2O_3	17.3	15.7	17.7	15.7	17.2	15.7	16.8	15.6	17.6	15.9
FeO	8.7	10.3	8.9	10.5	8.8	10.3	10.1	10.3	9.6	10.3
MnO	0.12	0.17	0.13	0.18	0.14	0.18	0.14	0.18	0.13	0.18
MgO	5.95	8.43	5.75	8.48	6.31	8.39	5.80	8.34	5.08	8.54
CaO	12.6	12.0	12.3	12.0	12.5	12.1	13.1	12.1	13.0	12.1
Na_2O	2.27	2.56	2.35	2.59	2.29	2.63	2.19	2.54	2.14	2.58
K_2O	0.07	0.15	0.08	0.15	0.07	0.15	0.08	0.15	0.14	0.15
P_2O_5	0.13	0.09	0.14	0.08	0.14	0.07	0.13	0.08	0.14	0.08
LOI	1.42		1.52		1.95		1.09		1.47	
Total	98.70	99.35	98.59	100.63	98.84	100.50	98.52	99.90	98.29	100.80
ICP-MS (whole-rock), LA-ICP-MS (fresh glass), ppm										
Sc	37.5	40.7	42.7	39.5	38.5	38.4	36.5	39.2	43.8	38.5
V	320	281	344	287	311	281	285	282	344	280
Rb	0.442	2.10	0.495	2.10	0.399	2.10	0.713	2.10	0.645	2.10
Sr	209	193	219	189	213	192	201	192	205	192
Y	21.4	23.4	21.3	23.2	20.9	23.4	20.9	23.4	25.4	23.2
Zr	84.9	85.8	87.6	84.8	86.2	84.0	82.2	84.4	89.6	82.9
Nb	4.11	4.60	4.31	4.50	4.17	4.60	3.97	4.60	4.39	4.50
Ba	14.2	22.6	13.7	23.1	14.0	23.0	10.6	23.8	9.70	22.9
La	4.12	4.13	4.30	4.33	4.16	4.35	3.87	4.42	4.59	4.21
Ce	11.9	12.3	12.2	12.4	11.9	12.2	11.2	12.4	13.8	12.3
Pr	1.92	1.91	1.94	1.95	1.92	1.97	1.83	1.97	2.29	1.96
Nd	10.1	10.2	10.2	9.98	10.1	10.2	9.59	10.4	12.2	10.2
Sm	3.23	3.24	3.23	3.08	3.21	3.16	3.11	3.19	3.92	3.11
Eu	1.22	1.18	1.23	1.20	1.22	1.22	1.17	1.23	1.45	1.14
Gd	4.05	3.53	4.03	3.96	3.92	3.86	3.87	3.87	4.95	3.88
Tb	0.707	0.600	0.707	0.630	0.691	0.640	0.678	0.650	0.844	0.600
Dy	4.46	4.15	4.37	4.31	4.31	4.22	4.26	4.19	5.11	4.09
Ho	0.915	0.890	0.888	0.850	0.882	0.880	0.882	0.880	1.03	0.900
Er	2.59	2.58	2.49	2.47	2.50	2.53	2.51	2.45	2.84	2.35
Tm	0.361	0.370	0.344	0.350	0.346	0.350	0.346	0.360	0.376	0.330
Yb	2.30	2.42	2.16	2.51	2.21	2.09	2.22	2.11	2.33	2.33
Lu	0.339	0.350	0.321	0.370	0.325	0.330	0.325	0.330	0.353	0.290
Hf	2.49	2.38	2.56	2.39	2.53	2.08	2.40	2.46	2.60	2.34
Ta	0.296	0.270	0.300	0.300	0.298	0.280	0.284	0.270	0.309	0.280
Pb	0.804	0.440	0.548	0.480	0.549	0.460	0.558	0.500	0.501	0.430
Th	0.268	0.240	0.266	0.270	0.272	0.260	0.257	0.280	0.269	0.260
U	0.091	0.080	0.097	0.070	0.091	0.090	0.127	0.090	0.146	0.090

Appendix C. Continued

Pair №	16		17		18		19		20	
Stat. group	B 2		B 1 b		B 1 a		A 1 a		A 1 b	
Sample type	w.r.	f.g.	w.r.	f.g.	w.r.	f.g.	w.r.	f.g.	w.r.	f.g.
Site	U1350		U1350		U1347		U1347		U1347	
Core section	24R-2	24R-2	24R-3	24R-3	12R-1	11R-1	13R-6	11R-1	15R-1	15R-1
Interval (cm)	101-104	110-113	15-18	44-47	63-65	24-26	91-93	24-26	20-23	5-7
Depth (mbsf)	289.49	289.58	290.03	290.31	160.23	157.64	173.73	157.64	186.40	186.25
Strat. unit	IIc	IIc	IIc	IIc	IV	IV	V	IV	VII	V
Lith. unit	88	88	90	90	4	4	4	4	5	5
Morphology	Pillow lava		Pillow lava		Lava flow		Lava flow		Lava flow	
Magma type	Normal		Normal		Normal		Normal		Normal	
Compos. group	Higher-Mg		Higher-Mg		Higher-Fe		Higher-Fe		Higher-Fe	
XRF (whole-rock), EPMA (fresh glass), wt. %										
SiO_2	47.81	49.33	47.84	48.72	47.97	50.60	48.61	50.60	47.92	48.55
TiO_2	1.65	1.43	1.55	1.38	2.31	2.35	2.20	2.35	2.14	2.36
Al_2O_3	17.8	15.8	17.4	15.5	14.2	12.9	13.7	12.9	13.0	12.5
FeO	9.0	10.3	9.7	10.3	12.5	14.1	12.5	14.1	12.5	14.0
MnO	0.13	0.18	0.12	0.17	0.14	0.24	0.15	0.24	0.21	0.23
MgO	5.56	8.52	5.58	8.19	6.88	5.94	6.59	5.94	6.56	5.84
CaO	12.4	12.1	12.4	12.2	10.4	10.3	10.4	10.3	11.5	10.3
Na_2O	2.50	2.55	2.14	2.59	2.38	2.85	2.36	2.85	2.27	2.62
K_2O	0.14	0.15	0.14	0.16	0.09	0.26	0.18	0.26	0.17	0.27
P_2O_5	0.17	0.09	0.11	0.08	0.19	0.17	0.17	0.17	0.19	0.16
LOI	1.23		1.49		1.36		1.69		2.03	
Total	98.41	100.37	98.50	99.31	98.37	99.71	98.48	99.71	98.48	96.84
ICP-MS (whole-rock), LA-ICP-MS (fresh glass), ppm										
Sc	42.1	39.5	42.0	39.5	43.0	43.9	44.2	43.9	41.8	46.3
V	358	274	334	282	582	467	584	467	488	467
Rb	0.538	2.000	0.604	2.10	0.399	4.50	1.35	4.50	2.04	4.40
Sr	222	189	206	192	202	200	191	200	182	177
Y	28.1	23.5	21.7	23.7	28.8	37.9	25.7	37.9	29.7	37.1
Zr	93.9	83.0	86.0	84.7	125	152	111	152	123	147
Nb	4.55	4.60	4.21	4.60	6.48	8.00	5.60	8.00	6.30	7.80
Ba	13.0	23.0	11.8	23.1	19.5	38.1	28.1	38.1	22.5	35.7
La	5.52	4.17	4.09	4.31	6.58	7.50	5.49	7.50	6.58	7.87
Ce	15.8	11.8	12.4	12.3	18.8	20.5	15.7	20.5	18.4	20.8
Pr	2.52	1.91	2.03	1.93	2.95	3.28	2.47	3.28	2.89	3.43
Nd	13.3	9.44	10.8	10.2	15.1	15.4	12.9	15.4	14.8	17.9
Sm	4.17	2.93	3.48	3.15	4.58	4.89	4.00	4.89	4.52	5.64
Eu	1.57	1.14	1.29	1.23	1.65	1.60	1.44	1.60	1.59	1.84
Gd	5.30	3.83	4.31	3.70	5.67	5.85	4.96	5.85	5.59	6.22
Tb	0.907	0.570	0.748	0.680	0.946	0.910	0.840	0.910	0.941	1.08
Dy	5.62	4.11	4.57	4.31	5.88	6.02	5.22	6.02	5.86	6.47
Ho	1.14	0.830	0.910	0.890	1.18	1.24	1.06	1.24	1.19	1.45
Er	3.14	2.48	2.53	2.50	3.30	3.73	2.98	3.73	3.39	3.92
Tm	0.416	0.340	0.343	0.37	0.451	0.59	0.416	0.59	0.464	0.550
Yb	2.55	2.35	2.16	2.31	2.78	3.72	2.62	3.72	2.96	3.51
Lu	0.369	0.300	0.323	0.370	0.407	0.530	0.388	0.530	0.437	0.520
Hf	2.75	2.23	2.5	2.24	3.57	4.12	3.09	4.12	3.38	3.83
Ta	0.326	0.310	0.296	0.260	0.442	0.520	0.377	0.520	0.419	0.550
Pb	0.505	0.430	0.576	0.470	0.672	0.710	0.572	0.710	0.708	0.790
Th	0.300	0.250	0.259	0.280	0.495	0.470	0.411	0.470	0.466	0.560
U	0.267	0.080	0.186	0.080	0.235	0.110	0.128	0.110	0.146	0.160

Appendix C. Continued

Pair №	21		22		23		24		25	
Stat. group	A 1 a		A 1 b		A 1 b		A 1 b		A 1 b	
Sample type	w.r.	f.g.	w.r.	f.g.	w.r.	f.g.	w.r.	f.g.	w.r.	f.g.
Site	U1347		U1347		U1347		U1347		U1347	
Core section	18R-1	18R-3	18R-4	18R-4	20R-1	20R-1	22R-5	22R-5	23R-2	23R-2
Interval (cm)	51-54	89-91	24-28	44-46	43-47	110-112	94-99	73-76	97-100	138-141
Depth (mbsf)	214.51	217.48	218.29	218.49	233.63	234.30	259.04	258.83	263.19	263.60
Strat. unit	IX	IX	X	X	X	X	XII	XII	XII	XII
Lith. unit	11	11	13	13	30	30	46	46	48	48
Morphology	Lava flow		Pillow lava		Pillow lava		Pillow lava		Lava flow	
Magma type	Low-Ti		Normal		Normal		Normal		Normal	
Compos. group	Higher-Fe		Higher-Fe		Higher-Fe		Higher-Fe		Higher-Fe	
XRF (whole-rock), EPMA (fresh glass), wt. %										
SiO_2	47.68	51.20	48.50	49.24	48.70	49.66	48.98	50.38	48.43	50.37
TiO_2	1.92	2.09	1.78	2.00	1.71	2.02	1.90	2.18	1.85	2.17
Al_2O_3	15.0	13.1	14.9	13.2	14.7	13.1	14.4	12.9	13.7	12.8
FeO	11.3	13.7	11.1	12.7	11.1	13.0	11.4	13.4	11.9	13.6
MnO	0.10	0.23	0.20	0.22	0.18	0.22	0.18	0.23	0.18	0.22
MgO	6.53	5.46	6.25	6.53	6.52	6.48	6.58	6.13	7.20	6.14
CaO	9.42	10.0	12.4	11.3	12.3	11.2	11.8	10.7	11.6	10.6
Na_2O	2.64	3.18	2.31	2.61	2.22	2.70	2.33	2.78	2.18	2.85
K_2O	0.10	0.32	0.17	0.21	0.16	0.22	0.15	0.26	0.14	0.25
P_2O_5	0.21	0.20	0.16	0.13	0.15	0.13	0.18	0.17	0.17	0.17
LOI	3.91		0.62		0.94		0.79		1.25	
Total	98.83	99.49	98.37	98.20	98.70	98.70	98.71	99.06	98.53	99.15
ICP-MS (whole-rock), LA-ICP-MS (fresh glass), ppm										
Sc	42.0	46.7	39.5	48.7	39.9	49.5	41.7	48.3	40.2	46.8
V	536	437	393	402	352	407	454	414	419	419
Rb	0.391	5.90	1.84	3.20	1.82	3.40	1.61	3.70	1.55	3.90
Sr	176	167	178	178	184	174	168	161	160	161
Y	27.5	41.9	25.7	34.7	24.6	36.0	27.8	38.4	27.6	38.1
Zr	129	162	98.9	129	95.3	130	110	142	106	142
Nb	7.35	9.70	4.56	6.30	4.34	6.30	5.24	7.20	5.05	7.20
Ba	25.7	49.8	17.8	30.1	17.1	30.3	21.8	34.8	17.0	36.1
La	7.22	9.21	4.89	6.29	4.68	6.45	5.58	6.97	5.34	7.05
Ce	19.1	23.1	13.9	17.2	13.3	17.4	15.6	18.6	15.2	19.4
Pr	2.85	3.60	2.23	2.82	2.15	2.94	2.49	3.06	2.42	3.17
Nd	14.1	17.9	11.7	15.0	11.3	15.1	12.8	15.4	12.5	15.6
Sm	4.16	5.35	3.74	4.78	3.62	4.67	4.05	4.89	3.96	4.76
Eu	1.45	1.76	1.38	1.64	1.33	1.83	1.46	1.76	1.41	1.78
Gd	5.16	6.79	4.75	5.88	4.61	6.01	5.13	6.19	5.03	6.41
Tb	0.875	1.18	0.816	1.02	0.789	1.10	0.888	1.04	0.87	1.06
Dy	5.46	7.13	5.11	6.75	4.95	6.84	5.58	6.56	5.49	6.87
Ho	1.12	1.58	1.06	1.27	1.01	1.45	1.14	1.36	1.14	1.40
Er	3.19	4.64	2.99	3.79	2.85	4.10	3.25	3.89	3.23	3.75
Tm	0.443	0.600	0.421	0.540	0.399	0.540	0.452	0.550	0.453	0.520
Yb	2.84	4.02	2.64	3.41	2.54	3.45	2.89	3.64	2.89	3.60
Lu	0.418	0.600	0.388	0.500	0.380	0.440	0.424	0.470	0.429	0.470
Hf	3.41	4.21	2.87	3.33	2.80	3.51	3.22	3.61	3.09	3.63
Ta	0.474	0.650	0.312	0.410	0.305	0.390	0.363	0.490	0.345	0.500
Pb	0.752	0.910	0.595	0.670	0.554	0.700	0.640	0.630	0.617	0.690
Th	0.530	0.740	0.326	0.430	0.318	0.420	0.402	0.470	0.388	0.430
U	0.191	0.210	0.155	0.110	0.106	0.110	0.141	0.130	0.127	0.130

Appendix C. Continued

Pair №	26		27		28			29		
Stat. group	A 1 a		A 1 b		A 1 b			B 1 a		
Sample type	w.r.	f.g.	w.r.	f.g.	w.r.	f.g.	f.g.	w.r.	f.g.	f.g.
Site	U1347		U1347		U1347			U1347		
Core section	24R-1	23R-4	24R-5	24R-5	28R-4	26R-2	26R-2	29R-4	26R-2	26R-2
Interval (cm)	63-66	90-92	32-35	57-58	47-50	0-1	0-2	41-45	0-1	0-2
Depth (mbsf)	272.23	265.95	277.29	277.54	304.48	292.20	292.20	314.06	292.20	292.20
Strat. unit	XII	XII	XII	XII	XV	XV	XV	XV	XV	XV
Lith. unit	53	53	57	57	81	81	81	81	81	81
Morphology	Lava flow		Pillow lava		Lava flow			Lava flow		
Magma type	Normal		Normal		Normal			Normal		
Compos. group	Higher-Fe		Higher-Fe		Higher-Fe			Higher-Fe		
XRF (whole-rock), EPMA (fresh glass), wt. %										
SiO_2	49.04	50.19	48.04	49.15	49.07	50.17	50.54	48.76	50.17	50.54
TiO_2	1.81	2.14	1.91	2.15	2.04	2.17	2.20	2.16	2.17	2.20
Al_2O_3	13.8	12.9	14.5	13.1	13.5	12.8	12.9	13.7	12.8	12.9
FeO	12.0	13.6	11.6	13.3	12.5	13.8	13.7	12.3	13.8	13.7
MnO	0.13	0.23	0.15	0.22	0.18	0.23	0.22	0.17	0.23	0.22
MgO	7.37	6.19	7.46	6.18	6.02	6.20	6.03	6.22	6.20	6.03
CaO	10.5	10.7	11.3	10.9	11.0	10.8	10.6	11.0	10.8	10.6
Na_2O	2.31	2.76	2.22	2.65	2.35	2.80	2.80	2.42	2.80	2.80
K_2O	0.18	0.25	0.08	0.27	0.21	0.23	0.25	0.21	0.23	0.25
P_2O_5	0.16	0.15	0.16	0.16	0.18	0.16	0.17	0.19	0.16	0.17
LOI	1.41		1.08		1.51			0.81		
Total	98.66	99.12	98.52	98.05	98.62	99.29	99.35	97.93	99.29	99.35
ICP-MS (whole-rock), LA-ICP-MS (fresh glass), ppm										
Sc	42.7	46.4	45.0	46.1	42.2	47.4	49.2	40.8	47.4	49.2
V	436	439	469	438	453	452	440	502	452	440
Rb	1.65	3.90	0.403	4.20	2.94	4.00	4.00	3.03	4.00	4.00
Sr	158	164	170	167	180	175	176	169	175	176
Y	25.2	38.2	27.7	35.4	28.4	36.6	38.4	29.3	36.6	38.4
Zr	106	140	113	132	115	134	134	113	134	134
Nb	4.99	7.20	5.35	7.20	5.66	7.20	7.00	5.63	7.20	7.00
Ba	24.4	35.9	13.5	37.5	30.9	36.2	36.5	30.8	36.2	36.5
La	4.96	6.75	5.34	6.75	5.63	6.88	6.96	5.72	6.88	6.96
Ce	14.2	19.1	15.3	19.4	16.3	19.6	19.3	16.3	19.6	19.3
Pr	2.25	2.99	2.43	3.07	2.62	3.18	3.00	2.61	3.18	3.00
Nd	11.6	15.7	12.6	15.5	13.7	16.4	15.6	13.5	16.4	15.6
Sm	3.67	4.62	4.01	5.02	4.37	5.31	4.80	4.26	5.31	4.80
Eu	1.33	1.75	1.44	1.66	1.57	1.80	1.67	1.55	1.80	1.67
Gd	4.67	6.10	5.10	5.72	5.44	6.49	6.35	5.39	6.49	6.35
Tb	0.80	1.00	0.87	1.01	0.94	1.07	1.03	0.93	1.07	1.03
Dy	5.05	6.73	5.51	6.38	5.93	6.76	6.69	5.86	6.76	6.69
Ho	1.03	1.29	1.12	1.29	1.21	1.40	1.37	1.21	1.40	1.37
Er	2.97	3.80	3.22	3.53	3.42	3.72	4.11	3.43	3.72	4.11
Tm	0.411	0.540	0.448	0.520	0.489	0.510	0.590	0.483	0.510	0.590
Yb	2.64	3.18	2.89	3.07	3.14	3.23	3.68	3.08	3.23	3.68
Lu	0.388	0.520	0.428	0.430	0.464	0.460	0.530	0.459	0.460	0.530
Hf	2.93	3.65	3.12	3.33	3.39	3.46	3.39	3.34	3.46	3.39
Ta	0.33	0.450	0.351	0.440	0.392	0.450	0.450	0.390	0.450	0.450
Pb	0.542	0.730	0.615	0.780	0.560	0.730	0.770	1.210	0.730	0.770
Th	0.362	0.510	0.389	0.490	0.406	0.490	0.440	0.399	0.490	0.440
U	0.115	0.150	0.124	0.130	0.131	0.130	0.130	0.132	0.130	0.130

APPENDIX D. MINERAL XRD PATTERNS FOR SAMPLES FROM ORI AND TAMU MASSIFS

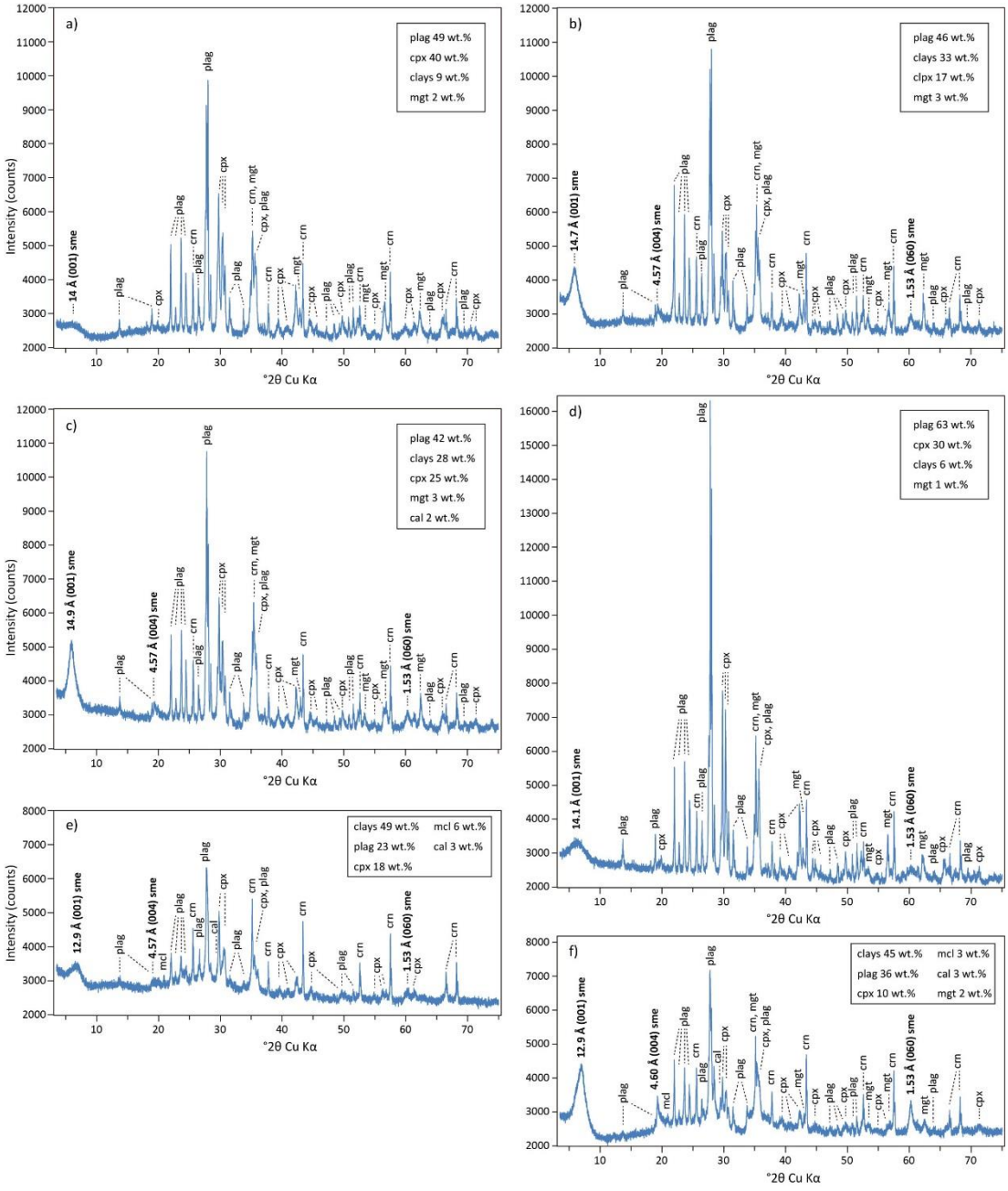

Figure description. XRD patterns and identified phase quantities (rounded) for representative Higher-Fe (a-c) and Higher-Mg (d-f) tholeiitic basalts. Alteration degree increases from (a) to (c) and from (d) to (f). a) U1347 18R4 24-28 (pair 22, subcluster A1b); b) U1347 18R1 51-54 (pair 21, subcluster A1a); c) U1350 18R1 33-36 (pair 5, subcluster B1a); d) U1350 22R2 117-120 (pair 8, subcluster B1b); e) U1350 22R4 31-35 (pair 9, subcluster A2); f) U1350 26R5 28-30 (stratigraphic unit IV). Most of the peaks for magmatic minerals and clays are labelled, d-spacing values in angstroms and planes for clays are in bold. Abbreviations: crn = corundum (internal standard), plag = plagioclase, cpx = clinopyroxene, mgt = magnetite, cal = calcite, mcl = microcline, sme = smectite.

APPENDIX E. CLAY XRD PATTERNS FOR SAMPLES FROM ORI AND TAMU MASSIFS

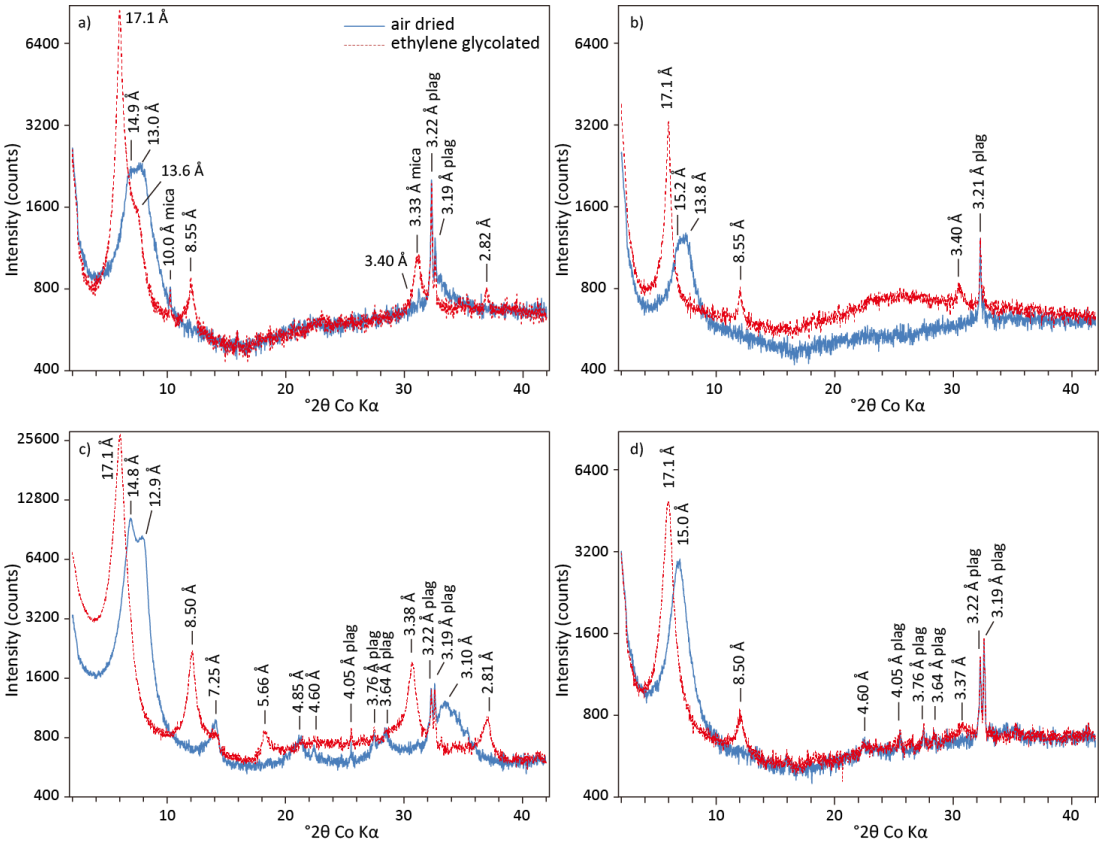

Figure description. XRD patterns of oriented air-dried and ethylene glycolated mounts for representative samples: a) three clays with 0 (10 Å), 1 (~13 Å) and 2 water layers, U1350 18R1 33-36 (pair 5, subcluster B1a); b) two clays with 1 and 2 water layers (randomly-oriented mixed-layer structures?), U1350 22R5 42-46 (pair 10, subcluster A2); c) two clays with 1 and 2 water layers, U1350 26R4 100-101 (stratigraphic unit IV); d) one clay with 2 water layers, U1347 18R1 51-54 (pair 21, subcluster A1a). Clays with 0, 1 and 2 water layers correspond to peaks at 10 Å (mica), ~13 Å (nontronite) and ~15 Å (saponite) in the air-dried samples, respectively. The d-spacing values in angstroms are labelled for clays, plagioclase (plag) and mica.

APPENDIX F. MEDIAN VALUES FOR VARIABLES WITHIN EACH SUBCLUSTER AFTER HIERARCHICAL CLUSTER ANALYSIS

Elements	Subclusters					
	A 1 1	A 1 2	A 2	B 1 1	B 1 2	B 2
SiO_2	97	98	100	95	98	97
TiO_2	93	89	101	100	105	111
Al_2O_3	107	111	102	105	110	110
FeO_{total}	88	87	101	96	90	90
MnO	**54**	81	78	72	73	71
MgO	**119**	107	96	**115**	**70**	**65**
CaO	96	**109**	91	94	104	102
Na_2O	83	84	91	85	87	84
K_2O	65	62	**247**	55	49	**96**
P_2O_5	105	108	128	118	**154**	**178**
V	**124**	102	109	**129**	112	124
Sc	94	**86**	94	96	97	**107**
Rb	23	46	**138**	13	26	31
Sr	101	103	100	105	108	113
Y	**67**	74	77	82	90	**120**
Zr	**78**	**77**	92	94	100	**108**
Nb	**73**	**73**	87	85	91	**98**
Ba	68	**59**	**90**	**90**	59	57
La	**76**	79	86	90	95	**126**
Ce	**78**	81	86	94	97	**116**
Pr	77	79	82	91	98	**117**
Nd	80	81	80	94	99	**119**
Sm	81	80	80	95	101	**126**
Eu	86	84	83	99	103	**127**
Gd	78	83	78	95	102	**128**
Tb	81	85	83	98	109	**141**
Dy	79	85	81	96	102	**125**
Ho	78	83	82	92	101	**129**
Er	77	86	81	90	101	**125**
Tm	72	84	84	88	97	**122**
Yb	71	80	83	83	94	**109**
Lu	72	90	85	88	94	**122**
Hf	81	88	101	102	106	**111**
Ta	73	76	99	92	106	106
Pb	82	89	98	98	**121**	117
Th	80	83	88	107	102	103
U	104	98	**206**	123	126	**334**

Bibliography

Albarède, F. & Michard, A. (1986) Transfer of continental Mg, S, O and U to the mantle through hydrothermal alteration of the oceanic crust. *Chemical Geology, 57* (1–2): 1-15.

Almeev, R., Portnyagin, M., Wengorsch, T., Sano, T., Natland, J.H. & Garbe-Schönberg, D. (2011) Highly depleted melt inclusions in olivine from Shatsky Rise. *Mineralogical Magazine, 75* (3): 426.

Alt, J. (1995) *Subseafloor processes in mid-ocean ridge hydrothermal systems*. In: Humphreys, S.E., Zierenberg, R.A., Mullineaux, L.S. & Thomson, R.E. (Eds.), Seafloor Hydrothermal Systems: Physical, Chemical, Biological, and Geological Interactions. American Geophysical Union, Washington, DC, 91, pp. 85-114.

Alt, J.C. & Honnorez, J. (1984) Alteration of the upper oceanic crust, DSDP site 417: mineralogy and chemistry. *Contributions to Mineralogy and Petrology, 87* (2): 149-169.

Alt, J.C. & Mata, P. (2000) On the role of microbes in the alteration of submarine basaltic glass: a TEM study. *Earth and Planetary Science Letters, 181* (3): 301-313.

Alt, J.C. & Teagle, D.A.H. (2003) Hydrothermal alteration of upper oceanic crust formed at a fast-spreading ridge: mineral, chemical, and isotopic evidence from ODP Site 801. *Chemical Geology, 201* (3-4): 191-211.

Anderson, D.L. (2005a) Large igneous provinces, delamination, and fertile mantle. *Elements, 1* (5): 271-275.

Anderson, D.L. (2005b) *Scoring hotspots: The plume and plate paradigms*. In: Foulger, G.R., Natland, J.H., Presnall, D.C. & Anderson, D.L. (Eds.), Plates, Plumes, and Paradigms. Geological Society of America, Inc., Boulder, Colorado, 388, pp. 31-54.

Anderson, D.L. (2007) The eclogite engine: Chemical geodynamics as a Galileo thermometer. *Geological Society of America Special Papers, 430*: 47-64.

Anderson, D.L. & Natland, J.H. (2007) Evidence for mantle plumes? *Nature, 450* (7169): E15-E15.

Arndt, N.T., Czamanske, G.K., Wooden, J.L. & Fedorenko, V.A. (1993) Mantle and crustal contributions to continental flood volcanism. *Tectonophysics, 223* (1–2): 39-52.

Bach, W., Alt, J.C., Niu, Y., Humphris, S.E., Erzinger, J. & Dick, H.J.B. (2001) The geochemical consequences of late-stage low-grade alteration of lower ocean crust at the SW Indian Ridge: results from ODP Hole 735B (Leg 176). *Geochimica Et Cosmochimica Acta, 65* (19): 3267-3287.

Bach, W., Peucker-Ehrenbrink, B., Hart, S.R. & Blusztajn, J.S. (2003) Geochemistry of hydrothermally altered oceanic crust: DSDP/ODP Hole 504B -

Implications for seawater-crust exchange budgets and Sr- and Pb-isotopic evolution of the mantle. *Geochem. Geophys. Geosyst., 4* (3): 8904.

Bach, W. & Früh-Green, G.L. (2010) Alteration of the Oceanic Lithosphere and Implications for Seafloor Processes. *Elements, 6* (3): 173-178.

Baldermann, A., Warr, L.N., Grathoff, G.H. & Dietzel, M. (2013) The rate and mechanism of deep-sea glauconite formation at the Ivory Coast-Ghana marginal ridge. *Clays And Clay Minerals, 61* (3): 258-276.

Banerjee, N.R., Honnorez, J. & Muehlenbachs, K. (2004) *Low-temperature alteration of submarine basalts from the Ontong Java Plateau*. In: Fitton, J.G., Mahoney, J.J., Wallace, P.J. & Saunders, A.D. (Eds.), Origin and Evolution of the Ontong Java Plateau. Geological Society of London, Special Publications, London, 229, pp. 259-273.

Bardintzeff, J.-M., Liegeois, J.-P., Bonin, B., Bellon, H. & Rasamimanana, G. (2010) Madagascar volcanic provinces linked to the Gondwana break-up: Geochemical and isotopic evidences for contrasting mantle sources. *Gondwana Research, 18* (2-3): 295-314.

Becker, T.W. & Boschi, L. (2002) A comparison of tomographic and geodynamic mantle models. *Geochemistry, Geophysics, Geosystems, 3* (1).

Befus, K.S., Hanson, R.E., Lehman, T.M. & Griffin, W.R. (2008) Cretaceous basaltic phreatomagmatic volcanism in West Texas: Maar complex at Peña Mountain, Big Bend National Park. *Journal of Volcanology and Geothermal Research, 173* (3–4): 245-264.

Beiersdorf, H., Bach, W., Duncan, R., Erzinger, J. & Weiss, W. (1995) New evidence for the production of EM-type ocean island basalts and large volumes of volcaniclastites during the early history of the Manihiki Plateau. *Marine Geology, 122* (3): 181-205.

Ben-Avraham, Z., Nur, A., Jones, D. & Cox, A. (1981) Continental Accretion: From Oceanic Plateaus to Allochthonous Terranes. *Science, 213* (4503): 47-54.

Ben-Avraham, Z., Hartnady, C.J.H. & le Roex, A.P. (1995) Neotectonic activity on continental fragments in the Southwest Indian Ocean: Agulhas Plateau and Mozambique Ridge. *Journal of Geophysical Research: Solid Earth, 100* (B4): 6199-6211.

Bénard, F., Callot, J.-P., Vially, R., Schmitz, J., Roest, W., Patriat, M. & Loubrieu, B. (2010) The Kerguelen plateau: Records from a long-living/composite microcontinent. *Marine and Petroleum Geology, 27* (3): 633-649.

Benzerara, K., Menguy, N., Banerjee, N.R., Tyliszczak, T., Brown Jr, G.E. & Guyot, F. (2007) Alteration of submarine basaltic glass from the Ontong Java Plateau: A STXM and TEM study. *Earth and Planetary Science Letters, 260* (1-2): 187-200.

Bercovici, D. & Mahoney, J. (1994) Double Flood Basalts and Plume Head Separation at the 660-Kilometer Discontinuity. *Science, 266* (5189): 1367-1369.

Best, M.G. (Ed.) (2003). *Igneous and metamorphic petrology* (2nd ed. ed.): Blackwell Publishing.

Bienvenu, P., Bougault, H., Joron, J.L., Treuil, M. & Dmitriev, L. (1990) MORB alteration: Rare-earth element/non-rare-earth hygromagmaphile element fractionation. *Chemical Geology, 82* (0): 1-14.

Bitschene, P.R., Mehl, K.W. & Schmincke, H.-U. (Eds.). (1992). *Geochemistry of marine ash layers and epiclastic rocks from the Kerguelen Plateau, Southern Indian Ocean (Legs 119 and 120).* College Station, TX (Ocean Drilling Program).

Black, B.A., Weiss, B.P., Elkins-Tanton, L.T., Veselovskiy, R.V. & Latyshev, A. (2015) Siberian Traps volcaniclastic rocks and the role of magma-water interactions. *Geological Society of America Bulletin, 127* (9-10): 1437-1452.

Blichert-Toft, J. & Albarede, F. (1997) The Lu-Hf isotope geochemistry of chondrites and the evolution of the mantle-crust system. *Earth and Planetary Science Letters, 148* (1-2): 243-258.

Boschi, L., Becker, T.W. & Steinberger, B. (2007) Mantle plumes: Dynamic models and seismic images. *Geochemistry Geophysics Geosystems, 8* (10): 20p.

Bouvier, A., Vervoort, J.D. & Patchett, P.J. (2008) The Lu-Hf and Sm-Nd isotopic composition of CHUR: Constraints from unequilibrated chondrites and implications for the bulk composition of terrestrial planets. *Earth and Planetary Science Letters, 273* (1-2): 48-57.

Bralower, T.J., Premoli Silva, I., Malone, M.J. & et al. (2002). *Proceedings of the Ocean Drilling Program, Initial Reports, Volume 198* (pp. 110).

Brown, R.J. & Andrews, G.D.M. (2015) *Chapter 36 - Deposits of Pyroclastic Density Currents*. In: Sigurdsson, H., Houghton, B.F., McNutt, S.R., Rymer, H. & Stix, J. (Eds.), The Encyclopedia of Volcanoes (Second Edition). Academic Press, Amsterdam, pp. 631-648.

Bryan, S.E., Marti, J. & Cas, R.A.F. (1998) Stratigraphy of the Bandas del Sur Formation: an extracaldera record of Quaternary phonolitic explosive eruptions from the Las Canadas edifice, Tenerife (Canary Islands). *Geological Magazine, 135* (5): 605-636.

Bryan, S.E., Riley, T.R., Jerram, D.A., Leat, P.T. & Stephens, C.J. (2002) *Silicic volcanism: an under-valued component of large igneous provinces and volcanic rifted margins*. In: Menzies, M.A., Klemperer, S.L., Ebinger, C.J. & Baker, J. (Eds.), Magmatic Rifted Margins. Geological Society of America, Inc., Boulder, Colorado, 362, pp. 99-120.

Bryan, S.E. & Ernst, R.E. (2008) Revised definition of large igneous provinces (LIPs). *Earth-Science Reviews, 86* (1-4): 175-202.

Bryan, S.E., Ukstins Peate, I., Peate, D.W., Self, S., Jerram, D.A., Mawby, M.R., Marsh, J.S. & Miller, J.A. (2010) The largest volcanic eruptions on Earth. *Earth-Science Reviews, 102* (3-4): 207-229.

Bryan, S.E. & Ferrari, L. (2013) Large Igneous Provinces and Silicic Large Igneous Provinces: Progress in our understanding over the last 25 years. *Geological Society of America Bulletin, 125*: 1053–1078.

Bull, S.W. & Cas, R.A.F. (2000) Distinguishing base-surge deposits and volcaniclastic fluviatile sediments: an ancient example from the Lower Devonian Snowy River Volcanics, south-eastern Australia. *Sedimentology, 47* (1): 87-98.

Burke, K. (1988) Tectonic Evolution of the Caribbean. *Annual Review of Earth and Planetary Sciences, 16* (1): 201-230.

Burke, K. & Torsvik, T.H. (2004) Derivation of Large Igneous Provinces of the past 200 million years from long-term heterogeneities in the deep mantle. *Earth and Planetary Science Letters, 227* (3–4): 531-538.

Burke, K., Steinberger, B., Torsvik, T.H. & Smethurst, M.A. (2008) Plume Generation Zones at the margins of Large Low Shear Velocity Provinces on the core-mantle boundary. *Earth and Planetary Science Letters, 265* (1-2): 49-60.

Burov, E. & Gerya, T. (2014) Asymmetric three-dimensional topography over mantle plumes. *Nature, 513* (7516): 85-89.

Camboa, L.A.P. & Rabinowitz, P.D. (1984) Research on the Vema Channel The evolution of the Rio Grande Rise in the southwest Atlantic Ocean. *Marine Geology, 58* (1): 35-58.

Campbell, I.H. & Griffiths, R.W. (1990) Implications of Mantle Plume Structure for the Evolution of Flood Basalts. *Earth and Planetary Science Letters, 99* (1-2): 79-93.

Campbell, I.H. (2001) *Identification of ancient mantle plumes*. In: Ernst, R.E., Buchan, K.L. (Ed.), Mantle Plumes: Their Identification through Time. Geological Society of America, Inc., Boulder, Colorado, 352, pp. 5-21.

Campbell, I.H. (2005) Large igneous provinces and the mantle plume hypothesis. *Elements, 1* (5): 265-269.

Campbell, I.H. (2007) Testing the plume theory. *Chemical Geology, 241* (3-4): 153-176.

Cantrell, K.J. & Byrne, R.H. (1987) Rare earth element complexation by carbonate and oxalate ions. *Geochimica Et Cosmochimica Acta, 51* (3): 597-605.

Carlson, R.L., Christensen, N.I. & Moore, R.P. (1980) Anomalous crustal structures in ocean basins: Continental fragments and oceanic plateaus. *Earth and Planetary Science Letters, 51* (1): 171-180.

Carvallo, C., Camps, P., Ooga, M., Fanjat, G. & Sager, W.W. (2013) Palaeointensity determinations and rock magnetic properties on basalts from Shatsky Rise: new evidence for a Mesozoic dipole low. *Geophysical Journal International, 192* (3): 986-999.

Cas, R.A.F. & Wright, J.V. (1988) *Volcanic Successions Modern and Ancient*. Springer, Netherlands.

Cashman, K.V. & Scheu, B. (2015) *Chapter 25 - Magmatic Fragmentation*. In: Sigurdsson, H., Houghton, B.F., McNutt, S.R., Rymer, H. & Stix, J. (Eds.), The Encyclopedia of Volcanoes (Second Edition). Academic Press, Amsterdam, pp. 459-471.

Castillo, P.R. (2004) *Geochemistry of Cretaceous volcaniclastic sediments in the Nauru and East Mariana basins provides insights into the mantle sources of giant oceanic plateaus*. In: Fitton, J.G., Mahoney, J.J., Wallace, P.J. & Saunders, A.D. (Eds.), Origin and Evolution of the Ontong Java Plateau. Geological Society of London, London, 229, pp. 353-368.

Chafetz, H.S. & Reid, A. (2000) Syndepositional shallow-water precipitation of glauconitic minerals. *Sedimentary Geology, 136* (1–2): 29-42.

Chandler, M.T., Wessel, P., Taylor, B., Seton, M., Kim, S.-S. & Hyeong, K. (2012) Reconstructing Ontong Java Nui: Implications for Pacific absolute plate motion, hotspot drift and true polar wander. *Earth and Planetary Science Letters, 331–332* (0): 140-151.

Chandler, M.T., Wessel, P. & Taylor, B. (2015) Tectonic reconstructions in magnetic quiet zones: Insights from the Greater Ontong Java Plateau. *Geological Society of America Special Papers, 511*: 185-193.

Charvis, P., Recq, M., Operto, S. & Brefort, D. (1995) Deep structure of the northern Kerguelen Plateau and hotspot-related activity. *Geophysical Journal International, 122* (3): 899-924.

Chauvel, C. & Blichert-Toft, J. (2001) A hafnium isotope and trace element perspective on melting of the depleted mantle. *Earth and Planetary Science Letters, 190* (3–4): 137-151.

Chipera, S. & Bish, D. (2013) Fitting Full X-Ray Diffraction Patterns for Quantitative Analysis: A Method for Readily Quantifying Crystalline and Disordered Phases. *Advances in Materials Physics and Chemistry, 3* (1A): 47-53.

Chough, S.K. & Sohn, Y.K. (1990) Depositional mechanics and sequences of base surges, Songaksan tuff ring, Cheju Island, Korea. *Sedimentology, 37* (6): 1115-1135.

Cioni, R., Pistolesi, M., Bertagnini, A., Bonadonna, C., Hoskuldsson, A. & Scateni, B. (2014) Insights into the dynamics and evolution of the 2010 Eyjafjallajökull summit eruption (Iceland) provided by volcanic ash textures. *Earth and Planetary Science Letters, 394* (0): 111-123.

Cioni, R., Pistolesi, M. & Rosi, M. (2015) *Chapter 29 - Plinian and Subplinian Eruptions*. In: Sigurdsson, H., Houghton, B.F., McNutt, S.R., Rymer, H. & Stix, J. (Eds.), The Encyclopedia of Volcanoes (Second Edition). Academic Press, Amsterdam, pp. 519-535.

Clayton, T. & Pearce, R.B. (2000) Alteration mineralogy of Cretaceous basalt from ODP Site 1001, Leg 165 (Caribbean Sea). *Clay Minerals, 35* (4): 719-733.

Clément, J.-P., Caroff, M., Dudoignon, P., Launeau, P., Bohn, M., Cotten, J., Blais, S. & Guille, G. (2007) A possible link between gabbros bearing High Temperature Iddingsite alteration and huge pegmatoid intrusions: The Society Islands, French Polynesia. *Lithos, 96* (3–4): 524-542.

Clift, P.D. (2005) Sedimentary evidence for moderate mantle temperature anomalies associated with hotspot volcanism. *Geological Society of America Special Papers, 388*: 279-287.

Cloos, M. (1993) Lithospheric buoyancy and collisional orogenesis: Subduction of oceanic plateaus, continental margins, island arcs, spreading ridges, and seamounts. *Geological Society of America Bulletin, 105* (6): 715-737.

Coffin, M.F. & Eldholm, O. (1991). *Large Igneous Provinces: JOI/USSAC workshop report*. The University of Texas at Austin Institute for Geophysics Technical Report, p. 79.

Coffin, M.F. (1992) *Emplacement and Subsidence of Indian Ocean Plateaus and Submarine Ridges*. In: Duncan, R.A., Rea, D.K., Kidd, R.B., von Rad, U. & Weissel, J.K. (Eds.), Synthesis of Results from Scientific Drilling in the Indian Ocean. American Geophysical Union, pp. 115-125.

Coffin, M.F. & Eldholm, O. (1993) Scratching the Surface - Estimating Dimensions of Large Igneous Provinces. *Geology, 21* (6): 515-518.

Coffin, M.F. & Eldholm, O. (1994a) Exploring Large Subsea Igneous Provinces. *Oceanus, 36* (4): 75-78.

Coffin, M.F. & Eldholm, O. (1994b) Large Igneous Provinces - Crustal Structure, Dimensions, and External Consequences. *Reviews of Geophysics, 32* (1): 1-36.

Collerson, K.D., Williams, Q., Ewart, A.E. & Murphy, D.T. (2010) Origin of HIMU and EM-1 domains sampled by ocean island basalts, kimberlites and carbonatites: The role of CO2-fluxed lower mantle melting in thermochemical upwellings. *Physics of the Earth and Planetary Interiors, 181* (3-4): 112-131.

Colwell, J.B., Symonds, P.A. & Crawford, A.J. (1994) The nature of the Wallaby (Cuvier) Plateau and other igneous provinces of the west Australian margin. *AGSO Journal of Australian Geology & Geophysics, 15* (1): 137-156.

Condie, K.C. (2001) *Mantle Plumes and their Record in Earth History*. Cambridge University Press, Cambridge.

Condie, K.C. (2004) Supercontinents and superplume events: distinguishing signals in the geologic record. *Physics of the Earth and Planetary Interiors, 146* (1-2): 319-332.

Cotten, J., Le Dez, A., Bau, M., Caroff, M., Maury, R.C., Dulski, P., Fourcade, S., Bohn, M. & Brousse, R. (1995) Origin of anomalous rare-earth element and yttrium enrichments in subaerially exposed basalts: Evidence from French Polynesia. *Chemical Geology, 119* (1): 115-138.

Courtillot, V. (2002) *Evolutionary Catastrophes: the Science of Mass Extinction*. Cambridge University Press, Cambridge.

Courtillot, V., Davaille, A., Besse, J. & Stock, J. (2003) Three distinct types of hotspots in the Earth's mantle. *Earth and Planetary Science Letters, 205* (3-4): 295-308.

Creager, K.C. & Jordan, T.H. (1984) Slab penetration into the lower mantle. *Journal of Geophysical Research, 89(B5)*: 3031-3049.

Creager, K.C. & Jordan, T.H. (1986) Slab penetration into the lower mantle beneath the Mariana and other island arcs of the northwest Pacific. *Journal of Geophysical Research, 91(B3)*: 3573-3589.

Czamanske, G.K., Gurevitch, A.B., Fedorenko, V. & Simonov, O. (1998) Demise of the Siberian plume: Paleogeographic and paleotectonic reconstruction from the prevolcanic and volcanic record, north-central Siberia. *International Geology Review, 40* (2): 95-115.

D'Antonio, M. & Kristensen, M.B. (2005) Hydrothermal alteration of oceanic crust in the West Philippine Sea Basin (Ocean Drilling Program Leg 195, Site 1201): inferences from a mineral chemistry investigation. *Mineralogy and Petrology, 83* (1-2): 87-112.

Dannberg, J. & Sobolev, S.V. (2015) Low-buoyancy thermochemical plumes resolve controversy of classical mantle plume concept. *Nat Commun, 6*.

Davy, B., Hoernle, K. & Werner, R. (2008) Hikurangi Plateau: Crustal structure, rifted formation, and Gondwana subduction history. *Geochemistry, Geophysics, Geosystems, 9* (7): Q07004.

Delacour, A. & Guillaume, D. (2013). Data report: Alteration of basalts from Sites U1346 and U1349 at Shatsky Rise oceanic plateau, IODP Expedition 324. In Sager, W.W., Sano, T., Geldmacher, J. & the Expedition 324 Scientists (Eds.), Proceedings of the Integrated Ocean Drilling Program (Vol. 324): Tokyo, Integrated Ocean Drilling Program Management International, Inc.

Dobretsov, N.L. & Vernikovsky, V.A. (2001) Mantle plumes and their geologic manifestations. *International Geology Review, 43* (9): 771-787.

Downs, R.T. & Hall-Wallace, M. (2003) The American Mineralogist crystal structure database. *American Mineralogist, 88* (1): 247-250.

Drief, A. & Schiffman, P. (2004) Very low-temperature alteration of sideromelane in hyaloclastites and hyalotuffs from Kilauea and Mauna Kea volcanoes: implications for the mechanism of palagonite formation. *Clays And Clay Minerals, 52* (5): 622-634.

Dufek, J., Esposti Ongaro, T. & Roche, O. (2015) *Chapter 35 - Pyroclastic Density Currents: Processes and Models*. In: Sigurdsson, H., Houghton, B.F., McNutt, S.R., Rymer, H. & Stix, J. (Eds.), The Encyclopedia of Volcanoes (Second Edition). Academic Press, Amsterdam, pp. 617-629.

Duncan, R.A. & Richards, M.A. (1991) Hotspots, Mantle Plumes, Flood Basalts, and True Polar Wander. *Reviews of Geophysics, 29* (1): 31-50.

Duncan, R.A. (2002) A Time Frame for Construction of the Kerguelen Plateau and Broken Ridge. *Journal of Petrology, 43* (7): 1109-1119.

Eggins, S.M., Woodhead, J.D., Kinsley, L.P.J., Mortimer, G.E., Sylvester, P., McCulloch, M.T., Hergt, J.M. & Handler, M.R. (1997) A simple method for the

precise determination of ≥ 40 trace elements in geological samples by ICPMS using enriched isotope internal standardisation. *Chemical Geology, 134* (4): 311-326.

Elliot, D.H. & Fleming, T.H. (2008) Physical volcanology and geological relationships of the Jurassic Ferrar Large Igneous Province, Antarctica. *Journal of Volcanology and Geothermal Research, 172* (1-2): 20-37.

Emelyanov, E.M., Elnikov, I.N., Trimonis, E.S. & Kharin, G.S. (1990) Geology of the Sierra Leone Rise. *Geologische Rundschau, 79* (3): 823-848.

Ernst, R.E. & Buchan, K.L. (2001) *Large mafic magmatic events through time and links to mantle plume heads*. In: Ernst, R.E. & Buchan, K.L. (Eds.), Mantle Plumes: Their Identification through Time. Geological Society of America, Inc., Boulder, Colorado, Vol. 352, pp. p. 483-575.

Ernst, R.E. & Buchan, K.L. (2003) Recognizing mantle plumes in the geological record. *Annual Review of Earth and Planetary Sciences, 31*: 469-523.

Ernst, R.E., Buchan, K.L. & Campbell, I.H. (2005) Frontiers in Large Igneous Province research. *Lithos, 79* (3-4): 271-297.

Ernst, R.E. & Bell, K. (2010) Large igneous provinces (LIPs) and carbonatites. *Mineralogy and Petrology, 98* (1-4): 55-76.

Farnetani, C.G. & Richards, M.A. (1994) Numerical investigations of the mantle plume initiation model for flood basalt events. *Journal of Geophysical Research: Solid Earth, 99* (B7): 13813-13833.

Farnetani, C.G., Legras, B. & Tackley, P.J. (2002) Mixing and deformations in mantle plumes. *Earth and Planetary Science Letters, 196* (1–2): 1-15.

Farnetani, C.G. & Hofmann, A.W. (2011) *Mantle plumes*. In: Gupta, H.K. (Ed.), Encyclopedia of Solid Earth Geophysics. Springer, p. 1620 p.

Fischer, A.G., Heezen, B.C., Boyce, R.E., Bukry, D., Garrison, R.E., Kling, S.A., Krasheninnikov, V., Lisitzin, A.P. & Pimm, A.C. (1971). *Initial Reports DSDP, 6* Vol. 6.

Fischer, M.D., Uenzelmann-Neben, G., Jacques, G. & Werner, R. (2017) The Mozambique Ridge: a document of massive multistage magmatism. *Geophysical Journal International, 208* (1): 449-467.

Fisher, R.V. & Schmincke, H.-U. (1984) *Pyroclastic Rocks*. Springer, Heidelberg.

Fleet, A.J. (1984) *Chapter 10 - Aqueous and Sedimentary Geochemistry of the Rare Earth Elements*. In: Henderson, P. (Ed.), Developments in Geochemistry. Elsevier, Volume 2, pp. 343-373.

Forte, A.M. & Peltier, W.R. (1991) Mantle convection and core-mantle boundary topography: explanations and implications. *Tectonophysics, 187* (1-3): 91-116.

Foulger, G.R. & Anderson, D.L. (2005) A cool model for the Iceland hotspot. *Journal of Volcanology and Geothermal Research, 141* (1-2): 1-22.

Foulger, G.R. (2005) Mantle plumes: Why the current skepticism? *Chinese Science Bulletin, 50* (15): 1555-1560.

Foulger, G.R., Natland, J.H., Presnall, D.C. & Anderson, D.L. (2005) *Plates, Plumes, and Paradigms*. Geological Society of America, Inc., Boulder, Colorado.

Foulger, G.R. (2010) *Plates vs Plumes: A Geological Controversy*. John Wiley & Sons Ltd., Chichester, West Sussex.

Frey, F.A., Coffin, M.F., Wallace, P.J., Weis, D., Zhao, X., Wise, S.W., Wahnert, V., Teagle, D.A.H., Saccocia, P.J., Reusch, D.N., Pringle, M.S., Nicolaysen, K.E., Neal, C.R., Muller, R.D., Moore, C.L., Mahoney, J.J., Keszthelyi, L., Inokuchi, H., Duncan, R.A., Delius, H., Damuth, J.E., Damasceno, D., Coxall, H.K., Borre, M.K., Boehm, F., Barling, J., Arndt, N.T. & Antretter, M. (2000) Origin and evolution of a submarine large igneous province: the Kerguelen Plateau and Broken Ridge, southern Indian Ocean. *Earth and Planetary Science Letters, 176* (1): 73-89.

Frey, F.A., Weis, D. & Coffin, M.F. (2003) Kerguelen plume: A 120 Myr record of volcanism. *Geochimica Et Cosmochimica Acta, 67* (18): A104-A104.

Gale, A., Dalton, C.A., Langmuir, C.H., Su, Y. & Schilling, J.-G. (2013) The mean composition of ocean ridge basalts. *Geochemistry, Geophysics, Geosystems, 14* (3): 489-518.

Garcia, M.O., Grooms, D.G. & Naughton, J.J. (1987) Petrology and geochronology of volcanic rocks from seamounts along and near the Hawaiian Ridge: Implications for propagation rate of the ridge. *Lithos, 20* (4): 323-336.

Geldmacher, J., Hanan, B.B., Blichert-Toft, J., Harpp, K., Hoernle, K., Hauff, F., Werner, R. & Kerr, A.C. (2003) Hafnium isotopic variations in volcanic rocks from the Caribbean Large Igneous Province and Galapagos hot spot tracks. *Geochemistry Geophysics Geosystems, 4*: 24p.

Geldmacher, J., van den Bogaard, P., Heydolph, K. & Hoernle, K. (2014) The age of Earth's largest volcano: Tamu Massif on Shatsky Rise (northwest Pacific Ocean). *International Journal of Earth Sciences*: 1-7.

Gençalioğlu-Kuşcu, G., Atilla, C., Cas, R.A.F. & Kuşcu, İ. (2007) Base surge deposits, eruption history, and depositional processes of a wet phreatomagmatic volcano in Central Anatolia (Cora Maar). *Journal of Volcanology and Geothermal Research, 159* (1–3): 198-209.

German, C.R. & Von Damm, K.L. (2003) *Hydrothermal Processes*. In: Holland, H.D. & Turekian, K.K. (Eds.), Treatise on Geochemistry. Pergamon, Oxford, 6, 6.07, pp. 181-222.

Gettrust, J.F., Furukawa, K. & Kroenke, L.W. (1980) Crustal Structure of the Shatsky Rise from Seismic Refraction Measurements. *Journal of Geophysical Research, 85* (10): 5411-5415.

Gibbons, A.D., Whittaker, J.M. & Müller, R.D. (2013) The breakup of East Gondwana: Assimilating constraints from Cretaceous ocean basins around India into a best-fit tectonic model. *Journal of Geophysical Research: Solid Earth, 118* (3): 808-822.

Gillis, K.M., Muehlenbachs, K., Stewart, M., Gleeson, T. & Karson, J. (2001) Fluid flow patterns in fast spreading East Pacific Rise crust exposed at Hess Deep. *J. Geophys. Res., 106* (B11): 26311-26329.

Gohl, K., Uenzelmann-Neben, G. & Grobys, N. (2011) Growth and dispersal of a Southeast African Large Igneous Province. *South African Journal of Geology, 114* (3-4): 379-386.

Goldstein, S.L. & Hemming, S.R. (2003) *Long-lived Isotopic Tracers in Oceanography, Paleoceanography, and Ice-sheet Dynamics*. In: Holland, H.D. & Turekian, K.K. (Eds.), Treatise on Geochemistry. Pergamon, Oxford, 6, 6.17, pp. 453-489.

Goodfellow, B.W., Chadwick, O.A. & Hilley, G.E. (2014) Depth and character of rock weathering across a basaltic-hosted climosequence on Hawai'i. *Earth Surface Processes and Landforms, 39* (3): 381-398.

Goslin, J. & Diament, M. (1987) Mechanical and thermal isostatic response of the Del Cano Rise and Crozet Bank (southern Indian Ocean) from altimetry data. *Earth and Planetary Science Letters, 84* (2): 285-294.

Graettinger, A.H., Skilling, I., McGarvie, D. & Höskuldsson, Á. (2013) Subaqueous basaltic magmatic explosions trigger phreatomagmatism: A case study from Askja, Iceland. *Journal of Volcanology and Geothermal Research, 264* (0): 17-35.

Grant, J.A. (2005) Isocon analysis: A brief review of the method and applications. *Physics and Chemistry of the Earth, Parts A/B/C, 30* (17–18): 997-1004.

Greene, A.R., Scoates, J.S. & Weis, D. (2008) Wrangellia flood basalts in Alaska: A record of plume-lithosphere interaction in a Late Triassic accreted oceanic plateau. *Geochemistry, Geophysics, Geosystems, 9* (12).

Greene, A.R., Scoates, J.S., Weis, D., Katvala, E.C., Israel, S. & Nixon, G.T. (2010) The architecture of oceanic plateaus revealed by the volcanic stratigraphy of the accreted Wrangellia oceanic plateau. *Geosphere, 6* (1): 47-73.

Gresens, R.L. (1967) Composition-volume relationships of metasomatism. *Chemical Geology, 2* (0): 47-65.

Griffiths, R.W. & Campbell, I.H. (1990) Stirring and Structure in Mantle Starting Plumes. *Earth and Planetary Science Letters, 99* (1-2): 66-78.

Guillot, S. & Hattori, K. (2013) Serpentinites: Essential Roles in Geodynamics, Arc Volcanism, Sustainable Development, and the Origin of Life. *Elements, 9* (2): 95-98.

Hair, J.F.J., Black, W.C., Babin, B.J., Anderson, R.E. & Tatham, R.L. (2006) *Multivariate data analysis: Sixth edition*. Pearson Prentice Hall, New Jersey, USA.

Hales, T.C., Abt, D.L., Humphreys, E.D. & Roering, J.J. (2005) A lithospheric instability origin for Columbia River flood basalts and Wallowa Mountains uplift in northeast Oregon. *Nature, 438* (7069): 842-845.

Hanan, B.B. & Schilling, J.-G. (1997) The dynamic evolution of the Iceland mantle plume: the lead isotope perspective. *Earth and Planetary Science Letters, 151* (1–2): 43-60.

Hanyu, T., Shimizu, K. & Sano, T. (2015) Noble gas evidence for the presence of recycled material in magma sources of the Shatsky Rise. *Geological Society of America Special Papers, 511*: 57-67.

Hart, S.R., Hauri, E.H., Oschmann, L.A. & Whitehead, J.A. (1992) Mantle Plumes and Entrainment: Isotopic Evidence. *Science, 256* (5056): 517-520.

Hastie, A.R. & Kerr, A.C. (2010) Mantle plume or slab window?: Physical and geochemical constraints on the origin of the Caribbean oceanic plateau. *Earth-Science Reviews, 98* (3-4): 283-293.

Hastie, A.R., Mitchell, S.F., Treloar, P.J., Kerr, A.C., Neill, I. & Barfod, D.N. (2013) Geochemical components in a Cretaceous island arc: The Th/La–(Ce/Ce*)Nd diagram and implications for subduction initiation in the inter-American region. *Lithos, 162–163* (0): 57-69.

Head, J.W. & Wilson, L. (2003) Deep submarine pyroclastic eruptions: theory and predicted landforms and deposits. *Journal of Volcanology and Geothermal Research, 121* (3–4): 155-193.

Heaton, D.E. & Koppers, A.A.P. (2014). *Constraining the rapid construction of Tamu Massif at an ~145 Myr old triple junction, Shatsky Rise.* Paper presented at the Goldschmidt Conference, Sacramento, p. 948.

Hein, J.R., Yeh, H.-W., Gunn, S.H., Sliter, W.V., Benninger, L.M. & Wang, C.-H. (1993) Two Major Cenozoic Episodes of Phosphogenesis Recorded in Equatorial Pacific Seamount Deposits. *Paleoceanography, 8* (2): 293-311.

Hein, J.R., Conrad, T.A., Frank, M., Christl, M. & Sager, W.W. (2012) Copper-nickel-rich, amalgamated ferromanganese crust-nodule deposits from Shatsky Rise, NW Pacific. *Geochemistry, Geophysics, Geosystems, 13* (10): Q10022.

Heydolph, K., Murphy, D.T., Geldmacher, J., Romanova, I.V., Greene, A., Hoernle, K., Weis, D. & Mahoney, J. (2014) Plume versus plate origin for the Shatsky Rise oceanic plateau (NW Pacific): Insights from Nd, Pb and Hf isotopes. *Lithos, 200-201*: 49-63.

Hill, R.I. (1991) Starting Plumes and Continental Break-Up. *Earth and Planetary Science Letters, 104* (2-4): 398-416.

Hillier, J.K. & Watts, A.B. (2005) Relationship between depth and age in the North Pacific Ocean. *Journal of Geophysical Research: Solid Earth, 110* (B2): B02405.

Hoernle, K., Abt, D.L., Fischer, K.M., Nichols, H., Hauff, F., Abers, G.A., van den Bogaard, P., Heydolph, K., Alvarado, G., Protti, M. & Strauch, W. (2008) Arc-parallel flow in the mantle wedge beneath Costa Rica and Nicaragua. *Nature, 451* (7182): 1094-1097.

Hoernle, K., Hauff, F., van den Bogaard, P., Werner, R., Mortimer, N., Geldmacher, J., Garbe-Schönberg, D. & Davy, B. (2010) Age and geochemistry of

volcanic rocks from the Hikurangi and Manihiki oceanic Plateaus. *Geochimica Et Cosmochimica Acta, 74* (24): 7196-7219.

Hoernle, K., Hauff, F., Werner, R., van den Bogaard, P., Gibbons, A.D., Conrad, S. & Müller, R.D. (2011) Origin of Indian Ocean Seamount Province by shallow recycling of continental lithosphere. *Nature Geoscience, 4* (27 Nov): 883-887.

Hofmann, A.W. (2003) *Sampling Mantle Heterogeneity through Oceanic Basalts: Isotopes and Trace Elements*. In: Heinrich, D.H. & Karl, K.T. (Eds.), Treatise on Geochemistry. Pergamon, Oxford, 2, 2.03, pp. 1-44.

Houghton, B., White, J.D.L. & Van Eaton, A.R. (2015) *Chapter 30 - Phreatomagmatic and Related Eruption Styles*. In: Sigurdsson, H., Houghton, B.F., McNutt, S.R., Rymer, H. & Stix, J. (Eds.), The Encyclopedia of Volcanoes (Second Edition). Academic Press, Amsterdam, pp. 537-552.

Houghton, B. & Carey, R.J. (2015) *Chapter 34 - Pyroclastic Fall Deposits*. In: Sigurdsson, H., Houghton, B.F., McNutt, S.R., Rymer, H. & Stix, J. (Eds.), The Encyclopedia of Volcanoes (Second Edition). Academic Press, Amsterdam, pp. 599-616.

Houghton, B.F. & Wilson, C.J.N. (1989) A vesicularity index for pyroclastic deposits. *Bulletin of Volcanology, 51* (6): 451-462.

Humphris, S.E. & Thompson, G. (1978) Hydrothermal alteration of oceanic basalts by seawater. *Geochimica Et Cosmochimica Acta, 42* (1): 107-125.

Husen, A., Almeev, R.R., Holtz, F., Koepke, J., Sano, T. & Mengel, K. (2013) Geothermobarometry of basaltic glasses from the Tamu Massif, Shatsky Rise oceanic plateau. *Geochemistry, Geophysics, Geosystems, 14* (10): 3908-3928.

Husen, A., Almeev, R.R. & Holtz, F. (2016) The Effect of H2O and Pressure on Multiple Saturation and Liquid Lines of Descent in Basalt from the Shatsky Rise. *Journal of Petrology, 57* (2): 309-344.

Ingle, S. & Coffin, M.F. (2004) Impact origin for the greater Ontong Java Plateau? *Earth and Planetary Science Letters, 218* (1-2): 123-134.

Irvine, T.N. & Baragar, W.R.A. (1971) A Guide to the Chemical Classification of the Common Volcanic Rocks. *Canadian Journal of Earth Sciences, 8* (5): 523-548.

Ishikawa, A., Nakamura, E. & Mahoney, J.J. (2005) Jurassic oceanic lithosphere beneath the southern Ontong Java Plateau: Evidence from xenoliths in alnoite, Malaita, Solomon Islands. *Geology, 33* (5): 393-396.

Ito, G. & Clift, P.D. (1998) Subsidence and growth of Pacific Cretaceous plateaus. *Earth and Planetary Science Letters, 161* (1–4): 85-100.

Ito, G. & Mahoney, J.J. (2005) Flow and melting of a heterogeneous mantle: 2. Implications for a chemically nonlayered mantle. *Earth and Planetary Science Letters, 230* (1-2): 47-63.

Jackson, M.G. & Jellinek, A.M. (2013) Major and trace element composition of the high $^{3}He/^{4}He$ mantle: Implications for the composition of a nonchonditic Earth. *Geochemistry, Geophysics, Geosystems*.

James, D.E., Fouch, M.J., Carlson, R.W. & Roth, J.B. (2011) Slab fragmentation, edge flow and the origin of the Yellowstone hotspot track. *Earth and Planetary Science Letters, 311* (1–2): 124-135.

James, K.H. (2009) In situ origin of the Caribbean: discussion of data. *Geological Society, London, Special Publications, 328* (1): 77-125.

Jenkyns, H. (1976). Sediments and sedimentary history of the Manihiki Plateau, South Pacific OceanInitial Report DSDP, pp. 873-890.

Jenner, F.E. & O'Neill, H.S.C. (2012) Analysis of 60 elements in 616 ocean floor basaltic glasses. *Geochemistry, Geophysics, Geosystems, 13* (2): Q02005.

Jensen, L.S. & Pyke, D.R. (1982) *Komatiites in the Ontario portion of the Abitibi belt*. In: Arndt, N.T. & Nisbet, E.G. (Eds.), Komatiites. George Allen and Unwin, London, pp. 147–157.

Jerram, D.A. & Widdowson, M. (2005) The anatomy of Continental Flood Basalt Provinces: geological constraints on the processes and products of flood volcanism. *Lithos, 79* (3–4): 385-405.

Jerram, D.A., Svensen, H.H., Planke, S., Polozov, A.G. & Torsvik, T.H. (2016) The onset of flood volcanism in the north-western part of the Siberian Traps: Explosive volcanism versus effusive lava flows. *Palaeogeography, Palaeoclimatology, Palaeoecology, 441* (1): 38-50.

Jones, A.P. (2005) Meteorite Impacts as Triggers to Large Igneous Provinces. *Elements, 1* (5): 277-281.

Jones, E.J.W., McMechan, G.A. & Zeng, X. (2015) Seismic evidence for crustal underplating beneath a large igneous province: The Sierra Leone Rise, equatorial Atlantic. *Marine Geology, 365*: 52-60.

Kaiser, H.F. (1960) The Application of Electronic Computers to Factor Analysis. *Educational And Psychological Measurement, 20* (1): 141-151.

Kamber, B.S. (2010) Archean mafic–ultramafic volcanic landmasses and their effect on ocean–atmosphere chemistry. *Chemical Geology, 274* (1–2): 19-28.

Kanazawa, T., Sager, W.W., Escutia, C., Araki, E., Arney, J.E., Carlson, R.L., Downey, W.S., Einaudi, F., Haggas, S.L., Hayasaka, Y., Hirata, K., Horner-Johnson, B.C., Mandernack, K.W., McCarthy, F.M.G., Moberly, R., Mochizuki, M., Øhlenschlaeger Pedersen, R., Salimullah, A.R.M., Shinohara, M. & Werner, C.-D. (2001). Northwest Pacific Seismic Observatory and Hammer Drill Tests. Proceedings of the Ocean Drilling Program, Initial reports (Vol. 191, 49p.). College Station, Texas: Ocean Drilling Program.

Kang, M.H., Sager, W.W. & the Expedition 324 Scientists. (2010). Data report: underway geophysics. In Sager, W.W., Sano, T., Geldmacher, J. & the Expedition 324 Scientists (Eds.), Proceedings of the Integrated Ocean Drilling Program (Vol. 324). Tokyo: Integrated Ocean Drilling Program Management International, Inc.

Keith, M. (2001) Evidence for a plate tectonics debate. *Earth-Science Reviews, 55* (3-4): 235-336.

Kelley, K.A., Plank, T., Ludden, J. & Staudigel, H. (2003) Composition of altered oceanic crust at ODP Sites 801 and 1149. *Geochemistry, Geophysics, Geosystems, 4* (6): 8910.

Kempton, P.D., Fitton, J.G., Saunders, A.D., Nowell, G.M., Taylor, R.N., Hardarson, B.S. & Pearson, G. (2000) The Iceland plume in space and time: a Sr-Nd-Pb-Hf study of the North Atlantic rifted margin. *Earth and Planetary Science Letters, 177* (3-4): 255-271.

Kempton, P.D., Pearce, J.A., Barry, T.L., Fitton, J.G., Langmuir, C. & Christie, D.M. (2002) Sr-Nd-Pb-Hf Isotope Results from ODP Leg 187: Evidence for Mantle Dynamics of the Australian-Antarctic Discordance and Origin of the Indian MORB Source. *Geochem. Geophys. Geosyst., 3* (12): 1074.

Kerr, A.C., White, R.V. & Saunders, A.D. (2000) LIP reading: Recognizing oceanic plateaux in the geological record. *Journal of Petrology, 41* (7): 1041-1056.

Kerr, A.C. (2005) Oceanic LIPs: The kiss of death. *Elements, 1* (5): 289-292.

Kerr, A.C. & Mahoney, J.J. (2007) Oceanic plateaus: Problematic plumes, potential paradigms. *Chemical Geology, 241* (3-4): 332-353.

Kerr, A.C. (2014) *Oceanic Plateaus*. In: Holland, H.D. & Turekian, K.K. (Eds.), Treatise on Geochemistry (Second Edition). Elsevier, Oxford, 4, 4.18, pp. 631-667.

Kim, S.-S. & Wessel, P. (2011) New global seamount census from altimetry-derived gravity data. *Geophysical Journal International, 186* (2): 615-631.

King, S.D. & Anderson, D.L. (1995) An alternative mechanism of flood basalt formation. *Earth and Planetary Science Letters, 136*: 269-279.

King, S.D. & Anderson, D.L. (1998) Edge-driven convection. *Earth and Planetary Science Letters, 160* (3-4): 289-296.

King, S.D. (2007) Hotspots and edge-driven convection. *Geology, 35* (3): 223-226.

Knesel, K.M., Souza, Z.S., Vasconcelos, P.M., Cohen, B.E. & Silveira, F.V. (2011) Young volcanism in the Borborema Province, NE Brazil, shows no evidence for a trace of the Fernando de Noronha plume on the continent. *Earth and Planetary Science Letters, 302* (1–2): 38-50.

Kokelaar, B.P. & Durant, G.P. (1983) The submarine eruption and erosion of Surtla (Surtsey), Iceland. *Journal of Volcanology and Geothermal Research, 19* (3): 239-246.

Kokfelt, T.F., Hoernle, K., Hauff, F., Fiebig, J., Werner, R. & Garbe-Schönberg, D. (2006) Combined Trace Element and Pb-Nd–Sr-O Isotope Evidence for Recycled Oceanic Crust (Upper and Lower) in the Iceland Mantle Plume. *Journal of Petrology, 47* (9): 1705-1749.

König, M. & Jokat, W. (2010) Advanced insights into magmatism and volcanism of the Mozambique Ridge and Mozambique Basin in the view of new potential field data. *Geophysical Journal International, 180* (1): 158-180.

Koornneef, J.M., Stracke, A., Bourdon, B., Meier, M.A., Jochum, K.P., Stoll, B. & Grönvold, K. (2012) Melting of a Two-component Source beneath Iceland. *Journal of Petrology, 53* (1): 127-157.

Koppers, A.A.P., Staudigel, H., Christie, D.M., Dieu, J.J. & Pringle, M.S. (1995) *Sr-Nd-Pb isotope geochemistry of leg 144 West Pacific guyouts: Implications for the geochemical evolution of the "SOPITA" mantle anomaly*. Proceedings of the Ocean Drilling Program, Scientific Results, 144, pp. 535-545.

Koppers, A.A.P. & Watts, A.B. (2010) Intraplate Seamounts as a Window into Deep Earth Processes. *Oceanography, 23* (1): 42-57.

Koppers, A.A.P., Sano, T., Natland, J.H., Widdowson, M., Almeev, R., Greene, A.R., Murphy, D.T., Delacour, A., Miyoshi, M., Shimizu, K., Li, S., Hirano, N., Geldmacher, J. & and the Expedition 324 Scientists (2010) *Massive basalt flows on the southern flank of Tamu Massif, Shatsky Rise: a reappraisal of ODP Site 1213 basement units.* In: Sager, W.W., Sano, T., Geldmacher, J. & the Expedition 324 Scientists (Eds.), Proceedings of the Integrated Ocean Drilling Program. Integrated Ocean Drilling Program Management International, Inc., Tokyo, 324.

Korenaga, J. (2005) Why did not the Ontong Java Plateau form subaerially? *Earth and Planetary Science Letters, 234* (3-4): 385-399.

Korenaga, J. & Sager, W.W. (2012) Seismic tomography of Shatsky Rise by adaptive importance sampling. *Journal of Geophysical Research. Solid Earth, 117* (8).

Korenaga, T. & Korenaga, J. (2008) Subsidence of normal oceanic lithosphere, apparent thermal expansivity, and seafloor flattening. *Earth and Planetary Science Letters, 268* (1–2): 41-51.

Kruber, C., Thorseth, I.H. & Pedersen, R.B. (2008) Seafloor alteration of basaltic glass: Textures, geochemistry, and endolithic microorganisms. *Geochemistry, Geophysics, Geosystems, 9* (12): Q12002.

Kurz, M.D., Jenkins, W.J. & Hart, S.R. (1982) Helium isotopic systematics of oceanic islands and mantle heterogeneity. *Nature, 297* (5861): 43-47.

Kuz'min, M.I., Al'mukhamedov, A.I., Yarmolyuk, V.V. & Kravchinsky, V.A. (2003) Rift and within-plate magmatism in the context of hot and cold mantle fields. *Geologiya I Geofizika, 44* (12): 1270-1279.

Larson, R.L., Moberly, R., Bukry, D., Foreman, H.P., Gardner, J.V., Keene, J.B., Lancelot, Y., Luterbacher, H., Marshall, M.C. & Matter, A. (1975). *Initial Reports DSDP, 32* Vol. 32.

Larson, R.L. (1991) Latest pulse of Earth: Evidence for a mid-Cretaceous superplume. *Geology, 19*: 547-550.

Le Maitre, R.W. (2002) Igneous Rocks. A Classification and Glossary of Terms. Recommendations of the International Union of Geological Sciences Subcommission on the Systematics of Igneous Rocks. 236 p.

Li, S., Geldmacher, J., Hauff, F., Garbe-Schönberg, D., Yu, S., Zhao, S. & Rausch, S. (2014) Composition and timing of carbonate vein precipitation within the

igneous basement of the Early Cretaceous Shatsky Rise, NW Pacific. *Marine Geology, 357*: 321-333.

Li, S., Suo, Y., Yu, S., Wu, T., Somerville, I., Sager, W., Li, X., Hui, G., Zhang, Y., Zang, Y. & Zheng, Q. (2016) Orientation of joints and arrangement of solid inclusions in fibrous veins in the Shatsky Rise, NW Pacific: implications for crack-seal mechanisms and stress fields. *Geological Journal, 51*: 562-578.

Li, Z.-X. & Zhong, S. (2009) Supercontinent-superplume coupling, true polar wander and plume mobility: Plate dominance in whole-mantle tectonics. *Physics of the Earth and Planetary Interiors, 176* (3-4): 143-156.

Ligi, M., Bonatti, E., Cuffaro, M. & Brunelli, D. (2013) Post-Mesozoic Rapid Increase of Seawater Mg/Ca due to Enhanced Mantle-Seawater Interaction. *Scientific Reports, 3*.

Lin, S.-C. & van Keken, P.E. (2005) Multiple volcanic episodes of flood basalts caused by thermochemical mantle plumes. *Nature, 436* (7048): 250-252.

Lipman, P.W. & Calvert, A.T. (2013) Modeling volcano growth on the Island of Hawaii: Deep-water perspectives. *Geosphere, 9* (5): 1348-1383.

Long, M.D., Till, C.B., Druken, K.A., Carlson, R.W., Wagner, L.S., Fouch, M.J., James, D.E., Grove, T.L., Schmerr, N. & Kincaid, C. (2012) Mantle dynamics beneath the Pacific Northwest and the generation of voluminous back-arc volcanism. *Geochemistry, Geophysics, Geosystems, 13* (8).

Loper, D.E. & Stacey, F.D. (1983) The dynamical and thermal structure of deep mantle plumes. *Physics of the Earth and Planetary Interiors, 33* (4): 304-317.

Lowe, D.R. (1982) Sediment gravity flows; II, Depositional models with special reference to the deposits of high-density turbidity currents. *Journal of Sedimentary Research, 52* (1): 279-297.

Ludden, J.N. & Thompson, G. (1979) An evaluation of the behavior of the rare earth elements during the weathering of sea-floor basalt. *Earth and Planetary Science Letters, 43* (1): 85-92.

Machida, S., Hirano, N. & Kimura, J.-I. (2009) Evidence for recycled plate material in Pacific upper mantle unrelated to plumes. *Geochimica Et Cosmochimica Acta, 73* (10): 3028-3037.

Mahoney, J.J., Fitton, J.G., Wallace, P.J. & Shipboard Scientific Party. (2001). *Leg 192 summary* Vol. vol. 192. *Proceedings of the Ocean Drilling Program, Initial Report*. Ocean Drilling Program Management International, Inc., College Station, TX.

Mahoney, J.J., Duncan, R.A., Tejada, M.L.G., Sager, W.W. & Bralower, T.J. (2005) Jurassic-Cretaceous boundary age and mid-ocean-ridge-type mantle source for Shatsky Rise. *Geology, 33* (3): 185-188.

Manville, V., Németh, K. & Kano, K. (2009) Source to sink: A review of three decades of progress in the understanding of volcaniclastic processes, deposits, and hazards. *Sedimentary Geology, 220* (3–4): 136-161.

Maria, A. & Carey, S. (2007) Quantitative discrimination of magma fragmentation and pyroclastic transport processes using the fractal spectrum technique. *Journal of Volcanology and Geothermal Research, 161* (3): 234-246.

Marks, N., Schiffman, P., Zierenberg, R.A., Franzson, H. & Fridleifsson, G.Ó. (2010) Hydrothermal alteration in the Reykjanes geothermal system: Insights from Iceland deep drilling program well RN-17. *Journal of Volcanology and Geothermal Research, 189* (1–2): 172-190.

Mattsson, H.B. & Höskuldsson, Á. (2011) Contemporaneous phreatomagmatic and effusive activity along the Hverfjall eruptive fissure, north Iceland: Eruption chronology and resulting deposits. *Journal of Volcanology and Geothermal Research, 201* (1–4): 241-252.

McCaig, A.M., Cliff, R.A., Escartin, J., Fallick, A.E. & MacLeod, C.J. (2007) Oceanic detachment faults focus very large volumes of black smoker fluids. *Geology, 35* (10): 935-938.

McClintock, M. & White, J.L. (2006) Large phreatomagmatic vent complex at Coombs Hills, Antarctica: Wet, explosive initiation of flood basalt volcanism in the Ferrar-Karoo LIP. *Bulletin of Volcanology, 68* (3): 215-239.

McDonough, W.F. & Sun, S.-s. (1995) The composition of the Earth. *Chemical Geology, 120* (3-4): 223-253.

McHone, J.G. (2000) Non-plume magmatism and rifting during the opening of the central Atlantic Ocean. *Tectonophysics, 316* (3–4): 287-296.

McPhie, J., Doyle, M. & Allen, R.L. (1993) *Volcanic textures : a guide to the interpretation of textures in volcanic rocks*. Hobart : Centre for ore deposit and exploration studies, University of Tasmania.

Menzies, M.A., Klemperer, S.L., Ebinger, C.J. & Baker, J. (2002) Characteristics of volcanic rifted margins. *Geological Society of America Special Papers, 362*: 1-14.

Meunier, A. (2005) *Clays*. Springer Berlin Heidelberg New York.

Michael, P.J. (1999) Implications for magmatic processes at Ontong Java Plateau from volatile and major element contents of Cretaceous basalt glasses. *Geochemistry, Geophysics, Geosystems, 1* (12).

Miyazaki, T., Kimura, J.-I., Senda, R., Vaglarov, B.S., Chang, Q., Takahashi, T., Hirahara, Y., Hauff, F., Hayasaka, Y., Sano, S., Shimoda, G., Ishizuka, O., Kawabata, H., Hirano, N., Machida, S., Ishii, T., Tani, K. & Yoshida, T. (2015) Missing western half of the Pacific Plate: Geochemical nature of the Izanagi-Pacific Ridge interaction with a stationary boundary between the Indian and Pacific mantles. *Geochemistry, Geophysics, Geosystems, 16* (9): 3309-3332.

Miyoshi, M., Sano, T., Shimizu, K., Delacour, A., Hasenaka, T., Mori, Y. & Fukuoka, T. (2015) Boron and chlorine contents of basalts from the Shatsky Rise, IODP Expedition 324: Implications for the alteration of oceanic plateaus. *Geological Society of America Special Papers, 511*: 69-84.

Montelli, R., Nolet, G., Dahlen, F.A., Masters, G., Engdahl, E.R. & Hung, S.H. (2004) Finite-frequency tomography reveals a variety of plumes in the mantle. *Science, 303* (5656): 338-343.

Montelli, R., Nolet, G., Dahlen, F.A. & Masters, G. (2006) A catalogue of deep mantle plumes: New results from finite-frequency tomography. *Geochemistry Geophysics Geosystems, 7* (11): 69p.

Moore, J.G. (1985) Structure and eruptive mechanisms at Surtsey Volcano, Iceland. *Geological Magazine, 122* (06): 649-661.

Morgan, J.P. & Shearer, P.M. (1993) Seismic constraints on mantle flow and topography of the 660-km discontinuity: evidence for whole-mantle convection. *Nature, 365* (6446): 506-511.

Morris, J.D. & Hart, S.R. (1983) Isotopic and incompatible element constraints on the genesis of island arc volcanics from Cold Bay and Amak Island, Aleutians, and implications for mantle structure. *Geochimica Et Cosmochimica Acta, 47* (11): 2015-2030.

Morrissey, M., Zimanowski, B., Wohletz, K.H. & Buettner, R. (2000) *Phreatomagmatic fragmentation*. In: Sigurdsson, H., Houghton, B.F., McNutt, S.R., Rymer, H. & Stix, J. (Eds.), The Encyclopedia of Volcanoes, Second ed. Academic Press, Amsterdam, pp. 431-445.

Mottl, M.J. & Holland, H.D. (1978) Chemical exchange during hydrothermal alteration of basalt by seawater—I. Experimental results for major and minor components of seawater. *Geochimica Et Cosmochimica Acta, 42* (8): 1103-1115.

Mottl, M.J. (1983) *Hydrothermal Processes at Seafloor Spreading Centers: Application of Basalt-Seawater Experimental Results*. In: Rona, P., Boström, K., Laubier, L. & Smith, K., Jr. (Eds.), Hydrothermal Processes at Seafloor Spreading Centers. Springer US, 12, 10, pp. 199-224.

Mulder, T. & Alexander, J. (2001) The physical character of subaqueous sedimentary density flows and their deposits. *Sedimentology, 48* (2): 269-299.

Murtagh, R.M. & White, J.D.L. (2013) Pyroclast characteristics of a subaqueous to emergent Surtseyan eruption, Black Point volcano, California. *Journal of Volcanology and Geothermal Research, 267*: 75-91.

Nakanishi, M., Sager, W.W. & Klaus, A. (1999) Magnetic lineations within Shatsky Rise, northwest Pacific Ocean: Implications for hot spot-triple junction interaction and oceanic plateau formation. *Journal of Geophysical Research Solid Earth, 104* (B4): 7539-7556.

Nakanishi, M., Sager, W.W. & Korenaga, J. (2015a) Reorganization of the Pacific-Izanagi-Farallon triple junction in the Late Jurassic: Tectonic events before the formation of the Shatsky Rise. *Geological Society of America Special Papers, 511*: 85-101.

Nakanishi, M., Nakamura, Y., Coffin, M.F., Hoernle, K. & Werner, R. (2015b) Topographic expression of the Danger Islands Troughs and implications for the

tectonic evolution of the Manihiki Plateau, western equatorial Pacific Ocean. *Geological Society of America Special Papers, 511*: 195-220.

Naldrett, A.J. (1999) World-class Ni-Cu-PGE deposits: key factors in their genesis. *Mineralium Deposita, 34* (3): 227-240.

Németh, K. & Cronin, S.J. (2009) Phreatomagmatic volcanic hazards where rift-systems meet the sea, a study from Ambae Island, Vanuatu. *Journal of Volcanology and Geothermal Research, 180* (2–4): 246-258.

Norton, I.O. (2007) *Speculations on Cretaceous tectonic history of the Northwest Pacific and a tectonic origin for the Hawaii hotspot*. In: Foulger, G.R. & Jurdy, D.M. (Eds.), Plates, Plumes, and Planetary Processes. Geological Society of America, Inc., Boulder, Colorado, 430, pp. 451-470.

Nowell, G.M., Kempton, P.D., Noble, S.R., Fitton, J.G., Saunders, A.D., Mahoney, J.J. & Taylor, R.N. (1998) High precision Hf isotope measurements of MORB and OIB by thermal ionisation mass spectrometry: insights into the depleted mantle. *Chemical Geology, 149* (3–4): 211-233.

Nozaka, T., Fryer, P. & Andreani, M. (2008) Formation of clay minerals and exhumation of lower-crustal rocks at Atlantis Massif, Mid-Atlantic Ridge. *Geochemistry, Geophysics, Geosystems, 9* (11): Q11005.

O'Connor, J.M. & Duncan, R.A. (1990) Evolution of the Walvis Ridge-Rio Grande Rise Hot Spot System: Implications for African and South American Plate motions over plumes. *Journal of Geophysical Research: Solid Earth, 95* (B11): 17475-17502.

O'Connor, J.M., Jokat, W., le Roex, A.P., Class, C., Wijbrans, J.R., Keßling, S., Kuiper, K.F. & Nebel, O. (2012) Hotspot trails in the South Atlantic controlled by plume and plate tectonic processes. *Nature Geoscience, 5* (10): 735-738.

Owen, R.M. & Olivarez, A.M. (1988) Inorganic Marine Chemistry Geochemistry of rare earth elements in pacific hydrothermal sediments. *Marine Chemistry, 25* (2): 183-196.

Parsiegla, N., Gohl, K. & Uenzelmann-Neben, G. (2008) The Agulhas Plateau: Structure and evolution of a Large Igneous Province. *Geophysical Journal International, 174* (1): 336-350.

Pauly, B.D., Schiffman, P., Zierenberg, R.A. & Clague, D.A. (2011) Environmental and chemical controls on palagonitization. *Geochemistry, Geophysics, Geosystems, 12* (12): Q12017.

Pearce, J.A., Kempton, P.D., Nowell, G.M. & Noble, S.R. (1999) Hf-Nd Element and Isotope Perspective on the Nature and Provenance of Mantle and Subduction Components in Western Pacific Arc-Basin Systems. *Journal of Petrology, 40* (11): 1579-1611.

Pearce, J.A., Kempton, P.D. & Gill, J.B. (2007) Hf–Nd evidence for the origin and distribution of mantle domains in the SW Pacific. *Earth and Planetary Science Letters, 260* (1–2): 98-114.

Peate, D.W., Baker, J.A., Jakobsson, S.P., Waight, T.E., Kent, A.J.R., Grassineau, N.V. & Skovgaard, A.C. (2009) Historic magmatism on the Reykjanes Peninsula, Iceland: a snap-shot of melt generation at a ridge segment. *Contributions to Mineralogy and Petrology, 157* (3): 359-382.

Peate, D.W., Breddam, K., Baker, J.A., Kurz, M.D., Barker, A.K., Prestvik, T., Grassineau, N. & Skovgaard, A.C. (2010) Compositional Characteristics and Spatial Distribution of Enriched Icelandic Mantle Components. *Journal of Petrology, 51* (7): 1447-1475.

Perlingeiro, G., Vasconcelos, P.M., Knesel, K.M., Thiede, D.S. & Cordani, U.G. (2013) 40Ar/39Ar geochronology of the Fernando de Noronha Archipelago and implications for the origin of alkaline volcanism in the NE Brazil. *Journal of Volcanology and Geothermal Research, 249* (0): 140-154.

Pertsev, N.N. & Boronikhin, V.A. (1983). Secondary K-feldspar in basalts at Deep Sea Drilling Project Hole 504B and the problem of K-feldspathization in oceanic basalts. In Cann, J.R., Langseth, M.G., Honnorez, J., Von Herzen, R.P., White, S.M. & et al (Eds.), Initial Reports, DSDP 69 (pp. 589–592). Washington: U.S. Government Printing Office.

Phipps Morgan, J. & Morgan, W.J. (1999) Two-stage melting and the geochemical evolution of the mantle: a recipe for mantle plum-pudding. *Earth and Planetary Science Letters, 170* (3): 215-239.

Pichler, T., Ridley, W.I. & Nelson, E. (1999) Low-temperature alteration of dredged volcanics from the Southern Chile Ridge: additional information about early stages of seafloor weathering. *Marine Geology, 159* (1–4): 155-177.

Pimm, A.C., Garrison, R.E. & Boyce, R.E. (1971). Sedimentology Synthesis: Lithology, Chemistry and Physical Properties of Sediments in the Northwestern Pacific OceanInitial Reports Deep Sea Drilling Project, Volume 6, Chapter 38 (pp. 1131-1252): U.S. Government Printing Office, Washington.

Piper, D.Z. (1974) Rare earth elements in the sedimentary cycle: A summary. *Chemical Geology, 14* (4): 285-304.

Pirajno, F. (2007) Mantle plumes, associated intraplate tectono-magmatic processes and ore systems. *Episodes, 30* (1): 6-19.

Pomar, L. & Hallock, P. (2008) Carbonate factories: A conundrum in sedimentary geology. *Earth-Science Reviews, 87* (3–4): 134-169.

Portner, R.A., Daczko, N.R. & Dickinson, J.A. (2010) Vitriclastic lithofacies from Macquarie Island (Southern Ocean): compositional influence on abyssal eruption explosivity in a dying Miocene spreading ridge. *Bulletin of Volcanology, 72* (2): 165-183.

Portner, R.A., Clague, D.A., Helo, C., Dreyer, B.M. & Paduan, J.B. (2015) Contrasting styles of deep-marine pyroclastic eruptions revealed from Axial Seamount push core records. *Earth and Planetary Science Letters, 423* (0): 219-231.

Pringle, M.S. & Dalrymple, G.B. (1993) *Geochronological Constraints on a Possible Hot Spot Origin for Hess Rise and the Wentworth Seamount Chain*. The

Mesozoic Pacific: Geology, Tectonics, and Volcanism. American Geophysical Union, pp. 263-277.

Prytulak, J., Nielsen, S.G., Ionov, D.A., Halliday, A.N., Harvey, J., Kelley, K.A., Niu, Y.L., Peate, D.W., Shimizu, K. & Sims, K.W.W. (2013) The stable vanadium isotope composition of the mantle and mafic lavas. *Earth and Planetary Science Letters, 365* (0): 177-189.

Putirka, K. (2008) Excess temperatures at ocean islands: Implications for mantle layering and convection. *Geology, 36* (4): 283-286.

Rampone, E. & Hofmann, A.W. (2012) A global overview of isotopic heterogeneities in the oceanic mantle. *Lithos, 148* (0): 247-261.

Regelous, M., Niu, Y., Abouchami, W. & Castillo, P.R. (2009) Shallow origin for South Atlantic Dupal Anomaly from lower continental crust: Geochemical evidence from the Mid-Atlantic Ridge at 26°S. *Lithos, 112* (1–2): 57-72.

Révillon, S., Teagle, D.A.H., Boulvais, P., Shafer, J. & Neal, C.R. (2007) Geochemical fluxes related to alteration of a subaerially exposed seamount: Nintoku seamount, ODP Leg 197, Site 1205. *Geochemistry, Geophysics, Geosystems, 8* (2).

Richards, M.A., Duncan, R.A. & Courtillot, V.E. (1989) Flood Basalts and Hot-Spot Tracks - Plume Heads and Tails. *Science, 246* (4926): 103-107.

Richards, M.A., Jones, D.L., Duncan, R.A. & DePaolo, D.J. (1991) A Mantle Plume Initiation Model for the Wrangellia Flood Basalt and Other Oceanic Plateaus. *Science, 254* (5029): 263-267.

Risso, C., Németh, K., Combina, A.M., Nullo, F. & Drosina, M. (2008) The role of phreatomagmatism in a Plio-Pleistocene high-density scoria cone field: Llancanelo Volcanic Field (Mendoza), Argentina. *Journal of Volcanology and Geothermal Research, 169* (1–2): 61-86.

Roberge, J., White, R.V. & Wallace, P.J. (2004) Volatiles in submarine basaltic glasses from the Ontong Java Plateau (ODP Leg 192): implications for magmatic processes and source region compositions. *Geological Society, London, Special Publications, 229* (1): 239-257.

Robinson, D., Bevins, R.E. & Rowbotham, G. (1993) The characterization of mafic phyllosilicates in low-grade metabasalts from eastern North Greenland. *American Mineralogist, 78* (3-4): 377-390.

Romanowicz, B. & Gung, Y. (2002) Superplumes from the Core-Mantle Boundary to the Lithosphere: Implications for Heat Flux. *Science, 296* (5567): 513-516.

Ross, P.S., Ukstins Peate, I., McClintock, M.K., Xu, Y.G., Skilling, I.P., White, J.D.L. & Houghton, B.F. (2005) Mafic volcaniclastic deposits in flood basalt provinces: A review. *Journal of Volcanology and Geothermal Research, 145* (3–4): 281-314.

Ross, P.S. & White, J.D.L. (2005) Mafic, large-volume, pyroclastic density current deposits from phreatomagmatic eruptions in the Ferrar large igneous province, Antarctica. *Journal of Geology, 113* (6): 627-649.

Rudge, J.F., Shaw Champion, M.E., White, N., McKenzie, D. & Lovell, B. (2008) A plume model of transient diachronous uplift at the Earth's surface. *Earth and Planetary Science Letters, 267* (1–2): 146-160.

Rudnick, R.L. & Goldstein, S.L. (1990) The Pb isotopic compositions of lower crustal xenoliths and the evolution of lower crustal Pb. *Earth and Planetary Science Letters, 98* (2): 192-207.

Sager, W.W., Handschumacher, D.W., Hilde, T.W.C. & Bracey, D.R. (1988) Tectonic evolution of the northern Pacific plate and Pacific-Farallon Izanagi triple junction in the Late Jurassic and Early Cretaceous (M21-M10). *Tectonophysics, 155* (1-4): 345-364.

Sager, W.W. & Han, H.C. (1993) Rapid Formation of the Shatsky Rise Oceanic Plateau Inferred from Its Magnetic Anomaly. *Nature, 364* (6438): 610-613.

Sager, W.W., Klaus, A., Nakanishi, M., Brown, G.R. & Khankishieva, L.M. (1995). *Shatsky Rise expedition: R/V Thomas G. Thompson Cruise TN037 Technical Report 95-5-T* (pp. 95).

Sager, W.W., Kim, J., Klaus, A., Nakanishi, M. & Khankishieva, L.M. (1999) Bathymetry of Shatsky Rise, northwest Pacific Ocean: Implications for ocean plateau development at a triple junction. *Journal of Geophysical Research-Solid Earth, 104* (B4): 7557-7576.

Sager, W.W. (2005) What built Shatsky Rise, a mantle plume or ridge tectonics? *Geological Society of America Bulletin, 388*: 721-733.

Sager, W.W., Sano, T., Geldmacher, J. & Expedition 324 Scientists. (2010). *Proceedings of the Integrated Ocean Drilling Program* Vol. 324. Integrated Ocean Drilling Program Management International, Inc., Tokyo.

Sager, W.W., Sano, T. & Geldmacher, J. (2011) How do oceanic plateaus form? Clues from drilling at Shatsky Rise. *Eos, 92* (5): 37-38.

Sager, W.W., Zhang, J., Korenaga, J., Sano, T., Koppers, A.A.P., Widdowson, M. & Mahoney, J.J. (2013) An immense shield volcano within the Shatsky Rise oceanic plateau, northwest Pacific Ocean. *Nature Geoscience, 6* (11): 976-981.

Sager, W.W., Pueringer, M., Carvallo, C., Ooga, M., Housen, B. & Tominaga, M. (2015) Paleomagnetism of igneous rocks from the Shatsky Rise: Implications for paleolatitude and oceanic plateau volcanism. *Geological Society of America Special Papers, 511*: 147-171.

Sager, W.W., Sano, T. & Geldmacher, J. (2016) Formation and evolution of Shatsky Rise oceanic plateau: Insights from IODP Expedition 324 and recent geophysical cruises. *Earth-Science Reviews*.

Salters, V.J.M. & White, W.M. (1998) Hf isotope constraints on mantle evolution. *Chemical Geology, 145* (3-4): 447-460.

Sano, T. & Yamashita, S. (2004) Experimental petrology of basement lavas from Ocean Drilling Program Leg 192: implications for differentiation processes in Ontong Java Plateau magmas. *Geological Society, London, Special Publications, 229* (1): 185-218.

Sano, T., Shimizu, K., Ishikawa, A., Senda, R., Chang, Q., Kimura, J.-I., Widdowson, M. & Sager, W.W. (2012) Variety and origin of magmas on Shatsky Rise, northwest Pacific Ocean. *Geochemistry Geophysics Geosystems, 13*: 8010-8010.

Santelli, C.M., Edgcomb, V.P., Bach, W. & Edwards, K.J. (2009) The diversity and abundance of bacteria inhabiting seafloor lavas positively correlate with rock alteration. *Environmental Microbiology, 11* (1): 86-98.

Santosh, M., Maruyama, S. & Yamamoto, S. (2009) The making and breaking of supercontinents: Some speculations based on superplumes, super downwelling and the role of tectosphere. *Gondwana Research, 15* (3-4): 324-341.

Saunders, A.D., Tarney, J., Kerr, A.C. & Kent, R.W. (1996) The formation and fate of large oceanic igneous provinces. *Lithos, 37* (2-3): 81-95.

Saunders, A.D. (2005) Large igneous provinces: Origin and environmental consequences. *Elements, 1* (5): 259-263.

Saunders, A.D., England, R.W., Reichow, M.K. & White, R.V. (2005) A mantle plume origin for the Siberian traps: uplift and extension in the West Siberian Basin, Russia. *Lithos, 79* (3-4): 407-424.

Saunders, A.D., Jones, S.M., Morgan, L.A., Pierce, K.L., Widdowson, M. & Xu, Y.G. (2007) Regional uplift associated with continental large igneous provinces: The roles of mantle plumes and the lithosphere. *Chemical Geology, 241* (3-4): 282-318.

Schipper, C.I., White, J.D.L. & Houghton, B.F. (2010) Syn- and post-fragmentation textures in submarine pyroclasts from Lō`ihi Seamount, Hawai`i. *Journal of Volcanology and Geothermal Research, 191* (1–2): 93-106.

Schissel, D. & Smail, R. (2001) *Deep-mantle plumes and ore deposits*. In: Ernst, R.E. & Buchan, K.L. (Eds.), Mantle Plumes: Their Identification through Time. Geological Society of America, Inc., Boulder, Colorado, Vol. 352, pp. p. 291-322.

Schlanger, S.O., Douglas, R.G., Lancelot, Y., Moore, T.C. & Roth, P.H. (1973). Fossil Preservation and Diagenesis of Pelagic Carbonates from the Magellan Rise, Central North Pacific Ocean. In Roth, P.H. & Herring, J.R. (Eds.), Initial Reports of the Deep-Sea Drilling Project (Vol. 17, pp. 407-427). Washington, D.C.: U.S. Gov. Print. Off.

Schneider, C.A., Rasband, W.S. & Eliceiri, K.W. (2012) NIH Image to ImageJ: 25 years of image analysis. *Nature methods, 9* (7): 671-675.

Scholz, F., Hensen, C., Schmidt, M. & Geersen, J. (2013) Submarine weathering of silicate minerals and the extent of pore water freshening at active continental margins. *Geochimica Et Cosmochimica Acta, 100* (0): 200-216.

Schramm, B., Devey, C.W., Gillis, K.M. & Lackschewitz, K. (2005) Quantitative assessment of chemical and mineralogical changes due to progressive low-temperature alteration of East Pacific Rise basalts from 0 to 9 Ma. *Chemical Geology, 218* (3-4): 281-313.

Schumacher, R. & Schmincke, H.U. (1995) Models for the origin of accretionary lapilli. *Bulletin of Volcanology, 56* (8): 626-639.

Şengör, A.M.C. (2001) *Elevation as indicator of mantle plume activity*. In: Ernst, R.E. & Buchan, K.L. (Eds.), Mantle Plumes: Their Identification through Time. Geological Society of America, Boulder, Colorado, 352, pp. 183-225.

Seton, M., Muller, R.D., Zahirovic, S., Gaina, C., Torsvik, T., Shephard, G., Talsma, A., Gurnis, M., Turner, M., Maus, S. & Chandler, M. (2012) Global continental and ocean basin reconstructions since 200 Ma. *Earth-Science Reviews, 113* (3-4): 212-270.

Severs, M.J., Beard, J.S., Fedele, L., Hanchar, J.M., Mutchler, S.R. & Bodnar, R.J. (2009) Partitioning behavior of trace elements between dacitic melt and plagioclase, orthopyroxene, and clinopyroxene based on laser ablation ICPMS analysis of silicate melt inclusions. *Geochimica Et Cosmochimica Acta, 73* (7): 2123-2141.

Seyfried, W.E., Mottl, M.J. & Bischoff, J.L. (1978) Seawater/basalt ratio effects on the chemistry and mineralogy of spilites from the ocean floor. *Nature, 275* (5677): 211-213.

Seyfried, W.E. & Mottl, M.J. (1982) Hydrothermal alteration of basalt by seawater under seawater-dominated conditions. *Geochimica Et Cosmochimica Acta, 46* (6): 985-1002.

Shafer, J.T., Neal, C.R. & Castillo, P.R. (2004) *Compositional variability in lavas from the Ontong Java Plateau: results from basalt clasts within the volcaniclastic succession at Ocean Drilling Program Site 1184*. In: Fitton, J.G., Mahoney, J.J., Wallace, P.J. & Saunders, A.D. (Eds.), Origin and Evolution of the Ontong Java Plateau. Geological Society of London, London, 229, pp. 333-351.

Sheth, H.C. (2007) Plume-related regional prevolcanic uplift in the Deccan Traps: Absence of evidence, evidence of absence. *Geological Society of America Special Papers, 430*: 785-813.

Shimizu, K., Shimizu, N., Sano, T., Matsubara, N. & Sager, W. (2013) Paleo-elevation and subsidence of Shatsky Rise inferred from CO2 and H2O in fresh volcanic glass. *Earth and Planetary Science Letters, 383* (0): 37-44.

Sims, K.W.W., Goldstein, S.J., Blichert-toft, J., Perfit, M.R., Kelemen, P., Fornari, D.J., Michael, P., Murrell, M.T., Hart, S.R., DePaolo, D.J., Layne, G., Ball, L., Jull, M. & Bender, J. (2002) Chemical and isotopic constraints on the generation and transport of magma beneath the East Pacific Rise. *Geochimica Et Cosmochimica Acta, 66* (19): 3481-3504.

Sinha, M.C., Louden, K.E. & Parsons, B. (1981) The crustal structure of the Madagascar Ridge. *Geophysical Journal of the Royal Astronomical Society, 66* (2): 351-377.

Sliter, W.V. & Brown, G.R. (1993) Shatsky Rise: Seismic stratigraphy and sedimentary record of Pacific paleoceanography since the Early Cretaceous. *Proceedings Ocean Drilling Program, Scientific Results, 132*: 3-13.

Smallwood, J.R., White, R.S. & Minshull, T.A. (1995) Sea-floor spreading in the presence of the Iceland plume: the structure of the Reykjanes Ridge at 61-40N. *Journal of the Geological Society, 152* (6): 1023-1029.

Smith, A.D. (2007) *A plate model for Jurassic to Recent intraplate volcanism in the Pacific Ocean basin*. In: Foulger, G.R. & Jurdy, D.M. (Eds.), Plates, Plumes, and Planetary Processes. Geological Society of America, Inc., Boulder, Colorado, 430, pp. 471-489.

Smith, W.H.F. & Sandwell, D.T. (1997) Global Sea Floor Topography from Satellite Altimetry and Ship Depth Soundings. *Science, 277* (5334): 1956.

Snow, J.E. & Dick, H.J.B. (1995) Pervasive magnesium loss by marine weathering of peridotite. *Geochimica Et Cosmochimica Acta, 59* (20): 4219-4235.

Sobolev, S.V., Sobolev, A.V., Kuzmin, D.V., Krivolutskaya, N.A., Petrunin, A.G., Arndt, N.T., Radko, V.A. & Vasiliev, Y.R. (2011) Linking mantle plumes, large igneous provinces and environmental catastrophes. *Nature, 477* (7364): 312-316.

Sohn, Y.K. & Chough, S.K. (1992) The Ilchulbong tuff cone, Cheju Island, South Korea. *Sedimentology, 39* (4): 523-544.

Sohn, Y.K. & Park, K.H. (2004) Early-stage volcanism and sedimentation of Jeju Island revealed by the Sagye borehole, SW Jeju Island, Korea. *Geosciences Journal, 8* (1): 73-84.

Sohn, Y.K., Park, K.H. & Yoon, S.-H. (2008) Primary versus secondary and subaerial versus submarine hydrovolcanic deposits in the subsurface of Jeju Island, Korea. *Sedimentology, 55* (4): 899-924.

Sorrentino, L., Cas, R.A.F. & Stilwell, J.D. (2011) Evolution and facies architecture of Paleogene Surtseyan volcanoes on Chatham Islands, New Zealand, Southwest Pacific Ocean. *Journal of Volcanology and Geothermal Research, 202* (1–2): 1-21.

Stagg, H.M.J., Alcock, M.B., Bernardel, G., Moore, A.M.G., Symonds, P.A. & Exon, N.F. (2004). *Geological framework of the outer Exmouth Plateau and adjacent ocean basins*. Canberra City, ACT: Geoscience Australia Record.

Staudigel, H., Park, K.H., Pringle, M., Rubenstone, J.L., Smith, W.H.F. & Zindler, A. (1991) The longevity of the South Pacific isotopic and thermal anomaly. *Earth and Planetary Science Letters, 102* (1): 24-44.

Staudigel, H., Plank, T., White, B. & Schmincke, H.-U. (1996) *Geochemical Fluxes During Seafloor Alteration of the Basaltic Upper Oceanic Crust: DSDP Sites 417 and 418*. Subduction Top to Bottom. American Geophysical Union, pp. 19-38.

Staudigel, H. (2003) *Hydrothermal Alteration Processes in the Oceanic Crust*. In: Holland, H.D. & Turekian, K.K. (Eds.), Treatise on Geochemistry. Pergamon, Oxford, 3, 3.15, pp. 511-535.

Staudigel, H., Hart, S.R., Koppers, A.A.P., Constable, C., Workman, R., Kurz, M. & Baker, E.T. (2004) Hydrothermal venting at Vailulu'u Seamount: The smoking end of the Samoan chain. *Geochemistry, Geophysics, Geosystems, 5* (2): Q02003.

Staudigel, H. & Clague, D.A. (2010) The geological history of deep-sea volcanoes: Biosphere, hydrosphere, and lithosphere interactions. *Oceanography, 23* (1): 58-71.

Stein, C.A. & Stein, S. (1992) A model for the global variation in oceanic depth and heat flow with lithospheric age. *Nature, 359* (6391): 123-129.

Stein, C.A. & Stein, S. (1994) Constraints on hydrothermal heat flux through the oceanic lithosphere from global heat flow. *Journal of Geophysical Research: Solid Earth, 99* (B2): 3081-3095.

Stetzenbach, K.J., Farnham, I.M., Hodge, V.F. & Johannesson, K.H. (1999) Using multivariate statistical analysis of groundwater major cation and trace element concentrations to evaluate groundwater flow in a regional aquifer. *Hydrological Processes, 13* (17): 2655-2673.

Stoffler, D., Deutsch, A., Avermann, M., Bischoff, L., Brockmeyer, P., Buhl, D., Lakomy, R. & Muller-Mohr, V. (1994) *The formation of the Sudbury structure, Canada: toward a unified impact model*. In: Dressler, B.O., Grieve, R.A.F. & Sharpton, V.L. (Eds.), Large Meteorite Impacts and Planetary Evolution. Geological Society of America, Inc., Boulder, Colorado, 293, pp. 303-318.

Storms, M.A., Natland, J.H. & et al. (1971). *Proc. ODP, Init. Repts., 132*. Ocean Drilling Program, College Station, TX.

Stracke, A., Hofmann, A.W. & Hart, S.R. (2005) FOZO, HIMU, and the rest of the mantle zoo. *Geochem. Geophys. Geosyst., 6* (5): Q05007.

Stracke, A. & Bourdon, B. (2009) The importance of melt extraction for tracing mantle heterogeneity. *Geochimica Et Cosmochimica Acta, 73* (1): 218-238.

Stracke, A. (2012) Earth's heterogeneous mantle: A product of convection-driven interaction between crust and mantle. *Chemical Geology, 330-331*: 274-299.

Stroncik, N. & Schmincke, H.-U. (2002) Palagonite – a review. *International Journal of Earth Sciences, 91* (4): 680-697.

Sun, S.-s. & McDonough, W.F. (1989) *Chemical and Isotopic systematics of oceanic basalts: implications for Mantle Composition and Processes*. In: Saunders, A.D. & Norry, M.J. (Eds.), Magmatism in the Ocean Basins. Geological Society of London, London, 42, pp. 313-345.

Sun, Y.D., Lai, X.L., Wignall, P.B., Widdowson, M., Ali, J.R., Jiang, H.S., Wang, W., Yan, C.B., Bond, D.P.G. & Vedrine, S. (2010) Dating the onset and nature of the Middle Permian Emeishan large igneous province eruptions in SW China using conodont biostratigraphy and its bearing on mantle plume uplift models. *Lithos, 119* (1-2): 20-33.

Taddeucci, J., Edmonds, M., Houghton, B., James, M.R. & Vergniolle, S. (2015) *Chapter 27 - Hawaiian and Strombolian Eruptions*. In: Sigurdsson, H., Houghton, B.F., McNutt, S.R., Rymer, H. & Stix, J. (Eds.), The Encyclopedia of Volcanoes (Second Edition). Academic Press, Amsterdam, pp. 485-503.

Talbi, E.H. & Honnorez, J. (2003) Low-temperature alteration of mesozoic oceanic crust, Ocean Drilling Program Leg 185. *Geochemistry, Geophysics, Geosystems, 4* (5).

Tatsumi, Y., Shinjoe, H., Ishizuka, H., Sager, W.W. & Klaus, A. (1998) Geochemical evidence for a mid-Cretaceous superplume. *Geology, 26* (2): 151-154.

Taylor, B. (2006) The single largest oceanic plateau: Ontong Java–Manihiki–Hikurangi. *Earth and Planetary Science Letters, 241* (3–4): 372-380.

Tejada, M.L.G., Mahoney, J.J., Tatsumi, Y. & Sager, W.W. (2001). *Water-rock interaction in dredged lavas from Shatsky Rise, Pacific Ocean*. Paper presented at the Proceedings of the Tenth International Symposium on Water-Rock Interaction, pp. 935-938.

Tejada, M.L.G., Mahoney, J.J., Neal, C.R., Duncan, R.A. & Petterson, M.G. (2002) Basement geochemistry and geochronology of Central Malaita, Solomon Islands, with implications for the origin and evolution of the Ontong Java Plateau. *Journal of Petrology, 43* (3): 449-484.

Tejada, M.L.G., Mahoney, J.J., Castillo, P.R., Ingle, S.P., Sheth, H.C. & Weis, D. (2004) *Pin-pricking the elephant: evidence on the origin of the Ontong Java Plateau from Pb-Sr-Hf-Nd isotopic characteristics of ODP Leg 192 basalts*. In: Fitton, J.G., Mahoney, J.J., Wallace, P.J. & Saunders, A.D. (Eds.), Origin and Evolution of the Ontong Java Plateau. Geological Society of London, London, 229, pp. 133-150.

Tejada, M.L.G., Suzuki, K., Hanyu, T., Mahoney, J.J., Ishikawa, A., Tatsumi, Y., Chang, Q. & Nakai, S. (2013) Cryptic lower crustal signature in the source of the Ontong Java Plateau revealed by Os and Hf isotopes. *Earth and Planetary Science Letters, 377–378*: 84-96.

Tejada, M.L.G., Geldmacher, J., Hauff, F., Heaton, D., Koppers, A.A.P., Garbe-Schönberg, D., Hoernle, K., Heydolph, K. & Sager, W.W. (2016) Geochemistry and Age of Shatsky, Hess, and Ojin Rise seamounts: Implications for a connection between the Shatsky and Hess Rises. *Geochimica Et Cosmochimica Acta*.

Templ, M., Filzmoser, P. & Reimann, C. (2008) Cluster analysis applied to regional geochemical data: Problems and possibilities. *Applied Geochemistry, 23* (8): 2198-2213.

Thal, J., Tivey, M., Yoerger, D.R. & Bach, W. (2016) Subaqueous cryptodome eruption, hydrothermal activity and related seafloor morphologies on the andesitic North Su volcano. *Journal of Volcanology and Geothermal Research, 323*: 80-96.

Thiede, J., Vallier, T.L. & Adelseck, C.G. (1981). *Deep Sea Drilling Project Leg 62, North Central Pacific Ocean: Introduction, cruise narrative, principal results, and explanatory notes* Thiede, J., Vallier, T.L. & et al. (Eds.), *Deep-Sea Drilling Project Initial Reports 62* (pp. 5-31).

Thirlwall, M.F., Gee, M.A.M., Taylor, R.N. & Murton, B.J. (2004) Mantle components in Iceland and adjacent ridges investigated using double-spike Pb isotope ratios. *Geochimica Et Cosmochimica Acta, 68* (2): 361-386.

Thompson, P.M.E., Kempton, P.D., White, R.V., Kerr, A.C., Tarney, J., Saunders, A.D., Fitton, J.G. & McBirney, A. (2003) Hf-Nd isotope constraints on the origin of the Cretaceous Caribbean plateau and its relationship to the Galapagos plume. *Earth and Planetary Science Letters, 217* (1-2): 59-75.

Thompson, P.M.E., Kempton, P.D. & Kerr, A.C. (2008) Evaluation of the effects of alteration and leaching on Sm–Nd and Lu–Hf systematics in submarine mafic rocks. *Lithos, 104* (1–4): 164-176.

Thordarson, T. (2004) Accretionary-lapilli-bearing pyroclastic rocks at ODP Leg 192 Site 1184: a record of subaerial phreatomagmatic eruptions on the Ontong Java Plateau. *Geological Society, London, Special Publications, 229* (1): 275-306.

Thordarson, T. & Larsen, G. (2007) Volcanism in Iceland in historical time: Volcano types, eruption styles and eruptive history. *Journal of Geodynamics, 43* (1): 118-152.

Thordarson, T., Rampino, M., Keszthelyi, L.P. & Self, S. (2009) Effects of megascale eruptions on Earth and Mars. *Geological Society of America Special Papers, 453*: 37-53.

Timm, C., Hoernle, K., Werner, R., Hauff, F., den Bogaard, P.v., Michael, P., Coffin, M.F. & Koppers, A. (2011) Age and geochemistry of the oceanic Manihiki Plateau, SW Pacific: New evidence for a plume origin. *Earth and Planetary Science Letters, 304* (1–2): 135-146.

Tominaga, M. & Sager, W.W. (2010) Revised Pacific M-anomaly geomagnetic polarity timescale. *Geophysical Journal International, 182* (1): 203-232.

Tominaga, M., Evans, H.F. & Iturrino, G. (2012) "Equator Crossing" of Shatsky Rise?: New insights on Shatsky Rise tectonic motion from the downhole magnetic architecture of the uppermost lava sequences at Tamu Massif. *Geophysical Research Letters, 39* (21): L21301.

Tominaga, M., Iturrino, G. & Evans, H.F. (2015) Volcanic evolution of the submarine super volcano, Tamu Massif of Shatsky Rise: New insights from Formation MicroScanner logging imagery. *Geophysical Research Letters, 42* (1): 2014GL061630.

Tomlinson, K.Y. & Condie, K.C. (2001) *Archean mantle plumes: Evidence from greenstone belt geochemistry*. In: Ernst, R.E. & Buchan, K.L. (Eds.), Mantle Plumes: Their Identification through Time. Geological Society of America, Inc., Boulder, Colorado, 352, pp. p. 341-357.

Torsvik, T.H., Smethurst, M.A., Burke, K. & Steinberger, B. (2006) Large igneous provinces generated from the margins of the large low-velocity provinces in the deep mantle. *Geophysical Journal International, 167* (3): 1447-1460.

Torsvik, T.H., Burke, K., Steinberger, B., Webb, S.J. & Ashwal, L.D. (2010a) Diamonds sampled by plumes from the core-mantle boundary. *Nature, 466* (7304): 352-355.

Torsvik, T.H., Steinberger, B., Gurnis, M. & Gaina, C. (2010b) Plate tectonics and net lithosphere rotation over the past 150 My. *Earth and Planetary Science Letters, 291* (1-4): 106-112.

Trofimovs, J., Sparks, R.S.J. & Talling, P.J. (2008) Anatomy of a submarine pyroclastic flow and associated turbidity current: July 2003 dome collapse, Soufrière Hills volcano, Montserrat, West Indies. *Sedimentology, 55* (3): 617-634.

Ukstins Peate, I. & Bryan, S.E. (2008) Re-evaluating plume-induced uplift in the Emeishan large igneous province. *Nature Geoscience, 1* (9): 625-629.

Ukstins Peate, I. & Bryan, S.E. (2009) Pre-eruptive uplift in the Emeishan? Reply. *Nature Geoscience, 2* (8): 531-532.

Ussami, N., Chaves, C.A.M., Marques, L.S. & Ernesto, M. (2013) Origin of the Rio Grande Rise–Walvis Ridge reviewed integrating palaeogeographic reconstruction, isotope geochemistry and flexural modelling. *Geological Society, London, Special Publications, 369* (1): 129-146.

Valentine, G.A., Graettinger, A.H. & Sonder, I. (2014) Explosion depths for phreatomagmatic eruptions. *Geophysical Research Letters, 41* (9): 3045-3051.

Vallier, T.L., Dean, W.E., Rea, D.K. & Thiede, J. (1983) Geologic evolution of Hess Rise, central North Pacific Ocean. *Geological Society of America Bulletin, 94* (11): 1289-1307.

Van der Hilst, R.D., Widiyantoro, S. & Engdahl, E.R. (1997) Evidence for deep mantle circulation from global tomography. *Nature, 386* (6625): 578-584.

Van Houten, F.B. & Purucker, M.E. (1984) Glauconitic peloids and chamositic ooids - favorable factors, constraints, and problems. *Earth-Science Reviews, 20* (3): 211-243.

van Keken, P.E., Hauri, E.H. & Ballentine, C.J. (2002) Mantle mixing: The generation, preservation, and destruction of chemical heterogeneity. *Annual Review of Earth and Planetary Sciences, 30*: 493-525.

van Keken, P.E., Ballentine, C.J. & Hauri, E.H. (2003) *Convective Mixing in the Earth's Mantle*. In: Heinrich, D.H. & Karl, K.T. (Eds.), Treatise on Geochemistry. Pergamon, Oxford, 2, 2.12, pp. 1-21.

Vanderkluysen, L., Mahoney, J.J., Koppers, A.A.P., Beier, C., Regelous, M., Gee, J.S. & Lonsdale, P.F. (2014) Louisville Seamount Chain: Petrogenetic processes and geochemical evolution of the mantle source. *Geochemistry, Geophysics, Geosystems, 15* (6): 2380-2400.

Velde, B. & Meunier, A. (2008) *The Origin of Clay Minerals in Soils and Weathered Rocks*. Springer-Verlag Berlin Heidelberg.

Vervoort, J.D. & Blichert-Toft, J. (1999) Evolution of the depleted mantle: Hf isotope evidence from juvenile rocks through time. *Geochimica Et Cosmochimica Acta, 63* (3–4): 533-556.

Vlastélic, I., Aslanian, D., Dosso, L., Bougault, H., Olivet, J.L. & Géli, L. (1999) Large-scale chemical and thermal division of the Pacific mantle. *Nature, 399* (27 May): 345-350.

Von Damm, K.L. (2013) *Controls on the Chemistry and Temporal Variability of Seafloor Hydrothermal Fluids*. Seafloor Hydrothermal Systems: Physical, Chemical, Biological, and Geological Interactions. American Geophysical Union, pp. 222-247.

von Stackelberg, U., Exon, N.F., von Rad, U., Quilty, P., Shafik, S., Beiersdorf, H., Seibertz, E. & Veevers, J.J. (1980) Geology of the Exmouth and Wallaby Plateaus off northwest Australia: sampling of seismic sequences. *BMR Journal of Australian Geology & Geophysics, 5*: 113-140.

Waitt, R.B. (2007) Primary volcaniclastic rocks: COMMENT and REPLY: COMMENT. *Geology, 35* (1): e141.

Walton, A.W., Schiffman, P. & Macpherson, G.L. (2005) Alteration of hyaloclastites in the HSDP 2 Phase 1 Drill Core: 2. Mass balance of the conversion of sideromelane to palagonite and chabazite. *Geochemistry, Geophysics, Geosystems, 6* (9): Q09G19.

Weis, D., Ingle, S., Damasceno, D., Frey, F.A., Nicolaysen, K., Barling, J. & Leg 183 Shipboard Scientific Party (2001) Origin of continental components in Indian Ocean basalts: Evidence from Elan Bank (Kerguelen Plateau, ODP Leg 183, Site 1137). *Geology, 29* (2): 147-150.

Wheat, C.G., Mottl, M.J. & Rudnicki, M. (2002) Trace element and REE composition of a low-temperature ridge-flank hydrothermal spring. *Geochimica Et Cosmochimica Acta, 66* (21): 3693-3705.

White, J.D.L. (1996) Impure coolants and interaction dynamics of phreatomagmatic eruptions. *Journal of Volcanology and Geothermal Research, 74* (3–4): 155-170.

White, J.D.L. (2000) Subaqueous eruption-fed density currents and their deposits. *Precambrian Research, 101* (2–4): 87-109.

White, J.D.L. & Houghton, B.F. (2006) Primary volcaniclastic rocks. *Geology, 34* (8): 677-680.

White, J.D.L., Bryan, S.E., Ross, P.S., Self, S. & Thordarson, T. (2009) *Physical volcanology of continental large igneous provinces: update and review.* In: Thordarson, T., Self, S., Larsen, G., Rowland, S.K. & Hoskuldsson, A. (Eds.), Studies in Volcanology: The Legacy of George Walker. Geological Society, London, 2, pp. 291-321.

White, J.D.L., Schipper, C.I. & Kano, K. (2015) *Chapter 31 - Submarine Explosive Eruptions*. In: Sigurdsson, H., Houghton, B.F., McNutt, S.R., Rymer, H. & Stix, J. (Eds.), The Encyclopedia of Volcanoes (Second Edition). Academic Press, Amsterdam, pp. 553-569.

White, R.S., McKenzie, D. & O'Nions, R.K. (1992) Oceanic Crustal Thickness From Seismic Measurements and Rare Earth Element Inversions. *Journal of Geophysical Research, 97* (B13): 19683-19715.

White, R.V., Castillo, P.R., Neal, C.R., Fitton, J.G. & Godard, M. (2004) *Phreatomagmatic eruptions on the Ontong Java Plateau: chemical and isotopic relationship to Ontong Java Plateau basalts*. In: Fitton, J.G., Mahoney, J.J., Wallace, P.J. & Saunders, A.D. (Eds.), Origin and Evolution of the Ontong Java Plateau. Geological Society of London, London, 229, pp. 307-323.

White, R.V. & Saunders, A.D. (2005) Volcanism, impact and mass extinctions: incredible or credible coincidences? *Lithos, 79* (3-4): 299-316.

Whittaker, J.M., Afonso, J.C., Masterton, S., Muller, R.D., Wessel, P., Williams, S.E. & Seton, M. (2015) Long-term interaction between mid-ocean ridges and mantle plumes. *Nature Geosci, 8* (6): 479-483.

Wignall, P. (2005) The link between large igneous province eruptions and mass extinctions. *Elements, 1* (5): 293-297.

Wilson, J.T. (1963) A possible origin of the Hawaiian Islands. *Canadian Journal of Physics, 41*: 863-870.

Wilson, M.J. (2013) *Sheet Silicates–Clay Minerals*. In: Deer, W.A., Howie, R.A. & Zussmann, J. (Eds.), Rock-Forming Minerals, 2nd ed. The Geological Society, London, 3C, p. 724 p.

Wolfe, C.J., Solomon, S.C., Laske, G., Collins, J.A., Detrick, R.S., Orcutt, J.A., Bercovici, D. & Hauri, E.H. (2009) Mantle Shear-Wave Velocity Structure Beneath the Hawaiian Hot Spot. *Science, 326* (5958): 1388-1390.

Wright, A.A., Bleil, U., Monechi, S., Michel, H.V., Shackleton, N.J., Simoneit, B.R.T. & Zachos, J.C. (1985) Summary of Cretaceous Tertiary Boundary Studies, Deep-Sea Drilling Project Site-577, Shatsky Rise. *Initial Reports of the Deep Sea Drilling Project, 86*: 799-804.

Wright, J.E. & Wyld, S.J. (2011) Late Cretaceous subduction initiation on the eastern margin of the Caribbean-Colombian Oceanic Plateau: One Great Arc of the Caribbean (?). *Geosphere, 7* (2): 468-493.

Yu, Z., Robinson, P. & McGoldrick, P. (2001) An Evaluation of Methods for the Chemical Decomposition of Geological Materials for Trace Element Determination using ICP-MS. *Geostandards Newsletter, 25* (2-3): 199-217.

Zhang, G.-L. & Smith-Duque, C. (2014) Seafloor basalt alteration and chemical change in the ultra thinly sedimented South Pacific. *Geochemistry, Geophysics, Geosystems, 15* (7): 3066-3080.

Zhang, J., Sager, W.W. & Korenaga, J. (2015) The Shatsky Rise oceanic plateau structure from two-dimensional multichannel seismic reflection profiles and implications for oceanic plateau formation. *Geological Society of America Special Papers, 511*: 103-126.

Zhang, J., Sager, W.W. & Durkin, W.J. (2016a) Morphology of Shatsky Rise oceanic plateau from high resolution bathymetry. *Marine Geophysical Research*: 1-17.

Zhang, J., Sager, W.W. & Korenaga, J. (2016b) The seismic Moho structure of Shatsky Rise oceanic plateau, northwest Pacific Ocean. *Earth and Planetary Science Letters, 441*: 143-154.

Zhang, M., O'Reilly, S.Y., Wang, K.L., Hronsky, J. & Griffin, W.L. (2008) Flood basalts and metallogeny: The lithospheric mantle connection. *Earth-Science Reviews, 86* (1-4): 145-174.

Zhang, T., Lin, J. & Gao, J.Y. (2011) Interactions between hotspots and the Southwest Indian Ridge during the last 90 Ma: Implications on the formation of oceanic plateaus and intra-plate seamounts. *Science China Earth Sciences, 54* (8): 1177-1188.

Zhao, D. (2001) Seismic structure and origin of hotspots and mantle plumes. *Earth and Planetary Science Letters, 192* (3): 251-265.

Zhao, D. (2007) Seismic images under 60 hotspots: Search for mantle plumes. *Gondwana Research, 12* (4): 335-355.

Zimanowski, B., Büttner, R., Dellino, P., White, J.D.L. & Wohletz, K.H. (2015) *Chapter 26 - Magma–Water Interaction and Phreatomagmatic Fragmentation*. In: Sigurdsson, H., Houghton, B.F., McNutt, S.R., Rymer, H. & Stix, J. (Eds.), The Encyclopedia of Volcanoes (Second Edition). Academic Press, Amsterdam, pp. 473-484.

Zindler, A. & Hart, S. (1986) Chemical Geodynamics. *Annual Review of Earth and Planetary Sciences, 14*: 493-571.